The Processing, Microstructure and Creep Properties of Pb-free Solders for Harsh Environments

Sophie Godard Desmarest

Corpus Christi College

University of Oxford



Submitted for the degree of

Doctor of Philosophy

Trinity 2013

This thesis is dedicated to my parents and to my sister Clarisse.

Abstract

The Processing, Microstructure and Creep Properties of Pb-free Solders for Harsh Environments

Sophie Godard Desmarest
Corpus Christi College
Submitted for the Degree of Doctor of Philosophy, Trinity Term 2013

The constitutive mechanical behaviour with a focus on creep of Sn-Pb and various Sn-Ag-Cu based Pb-free solders in the 25–150°C temperature range has been studied using nanoindentation and various new meso-scale tests. All alloys have been studied as bulk wave soldering bars, as-received solder balls and solder joints. Ball Grid Array (BGA) solder joints in a typical electronic configuration were manufactured in-house using both Cu and Pd-Ag metallizations. Microstructural characterisation of all configurations used various types of optical and electron microscopy and showed that the solder pad metallization type played a major role in intermetallic compound (IMC) formation. There were comparatively fine and coarse-grained microstructures in both as-received solder balls and BGA solder joints depending on ball diameter. Nanoindentation creep measurements in the stress range 20–500MPa showed that grain boundary sliding occurred together with dislocation glide and dislocation climb in the low temperature (25–50°C) and high temperature (100–150°C) regimes respectively. Smaller grain sizes ($\prec 20\mu$m) encouraged grain boundary sliding that enhanced creep.

New elevated temperature mechanical tests were developed using the nanoindentation platform to enable testing of entire solder joints in shear and compression, with stresses in the 10^{-2}–3MPa range, more relevant to in-service conditions than those in nanoindentation. Meso-scale spherical indentation creep behaviour in compression on as-reflowed solder balls showed good agreement with that obtained by conventional nanoindentation. However, when BGAs were tested in shear, the solder microstructure had relatively little influence on the creep response, which was significantly less creep resistant than individual phases in the ball obtained by nanoindentation or the ball itself obtained by meso-scale spherical indentation. In shear, the creep conformed to diffusion controlled behaviour and interfacial microstructure was suggested to now control creep response, with the microstructure of the majority of the solder joint playing only a minor role.

Preface

The work described in this thesis was carried out by the author in the Department of Materials, University of Oxford between October 2009 and July 2013 under the supervision of Prof. Patrick Grant.

No part of this thesis has been previously submitted for a degree at this or any other university. The work of others has been freely drawn upon and is duly acknowledged in the text.

Some of the work described in this thesis has been published or presented elsewhere:

1. S. Godard Desmarest, Reliability of Pb-free solders for harsh environment electronic assemblies, *Materials Science and Technology*, 28 (3), 257-273, 2012.

2. S. Godard Desmarest, C. Johnston and P. S. Grant, Determination of Creep Properties of Pb-free Solders for Harsh Environments Using Meso-scale Testing, *High Temperature Electronics Conference*, International Microelectronics Assembly and Packaging Society, Albuquerque – USA, May 2012.

3. S. Godard Desmarest, C. Johnston and P. S. Grant, Lead-free Solder Development and Analysis for Aerospace Applications, *Tomorrow's Solders Conference*, Soldertec, Slough – UK, March 2013.

Acknowledgements

I am deeply indebted to my supervisor Prof. Patrick Grant for his guidance through all the steps of this work and for his continual support. I am very grateful for the time he dedicated to my work. I would also like to thank my co-supervisor Dr. Colin Johnston as well as Dr. Alison Crossley who allowed me to have full access to BegbrokeNano equipment and gave me opportunities to present my work at seminars and conferences.

I sincerely thank Ms. Gabriella Chapman and Mr. Chris Salter for their kind assistance on microscopy and for sharing the facilities. I remain indebted to Mr. Richard Turner, Mr. Richard Cripps and Mr. Trevor Knibbs for their engineering expertise and good humour. My thanks also go to Ms. Marion Beckett and Mr. Barry Fellows for administrative support.

I would like to acknowledge the financial support I received from the Engineering and Physical Sciences Research Council and my industrial sponsors Goodrich and Oxatec. I would like to thank Dr. Geoff Armstrong at Goodrich for his insight into industrial requirements for electronics in harsh environments, and friendly and enthusiastic support. I thank other funding bodies: the Institute of Materials, Minerals and Mining and Corpus Christi College that granted me the opportunity to travel to Albuquerque in the United States to present my research.

My special thanks go to Ms. Jan Pearson for her kindness and invaluable assistance in everything. I would also like to thank my friends in the Department: David Lee, Enzo Liotti, Aoife Kelly and Micaela Sousa for sharing their experience with me and being great friends. Thank you to my close friends in Oxford, in particular Sophie Bocksberger, Laura Droessler, Lise Lørup and Katja Yafimava for their invaluable friendship.

I would like to express my deep gratitude to Corpus Christi College for giving me opportunities of personal development and for trusting me in a two-year position as Assistant Dean of the College. I have valued this responsibility and enjoyed it immensely. The wonderful Corpus community allowed me to meet many inspiring individuals.

Finally, I would like to express my devotion to my parents. My deepest love and admiration is for them. Thank you to my beloved sister Clarisse who has been an inspiration throughout my academic life and has guided my steps towards the British Isles.

Contents

1 Introduction **1**

1.1 The use of Sn-Pb solder alloys for harsh environment industries 1

1.2 Solder joints in microelectronic packages 3

1.3 Objectives 6

2 Literature Review **9**

2.1 Towards a 'drop-in' Pb-free solder material for Sn-Pb replacement 9

2.1.1 The worldwide move to Pb-free 9

2.1.2 Solder alloys for harsh environments 14

2.1.3 The microstructure of Sn-Pb and SAC solder alloys 17

2.1.4 Specific issues to harsh environments 20

2.2 Failure mechanisms of solder alloys in electronic assemblies 23

2.2.1 Deformation modes 23

2.2.2 Thermomechanical fatigue in Sn-Pb solder joints 24

2.2.3 Thermomechanical fatigue in Pb-free solder joints 25

2.3 Electronic package lifetime prediction 28

2.3.1 Effect of physical design on the reliability of electronic packages . 29

2.3.2 Accelerated thermal cycling (ATC) 30

2.3.3 Pb-free solders thermal fatigue reliability studies 33

2.4 Constitutive behaviour of solder alloys 35

2.4.1 Creep mechanisms in Pb-free solder joints . . . 36
2.4.2 Determination of constitutive properties . . . 39
2.5 Conclusions . . . 43

3 Experimental procedures **45**
3.1 Ball grid array (BGA) manufacture . . . 45
3.2 Microstructural characterisation . . . 50
3.2.1 Sample preparation . . . 50
3.2.2 Optical microscopy . . . 50
3.2.3 Scanning electron microscopy (SEM) . . . 51
3.2.4 Electron backscatter diffraction (EBSD) . . . 51
3.2.5 Focused ion beam microscopy (FIB) . . . 52
3.2.6 Atomic Force Microscopy (AFM) . . . 53
3.3 Mechanical testing . . . 53
3.3.1 Nanoindentation . . . 53
3.3.2 High temperature nanoindentation creep . . . 56
3.3.3 High temperature meso-scale testing . . . 59

4 Microstructural characterisation of solder alloys **64**
4.1 Bulk solder alloys and as-received solder balls . . . 64
4.1.1 Bulk solder alloys . . . 64
4.1.2 As-received solder balls . . . 65
4.2 BGA solder joints . . . 66
4.2.1 SAC305 solder joints . . . 66
4.2.2 SAC387 solder joints . . . 70
4.2.3 Innolot solder joints . . . 73
4.2.4 Sn-37Pb solder joints . . . 74

4.2.5 Influence of the metallization pad on SAC305 solder joint microstructure . . . 74
4.3 The solder joint/metallized pad interface . . . 77
4.3.1 The solder/Cu pad system . . . 77
4.3.2 The solder/Pd-Ag system . . . 81
4.4 Conclusions . . . 81

5 Grain structure of solder alloys **84**
5.1 Sn anisotropy . . . 84
5.2 As-received solder balls . . . 86
5.3 Grain characterisation of solder joints . . . 90
5.4 Thermal ageing of SAC solder joints . . . 93
5.5 Conclusions . . . 97

6 Nanoindentation creep testing **98**
6.1 Introduction and objectives . . . 98
6.2 Temperature-dependency of creep . . . 99
6.2.1 Hardness and elastic modulus . . . 99
6.2.2 Creep stress exponents . . . 101
6.2.3 Creep activation energy . . . 107
6.2.4 Limits to nanoindentation . . . 111
6.3 Effect of microstructure and Sn grain size . . . 114
6.3.1 Effect of microstructure . . . 114
6.3.2 Effect of solder manufacturing route . . . 118
6.4 Conclusions . . . 120

7 Meso-scale creep testing **122**
7.1 Compression of ceramic BGAs (CBGAs) – Test (2) . . . 123

7.2 Spherical indentation of as-reflowed solder balls – Test (3) 124

7.2.1 Background to spherical indentation 125

7.2.2 Results and discussion 126

7.3 Meso-scale shear testing of CBGAs – Test (4) 129

7.3.1 Stress-strain behaviour 129

7.3.2 Advantages and disadvantages of meso-scale shear testing 138

7.4 Conclusions 140

8 Conclusions and Future Work **142**

References **146**

List of Figures

1.1 Schematic of first-level packaging with (a) substrate; (b) wire bond; (c) flip-chip; and (d) tape-automated bond (adapted from [7]). 3

1.2 Schematic of second-level packaging. Typically, the substrate is made of a 250μm bismaleimide-triazine (BT) laminate with 18μm Cu thickness and is attached to an FR-4 laminate board with solder balls with diameters of 600–900μm and pitch sizes $\sim$0.9–1.3mm [8]. 4

1.3 Main factors responsible for failure of electronic solder joints in aerospace applications [9]. 4

1.4 Schematics of (a) a ball grid array (BGA) electronic assembly as found in the first or second level of microelectronic packaging; (b) temperature cycling induced shrinking of a BGA; and (c) optical micrograph of failure in a Sn-Ag-Cu BGA due to thermal cycling in the 0–100°C temperature range [10]. 5

2.1 Ranking of the toxicity of possible alloying elements for (a) health and safety; and (b) environmental impact [22]. 12

2.2 Binary phase diagrams of (a) Sn-Ag; (b) Sn-Cu; (c) Cu-Ag; and (d) Sn-rich part of the Sn-Ag-Cu ternary phase diagram [54]. Three IMCs may form in SAC systems: Ag_3Sn from the reaction of Sn and Ag, Cu_6Sn_5 and Cu_3Sn from the reaction of Sn and Cu. Cu_3Sn does not normally form at the eutectic point unless the Cu concentration and the temperature are high enough. 18

2.3 Scanning electron microscope (SEM) secondary electron image showing typical SAC387 microstructure [55]. SAC387 is a precipitation hardened alloy with Ag_3Sn and Cu_6Sn_5 IMCs dispersed in β-Sn. While Cu_6Sn_5 IMCs are equiaxed particles, Ag_3Sn are frequently elongated plates. . . . 19

2.4 SEM image showing the microstructure of eutectic Sn-37Pb (a) after slow cooling; (b) after rapid cooling [35]; and the microstructure of as-cast SAC387 (c) equiaxed and (d) dendritic β-Sn surrounded by a fine two-phase (Ag_3Sn + Cu_6Sn_5) eutectic matrix [58]. Slow cooling leads to an equiaxed structure for both eutectic Sn-Pb and SAC solders. Due to solder joint processing, the microstructure of SAC solders is very often dendritic. Upon recrystallization, the dendritic structure may evolve to the equiaxed structure. 20

2.5 Sn pest in as-cast samples with increased times of exposure to low temperatures from (a) to (f). (a) as-cast sample; (b) surface discoloration; (c) initial warting; (d) extensive warting; (e) cracking of surface layer; and (f) complete disintegration [66]. 21

2.6 SEM image of (a) fatigue crack initiation in dendritic Sn-3.5Ag alloy; and (b) fatigue crack propagation in dendritic Sn-3.5Ag alloy strained to 1% vertically, showing various growth paths: intergranular along Sn-dendrite boundary (A), intergranular along subgrain boundary (B) and transgranular through Sn-Ag eutectic (C) [88]. 26

2.7 SEM images of (a) unaged; (b) aged at 150°C for 1000 hours IMC layer at a SAC305/Cu pad interface showing the growth of the IMC layer with thermal ageing [93]; (c) eutectic Sn-Pb/Cu; (d) SAC387/Cu under bump metallurgy (UBM) interfaces showing the sharp elongated IMCs of Pb-free solder joints as opposed to the smoother IMC layer for Sn-Pb solder joints [10]; and (e) typical failure along a Pb-free solder joint/pad interface [94]. 27

2.8 Schematic of Solder Mask Defined (SMD) and Non Solder Mask defined (NSMD) pads 30

2.9 Creep hysteresis curves for various Sn-Pb and SAC solders of a chip resistor during a 90 min thermal cycle from 150°C to −40°C for a constant strain range [98]. 31

2.10 Scaled characteristic life (number of cycles to 63.2% of the total cycles to failure) against the average cyclic shear from failure distributions of SAC387, SAC396 and Sn-Pb soldered assemblies subjected to accelerated thermal cycling under different thermal conditions (0 to 100°C, -40 to 125°C, -55 to 125°C). A cross-over point at 6.2% cyclic shear strain was observed. At the left of the cross-over point, SAC assemblies had longer lives than Sn-Pb assemblies [102]. 34

2.11 Creep deformation map of Pb-based and Pb-free solder alloys (adapted from [107]). Dislocation glide occurs in the high stress region for all homologous temperatures (dislocations moving along a slip plane). Dislocation creep occurs at medium stresses and when $T_h \succ 0.5T_m$ (dislocations climbing away from dislocation barriers, diffusion controlled). Lattice diffusion mechanisms occur at low stresses and high temperatures (migration of interstitial atoms and lattice vacancies along the gradient of a grain boundary in the presence of tension or compression pressure in reversed directions). In materials with a high volume fraction of grain boundaries, diffusion creep was significant [108]. 36

2.12 Transmission Electron Microscopy (TEM) image of (a) the initial microstructure of Sn-3.5Ag; and (b) the pinning of the dislocations by Ag_3Sn particles after creep deformation induced by loading (22MPa at 60°C with a strain rate of $10^{-4}s^{-1}$) [109]. 38

2.13 Main factors influencing the mechanical properties of solder alloys . . . 43

3.1 Geometries of (a) the top of the FR-4 board without and with solder mask; (b) the cross-section of the FR-4 board; (c) the top of the alumina board with Cu pads; and (d) the cross-sections of the ceramic boards with Cu and Pd-Ag pads. 46

3.2 (a) SAC305 solder balls (600, 500 and 400μm diameters); (b) FR-4 BGA manufactured from solder balls with an initial diameter of 600μm; (c) ceramic BGA (CBGA) manufactured from solder balls with an initial diameter of 400μm and (d) 600μm; (e) initial FR-4 board with its Cu pads; (f) after solder paste deposition onto 4 Cu pads; (g) after placement of 4 solder balls; and (h) after the first reflow. 48

3.3 The key steps of the BGA manufacturing process. Alignment was checked by optical microscopy before each step. 49

3.4 JEDEC recommended reflow profile for BGA manufacturing (*black*) with typical industry reflow (*blue*) and reflow profile used for in-house (*green*) (a) Pb-free; and (b) Sn-37Pb BGA manufacturing (adapted from [169]). . 49

3.5 Optical image of the cross-section of a typical in-house manufactured SAC305 solder joint. 50

3.6 EBSD Sn diffraction patterns for different crystal orientations (a) and (c) before indexing; and (b) and (d) after indexing the Kikuchi patterns. . . 52

3.7 NanoTest platform showing the (a) chamber and (b) motor control units; and (c) schematic of the pendulum based nanoindentation system (adapted from MicroMaterials Ltd.). 53

3.8 (a) Schematic of indenter and specimen surface geometry at full load and full unload for a Berkovich indenter [170]; and (b) typical indentation load versus displacement curve for elastic-plastic loading followed by elastic unloading. h_r is the depth of the residual impression, h_t is the depth from the original specimen surface at maximum load P_{max}, h_e is the elastic displacement during unloading and h_s is the distance from the edge of the contact to the specimen surface at full load. Upon elastic reloading, the tip of the indenter moves through a distance h_e, and the eventual point of contact with the specimen surface moves through a distance h_s [170]. 55

3.9 Schematic of the high temperature testing equipment (MicroMaterials Ltd.). Both the indenter tip and the sample were heated to the same temperature. 57

3.10 Experimental creep results on bulk SAC387 at 25°C and the best-fit to Equation 3.3.7. 58

3.11 (a) Elevated temperature creep curves of SAC387; and (b) illustration of the approach to the determination of the creep activation energy, Q. . . . 59

3.12 (a) Schematic of the set-up of the high temperature meso-scale shear test; (b) heating of the liquid cell by means of two cartridge heaters and a thermocouple linked to an automatic temperature controller; and (c) detail of the interior of the liquid cell with two BGAs and a piece of fused silica attached to a central stub. 61

3.13 (a) The NanoTest platform with the liquid cell and temperature control unit; (b) the liquid cell was covered with an insulating cap during experiments to minimise heat dissipation; and (c) the liquid cell filled with low viscosity oil. A thermocouple was fitted in the cell so that the oil temperature was monitored at all times; (d) set-up for shear testing of a CBGA; and (e) set-up for spherical indentation of as-reflowed solder balls. 62

3.14 Schematic and summary of the various tests carried out in the NanoTest platform: Test (1) – elevated temperature nanoindentation on a bulk sample; Test (2) – compression test of the BGA assembly; Test (3) – spherical indentation of an as-reflowed solder joint; and Test (4) – shear test of a BGA assembly. 63

4.1 Scanning electron microscope (SEM) secondary electron images for (a) eutectic Sn-37Pb; (b) SAC387; (c) Innolot solder alloys. 65

4.2 (a) Secondary electron image of bulk Sn-37Pb solder alloy; and (b) Pb; and (c) Sn EDS elemental maps from the imaged area. 65

4.3 Secondary electron images of (a) and (b) 400μm diameter as-received SAC305 solder balls; and (c) and (d) 600μm diameter as-received SAC305 solder balls. 66

4.4 (a) Secondary electron image and (b) EDS spectra taken from region 1 to 4 of a cross-section of an as-reflowed SAC305 solder joint. 67

4.5 Secondary electron images of a cross-section of a SAC305 BGA solder joint with (a) relatively fine Ag_3Sn IMCs; and (b) Cu_6Sn_5 IMCs dispersed within the β-Sn matrix. 67

4.6 Secondary electron images of Cu_6Sn_5 whiskers (a) solid-type; and (b) hollow-type. 68

4.7 (a) Schematic diagram showing the growth of a Cu_6Sn_5 rod using the ledge mechanism model [177]; and (b) SEM secondary electron images of Cu_6Sn_5 rods. The arrows point at a shear band along the dislocation line. 69

4.8 Secondary electron images of Cu_6Sn_5 rods with Ag_3Sn nano-particles on their surface. 69

4.9 Secondary electron images of Ag_3Sn IMCs in the bulk of a SAC305 solder joint. 70

4.10 Secondary electron images of (a) the network of Ag_3Sn and Cu_6Sn_5 IMCs in the bulk of a SAC305 solder joint; (b) longer etching revealed the Cu_6Sn_5 whiskers; and (c) tilted view of the IMC network showing the small rod-like shape of some of the Ag_3Sn IMCs. 70

4.11 Secondary electron images of the network of Ag_3Sn IMCs. Ag_3Sn particles aligned due to their elongated structure, providing an interlocking network around the β-Sn dendrites. 71

4.12 Secondary electron images of the cross-section of a SAC387 BGA solder joint with Cu pad metallization: (a) bulk of the SAC387 solder joint; (b) SAC387-Cu pad interface showing the typical Cu_6Sn_5 scallop-shaped IMC layer; and (c) long Ag_3Sn IMCs developed preferentially from the IMC layer. 71

4.13 Secondary electron images of a deep etched BGA SAC387 solder joint with (a) the residual network of Ag_3Sn IMCs after β-Sn was etched away; (b) surface of the solder ball with large IMCs; (c) Hopper-like Ag_3Sn plate; (d) Ag_3Sn plates often developed in the vicinity of Cu_6Sn_5 whiskers; and (e) solid and hollow-type Cu_6Sn_5 whiskers. 72

4.14 Typical secondary electron images of a SAC387 solder joints and associated EDS spectra. 72

4.15 Secondary electron images of (a) the cross-section of an Innolot solder joint; and (b) deep etched Cu pad-solder joint interface revealing large Ag_3Sn plates. 73

4.16 Secondary electron image of a cross-section of an Innolot solder joint and Sn, Ag, Cu, Ni and Sb EDS elemental maps of the scanned area. . . 74

4.17 Secondary electron images of (a) a Sn-37Pb BGA with FR-4 boards; and (b) the cross-section of a joint. 74

4.18 Secondary electron image and corresponding Pb, Sn and Cu EDX elemental maps. 75

4.19 Secondary electron images of Ag_3Sn plates from deep etched SAC305 BGA solder joints manufactured with Pd-Ag pads. 75

4.20 Secondary electron images of the cross-section surface of a Sn-3.5Ag solder joint manufactured with Cu pads showing Cu_6Sn_5 and Ag_3Sn IMCs and corresponding morphologies from deep etching. 76

4.21 Secondary electron images of (a) a SAC305 solder/Cu pad interface showing Cu_6Sn_5 scallops; (b) detail of the interface with Cu_3Sn and Cu_6Sn_5 layers for a thermally aged sample (8 hours at 130°C). The grain structure of the Cu pad was also visible; and (c) micro-voids at the Cu pad/Cu_3Sn interface of the thermally aged sample. 78

4.22 Secondary electron images of the deep etched interface layer at the Cu pad of a SAC305 BGA solder joint: (a) tilted view of the Cu/solder cross-section; and (b) a plan view of the Cu pad, with small Ag_3Sn particles developing on or pinning the Cu_6Sn_5 scallops. 79

4.23 Deep etched SAC305 BGA solder joint showing Ag_3Sn particles alignment. 80

4.24 Secondary electron images of (a) the three-dimensional morphology of the interfacial Cu_6Sn_5 layer with the beginning of the growth of a whisker; (b) Cu_6Sn_5 whiskers developed from the IMC layer in a deep etched BGA solder joint; and (c) overall whisker distribution in a further etched BGA solder joint so that only the outer shell structure of the ball remained. 80

4.25 (a) Secondary electron image; and (b) EDX elemental maps of a Al_2O_3 board/Pd-Ag/SAC305 solder joint interface. 81

4.26 Secondary electron images of (a) deep etched SAC305 BGA solder joint with Pd-Ag metallization revealing the pad/solder interface; (b) deep etched Al_2O_3 board/Pd-Ag/Innolot BGA interface; (c) tilted view of the Al_2O_3 board/Pd-Ag pad/Innolot interface; and (d) top view of the IMC layer for an Innolot solder joint manufactured with Pd-Ag metallization pads. 82

4.27 Secondary electron image and EDS elemental maps from the interior of a SAC387 solder ball and solder joint manufactured with Pd-Ag metallization pads. 82

5.1 Schematic of single-crystal β-Sn (body centred tetragonal structure) [186]. 85

5.2 Cross-polarized images of cross-sections of SAC305 as-received solder (a) entire 400μm ball; (b) higher magnification view of its grain structure; and (c) entire 600μm ball. Variations in grey scale defined domains with different crystallographic orientation of the β-Sn phase. 86

5.3 EBSD investigation of 400μm as-received SAC305 ball: (a) Sn unique grain colour map taken from the ball centre; (b) corresponding image quality map with misorientation angle grain boundaries (low in *blue*, medium in *green* and high in *red*); (c) grain size plot; (d) Sn orientation map;(e) misorientation plot; and (f) pole and inverse pole figures. 87

5.4 Cross-polarized images of cross-sections of 600μm diameter SAC305 as-received solder balls for two different cross-polarizing angles: (a) and (b) with a single nucleation point; and (c) and (d) multiple nucleation sites. 89

5.5 (a) Cross-polarized images of a cross-section of an entire 600μm SAC305 ball for two different cross-polarizing angles; (b) superposition of the EBSD unique grain colour map with a secondary electron image of the solder ball; (c) orientation map with schematics of Sn crystal orientation; and (d) inverse pole figure. 89

5.6 (a) Cross-polarized images of cross-sections of as-received Innolot solder balls (500μm diameter); (b) unique grain colour map of the EBSDed region in the centre of a 400μm diameter as-received solder ball; (c) corresponding inverse pole figure; and (d) misorientation angle distribution within the scanned area. 90

5.7 (a) Sn EBSD unique grain colour map; (b) orientation map; (c) image quality map with superposition of grain boundaries; and (d) inverse pole figure showing strong texture in the Sn phase, due to a single grain. 91

5.8 Cross-polarized optical images of a Cu pad/SAC305 (400μm diameter) BGA solder joint interface at two positions of the cross polarizer near the extinction position. 92

5.9 EBSD data of a SAC305 400μm ball joint: (a) Sn unique grain colour map; (b) phase composition map based on simultaneous EDS; (c) image quality map with superimposed grain boundaries (low angle grain boundaries in *blue*, medium angle grain boundaries in *green* and high angle grain boundaries in *red*); and (d) grain size distribution. 92

5.10 Cross-polarized images of SAC305 BGA manufactured from solder balls with initial diameter of (a) 400μm; and (b) 600μm. 93

5.11 Cross-polarized images of (a) as-received Sn-37Pb solder balls (500μm diameter); and (b) Sn-37Pb BGA manufactured from these solder balls. . 93

5.12 Orientation maps of a SAC387 solder joint (a) unaged and (b) after 28 hours at 100°C; (c) and (d) corresponding inverse pole figures; and (e) and (f) grain size distribution. 94

5.13 (a) Optical microscopy image of the cross-section of a SAC305 solder joint showing the EBSD analysis area; image quality maps with misorientation angle grain boundaries (low, medium and high angle grain boundaries in *blue*, *green* and *red* respectively) (b) after 3 hours and (c) after 6 hours of thermal ageing at 100°C; orientation maps of (d) after 3 hours and (e) after 6 hours ageing at 100°C; and (f) and (g) the corresponding inverse pole figures. 95

5.14 Secondary electron image of SAC305 solder joint after 6 hours of thermal ageing at 100°C. 95

5.15 (a) Unaged SAC387/Cu pad interface; (b) after 28 hours of thermal ageing at 100°C; (c) and (d) other interface locations after 28 hours ageing showing Sn grain boundary decohesion and sliding. 96

6.1 (a) Elastic modulus of bulk Innolot, SAC387, Sn and Sn-37Pb alloys for various temperatures determined from creep tests at a maximum load of 100mN; and (b) the corresponding hardness and its linear fitting with hardness coefficients. 100

6.2 Elastic modulus of Sn, eutectic Sn-Pb, SAC387, SAC305 and Innolot obtained by the nanoindentation study and results obtained in various studies using different testing techniques for comparison [88, 108, 143, 193–201]. 100

6.3 (a) Nanoindentation load versus displacement to maximum loads of 5, 10, 30 and 50mN in the 25–175°C temperature range for bulk SAC387; and (b) creep curves showing the penetration depth during a 600s dwell time at a 50mN maximum load in the 25–175°C temperature range. . . . 102

6.4 Secondary electron images of indents in bulk SAC387 after creep tests at 2, 5 and 10mN and temperatures in the 25–150°C range. Images in the same line are for a particular load, whilst images in the same column are for a particular temperature. 102

6.5 Creep curves for bulk Innolot, SAC387, Sn, Sn-37Pb at 25 and 150°C, under a constant 100mN load for 600s. 103

6.6 Strain rate versus stress curves used to obtain stress exponents for Test (1) on bulk Sn-37Pb, β-Sn, SAC387 and Innolot alloys at 100mN iso-load and 25°C. 104

6.7 Best-fit stress exponent for bulk β-Sn, Sn-37Pb, SAC387 and Innolot at 25°C determined by Test (1). 104

6.8 Best-fit stress exponent for bulk SAC387, β-Sn, Sn-37Pb and Innolot as a function of temperature at 100mN. 105

6.9 Strain rate versus stress curves for bulk (a) β-Sn; (b) Sn-37Pb; (c) SAC387; (d) Innolot creep tests at 100mN in the 25–150°C temperature range; and (e) all alloys and temperatures. 106

6.10 Secondary electron images of indents at 25°C in eutectic Sn-37Pb, SAC387 and Innolot for loads of 10, 50, 100 and 200 mN – (a) to (d), (e) to (h) and (i) to (l) respectively. Sn-Pb showed little cracking from 10 to 200mN; there was no cracking in SAC387, while there was extensive cracking in Innolot at all loads. The arrows in (d) show the cracking direction. 108

6.11 Secondary electron images of (a) tilted indent on bulk eutectic Sn-37Pb for a 10mN iso-load; (b) indent on bulk Innolot for a 200mN iso-load; and (c) indent on as-received SAC305 solder ball (400μm diameter) for a 10mN iso-load. 109

6.12 Creep activation energies for bulk (a) β-Sn; (b) Sn-37Pb; (c) SAC387; and (d) Innolot determined from elevated temperature nanoindentation creep measurements at 100mN. 110

6.13 Creep stress exponents of bulk SAC387 as a function of iso-load at 25 and 175°C. 113

6.14 (a) AFM indentation line height profile across an indent obtained after iso-loading at 5mN for 400s dwell time at 25°C in bulk SAC387; and (b) three dimensional profile of the indent and AFM scanning line. 114

6.15 Load versus depth curves for nanoindentation tests on various BGA cross-sections (from 500μm balls). 115

6.16 Secondary electron images of indents in as-received (a) 400μm SAC305 ball; and (b) 600μm SAC305 ball. 115

6.17 Load-depth indentation profiles to maximum loads of 2, 5, 10, 20 and 30mN for various indents in as-cast SAC305 solder balls with a diameter of (a) 400μm; and (b) 600μm. 116

6.18 Stress exponents as a function of iso-loads for as-cast SAC305 solder balls with diameters of 400 and 600μm determined at 25°C. 117

6.19 Secondary electron images of indents on an as-received 400μm SAC305 solder ball with increasing load. 117

6.20 Stress exponents at 25°C for bulk and as-reflowed Sn-37Pb, SAC387 and Innolot alloys. Cross-polarized images showing typical grain structure for both manufacturing routes and the three types of alloy. 119

6.21 Stress exponents at 25°C for coarse-grained as-received 600μm SAC305 balls and SAC305 BGA joint (from 500μm balls) and fine-grained as-received 400μm SAC305 balls. 120

7.1 Optical image and higher magnification views of SAC387 and SAC305 CBGAs inside the liquid cell. Alignment was carefully checked prior to testing. 123

7.2 Creep curves for CBGA compression tests at 25°C and various maximum loads: (a) SAC305 and (b) SAC387 CBGAs with Cu pad metallization; and (c) SAC305; (d) SAC387; (e) Innolot; and (f) Sn-37Pb CBGAs with Pd-Ag pad metallization. 124

7.3 Schematic of a spherical indenter of diameter D; a the radius of contact; and h the total depth of penetration (adapted from [229]). 125

7.4 Secondary electron images of an as-reflowed 600μm SAC305 BGA solder ball after spherical indentation at 500mN and 100°C. 126

7.5 (a) Load versus depth for spherical indentation at various loads on an as-reflowed SAC305 solder ball at 25 and 100°C; and (b) corresponding creep curves. 127

7.6 Strain rate versus stress for spherical indentation at various loads on an as-reflowed SAC305 ball at 25 and 100°C. 127

7.7 Secondary electron images of an as-reflowed Sn-37Pb solder ball after spherical indentation: (a) top of the ball; (b) side view of the ball; (c) higher magnification image of the side view; (d) top view of the impression on another ball; and (e) corresponding higher magnification image. 128

7.8 (a) Spherical indentation creep curves obtained at 500mN on as-reflowed Sn-37Pb, SAC305, SAC387 and Innolot solder balls at 25°C (*straight lines*) and 100°C (*dashed lines*); and (b) corresponding stress-strain curves for SAC305, SAC387 and Innolot alloys. 129

7.9 Optical image and higher magnification image of a SAC305 CBGA prior to shear testing. A fused silica sample was used for depth calibration at each testing temperature. 130

7.10 Creep displacement versus time for shear testing of a SAC305 CBGA (400μm balls) with Cu pad metallization for various holding loads (100–500mN) and temperatures (25, 50 and 100°C) including zoom in view of the small displacement region. 130

7.11 (a) Strain rate versus shear stress data for a SAC305 BGA (400μm balls) with Cu pad metallization; and (b) creep activation energy determination for SAC305 BGAs. 131

7.12 Optical images of (a) the liquid cell; and (b) top view of a SAC305 CBGA (600μm balls) with Cu pad metallization. 132

7.13 (a) Creep displacement versus time for SAC305 BGAs (600μm solder balls) with Cu pad metallization after shear testing at various holding loads (100–500mN) and temperatures (25 and 100°C); and (b) corresponding strain rate versus stress plot. 132

7.14 Creep activation energy determination for SAC305 BGAs (600μm solder balls). 133

7.15 Secondary electron images of (a) a SAC305/Pd-Ag pad interface; and (b) interior of the SAC305 solder joint after shear testing at elevated temperature. 134

7.16 Secondary electron images of a SAC305 CBGA (400μm balls) with Cu pad after shear testing at 140°C. The dashed lines show the approximate 45° direction of elongation to the applied shear stress direction; and (b) interior of the solder joint. The arrows point at IMCs pinning grains. . . 135

7.17 Strain rate versus stress behaviour for SAC305 CBGAs with Cu and Pd-Ag pads at 25, 50 and 100°C. 136

7.18 Shear testing results for SAC387 and literature data in the intermediate stress range from [237]. 137

7.19 Stress exponent as a function of temperature for different stress regimes for SAC387 and Sn-37Pb. Literature data for Sn-37Pb was taken from [140]. 138

7.20 The effect of temperature oscillations on displacement measurements during a creep test in shear using a meso-scale hot oil cell approach. The temperature (*red curve*) was measured in the liquid close to the tested solder joint. 139

7.21 Optical images of failures of a SAC305 assembly after testing. Failure occurred at the ceramic/Cu pad interface. 139

List of Tables

2.1 Major research and development industrial projects on the reliability of Pb-free solder electronic assemblies [12–19] 10

2.2 Typical temperature limits and performance requirements of electronic assemblies for various applications [35]. 14

2.3 Typical Coefficients of Thermal Expansion (CTE) for various materials involved in BGA manufacturing 29

2.4 Coffin-Manson parameters obtained for various solder alloys 32

2.5 Literature data for the Dorn power law and the Garofalo hyperbolic sine law (after Ma and Suhling [107]) [10, 135–144]. 41

3.1 Materials used for the manufacturing of BGAs. 47

5.1 Coefficient of thermal expansion and Young's modulus of body centered tetragonal Sn, and polycrystalline Cu and Cu_6Sn_5 [186]. 85

6.1 Activation energies of bulk solder alloys. σ/E was calculated with the average of the elastic modulus in the selected temperature range. 109

Chapter 1

Introduction

1.1 The use of Sn-Pb solder alloys for harsh environment industries

Solders are amongst the most important materials for connections in electronic assemblies. For over fifty years, solder alloys for electronic assemblies have been the near eutectic Sn-Pb alloys such as 60Sn-40Pb, 63Sn-37Pb and Ag-bearing 62Sn-36Pb-2Ag (in *wt*%). These alloys have been essential to the electronic industry and applications ranged from consumer products to space communication systems. However, Pb is a highly poisonous metal that induces damage mainly to the nervous, cardiovascular and immune systems as well as to the kidneys. Pb poisoning usually results from ingestion of Pb-contaminated food or water or from accidental ingestion of contaminated soil, dust, or Pb-based paint. It is the concern about the role of Pb in cognitive deficits in children that triggered widespread reduction in its use. A broad move to Pb-free was initiated in the United Sates in the 1980s, with regulations reducing the use of Pb in non-battery products, including gasoline, paints, water systems and solders for domestic appliances [1]. As far as electronic packages were concerned, the issue was not the Pb contained in solder connections, but the cumulative effect of Pb in the waste stream. When end-of-life products are sent to landfills for final disposition, Pb may become part of the leachate and find its way into groundwater supplies or the incinerated waste may result in Pb emissions. Besides, Pb being manipulated by suppliers con-

stitute a health and environment hazard. Legislative initiatives were taken to address the huge evolving toxic e-waste problem. The RoHS directive (Restriction of the use of certain hazardous substances in electrical and electronic equipment 2002/95/EC [2]) banning the use of Pb in most electronic equipments was adopted in February 2003 by the European Union and took effect in July 2006. The RoHS directive is closely linked to the WEEE directive (Waste Electrical and Electronic Equipment 2002/96/EC [3]) which sets collection, recycling and recovery targets for electrical goods. Two key organisations for the electronic industry are the Joint Electronic Device Engineering Council (JEDEC) whose committees define and develop standards for the microelectronics industry and the International Electronics Manufacturing Initiative (iNEMI) that is a consortium of electronics manufacturers, suppliers, associations, government agencies and universities. Pb-free assemblies were defined by JEDEC as 'solid-state devices that contain no more than 0.2 percent by weight of elemental Pb' [4]. iNEMI defined Pb-free products as having 'no Pb intentionally added, and joints that have less than 0.2% Pb by weight' [5].

Although the RoHS legislation only applies to products on the European market, almost all global manufacturers have moved to Pb-free as it is uneconomical to produce both RoHS-compliant and non-RoHS-compliant electronic assemblies in parallel. However, high reliability industries (defence, aerospace, some equipment for the automotive industry and other specific industries) are exempt from this regulation because of concerns over the reliability of Pb-free solders operating in harsh environments. These industries account for a marginal share of the world electronic equipment production (8% for the automotive industry, 7% for the aerospace and defence industry [6]) and find it increasingly difficult and expensive to continue using Sn-Pb-based electronics. Besides, the European exemption for harsh environment industries is likely to be lifted in the near future. Due to the short field use of Pb-free solders, little data on performance has been gathered during the last decade and questions arise as to the field performance of Pb-free solders in relation to accelerated testing, in particular in harsh environments.

1.2 Solder joints in microelectronic packages

Solder joints are the key components of electronic assemblies. They provide mechanical and electrical connection between the different parts of microelectronic packages (e.g. the Si chip and the organic circuit board). Electronic components are embedded in different assembly levels. Figures 1.1 and 1.2 show typical interconnect levels where solder alloys are involved. Discrete circuit elements such as resistors or diodes are usually embedded into individual components, the integrated circuit chips or dies, with extremely small terminals. First-level packaging achieves the function of mechanical protection, cooling and electrical connection to the printed circuit board, which forms the second-level packaging. The second-level packaging is needed as some components such as high power resistors, mechanical switches and capacitors are not readily integrated onto a chip. More complex applications, for instance mainframe computers, require multiple packaging. The chip-to-package interconnection in the first level is typically achieved by either wire bonding, tape-automated bonding or solder ball flip-chip. The substrates for first level-packages vary within the organic and ceramic groups of materials, depending on whether the package supports a single integrated circuit chip (single chip module) or more than one chip (multichip module).

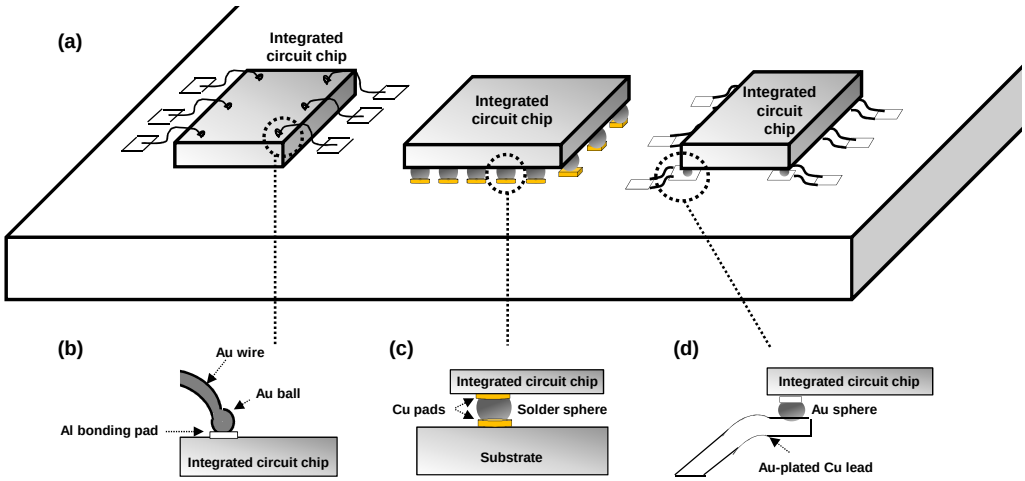


Figure 1.1: Schematic of first-level packaging with (a) substrate; (b) wire bond; (c) flip-chip; and (d) tape-automated bond (adapted from [7]).

Solder joints are the parts that are the most prone to failure in electronic packages. There are two major failure modes for board level solder joint interconnects: low-cycle fatigue of the solder joint as the assembly is submitted to constant/cyclic thermal

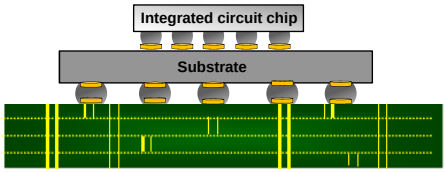


Figure 1.2: Schematic of second-level packaging. Typically, the substrate is made of a 250μm bismaleimide-triazine (BT) laminate with 18μm Cu thickness and is attached to an FR-4 laminate board with solder balls with diameters of 600–900μm and pitch sizes $\sim$0.9–1.3mm [8].

exposure due to both the environment and operation, and high-cycle fatigue caused by dynamic loads such as impact shock, vibration and bending, leading to brittle failure. Figure 1.3 shows the primary causes of failures in electronic equipment. Excessive temperatures of the critical components, such as semiconductors and transformers, are the dominant cause of equipment failure. The various parts of the assemblies respond

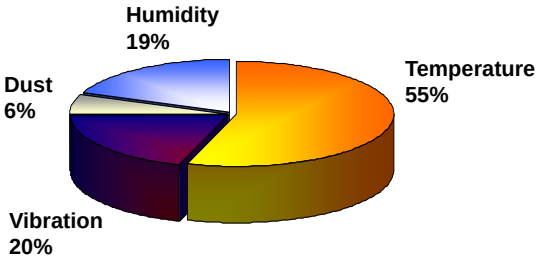


Figure 1.3: Main factors responsible for failure of electronic solder joints in aerospace applications [9].

differently to temperature cycles due to the thermal expansion mismatch between the various components, which induces low-cycle fatigue in solder joints. The board may shrink, as schematically represented in Figures 1.4 (a) and (b), or expand, resulting in mechanical stresses in the solder joints. Solders accommodate cyclic strains until eventual failure (Figure 1.4 (c)).

The low melting point of solder alloys means that their mechanical properties in operation depend on their creep behaviour. Even at room temperature, the homologous temperature of most solder alloys is higher than $0.5T_m$ (the homologous temperature is the ratio of the temperature of the material (T) to its melting temperature (T_m), in degrees Kelvin). Because of the severe thermal cycling in service, the creep properties of solder alloys play a key role in the performance and durability of electronic packages.

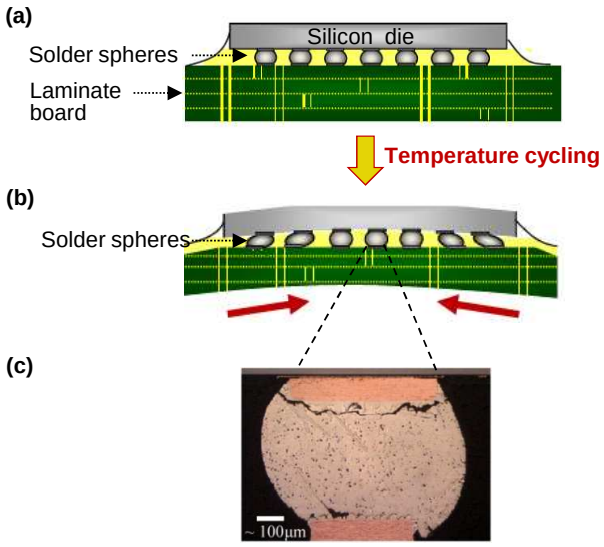


Figure 1.4: Schematics of (a) a ball grid array (BGA) electronic assembly as found in the first or second level of microelectronic packaging; (b) temperature cycling induced shrinking of a BGA; and (c) optical micrograph of failure in a Sn-Ag-Cu BGA due to thermal cycling in the 0–100°C temperature range [10].

Not only have most electronic assemblies moved to new solder alloys because of Pb-free requirements, but they also have to face the evolution of packaging architectures to advanced interconnects that meet the need for miniaturisation, to reduce both assembly sizes and electrical delay (in particular between processors and the memories they communicate with). The electronic industry is increasingly using surface-mount technology (SMT) with area-array packaging, in which packaged integrated circuits are directly soldered onto the pad surfaces of the printed circuit board (PCB), enabling significant space savings compared with traditional leaded packages. However, because of the lack of compliant leads, area-array packages such as Ceramic Ball Grid Arrays (CBGAs), Plastic Ball Grid Arrays (PBGAs), Ceramic Solder Column Carriers (CSCCs), Flip-Chip Ball Grid Arrays (FCBGAs), and Chip-Scale Packages (CSPs), rely entirely on the discrete solder balls absorbing the differential strains, which can lead to early failure. With the increase of I/O density requirements, the packages tend to increase in size while the pitch sizes get ever finer. Besides, grid array packages are costly, often the most expensive components on a PCB assembly. Therefore they cannot be deployed in a redundant design. The lack of redundancy creates critical path single points of failure (SPOFs). Hence failure of one of the packages can lead to

catastrophic system failures. A design that promotes solder joint reliability is the key to long lifetime electronic assemblies.

With the reduction of assembly sizes, thermal issues are increasingly critical for electronic packages. Electronics for aerospace must be able to withstand wider temperature range (-55–125°C) and longer lifetimes (up to 40 years) than domestic electronics (3–5 years). The Sn-Pb alloy combined properties necessary to a good solder alloy: wettability, low processing temperatures ($T_{m(Sn-37Pb)}$=183°C), limited reactivity, ductility (provided by Pb), relief of thermally induced strains, cost-effectiveness as well as more than thirty years of reliability data legacy. Whilst there is knowledge of traditional eutectic Sn-Pb alloy time to failure behaviour and there are reliable lifetime prediction models for the different assembly types, Pb-free solders do not have such a legacy of performance data and there remains a dearth of data for the constitutive behaviour of Pb-free solders under harsh environments.

1.3 Objectives

The sudden necessary move to Pb-free has fostered the development of many research projects which aim to find a suitable alloy for the electronics production that would match the manufacturing and reliability requirements of Sn-Pb. In order to validate a new solder material, extensive thermal cyclic testing is carried out to evaluate material behaviour under realistic operating conditions. Numerical models are commonly used to speed up electronic packages behaviour characterisation under different stress conditions and to compare various assembly design performances. One of the main criteria for reliable estimation of real life behaviour of electronics is the accuracy of the materials parameters inserted in the model. However, gaining this critical data by mechanical testing is an expensive and a long-winded process. Traditionally, new solders are firstly tested in bulk for weeks in tensile test machines to characterise their mechanical properties.

This thesis aims to investigate a quick and reliable way of characterising solder alloy constitutive properties for later insertion in numerical models. It focuses on the effect of temperature on the reliability of electronic packages. The Ball Grid Array

(BGA) interconnect was selected for this thesis as it is now a major electronic package architecture for the semiconductor industry. It offers many advantages: good reliability, reduced demands on coplanarity, self-centering, good PCB assembly yields, high interconnect density and fast design-to-production cycle time [11]. BGAs were manufactured in-house utilising alloys from the current preferred Pb-free alternative Sn-Ag-Cu alloy family and Sn-37Pb for solder connections between Al_2O_3 and FR-4 boards. Three solder balls sizes (400, 500 and 600μm) were used and two commonly used metallizations were studied (Cu and Pd-Ag).

Nanoindentation was investigated as a tool to characterise quickly the mechanical behaviour of various solder alloys at room and elevated temperatures. However, nanoindentation studies, like the majority of studies to determine the mechanical properties of solder alloys, have been carried out on bulk alloys, which means that the results are not necessarily relevant to the scale of microelectronic solder joints. Therefore a primary objective was to develop also an alternative method that would speed up the mechanical characterisation process in a test at a relevant length scale for BGAs, and thus provide reliable data for the development of new Pb-free solder materials for aerospace applications. The nanoindentation platform was modified to allow for the testing, especially creep, at room and elevated temperatures of single solder balls and BGA packages in compression and in shear. The constitutive behaviour of the studied alloys in the various testing conditions was characterised and compared with bulk results. At all stages, electron and other microscopies were used extensively to relate mechanical properties to the evolving microstructures.

The thesis is arranged as follows.

Chapter 2 reviews the literature concerning: (i) possible drop-in replacement solder alloys for the traditional Sn-Pb alloy; (ii) microstructure, mechanical properties and failure mechanisms of solder alloys; (iii) solder alloy constitutive behaviour characterisation; and (iv) lifetime prediction techniques for interconnect materials.

Chapter 3 describes the experimental methods including the in-house BGA manufacturing process, the microstructure characterisation techniques, the nanoindentation and meso-scale testing equipment and associated testing procedures.

Chapter 4 focuses on the microstructure of bulk solder alloys, as-received solder

balls and solder joints.

Chapter 5 characterises the grain structure of bulk solder alloys, as-received solder balls and solder joints.

Chapter 6 presents high temperature nanoindentation creep results on selected alloys and analyses the effect of microstructure and grain size on nanoindentation creep.

Chapter 7 is devoted to the meso-scale tests at room and elevated temperatures up to 100°C. It is divided into the following sections: (i) entire BGA compression tests; (ii) spherical indentation of as-reflowed single balls; and (iii) shear testing of entire BGAs.

Chapter 8 summarizes the main results found in this thesis and gives a brief description of suggested future work.

Chapter 2

Literature Review

2.1 Towards a 'drop-in' Pb-free solder material for Sn-Pb replacement

2.1.1 The worldwide move to Pb-free

Research on Pb-free soldering for electronic assemblies began in the early 1990s, when the US government wanted to restrict the use of Pb for health and environmental reasons but was unable to legislate because of the lack of Pb-free substitute materials for Sn-Pb. Research projects were subsequently catalysed by European Union legislations such as the RoHS and the WEEE directives [2, 3] as well as by the efforts of the Japanese government to encourage a move to Pb-free from their electronic manufacturers. Although the US does not have federal legislation regarding Pb in electronics, several States have enacted laws that legislate the content, manufacture and disposal of Pb in electronic assemblies. Since the first regulation projects, many industry groups and consortia have recommended a wide variety of compositions as shown in Table 2.1.

In 1994, an estimated 10^{13} soldered interconnections were manufactured per annum [20]. With the growth of the electronics industry, this number is likely to have increased substantially, rendering solder alloys development even more critical. Sn-Pb has been used successfully for decades because of its solderability and reliability. The Sn-Pb eutectic composition is Sn-37Pb (*wt*%). Sn-37Pb is a low melting point solder,

Table 2.1: Major research and development industrial projects on the reliability of Pb-free solder electronic assemblies [12–19]

Name of Project	Years	Participants	Short-listed solder materials for trials	Main conclusions
UK-DTI Department of Trade and Industry Lead-Free Project	1991-1993	GEC, UK BNR Europe (now Nortel), UK Multicore Solders (now Henkel Loctite Adhesives), UK	Bi-42Sn Sn-9Zn Sn-5Sb Sn-3.5Ag Sn-0.7Cu	Eliminated due to poor mechanical properties and low melting point Eliminated due to the corrosion of the zinc phase Eliminated due to the too high melting point
NCMS National Center for Manufacturing Sciences	1992-1996		Sn-58Bi Sn-3.5Ag-4.8Bi and Sn-3.5Ag	For consumer electronics and telecommunications applications For consumer electronics, telecommunications, aerospace and automotive applications
JEIDA Japan Institute of Electronics Industry Development Association	1998-1999		Sn/2-4Ag/0.5-1Cu for wave and reflow soldering	
IDEALS Improved Design Life and Environmentally Aware Manufacturing of Electronics Assemblies by Lead-Free Soldering	1996-1999	Multicore Solders Ltd., UK National Microelectronics Research Centre, Ireland Philips CFT, Netherlands Siemens AG, Germany Witmetaal BV, Netherlands	Sn-3.8Ag-0.7Cu eutectic alloy for reflow soldering Sn-3.8Ag-0.7Cu0.25Sb for general purpose wave soldering use Sn-5Bi-2Sb-1Ag for single-sided wave assembly	A Pb-free soldering technology based on SnAgCu(Sb) and SnBiSbAg alloys is technically and industrially viable
NCMS High Temperature Fatigue Resistant Solder Project	1996-2001	Allied Signal, US; Amkor Technologies, US Delphi Delco Electronics Systems, US Ford Motor Company, US Heraeus Corporation, US Indium Corporation, US Johnson Manufacturing, US Rockwell International Corporation, US Iowa State University, US; NIST, US	• Sn-3.5Ag Sn-4.0Ag-1.0Cu Sn-2.5Ag-0.8Cu-0.5Sb Sn-4.6Ag-1.6Cu-1Sb-1Bi Sn-3.3Ag-1Cu-3.3Bi Sn-3.5Ag-1.5In • For SMT applications Idem + Sn-4.0Ag-0.5Cu	• Six Pb-free alloy compositions were identified that exhibit fatigue performance superior to the industry standard eutectic Sn-Ag alloy during -55 ° C to +160 °C cycling of a wide range of components • Seven Pb-free alloys cycled with BGA packages through 0 °C to +100 °C and -40 °C to +125 °C cycling all outperformed Sn-Pb eutectic solder
NEMI Lead-free Assembly Project	1999-2002	NEMI Members	Sn-3.9Ag-0.6Cu (+/- 0.2%) for reflow Sn-0.7Cu for wave soldering	Electronic components with Pb-free are more reliable than their Sn-Pb counterparts
JIEP Low Temperature Lead-Free soldering	2000-2002	JIEP (Japan Institute of Electronics Packaging)	Sn-8Zn-3Bi	Thermal exposure beyond 125 °C may cause degradation of the Sn-8Zn-3Bi/Cu interface due to severe diffusion of Cu and Sn. Humidity/temperature degrades the Sn-8Zn-3Bi/Cu joint due to Zn segregation and coarsening and oxidation.
LEAP Lead-free Electronics in Aerospace Project	2004-2009	AIA - Aerospace Industries Association, US ARINC - Aeronautical Radio, Inc., US GEIA - Government Engineering and Engineering Technology Association, US IEC - International Electrotechnical Commission		Development of standards and guidelines for the electronics industry
ELF IPT Executive Lead-Free Integrated Process Team	2004-2009	Department of Defense (DoD), NASA and the Federal Aviation Administration (FAA)		Focused on awareness, training and policy.
PERM Pb-free Electronics Risk Management	2009-now	Aerospace Industries Associations (AIA)		Addresses research coordination, standards, training, communications, supply chain, advocacy, international cooperation.

with a eutectic temperature of 183°C, a reduction of melting temperature by almost 50°C from pure Sn at 232°C. Besides giving a low melting point eutectic, Pb has many benefits for a solder alloy: it provides ductility to the Sn-Pb solder and it reduces the surface tension of Sn and enhances wettability. Eutectic Sn-Pb solder has a very low wetting angle on Cu (11°) compared with that of pure Sn on Cu (35°) [21], it also has significant solid solubility in Sn, strengthens the Sn phase but does not entail the formation of intermetallic compounds (IMCs) with Sn, so that the alloys do not contain potentially brittle phases. Furthermore, Pb is cheap.

A Sn-Pb replacement alloy must comply with many soldering requirements. It must have a melting point (T_m) that is low enough to enable processing and to avoid component damage ($T_m \prec 230°C$) and high enough to withstand the operating temperature range from $-55°C$ to $+125°C$ ($T_m \succ 175°C$) [1]. Also, any mushy range of more than a few degrees is undesirable due to the danger of hot cracking developing during freezing, so a eutectic or near-eutectic composition is desirable. Besides, a solder must wet and bond to a metallic substrate, therefore constituents of the solder alloy must form IMCs with Cu, Ni and other metallizations used in electronic assemblies. Sn and In are the only two low melting elements that have these properties. Sn is preferred because of the high cost and limited availability of In. It also forms generally well understood IMCs with Cu.

Sn-Ag was the basis for the development of Pb-free solders. Alloying elements were subsequently added to Sn-Ag to improve its solderability and lower its melting point. Given the drive for the move to Pb-free was the toxicity of Pb, both during the manufacture of electronics but also when the electronics were discarded in landfills at the end of their life, resulting in possible contamination of ground waters an subsequent human poisoning, alternatives to Sn-Pb had to be free from similar risks. Figure 2.1 shows the toxicity ranking for both health and the environment impact of likely alloying elements.

One of the aims of solder alloys development was to improve their creep resistance, which is the main life-limiting property of electronic assemblies. Methods for raising an alloy creep resistance include solid solution strengthening and dispersion hardening. Alloying elements such as Cu, Bi, Zn, Sb and In were considered to be the

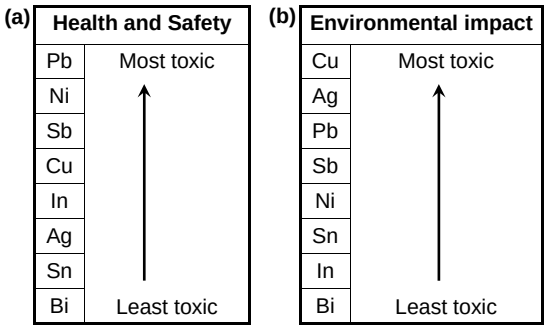


Figure 2.1: Ranking of the toxicity of possible alloying elements for (a) health and safety; and (b) environmental impact [22].

least toxic metals to be added to eutectic Sn-Ag in binary or ternary compositions. Zn oxidises quickly and must be reflowed in a reducing environment that is not typically available in the industry. The addition of In lowers the liquidus of the alloy but is too expensive to be used in electronics assembly processing. Ni enables IMC formation and has a solid solution hardening effect. Bi and Sb both provide solid solution hardening, but while Bi lowers the liquidus of Sn-based systems, Sb increases the liquidus temperature. Lowering the melting temperature of a solder also means higher homologous temperature in service, which enhances thermally activated processes (creep and grain growth), reducing the reliability of solder joints. Therefore Bi and Cu were the main alloying elements added to enhance the performance of eutectic Sn-Ag. Furthermore, the addition of Cu to a Sn matrix increases the hardness of the matrix more than the addition of Ag [23]. There are two reasons for such behaviour. First, the volume fraction of Cu_6Sn_5 is always larger than that of Ag_3Sn for the same *wt*% of Cu or Ag; secondly, the bulk hardness of Cu_6Sn_5 ($\sim$4.5GPa) is much higher than Ag_3Sn ($\sim$1.5GPa) [24].

Preferred solder materials have been identified but there is no 'drop-in' replacement alloy for Sn-Pb eutectic. Nonetheless, since 2000, the industry has converged towards the near ternary Sn-Ag-Cu (SAC) solder system. SAC solders are now considered the most suited to replace Sn-Pb solder because they exhibit good mechanical properties (in particular strength, elongation, creep and fatigue resistance). All alloy compositions will hereafter be expressed as Sn-xX-yY, where X and Y are alloying elements in Sn, with the composition being x mass fraction *100 of element X, y mass fraction *100 of element Y and remainder being Sn. The alloys studied by various large

industry consortia include Sn-3.8Ag-0.7Cu (SAC387) and Sn-4.0Ag-0.5 Cu (SAC405) in the EU, Sn-3.9Ag-0.6Cu (SAC396) in the US and Sn-3.0Ag-0.5Cu (SAC305) in Japan [25, 26]. The choice of the SAC305 alloy by Japanese industry was partly due to concerns over patent issues [27].

Many potential applications have not been studied systematically across the full SAC family and debate still continues over which alloy to use. The IPC Solder Products Value Council showed that there is no significant reliability difference between SAC305, SAC405 and SAC387 and recommended SAC305 as a general Pb-free solder paste alloy replacement [28]. However, in recent studies, SAC387 has exhibited improved performance under accelerated thermal cycling [29]. Sn-xAg-Cu solders with high silver contents (x=3–4 wt%) are reported to have long thermal fatigue lives, lower melting points and good solderability. However, they have poorer reliabilities in drop tests than solders with Ag content less than 2 wt% because of their greater hardness. Besides, their high Ag content makes them more expensive [30]. A survey gathered the replies from 48 European organisations and showed that in 2002, SAC alloys accounted for approximately 70% of the market for reflow soldering [31]. Currently, SAC305 and SAC387 are the most widely used Pb-free solder paste alloys for surface mount assemblies. The melting temperature of eutectic SAC alloys is close to 217°C, compared with a eutectic melting point of 183°C for Sn-37Pb. Therefore, a drawback for processing Pb-free solders is the higher reflow temperatures required, which leads to increased interfacial reactions and subsequent decreased soldered joint reliability.

Several companies have started abandoning first generation SAC solders [32] as a few reports highlight problems encountered with this alloy [33]. In particular, SAC solders do not match the requirements for high ductility, low modulus and enhanced impact resistance required for mobile electronics and flip-chip interconnects of high-performance systems [34]. For those cases, low-Ag or low-solute SAC solders have been recommended. But these alloys have unstable microstructure and other mechanical property drawbacks. Additional alloying is being investigated in order to solve these problems.

2.1.2 Solder alloys for harsh environments

Sn-Pb and In-Pb are currently the required solder alloys for the assembly of spacecraft electronic hardware. There have been fears that a RoHS2 directive would expand the RoHS scope to all electrical and electronic equipment sold in the European Union, including the currently exempted industries (aerospace, military, subsea and maritime, instruments for down-hole applications, power generation and power distribution and some instruments for automotive applications). There was a RoHS recast in July 2011 which provided a sunset date for new categories of electronics formerly excluded. The electronics for medical, control and monitoring devices now have to comply with the ban of Pb. The harsh environment sectors listed above are still excluded from the directive, but recasts of RoHS and WEEE are already planned for 2019. Table 2.2 highlights the harsh environment conditions in which electronics of these industries operate (extended operating thermal ranges and service lives) that more rapidly degrade reliability and lifetimes. Therefore, commercial Pb-free solutions may not apply

Table 2.2: Typical temperature limits and performance requirements of electronic assemblies for various applications [35].

Application	Tmin (°C)	Tmax (°C)	ΔT (°C)	Dwell (h)	Cycles (per year)	Life-time (years)
Consumer	0	60	35	12	365	1-3
Computers	15	60	20	2	1 460	~ 5
Telecommunications	- 40	85	35	12	365	7-20
Motor Vehicle (Passenger compartment)	- 55	65	40	12	100	~ 10
Motor Vehicle (Engine compartment)	- 55	125	100	1	300	~ 5
Commercial Aircraft	- 55	95	20	2	3 000	~ 10
Space (low earth orbit)	- 40	85	35	1	8 760	5-20
Military Avionics	- 55	95	60	2	500	~ 5

to harsh environment applications. In particular, higher reliability than conventional materials is needed because of the dramatic consequences of potential failure.

Although progress has been made in the knowledge of suitable Pb-free solder alloys for consumer electronics and telecommunication appliances, a preferred Pb-free candidate for the harsh operating conditions remains to be selected. As highlighted in Table 2.1, recent consortia focused on the reliability of Pb-free soldered electronic assemblies subjected to high-reliability accelerated testing. Research was based on

currently used Pb-free solders with the addition of alloying elements such as Fe, Bi, Mn, Sb, Ni, Co and Ce [36–40]. A major issue related to alloying was the coarsening of the IMCs that form during service, affecting the joint reliability. The presence of small amounts of Ni in the solder improved significantly the reliability of solder joints under situations with longer dwell times at the high temperature extremes [34]. A minute addition of Ni and Ge to Sn-0.7Cu solders improved soldering characteristics such as fluidity, reducing shrinkage defects and reducing the volume fraction of Sn dendrites to promote a more eutectic microstructure [41–43]. The addition of rare-earth metals, such as Ce, La, or Y, refined the Pb-free solder joint microstructure (decrease in length and spacing of Sn dendrites and Sn grain size refinement) as well as improved its wettability, creep strength and tensile strength [44–48]. Recently, a new approach has been to incorporate nanostructured reinforcements with surface-active radicals to promote bonding with metal, following which they become inert. Such inert reinforcement improved the reliability of Pb-free solder joints subjected to thermo-mechanical fatigue [34]. Various nanocomposite solders are being developed that incorporate monolithic metals such as Cu, Al or Ag, metallic oxides such as Al_2O_3, TiO_2, $SrTiO_3$, SnO_2, ZrO_2, metal alloys such as SAC305 or non-metallic components such as carbon nanotubes. Manufacturing techniques are being developed to produce the three most common forms of solder products: paste, bar and wire [49–51].

Most leading automotive electronic companies started moving to Pb-free solders in the early 2000s. Nissan Motors has been using SAC solder on PCBs for keyless entry systems since July 2000 [1]. Figures 1.1 and 1.2 in section 1.2 highlighted the necessity of a melting point hierarchy during the processing of a flip-chip PBGA between the chip terminal alloy (solder ball) and the package terminal alloy in order to prevent remelting of the chip terminals during the PCB assembly process. Typically, the flip-chip connections at the chip level is accomplished with high Pb alloys (Sn-95Pb, Sn-97Pb or Sn-90Pb) with high melting temperatures (325°C) while package connections are made with the eutectic Sn-37Pb (T_m=183°C). High Pb content Sn containing solders have a very narrow temperature gap of melting, e.g. 10°C between the liquidus and solidus point for Sn-95Pb and they are used as a high temperature solder with reflow temperatures around 350°C and two-level packagings may be obtained with a combination of high Pb and eutectic Sn-Pb solders at the chip and package levels

respectively.

Interconnect reliability depends on both the die packaging processes and surface-mount technologies that can impart stresses and create residual stresses in the final packaged assembly. High Pb containing alloys are exempt from the RoHS legislation that states the percentage of Pb content in the exempt solder alloys must be greater than 85 percent [2]. The automotive industry still uses high Pb solders (Sn-97Pb and Sn-95Pb) in flip-chip bump packages that are often mounted on high density laminates with heat sinks in engine control applications. High temperature alloys similar to high Pb alloys have not yet been developed for Pb-free. The reason for this is that Sn-based alloys with high contents of Ag or Cu tend to have large temperature separation between the liquidus and solidus points [52]. Pb-free alternatives include electroless Ni/Au bumps, epoxy bumps and 80Au-20Sn bumps. However these alternatives are costly. Other alternative alloys include Innolot, produced by Cookson Electronics for the automotive industry with composition $SnAg_{3.8}Cu_{0.7}Bi_{3.0}Sb_{1.4}Ni_{0.15}$ (T_m=217°C) and has shown improved reliability compared with SAC387 in both vibration testing after zero and 500 thermal cycles, and in thermal cycling testing in the -40 to +175°C temperature range [22].

The manufacturing of mixed Sn-Pb and Pb-free solders by electronic manufacturers raises the question of possible small traces of Pb in Bi-containing Pb-free alloys. Such traces of Pb can produce a ternary alloy with a very low eutectic temperature, resulting in catastrophic failure during thermal ageing. This is a serious issue as otherwise Bi-containing SAC alloys are very promising materials for harsh environments.

Nonetheless, some critics question the necessity of a move to Pb-free solder alloys for harsh environment applications. The European Space Agency states: 'there are no drop-in replacements for Sn-Pb or In-Pb solders for the applications utilized by the European space industry. The alternative alloys that are being researched and proposed to date will have a negative effect on both manufacturing/assembly processes and on the reliability of spacecraft electronics' [53]. In particular, there are concerns that the proposed solder alloys will cause defects related to [53]:

- Poor solderability
- Increase in solder ball sizes (may cause short circuits)

- Difficult inspection criteria (frosty, crystalline or orange-peel effects on solder fillets whereas Sn-Pb gives smooth bright, easily inspectable finishes)
- Higher melting points which damage both parts and multilayer PCBs
- Difficult rework
- Higher soldering and solder-rework temperatures that invalidate current component qualifications and the validation of their assembly processes
- Poor thermal fatigue resistance

It is also argued that Sn-Pb solder alloys do not constitute a direct health hazard as solder alloys have no way of being consumed. Moreover, the Pb-rich phases in the solder are surrounded by Sn-rich material, therefore the corrosion rate of solder is extremely slow. While Pb in solder alloys account for 0.5% of the world use, Pb containing automobile batteries and Pb sheets used for domestic roofing account for 95% of the Pb used worldwide [53]. Therefore, Pb containing solder alloys are not the main source of Pb release in land-filled sites. Besides, there are other environmental arguments in favour of Sn-Pb [53]:

- Alternative solder alloys require greater resources for extraction of those metals from ores and during the assembly of electronic units.
- Electronic circuits are more often recycled as it is much cheaper to leach Au, Cu, Sn and Pb from scrap, than to extract these elements from natural ores.
- The alternative solders are as toxic as Sn-Pb. In SAC solder alloys, Ag exists as minute nanoparticles within the Sn-rich solder. When released, Ag-rich particles are biocidal and may kill both plant and wildlife. Also, Bi is an appealing element for alloying SAC alloys but the restriction of Pb means the availability of Bi could also be restricted as Bi is a residual of the Pb refinement process.

2.1.3 The microstructure of Sn-Pb and SAC solder alloys

Eutectic and near-eutectic Sn-Pb alloys are composed of alternate lamellae of Pb-rich and Sn-rich phases in a small number of eutectic colonies (defined as areas where the lamellae have similar orientation). The formation of IMCs can be deduced from the binary phase diagrams of Sn-Ag, Sn-Cu and Cu-Ag shown in Figures 2.2 (a)–(c).

Figure 2.2 (d) is the top view in 2-D of the Sn-rich region of the 3-D ternary phase diagram of SAC systems. In the centre of the diagram, the isothermal lines reach the lowest point of the 3-D ternary diagram, which is the eutectic point of SAC systems (∼217°C). The expected equilibrium phase reaction at the eutectic point is: L ↔ Ag_3Sn + Cu_6Sn_5 + β-Sn. Therefore, ternary eutectic SAC solders consist of three different phases: β-Sn (T_m=232°C), Cu_6Sn_5 (T_m=415°C), and Ag_3Sn (T_m=480°C).

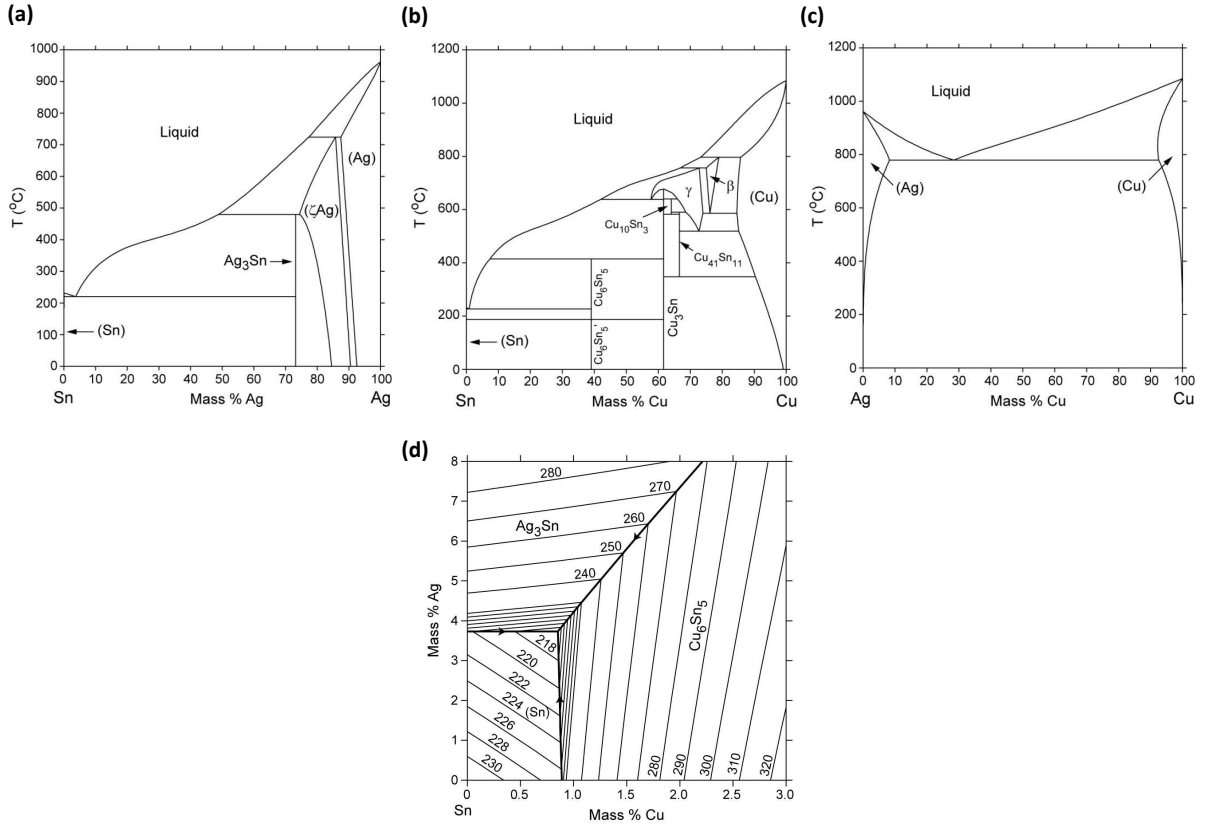


Figure 2.2: Binary phase diagrams of (a) Sn-Ag; (b) Sn-Cu; (c) Cu-Ag; and (d) Sn-rich part of the Sn-Ag-Cu ternary phase diagram [54]. Three IMCs may form in SAC systems: Ag_3Sn from the reaction of Sn and Ag, Cu_6Sn_5 and Cu_3Sn from the reaction of Sn and Cu. Cu_3Sn does not normally form at the eutectic point unless the Cu concentration and the temperature are high enough.

Figure 2.3 shows that after solidification, β-Sn cells are surrounded by the ternary eutectic region that is a mixture of fine IMC particles of Ag_3Sn and Cu_6Sn_5.

The microstructure suggests that Sn dendrites solidified first, followed by eutectic solidification. Cu_6Sn_5 and Ag_3Sn IMCs nucleate with minimal undercooling but the β-Sn phase requires 15 to 30°C undercooling to induce nucleation leading to final solidification [56, 57]. It is the supercooling of the liquid phase during solder joint

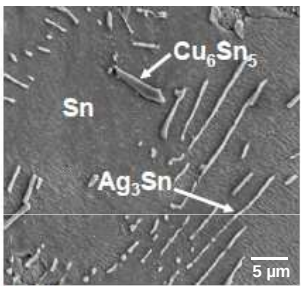


Figure 2.3: Scanning electron microscope (SEM) secondary electron image showing typical SAC387 microstructure [55]. SAC387 is a precipitation hardened alloy with Ag_3Sn and Cu_6Sn_5 IMCs dispersed in β-Sn. While Cu_6Sn_5 IMCs are equiaxed particles, Ag_3Sn are frequently elongated plates.

processing that enables the formation of metastable phases and comparatively rapid formation of β-Sn in Sn dendrites once nucleation has started as shown in Figure 2.4.

The presence of IMCs gives strength and creep resistance to SAC alloys through dispersion or precipitation strengthening, hence improved thermal fatigue resistance of SAC solders compared with Sn-Pb solders [59]. The varying Ag concentration in SAC alloys leads to varying volume fraction, size and distribution of IMCs and Sn dendrites [60]. In addition, the microstructure and mechanical properties of solder alloys depend on reflow temperature and time, cooling rate and ageing. The supercooling of SAC alloys enables large platelike Ag_3Sn IMCs to grow rapidly within the liquid phase before final solidification [61]. Such large IMCs should be avoided for greater solder joint reliability. The presence of these platelike structures can be minimised by adjusting the Ag concentration and the cooling rate. For compositions equal to or less than 2.7wt% Ag, the Ag_3Sn phase cannot nucleate or grow within the liquid without undercooling in excess of 20°C in the solder joint. At cooling rates below 1°C.s^{-1}, Ag_3Sn plates can extend the entire cross-section of a BGA solder joint, reaching lengths of 650μm. The plate size is reduced for cooling rates above 1.5-2°C.s^{-1} ($\prec$150μm).

The wide range of IMC morphologies (obtained through various compositions and processing techniques) and the presence of large anisotropic Sn grains in SAC solders give varying mechanical behaviours, resulting in a spread of failure mechanisms in SAC alloys compared with Sn-Pb alloys [62].

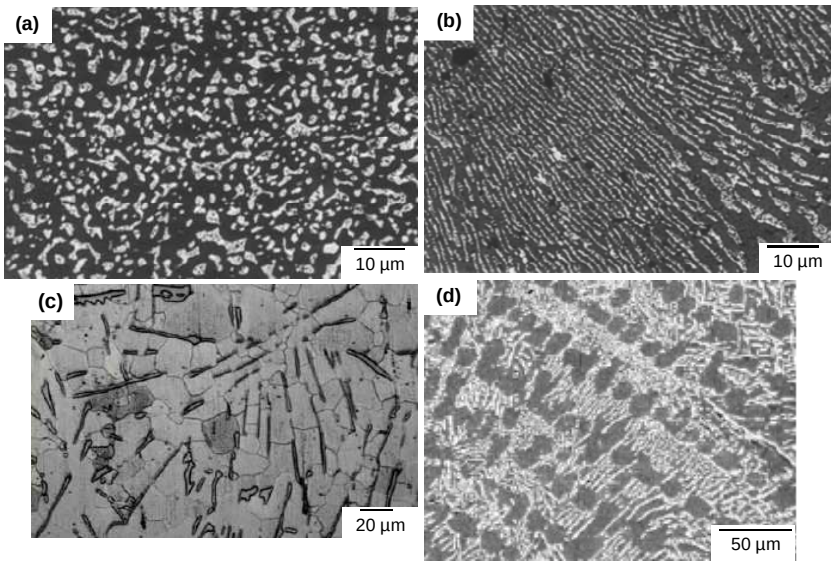


Figure 2.4: SEM image showing the microstructure of eutectic Sn-37Pb (a) after slow cooling; (b) after rapid cooling [35]; and the microstructure of as-cast SAC387 (c) equiaxed and (d) dendritic β-Sn surrounded by a fine two-phase (Ag_3Sn + Cu_6Sn_5) eutectic matrix [58]. Slow cooling leads to an equiaxed structure for both eutectic Sn-Pb and SAC solders. Due to solder joint processing, the microstructure of SAC solders is very often dendritic. Upon recrystallization, the dendritic structure may evolve to the equiaxed structure.

2.1.4 Specific issues to harsh environments

Sn pest

Sn exhibits polymorphism: above 13.2°C, the stable form of Sn has a body centered tetragonal form (β-Sn, or white Sn), below 13.2°C, the stable crystalline form of Sn is diamond cubic (α-Sn, or grey Sn). 'Sn pest' is when Sn undergoes the allotropic transformation β-Sn $\rightarrow$ α-Sn. Such a transformation induces a 27% volume change, which leads to embrittlement [63, 64]. The transformation is extremely sluggish and is very sensitive to the purity of the metal. Although 13.2°C is the thermodynamic transformation temperature, in practise grey Sn forms during long exposure to temperatures below 0°C. Pb-free alloys may be vulnerable to Sn pest in case of prolonged exposure to low temperatures, which is a reliability issue for electronics operating in aerospace applications or in extremely cold locations like the Polar regions. The major damage that Sn pest can cause after prolonged exposure at low temperatures has been widely studied and recently reviewed [65]. Tin pest is a slow process that can take

months or years. Figure 2.5 shows the various stages of Sn pest development with increased times of exposures to low temperatures. The wart-like appearance of grey Sn spreads over the sample surface, leading to internal embrittlement and ultimately disintegration of the sample.

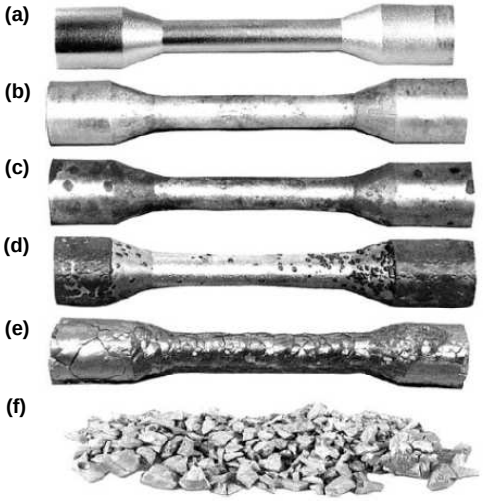


Figure 2.5: Sn pest in as-cast samples with increased times of exposure to low temperatures from (a) to (f). (a) as-cast sample; (b) surface discoloration; (c) initial warting; (d) extensive warting; (e) cracking of surface layer; and (f) complete disintegration [66].

Sn pest growth is a complex phenomenon with a lack of consistency in both occurrence and time scale, depending on the experimental conditions and composition of samples [65]. Partial reversal may occur upon heating from 60°C [65, 67]. However, in the case of phase reversal, the material was still porous and cracked.

A controlling factor for the growth of Sn pest is the 'matrix' into which Sn pest is growing, with growth depending on stress relaxation ahead of the expanding α-Sn [66, 68]. Alloys with a strong matrix were more resistant to Sn pest because stress relaxation ahead of the matrix became more difficult, inhibiting growth [68]. Strengthening factors such as a reduced grain size and solute atoms made Sn pest growth more difficult [66]. Therefore pesting is usually first and most easily manifest at a free surface.

Elements that are soluble in Sn (Pb, Sb or Bi) tend to suppress the transformation by raising the β-Sn $\longleftrightarrow$ α-Sn temperature gap, whereas elements that are insoluble in Sn (Zn, Al, Mg or Mn) accelerate the transformation by lowering the transformation

temperature [65]. Even impurity traces of Sn pest inhibitors can prevent Sn pest formation. The addition of Cu and Zn to pure Sn both promoted grey Sn formation and the influence of an alloying element depended on the presence of other elements [69, 70]. Also, heavy cold work (up to 90%) on a Sn-0.8Cu alloy enhanced the transformation at -30°C [70].

While Sn pest was observed in a range of Pb-free solders (Sn-3.5Ag, Sn-0.5Cu, SAC387 and SAC305) left at -18 and -40°C, no Sn pest was observed in Sn-8Zn-3Bi or in Sn-37Pb after exposure for up to four and ten years respectively [66]. In general, the presence of Pb, Sb or Bi in traditional solders has suppressed pesting in most practical applications.

Sn whiskers

Sn whiskers are Sn crystals growing spontaneously from finished metal surfaces [71]. While Sn whiskers are unlikely to appear in Pb-bearing solders (Pb is a Sn whisker growth inhibitor), Sn whiskers may develop on high Sn-containing alloy surfaces. After an unpredictable incubation period, the whiskers grow, with potential risks for electrical shorts or disruption of moving parts, resulting in potential catastrophic failure in high reliability equipment. Growth rates from 0.03 to 9 mm/year have been reported [72]. Although the phenomenon has been known for decades, the risk for whisker formation is still barely quantified because whisker risk has only recently been recognised due to the miniaturisation of electronic assemblies. Modern technology has been reducing the volume of solder from 10^{-6}–10^{-9}m^3 to flip-chip joints of the order $\prec 10^{-12}$m^3 [34], resulting in a $\sim$100μm spacing of current carrying lines. If whiskers grow to a length of approximately 50μm in adjacent lines, shorting may occur resulting in electrical failure.

Whisker growth depends on many variables but stress relief is the primary driving force. In particular, compressive stress is a necessary but not sufficient factor for Sn whisker formation [73]$^-$[74]. Such stresses can be induced by mechanical loading, residual stresses from processing, surface damage, CTE mismatch and formation of IMCs between the interface of plating and the substrate. Pressure can also induce and accelerate Sn whisker growth. Environmental factors such as elevated temperatures, barometric pressure, humidity, thermal cycling and electric fields may promote Sn dif-

fusion and formation of whiskers [72]. 'Bright' finishes, as opposed to 'matte' finishes are also more susceptible to whisker formation. However, the location and time for whisker growth is unpredictable.

The electronics industry attempts to minimise whisker growth by means of non-conductive barriers such as epoxies, selecting matte Sn finish, varying the thickness of Sn plating, or heat treatments that relieve internal stresses.

2.2 Failure mechanisms of solder alloys in electronic assemblies

Damage in electronic assemblies may result from multiple stress fields. Amongst such stress fields are electromigration, thermal migration, Joule heating, current stressing and thermomechanical fatigue. The actual temperature of a joint depends on the environment (primary) and Joule heating (secondary) [34].

2.2.1 Deformation modes

During operation, solder joints are submitted to both low cycle fatigue (associated with temperature cycling loads), and high cycle fatigue (usually associated with mechanical or vibration cyclic loads). These mechanisms can eventually lead to failure of the joint. For harsh environments, vibrations can be a major issue. There is very little work comparing high cycle fatigue performance of Pb-free with Sn-Pb alloys [75], probably because mechanical vibrations are considered a lesser issue for harsh environment applications, where traditional Pb-base packages are still being used. The rest of this review focuses on low cycle fatigue, generally considered to be the primary source of failure in electronic packages [76, 77]. Thermal fatigue occurs because of thermal cycling loads, either from environmental temperature changes or cyclic active power on/off.

Thermal cycling due to the environment or power cycling induces expansion or shrinkage of the components and the PCB because of the difference in the coefficients

of thermal expansion (CTE) between the PCB, the solder joint and the electronic component, producing stresses at the interfaces of the different parts (cf. section 1.2). Tensile and mixed-mode strains may occur due to component bending. However, for many solders, especially leadless solders, the shear strains developed often exceed 10% [35], and the crucial stress environment conditions is best approximated by strain controlled fatigue in shear. The imposed shear strain on solder joints due to the difference in CTE between the solder alloy and the board is [34]:

$$\gamma = \Delta\alpha \Delta T \frac{a}{h} \tag{2.2.1}$$

where γ is the shear strain, $\Delta\alpha$ is the CTE difference, ΔT is the temperature range of the thermal cycle, a is the distance from the neutral point of the joined materials and h is the thickness of the solder joint. Therefore, a large CTE difference in the joined materials will induce large shear strains.

The generated stresses are mainly relaxed by the less creep resistant solder joint. If the temperature varies on a larger time scale than stresses relax through creep, the deformation is plastic and leads to material fatigue. The plastic response of SAC and Sn-Pb solder alloys depends on both the processing and testing conditions. There can be significant variations in solder joint behaviour: for instance, while SAC solders have exhibited lower yield strength, lower hardening and lower ultimate strength than Sn-37Pb under identical shear loading conditions [78–81], others found the opposite [82, 83].

2.2.2 Thermomechanical fatigue in Sn-Pb solder joints

In many metals, failure from low cycle fatigue occurs because of cyclic deformation followed by microstructure-dependent damage mechanisms such as crack initiation and micro-crack growth. Under cyclic stress and elevated temperature, Sn-Pb solder joints also exhibit grain coarsening increasing the complexity of analysis. As described in section 2.1.3, the as-solidified structure of near-eutectic Sn-Pb solders consists of lamellar and globular regions of Pb-rich and Sn-rich phases. The eutectic colonies are often mistaken for individual solder grains. The grain size of the solder can be

much smaller as individual Sn and Pb lamella are polycrystalline, with average grain sizes of 1μm and 0.25μm for Pb and Sn respectively. Recrystallization occurs upon solder cooling as strains build up due to the CTE difference between Sn and Pb, and recrystallized Sn grains are defined by high angle boundaries. Pb-rich regions have larger grains than Sn-rich regions as Pb has a face-centered cubic crystal structure, which renders slip deformations much easier than for Sn that has a body-centered tetragonal structure favouring recrystallization instead of strain dissipation by slip [34]. Therefore, the large surface area between phases in eutectic Sn-Pb makes it liable to coarsening.

During thermal cycling, low temperatures provide an opportunity for damage (defects and dislocations) to be created. When external energy is applied (thermal or mechanical), material diffuses to regions of high stresses, mainly colony boundaries parallel to the imposed shear strain direction and the microstructure evolves to lower its high-energy configuration by coarsening. Further deformation concentrates at the weak coarsened cell boundaries, resulting in further coarsening. Cracking occurs when grains can no longer slide and rotate to accommodate strains, leading to intergranular separation and eventual failure. Eutectic Sn-37Pb solder joints submitted to shear stresses deformed inhomogeneously, and localized coarsening occurred in regions of concentrated shear deformation, often a band along the length of the joint [84]. The coarsened bands had an equiaxed, recrystallized microstructure, softer than the lamellar microstructure in the rest of the joint. Failure propagated along the coarsened band.

2.2.3 Thermomechanical fatigue in Pb-free solder joints

Crack initiation and propagation in SAC solders occurs at the highest strain regions of the solder joints and two main mechanisms for crack initiation are reported, either β-Sn grain coarsening or recrystallization. Sn grains coarsen at high strain regions due to enhanced diffusivity in the damaged regions during thermal cycling. Sn grains may also slide and rotate to accommodate strains until voids are too large to be backfilled by diffusion [34]. Damage and failure occur at β-Sn grain boundaries, particularly in

the presence of IMCs. Recrystallization also often occurs in SAC solder joints, resulting in finer grains. The smaller grain structure fosters enhanced grain boundary sliding and strain localization in the recrystallized regions. Intergranular cracking is then initiated, enabling crack growth and resulting in failure [32, 85, 86].

In SAC387, microcracking was the dominant fatigue damage mechanism resulting from low cycle fatigue followed by macro-crack development [87]. The number of microcracks increased with the number of fatigue cycles so that strong cyclic-dependent softening developed. When the density of microcracks was high enough, they linked to form a fatigue crack. These cracks were primarily located in recrystallized areas or regions with fine grains and a comparatively high density of grain boundaries. Consistently, another study on equiaxed SAC387 found that microcracks developed early ($\prec$5% of the fatigue life) and along the grain boundaries [58]. In dendritic structures, deformation was concentrated in the dendritic phase, as evidenced by the development of slip bands. Another study on Sn-3.5Ag suggested two different crack initiation locations in dendritic structures depending on the frequency of loading [88]. The initiation of fatigue cracks occurred either along the boundary between β-Sn dendrites and the eutectic mixture (at low frequency loading) or inside the β-Sn dendrite (at high frequency loading) (Figure 2.6).

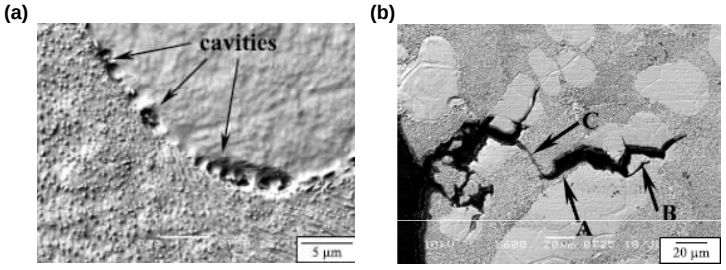


Figure 2.6: SEM image of (a) fatigue crack initiation in dendritic Sn-3.5Ag alloy; and (b) fatigue crack propagation in dendritic Sn-3.5Ag alloy strained to 1% vertically, showing various growth paths: intergranular along Sn-dendrite boundary (A), intergranular along subgrain boundary (B) and transgranular through Sn-Ag eutectic (C) [88].

Ag_3Sn plates may influence mechanical fatigue mechanisms [89, 90]. The large Ag_3Sn plates that can grow because of the easy nucleation of the Ag_3Sn phase compared to that of the β-Sn phase can have a profound effect on joint plasticity in Pb-free

solders. They promote strain localization at the interface between the plate and β-Sn that favours a failure path during thermomechanical fatigue. Although IMCs are generally understood to undermine fatigue life, the presence of IMCs could also impede the linkage of microcracks, slowing down subsequent crack propagation [58].

The interface at the circuit board metallization pad/solder and the interface between component pad/solder usually contains an IMC layer formed during manufacture. In the case of Cu pads, the scalloped-type interface is Cu_6Sn_5 (which forms first) whereas a layered-type reaction product is Cu_3Sn and forms after thermal exposure because of the high concentration of Cu at the solder/pad interface and the reduction in Sn concentration due to the formation of the Cu_6Sn_5 layer. Thermal ageing may result in interdiffusion mechanisms at the pad/solder interface and growth of the IMC layer [91]. The IMCs growth coarsen at room temperature and above, and growth may extend into the solder either by needle-like growth or by detached fragments from the IMC layer, leading to joint embrittlement. Cracking often occurs along or within the IMC layer leading to eventual failure as in Figure 2.7 [92].

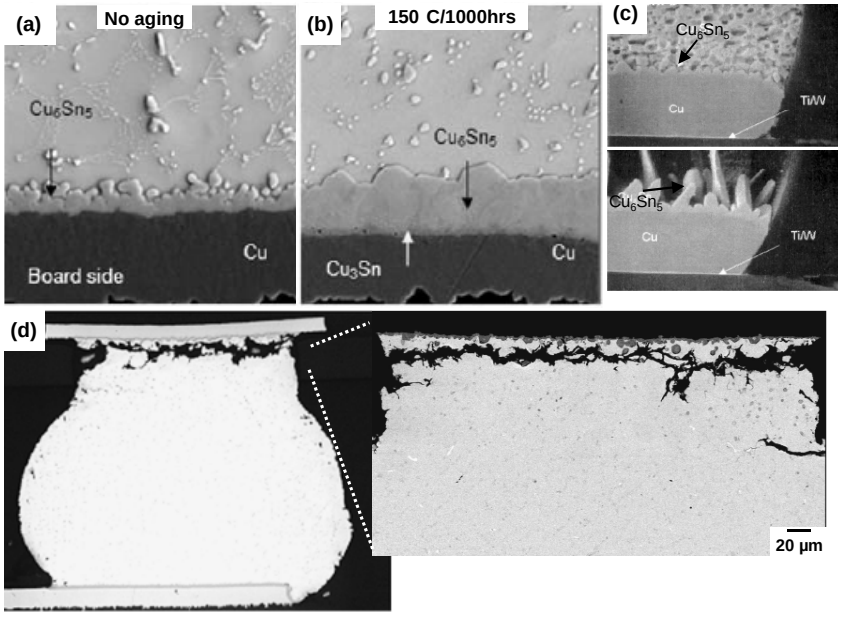


Figure 2.7: SEM images of (a) unaged; (b) aged at 150°C for 1000 hours IMC layer at a SAC305/Cu pad interface showing the growth of the IMC layer with thermal ageing [93]; (c) eutectic Sn-Pb/Cu; (d) SAC387/Cu under bump metallurgy (UBM) interfaces showing the sharp elongated IMCs of Pb-free solder joints as opposed to the smoother IMC layer for Sn-Pb solder joints [10]; and (e) typical failure along a Pb-free solder joint/pad interface [94].

IMC layer growth may deplete the solder matrix of atoms (e.g. Cu), enhancing the solubility of other solutes (e.g. Ag) and the coarsening of precipitates (e.g. Ag_3Sn) [95]. Further, the pad composition may contribute to the microstructure of the bulk solder joint as during the wetting and spreading phase of the processing of solder joints, a finite degree of pad base metal is dissolved into the molten solder, with potential effects on the composition and size of solder joint IMCs. The role of the pad metallization is greatly underestimated in the literature. Since the alloying content of Ag (3–4%), Cu (0–1%) and other additives (Bi, Ni, Sb etc.) is relatively little, the solution of pad metals (Cu, Ag, Pd, Au, Ni etc.) during the soldering process may change the composition of the solder dramatically. The higher reflow temperatures required for Pb-free alloys compared with eutectic Sn-Pb may increase the dissolution rate and solubility of Cu (or Ni, in the case of Ni-Au pads) in the molten solder as well as the rate of IMC formation. With electronic assembly miniaturisation, the length scale of IMCs becomes ever closer to that of solder joints and plays an increasing role in the overall mechanical properties of the assemblies. Hence the lack of systematic studies on pad metallization effect on solder joint microstructure should be addressed.

2.3 Electronic package lifetime prediction

The International Technology Roadmap for Semiconductors (ITRS) predicts a drastic reduction of I/O pitch size to 20μm in the coming years [96]. Such a change requires new package designs that include new materials and manufacturing processes. In order to assess the reliability of a design, thermal cycling tests are usually carried out. Thermal cycling tests allow for detection and quantification of failure mechanisms as well as evaluation of the reliability of the package design. Finite Element Analysis (FEA) complements thermal cycling by providing the means to suggest the causes of insufficient reliability and helps guide package design.

Table 2.3: Typical Coefficients of Thermal Expansion (CTE) for various materials involved in BGA manufacturing

Material	**CTE (x-y axis)** ppm/°C	**CTE (z axis)** ppm/°C
Tin-lead solder	24	24
Copper	16-18	16-18
FR-4 (glass-reinforced epoxy laminate PCB)	16-18	60-85
Polyimide	15-18	65
BT -Epoxy (Bismaleimide-Triazine resine)	15	50
Epoxy Overmold	15	15
Silicon die	~ 2.6	~ 2.6
Alumina oxide	3-6	3-6

2.3.1 Effect of physical design on the reliability of electronic packages

The thermal life of BGA solder joints depends on the physical design of the BGA package as well as the manufacturing process such as the layout pattern on the PCB and the application method and parameters of the solder material prior to solder reflow. Moreover, the package type influences the reliability: studies have shown that Plastic Ball Grid Array (PBGA) joints had longer lifetimes than Ceramic Ball Grid Array (CBGA) joints because PBGAs have better matched CTEs. Typical CTEs are listed in Table 2.3. Bismaleimide-Triazine (BT) is often used as the internal package substrate material. Since FR-4 and polyimide have a CTE closely matched to Bismaleimide-Triazine (BT), the selection of the PCB for a PBGA system is not critical. Ceramic BGAs have a CTE mismatch with all typical PCBs, and therefore are not recommended, unless a high conductivity package material is needed (the thermal conductivity of FR-4 is $0.003 W.cm^{-1}.°C^{-1}$ while that of alumina is $0.276 W.cm^{-1}.°C^{-1}$).

The package size/die size ratio may also alter the reliability of electronic packages. The BT substrate has a CTE closer to that of the PCB than to that of the Si die. The larger the die, the larger the effect of the CTE difference and the less reliable the package. Packages with larger solder balls tend to have higher reliability than smaller ones as large joints provide better compliance.

Figure 2.8 shows there are two main configurations for solder ball attachment in BGA packages: Solder Mask Defined (SMD) and Non-Solder Mask Defined (NSMD).

In the former, a solder mask comes up over the edge of the pad, resulting in a smaller ball to pad interface than for NSMD pads. The SMD configuration adds an element of strength to the pad as the solder mask overlap provides extra strength to the adhesion bond between the land and the base substrate material. Besides, the pad needs to extend beyond the edge of the solder mask, therefore the laminate can adhere to a larger Cu surface area. SMD joints are more robust in the case of board flexing in high temperature conditions. There is more room between pads for signal routing in NSMD configurations. With ever smaller packages, NSMD are increasingly used.

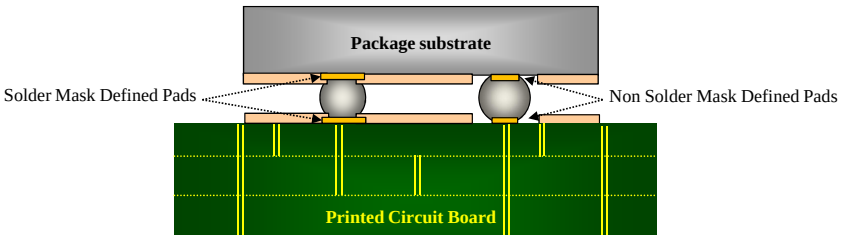


Figure 2.8: Schematic of Solder Mask Defined (SMD) and Non Solder Mask defined (NSMD) pads

2.3.2 Accelerated thermal cycling (ATC)

Thermal cycling tests that mimic operating conditions are too costly and time-consuming to implement. Therefore, accelerated thermal cycling (ATC) tests have been used for over forty years (since the first major paper by Norris and Landzberg in 1969) as a method to assess thermomechanical reliability of electronic assemblies [97]. Fatigue tests are used to calculate and plot shear stress versus shear strain, and Figure 2.9 shows typical hysteresis loops that allow for the observation of softening or hardening over cycles. After a few cycles, the maximum stress begins to drop due to a reduction of the load bearing area resulting from fatigue cracking. The number of failures as a function of thermal cycles can then be studied. Cycles to failure data are translated into lifetime predictions by means of experimentally determined acceleration factors.

The fatigue life is a strong function of the strain amplitude, cyclic frequency, temperature and microstructure, and there are now well-established thermal cycling conditions to evidence failure for specific classes of assemblies with Sn-Pb solders. However, the electronics industry has only just started establishing ATC conditions for

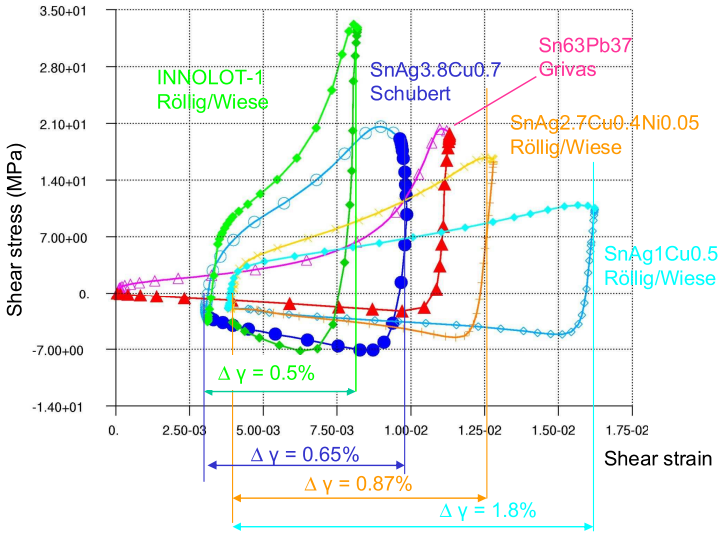


Figure 2.9: Creep hysteresis curves for various Sn-Pb and SAC solders of a chip resistor during a 90 min thermal cycle from 150°C to −40°C for a constant strain range [98].

Pb-free assemblies.

Coffin-Manson

Most models used to determine the number of cycles to failure are empirical, based on Coffin-Manson curves and were developed for eutectic Sn-Pb subjected to shear strain conditions [98]. The Coffin-Manson model uses fatigue life data and links the creep strain that has accumulated over one thermal cycle to the number of mean cycles to failure [99, 100]. It predicts the number of cycles needed to lead to failure of a given percentage of parts when exposed to temperature variations (i.e. low cycle fatigue). The extent of accumulated plastic creep strain over one thermal cycle can be related to the mean cycles to failure N_f by the following Coffin-Manson equation:

$$\Delta\gamma_p . N_f^{\alpha_1} = C_1 \tag{2.3.1}$$

where $\Delta\gamma_p$ is the strain range due to matrix creep (from the stress-strain hysteresis loops obtained during fatigue cycling), N_f is the number of cycles to failure, α_1 is the fatigue ductility exponent and C_1 is the fatigue ductility coefficient. These constants depend on the material and are obtained by best-fit to experiment.

Table 2.4 shows α_1 and C_1 for various solder alloys. Although there is generally reasonable agreement between studies, large variations also are reported [58] and

Table 2.4: Coffin-Manson parameters obtained for various solder alloys

Solder	α_1	C_1	Reference
Sn-3.5Ag	0.93	21.9	[86]
	0.5	0.9	[102]
SAC305	0.73	3.7	[86]
Sn-3.5Ag-1Cu	0.43	0.45	[102]
Sn-3.5Ag-2Cu	0.44	0.39	[102]
Sn-3.0Ag-0.5Cu-1Bi	1.14	57	[86]
Sn-3.5Ag-2Bi	0.55	0.47	[102]
Sn-3.5Ag-5Bi	0.60	0.22	[102]
Sn-3.5Ag-10Bi	0.54	0.06	[102]
Sn-3.5Ag-1Zn	0.55	0.86	[102]
Sn-3.5Ag-2Zn	0.49	0.56	[102]
Sn-3.0Ag-0.5Cu-3Bi	0.96	5.7	[86]

comparisons between the Coffin-Manson constants and different studies in the literature should be made carefully since they depend on the dimension of the soldered assembly, the difference in thermal expansion between assembly parts, the upper and the lower temperature of the temperature variation, the frequency of the temperature variation and the thermomechanical properties of the joint. They can also depend on the testing conditions: at smaller strain ranges, α may increase [35]. The slope of the Coffin-Manson curve (related to C_1) may also vary if data are obtained from shear straining or from actual solder joints. A true 'model' for lifetime prediction would include geometry-dependent parameters and these approaches are termed 'physics of failure models'.

Norris-Landzberg

The Norris-Landzberg equation is an extension of the Coffin-Manson equation that includes the effects of thermal cycling test frequency and maximum temperatures to determine the 'acceleration factor' (AF) that scales ATC test conditions to field conditions. The main assumption in the Norris-Landzberg acceleration model is that $\Delta T/\Delta\epsilon_p$ is constant (ΔT and $\Delta\epsilon_p$ are the cycle temperature range and plastic strain range respectively). The acceleration factor is:

$$AF = \frac{N_o}{N_t} = \left(\frac{\Delta T_t}{\Delta T_o}\right)^2 \left(\frac{f_o}{f_t}\right)^{\frac{1}{3}} \phi(T_{max}) \tag{2.3.2}$$

where N is the cycle life, ΔT is the temperature range, f is the thermal cycling frequency and ϕ is an empirical temperature factor that considers the peak temperature T_{max} attained during thermal cycling (in Kelvin). The 'o' and 't' subscripts refer to

operating and test conditions. Knowing the testing cycle life and the acceleration factor, the cycle life under operation can be deduced. This model has been well-studied for Sn-Pb and it has been widely accepted over the decades of use by the electronics industry. For Sn-Pb, the acceleration factor has been given as:

$$AF = \left(\frac{\Delta T_t}{\Delta T_o}\right)^2 \left(\frac{t_t}{t_o}\right)^{0.136} exp\left[1414\left(\frac{1}{T_{max,o}} - \frac{1}{T_{max,t}}\right)\right] \tag{2.3.3}$$

where t is the dwell time in minutes.

The corresponding equation for SAC solders has been proposed as [101]:

$$AF = \left(\frac{\Delta T_t}{\Delta T_o}\right)^{2.65} \left(\frac{t_t}{t_o}\right)^{0.136} exp\left[2185\left(\frac{1}{T_{max,o}} - \frac{1}{T_{max,t}}\right)\right] \tag{2.3.4}$$

The simplicity of the model and the good agreement between predicted and observed acceleration factors for Sn-Pb alloys make it the expected approach for SAC alloys [101]. However, as outlined above, the accuracy of the Norris-Landzberg model relies on the main assumption that $\Delta T/\Delta\epsilon_p$ is constant. But the $\Delta T/\Delta\epsilon_p$ factor may vary for very rigid or very compliant packages. Another concern is that when the ATC temperature range is very different from the operating conditions, it might not be possible to generalize fatigue life by the linear $\Delta T \rightarrow \Delta\epsilon_p$ translation implied in the Coffin-Manson model [101].

2.3.3 Pb-free solders thermal fatigue reliability studies

The reliability of Pb-free assemblies has been the subject of a large number of 'point studies' that address specific package geometries and soldering conditions. Figure 2.10 sums up reliability studies on Sn-Pb, SAC387 and SAC396 alloys showing that the ratio of SAC to Sn-Pb lifetime decreased with increases in either the temperature range/cyclic shear strains, the mean temperature, or the dwell times at the temperature extremes [27]. Under higher strains, the life of SAC solder joints was less than that of Sn-Pb. The difference in the slope of the SAC and Sn-Pb trendlines and the intersect of the trendlines suggested that although Sn-Pb assemblies perform better than SAC assemblies under highly accelerated tests, SAC solder joints are more reliable under

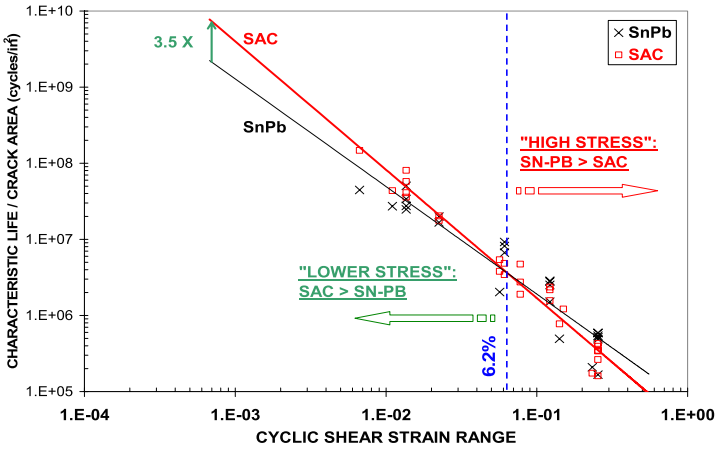


Figure 2.10: Scaled characteristic life (number of cycles to 63.2% of the total cycles to failure) against the average cyclic shear from failure distributions of SAC387, SAC396 and Sn-Pb soldered assemblies subjected to accelerated thermal cycling under different thermal conditions (0 to 100°C, -40 to 125°C, -55 to 125°C). A cross-over point at 6.2% cyclic shear strain was observed. At the left of the cross-over point, SAC assemblies had longer lives than Sn-Pb assemblies [102].

milder conditions. Similarly, in a joint study between the NASA and the US Department of Defense, SAC solders were as reliable as their Sn-Pb counterparts for $-20°C$ to $+80°C$ thermal cycling, but they were often less reliable during $-55°C$ to $+125°C$ thermal cycling. At low stresses, Pb-free solders generally outperformed Sn-Pb while the reverse occurred for high-stress conditions [103]. However, the correlation cannot be used for safe extrapolation to real temperature cycling as dwell times and test frequency were different. Besides, only one out of the 27 data points was below the 1% shear strain range, which is already a high strain, leading to reduced cyclic life. These results highlight the lack of data in the low to medium stress condition, most likely to be encountered in a wide range of applications. It is estimated that joints in service see a stress of 1 to 10MPa. Further testing in the low and medium stresses range is required to confirm the Sn-Pb reliability trend reversal [27].

There is a lack of cohesiveness among the available data, with varying results for different experimental conditions. There are also discrepancies within various compositions of the same type of alloy. The effect of Ag content on thermal fatigue life was investigated [104]. Solders with high Ag content (3 and 4 *wt*%) had a longer fatigue life compared to solders with lower Ag content (1 and 2 *wt*%). This is because a higher concentration of Ag gave a stable microstructure with a uniform dispersion of fine

Ag_3Sn particles while microstructures with lower Ag content experienced more rapid grain coarsening during thermal cycling. In addition, the cycles to failure relationship depends on the type of package used. Sn-Pb solder joints had improved fatigue life for stiff components and loads induced by high thermal mismatch whereas SAC solders had mechanical response in compliant packages and low thermal mismatch induced loads [105]. Depending on service conditions, the prediction of current models can easily have errors by 1-2 magnitude, which would mean errors in lifetime predictions from 1 to 100 years [19].

The high number of Pb-free options and electronic packages hinders the development of reliability databases, acceleration models and therefore life-prediction models. In many applications, a suitable soldering material for harsh environments is yet to be selected, therefore speeding up the life-prediction process through Finite Element Analysis (FEA) modelling is critical.

Accurate modelling requires a full understanding of failure modes, an accurate constitutive model and an experimental reliability database to characterise solder constitutive properties for later input of materials parameters in the model. The package geometry and the thermal cycles may be modelled in a FEA code that calculates stress-strain behaviour with time. The model constants being known, the damage model thus developed can be used on other assemblies and thermal cycling conditions. As already described, solder alloys have a complex temperature and time-dependent behaviour. Incorrect assumptions about solder alloys constitutive behaviour may lead to incorrect FEA simulation results. Therefore, the characterisation of constitutive properties of solder alloys is key to the development of new packages.

2.4 Constitutive behaviour of solder alloys

The constitutive behaviour of a material is the way it responds to various loading conditions (stress-strain behaviour, including creep). It is estimated that when $T \succ 0.5T_m$, creep dominates the deformation kinetics in metallic materials [106]. Therefore, operating at a high homologous temperature (0.6–0.9) makes solder joints prone to creep. Creep refers to the time-dependent plastic deformation under constant uniaxial stress.

The high temperature hold periods during operation are opportunities for creep (under stress controlled conditions) and for stress relaxation (under fixed strain range). The creep rate of a solder must be sufficiently fast so that there can be relaxation of thermally induced stresses, minimizing strains in the joined components. Low creep resistance can translate into a longer thermomechanical fatigue lifetime [34]. However, the creep rate must not be so fast that the components move over time, or significant plastic strain will accumulate on subsequent rapid cooling in thermal cycling.

2.4.1 Creep mechanisms in Pb-free solder joints

The mechanisms involved in creep are thermally driven diffusion processes that depend on strain rate and stress ranges and Figure 2.11 shows a proposed creep deformation map for Pb-free solders [107]. According to Figure 2.11, at low stress levels

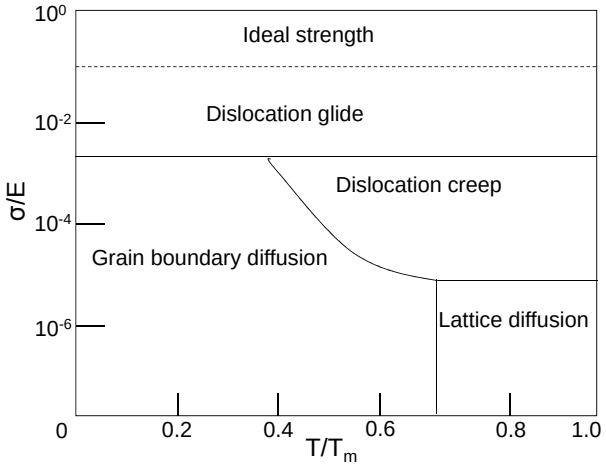


Figure 2.11: Creep deformation map of Pb-based and Pb-free solder alloys (adapted from [107]). Dislocation glide occurs in the high stress region for all homologous temperatures (dislocations moving along a slip plane). Dislocation creep occurs at medium stresses and when $T_h \succ 0.5T_m$ (dislocations climbing away from dislocation barriers, diffusion controlled). Lattice diffusion mechanisms occur at low stresses and high temperatures (migration of interstitial atoms and lattice vacancies along the gradient of a grain boundary in the presence of tension or compression pressure in reversed directions). In materials with a high volume fraction of grain boundaries, diffusion creep was significant [108].

($\sigma/E \prec 10^{-5}$), the deformation will be caused by lattice diffusion and grain boundary diffusion. Dislocation creep will occur at intermediate stress levels ($10^{-5} \prec \sigma/E \prec 10^{-3}$). High stresses ($\sigma/E \succ 10^{-3}$) will induce dislocation gliding [107]. Grain bound-

ary sliding may also occur at high temperatures in conjunction with any of the other creep mechanisms.

The two most important mechanisms in solder creep are considered dislocation climb and grain boundary sliding [8]. Dislocation climb involves the movement of individual atoms in the matrix, adjacent to dislocations, hence facilitating thermally activated non-glide movements. Therefore, when creep deformation is controlled by dislocation climb, the activation energy is the activation energy for self-diffusion. Other deformation mechanisms may involve dislocation jogs, cross slip or activation of Frank-Reed sources.

When dislocation climb dominated the deformation, values of the stress exponent (see Equation 2.4.1) for Sn-Pb were in the range of 5–12 and the average creep activation energy was 77kJ.mol^{-1} [8]. Although dislocation climb contributes to creep, crack growth in cyclic loading was largely intergranular or along the phase boundaries. Sn-Pb solders were susceptible to grain boundary sliding due to the dispersion of the soft Pb-rich phase in the Sn matrix. When creep was dominated by grain boundary shear, the stress exponent was in the range of 2–7, with an average activation energy of 48kJ.mol^{-1} [8]. Grain boundary shear was facilitated by transport through the grain boundary and therefore had an activation energy closer to that of grain boundary diffusion.

SAC alloys generally have an average stress exponent in the range of 6–8 and an activation energy $\sim$70kJ.mol^{-1}. However, there are stress exponent and activation energy discrepancies between bulk alloys and flip-chip joints, with some flip-chip data giving a stress exponent as high as 18 [108].

The dispersion of Ag_3Sn and Cu_6Sn_5 in the matrix of Sn generally reduces grain boundary sliding, giving superior creep resistance to SAC solders compared to Sn-Pb. This is particularly true at lower stresses where grain boundary sliding dominates. Figures 2.12 (a) and (b) show the transmission electron microscope images of Sn-3.5Ag before and after creep deformation [109]. Initially, many homogeneously dispersed Ag_3Sn particles pinned the Sn/eutectic boundary. Following deformation, more Ag_3Sn precipitates as well as dislocations produced by the deformation pinned the grain boundary.

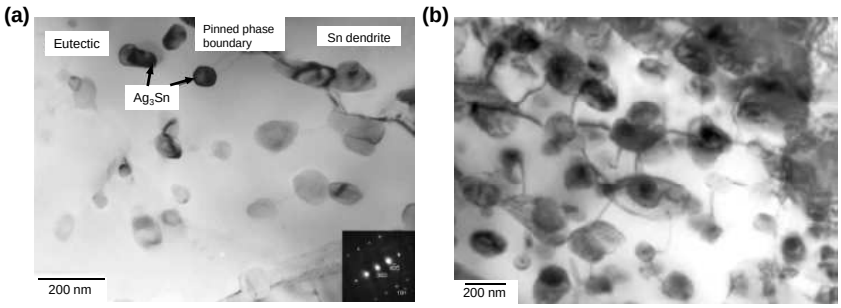


Figure 2.12: Transmission Electron Microscopy (TEM) image of (a) the initial microstructure of Sn-3.5Ag; and (b) the pinning of the dislocations by Ag_3Sn particles after creep deformation induced by loading (22MPa at 60°C with a strain rate of $10^{-4}s^{-1}$) [109].

Sn-3.5Ag had one of the highest creep resistance amongst Pb-free alloys, with greater strength and creep resistance than Sn-Pb [110]. However, creep deformation will occur when a threshold stress is exceeded, allowing for one of the following mechanisms to occur [111]:

- Particle shearing (or particle cutting), either by fracture of incoherent particles or by the glide of dislocation pairs through coherent particles.
- Orowan bowing (or looping between the precipitates), when there is bowing between particles. The matrix dislocation is extended in the matrix glide plane between particles by the applied stress to the extent that the dislocation is released, leaving loops around the particles. Below the Orowan stress, dislocations are trapped by the Ag_3Sn and Cu_6Sn_5.
- Dislocation climb around particles, when segments of the dislocation can extend normal to the glide plane.

The low melting point of SAC solder alloys also means that precipitate coarsening can be significant [112–118]. There is Ostwald ripening of both Ag_3Sn and Cu_6Sn_5 particles [113, 115, 118] that eventually undermines creep resistance [119, 120]. Grain boundary or interphase boundary diffusion often induced coarsening of the Pb-rich phase in Sn-Pb alloys and coarsening of Ag_3Sn IMCs or of a band of strained region in SAC alloys [34].

2.4.2 Determination of constitutive properties

Creep testing techniques

Traditionally, creep behaviour is studied by subjecting a specimen to prolonged constant tension or compression loading at constant temperature. The creep behaviour of solder alloys has been studied by various techniques such as conventional tensile testing [121–127], stress relaxation [128] and impression tests [129, 130]. The most widely used method for creep behaviour study is tensile creep test using standardised samples [131].

Primary creep (or transient) occurs with a comparatively high strain rate which then decreases to a steady-state in secondary creep. In this region, the competition between strain-hardening (network refinement due to dislocation glide) and strain-softening (network coarsening due to diffusion-controlled climb and subsequent annihilation of dislocations) leads to a stable strain rate. The third stage is tertiary creep: nucleation and growth of cavities induce micro-cracking and necking until rupture.

The high temperature deformation of crystalline materials is often assumed to follow the Bird-Dorn-Mukherjee equation [132]:

$$\dot{\epsilon} = \frac{ADGb}{kT}\left(\frac{b}{d}\right)^{p}\left(\frac{\sigma}{G}\right)^{n} \tag{2.4.1}$$

where $\dot{\epsilon}$ is the strain rate, D is the bulk diffusivity, A is a dimensionless constant, G is the shear modulus, b is the magnitude of the Burgers vector, d is the grain size, k is the Boltzmann's constant, T is the absolute temperature, p is the inverse grain size exponent, and n is the stress exponent. n is used to identify the creep deformation controlling mechanism. If it is constant over a range of applied stresses and temperatures, then the creep rate controlling mechanism is supposed to be constant.

Steady-state creep accounts for most of the creep time so most models concern the temperature and time-dependent secondary creep only. Steady-state creep behaviour is generally expressed by the simplified Dorn power law equation [133]:

$$\dot{\epsilon_s} = B\sigma^{n} exp\left(-\frac{Q}{RT}\right) \tag{2.4.2}$$

where $\dot{\epsilon_s}$ is the steady-state creep strain rate, B is a constant, R is the universal gas constant, σ is the stress and Q is the creep activation energy. Assuming that only one mechanism dominates the deformation in the applied stress range, the stress exponent is a constant for a given temperature. Hence equation (2.4.2) yields:

$$ln(\dot{\epsilon_s}) = lnB + nln\sigma - \frac{Q}{RT} \tag{2.4.3}$$

The stress exponent n and the activation energy Q may be estimated by a linear best-fit of equation (2.4.3) to the creep experimental data, as a function of stress and temperature respectively.

For some solders, the simple power law breaks down at low and high stresses and this behaviour was consolidated into a single expression, the Garofalo hyperbolic sine law, or sinh formulation [134]:

$$\dot{\epsilon_s} = C\left[sinh(\alpha\sigma)\right]^{n'} exp\left(-\frac{Q'}{kT}\right) \tag{2.4.4}$$

where α is the stress coefficient that prescribes the stress level at which the power law dependence breaks down (in MPa), Q' is the activation energy and C is a constant. The values of C, n' and Q' are again obtained by fitting experimental data to equation (2.4.4) by an iterative multivariable nonlinear regression method.

Table 2.5 summarises best-fit creep constants for both Sn-Pb and Pb-free solders for the most widely used Dorn power law and Garofalo hyperbolic sine law models. There are large discrepancies in creep data and materials constants, even among studies using the same creep models. Research groups often used different sets of strain rates and temperature, making the data difficult to compare as creep is strain rate and temperature-dependent. In order to gain results on a sensible time-scale, studies were often carried out at much higher strain rates ($\succ 10^{-4}$ s^{-1}) than in operation ($\sim 10^{-7}$ s^{-1}). Errors may also be induced by the varying cross-sectional area of a joint and the non-uniformity of the stress-strain distribution (the stress and strain distribution is modified at the constrained interfaces with the board and component). Furthermore, the plastic deformation of the solder can be restricted by the highly rigid substrate materials. The degree of restriction of the deformation depends on the size and geom-

Table 2.5: Literature data for the Dorn power law and the Garofalo hyperbolic sine law (after Ma and Suhling [107]) [10, 135–144].

Solder alloy	n	Q (kJ.mol^{-1})	Testing method	Reference
Constitutive model: Dorn power law				
Sn-40Pb	6.3	20	Lap joint, Shear/Tensile	[123]
Sn-3.5Ag	11	79.8	Flip chip, Tensile	[124]
	6.05	61.2	Bulk, Tensile	[125]
SAC387	3.69	36	Bulk, Tensile	[10]
	7	40	Bulk, Tensile	[127]
SAC405	18	83.1	Flip-chip, Tensile	[124]
Constitutive model: Garofalo Hyperbolic Sine law				
Sn-40Pb	3.3	52.9	Lap joints, Shear/Tensile	[128]
	3.04	56.9	Bulk, Compression	[10]
Sn-37Pb	1.38	50.0	Bulk, Tensile	[129]
	2	44.9	Flip-chip joints, Tensile	[124]
	2.1	54.1	Lap joints, Tensile	[126]
	3.3	52.8	Bulk, Tensile	[128]
	2.2	59.3	Flip-chip joints, Tensile	[126]
Sn-3.5Ag	4.75	57.1	Bulk, Tensile	[124]
	5.04	41.6	Bulk, Tensile	[125]
	8.67	77.4	Lap joints, Shear	[125]
	5.5	72.5	Lap joints, Shear	[125]
	5.5	72.4	Lap joints, Shear	[125]
SAC396	2.89	62.0	Bulk, Tensile	[129]
	4.2	45	Bulk, Compression	[130]
	3.79	62.3	Lap joints, Tensile	[126]
	4.0	71.3	Flip-chip joints, Tensile	[131]
SAC387	5.1	65.32	Bulk, Tensile	[131]
	6.41	54.0	108 datapoints from literature	[132]

etry of the solder joint as well as the microstructure of the solder (presence of internal defects such as oxide particles, microvoids and transverse grain boundaries) and the physical and mechanical properties of the solder and substrate materials [145, 146].

Critical appraisal of nanoindentation creep

In nanoindentation, a fine scale indenter is loaded into a sample and its displacement is continuously recorded. There are well-known procedures to extract materials parameters from the loading and unloading curves [147, 148]. Besides, nanoindentation has been proposed as a time-saving alternative methods to obtain creep properties of materials [149–154]. In particular, high temperature nanoindentation appears very promising. It has been steadily improved since the first measurements in 1995 when the nanoindenter was placed in a temperature-controlled room up to a mere 32-34°C [155], and nanoindentation can now be performed at temperatures up to 750°C. Section 3.3.2 shows how nanoindentation creep parameters that describe steady-state creep may be obtained by a best-fit of strain rate as a function of stress data to various expressions.

Caveats of nanoindentation creep measurements have been pointed out recently [156, 157]. In particular, a major source of concern is the neglect of primary creep in creep data analysis. Throughout the indentation process, previously unstrained material is continously entering the creeping domain and local regions under the indenter are undergoing primary creep. Primary creep generates much higher (and variable) strain rates than secondary creep, hence potential inaccurate creep data analysis. Besides, the self-similarity of the stress and strain fields has been pointed out and implies careful interpretation of nanoindentation creep data. The local stresses being very high, different mechanisms may happen at different locations and stages of the indentation process [158].

However, there are some arguments in support of steady-state laws [159]. The effect of primary creep and the sensitivity to changes in creep mechanism may be less significant for materials which creep rapidly at room temperature, such as solder alloys, and good correlation can be expected, especially for high temperature nanoindentation on these materials [156]. Nevertheless, there is little in the literature on the use of nanoindentation for creep measurements of solder alloys [150, 160–162]

The specimen microstructure (e.g. IMCs, grain size), which depends on processing, is expected to have an effect on both high temperature nanoindentation and traditional creep test results. The ever reducing size of electronic assemblies, with solder joint dimensions $\prec 1000\mu$m, makes the length scale of solder joints comparable to that of their microstructure (e.g. grain size). Most results stem from experiments carried out on samples from bulk solder material or melted solder paste in a mould. Not only do these test specimens have a significantly different microstructure from real solder joints, but testing bulk samples instead of real solder joints may result in inaccurate modelling of field mechanical properties. Models are increasingly accounting for the role of microstructure in creep, in particular by sets of macroscopic state variables that describe the microstructural state of the material (e.g. IMC coarsening with thermal cycling) [116, 163–165].

Figure 2.13 summarises the complex and dynamic situation in joints that makes development of optimum Pb-free alloys so complex, and comparison between works in the literature difficult.

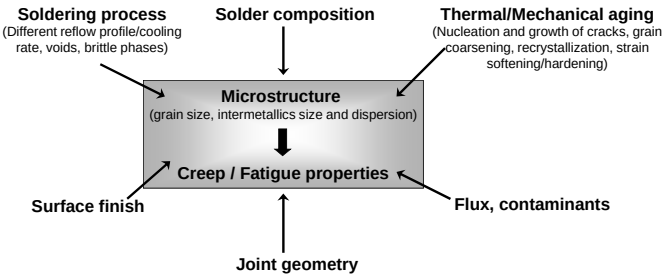


Figure 2.13: Main factors influencing the mechanical properties of solder alloys

Solder joints are highly heterogeneous, so that creep deformation is typically inhomogeneous [166]. Therefore, it can be argued that only by testing an entire solder joint can representative data be obtained. Methods for testing entire solder joint assemblies have been developed but they are complex and often limited to room operation only [167, 168].

2.5 Conclusions

The multiplicity of Pb-free solder materials for the replacement of Sn-Pb led to a multiplicity of reliability databases, test standards, acceleration factors and life-prediction models. Although SAC alloys are now the preferred alloys for Sn-Pb solder replacement in consumer electronics, comparatively little research has focused on the more complex harsh environment conditions. Long-time testing data on Pb-free solders under harsh environment conditions are not yet available, which is a concern as preliminary research tended to suggest that Pb-free assemblies do not perform as well as Sn-Pb assemblies under harsh conditions. Conclusions and recommendations of Pb-free studies are sometimes contradictory, mainly because reliability is package geometry-dependent. Thermal fatigue is considered to be the primary cause of concern for harsh environments and long service lifetimes and ATC tests are carried out to determine life-limiting features in a specific electronic package. However, the imposed temperature profiles in ATC tests required due to time constraints do not represent the heating/cooling rates and dwell times encountered in service. Therefore, analysis of ATC results does not always produce accurate predictions of the mechanical response of a solder joint in operation. Modelling alongside ATC is frequently used to speed up the

characterization of Pb-free alternatives for specific applications, but relies critically on accurate constitutive behaviour.

Creep models such as the power law or the Garofalo hyperbolic sine law have been applied successfully to fit data and are being improved to account for the solder microstructure and package geometry dependence of creep behaviour. Nano and macro-scale techniques that would speed up solder alloys constitutive behaviour characterisation are necessary for the development of new Pb-free alloys and their validity should be further investigated.

Chapter 3

Experimental procedures

This chapter presents details of the experimental methodologies and techniques used in this thesis. First, the in-house manufacturing process of ball grid arrays (BGAs) is described. The next section introduces the microscopic techniques used to investigate microstructures of both bulk solder alloys and solder joints. Then the high temperature nanoindentation technique used to characterise mechanical properties from 25 to 175°C is described. Lastly, new high temperature meso-scale tests based on the nanoindentation platform are presented.

3.1 Ball grid array (BGA) manufacture

BGA assemblies were designed based on the electronic industry requirements for second level electronic packaging using FR-4 and alumina boards. Alumina is a predominant choice for substrate in complex modules due to its high mechanical strength, chemical inertness, insulation properties and high temperature stability. Both FR-4 (epoxy resin and glass fibre) and alumina boards (5 mm x 5 mm) were used as the upper and lower boards of the assemblies. Each of these boards had six corner circular contact pads for solder ball attachment as shown in Figure 3.1. The boards with pads were provided by external suppliers as described in Table 3.1. Two types of pad commonly used for interconnect systems were used: Cu pads on FR-4 and ceramic boards and Pd-Ag pads on ceramic boards only. Cu pads were electroplated to a thickness

of 35 and 50μm for FR-4 and ceramic boards respectively. Pd-Ag pads were manufactured by screen printing onto the alumina substrate and firing at 1000°C to give a Pd-Ag contact pad thickness of 15μm.

SAC305 and SAC387 (T_m=217°C) solder balls (dimensions described in Figure 3.1) were selected as soldering materials for BGA assemblies. Sn-37Pb (T_m=183°C) solder joints were also manufactured for comparison. In addition, Innolot solder joints were manufactured to investigate the promising mechanical properties of this new alloy (see section 2.1.2). Three diameter sizes (400, 500 and 600μm) for SAC305 solder balls were studied while for SAC387, Sn-37Pb and Innolot, 500μm diameter solder balls were used. Such dimensions are common in second-level assembly packaging.

Table 3.1 summarises the materials used for the in-house manufacturing of BGAs and the suppliers.

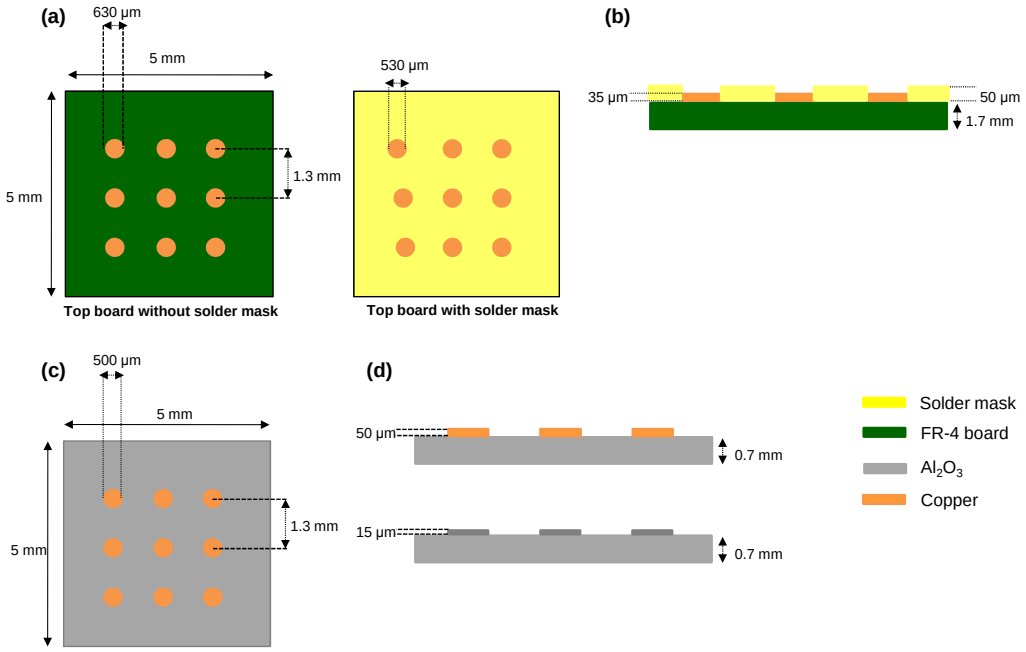


Figure 3.1: Geometries of (a) the top of the FR-4 board without and with solder mask; (b) the cross-section of the FR-4 board; (c) the top of the alumina board with Cu pads; and (d) the cross-sections of the ceramic boards with Cu and Pd-Ag pads.

The following steps were taken for the manufacture of BGA assemblies:

1. Solder paste was deposited onto the Cu pads through a 160μm thick aluminium stencil with six circular holes of 500μm diameter;
2. Solder balls were carefully deposited onto the six solder pasted pads;

Product	Composition (in wt%)	Comments	Supplier
Solder pastes	93Sn-37Pb	No-clean flux	Farnell UK
	96.5Sn3.0Ag0.5Cu (SAC305)		
	95.5Sn3.8Ag0.7Cu (SAC387)		
Solder spheres	93Sn-37Pb	500µm diameter	CAPLINQ Europe BV
	96.5Sn3.0Ag0.5Cu (SAC305)	400, 500, 600µm diameter	Indium corporation, CAPLINQ Europe BV
	95.5Sn3.8Ag0.7Cu (SAC387)	500µm diameter	CAPLINQ Europe BV
	Sn3.8Ag0.7Cu3.0Bi1.4Sb0.15Ni (Innolot)	500µm diameter	Alpha Advanced Materials
Boards	FR-4 + Cu	Metallization thickness: 35µm	Wrekin circuits Ltd.
	Al_2O_3 + Cu	Metallization thickness: 50µm	Advanced Interconnection Technology Ltd.
	Al_2O_3 + Pd-Ag	Metallization thickness: 15µm	GE Aviation

Table 3.1: Materials used for the manufacturing of BGAs.

3. Alignment was verified by optical microscopy;
4. The board/paste/solder ball assembly underwent a first reflow;
5. A second board was similarly prepared by screen printing;
6. The reflowed board was flipped over, the second board added, and alignment checked by optical microscopy;
7. The whole assembly underwent a second reflow.

Figure 3.2 and 3.3 show the different steps of the manufacturing process with the initial and final products. SAC305 solder balls with an initial diameter of 400, 500 and 600μm resulted in solder joints with a stand-off height of $\sim$380, 430 and 460μm respectively and a final diameter of $\sim$700–760, 720–750 and 800–860μm respectively. The solder pastes were 'no-clean' pastes with integrated flux so that no after-soldering cleaning or pre-fluxing was required. Matching ball and paste alloys were used as mixed alloy combinations tended to produce large and multiple voids; a minimal volume of solder paste was used to reduce voiding.

Reflow soldering of the assembled component boards was carried out in an IR forced convection reflow soldering oven (C.I.F. FT05) under air atmosphere. The heaters were electronically controlled, which enabled fast temperature changes and allowed for *in situ* control of the oven temperature. Figures 3.4 (a) and (b) show the reflow profiles used during the two reflow stages of the assembly manufacturing process for Pb-free and Sn-Pb solder alloys respectively. The pre-heating, reflow and cooling phases

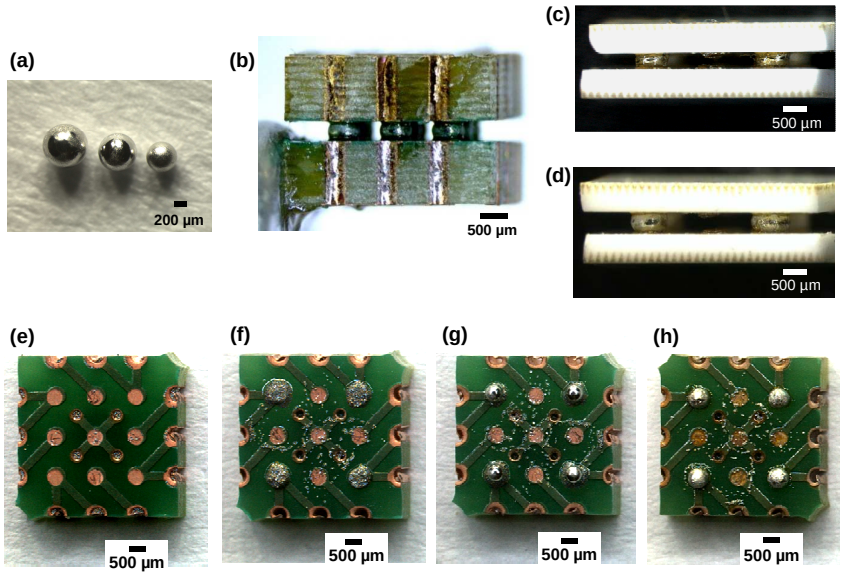


Figure 3.2: (a) SAC305 solder balls (600, 500 and 400μm diameters); (b) FR-4 BGA manufactured from solder balls with an initial diameter of 600μm; (c) ceramic BGA (CBGA) manufactured from solder balls with an initial diameter of 400μm and (d) 600μm; (e) initial FR-4 board with its Cu pads; (f) after solder paste deposition onto 4 Cu pads; (g) after placement of 4 solder balls; and (h) after the first reflow.

followed the Joint Industry Standard IPC/JEDEC J-STD-020B requirements [169].

During pre-heating, the solvents contained within the solder paste were evaporated, minimising subsequent void formation. The heating rate was in the range 1–3°C.s^{-1}. A faster rate caused excessive slumping of the paste and voiding. The pre-heating time was between 60 and 180s. The pre-heating temperature was 200°C for lead-free solders and 170°C for Sn-37Pb solders, which enabled good melting of the solder paste without significant voiding. In the reflow phase, the peak reflow temperature was 265°C and 220°C for Pb-free and Sn-37Pb solders respectively. The reflow profiles were performed to an accuracy of $\pm$5°C. The IPC Specification for the Design and Assembly Process Implementation for BGAs standard (IPC-7095A) defines a maximum void diameter of 20% of the solder joint diameter (9% of area) for voids in the bulk of solder balls and 30% of the solder joint diameter (4% of area) for voids at the interface of solder balls and the substrate for BGAs used in defence and aerospace applications. The selected reflow profiles enabled the formation of satisfactory BGA solder joints when compared with the IPC-7095A standard and there were generally low levels or total absence of voiding within all cross-sectioned solder joints [28]. Figure 3.5 shows an optical image of the cross-section of a typical manufactured SAC305

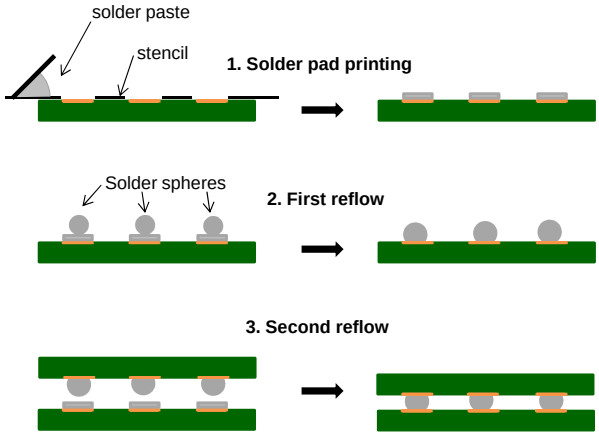


Figure 3.3: The key steps of the BGA manufacturing process. Alignment was checked by optical microscopy before each step.

joint.

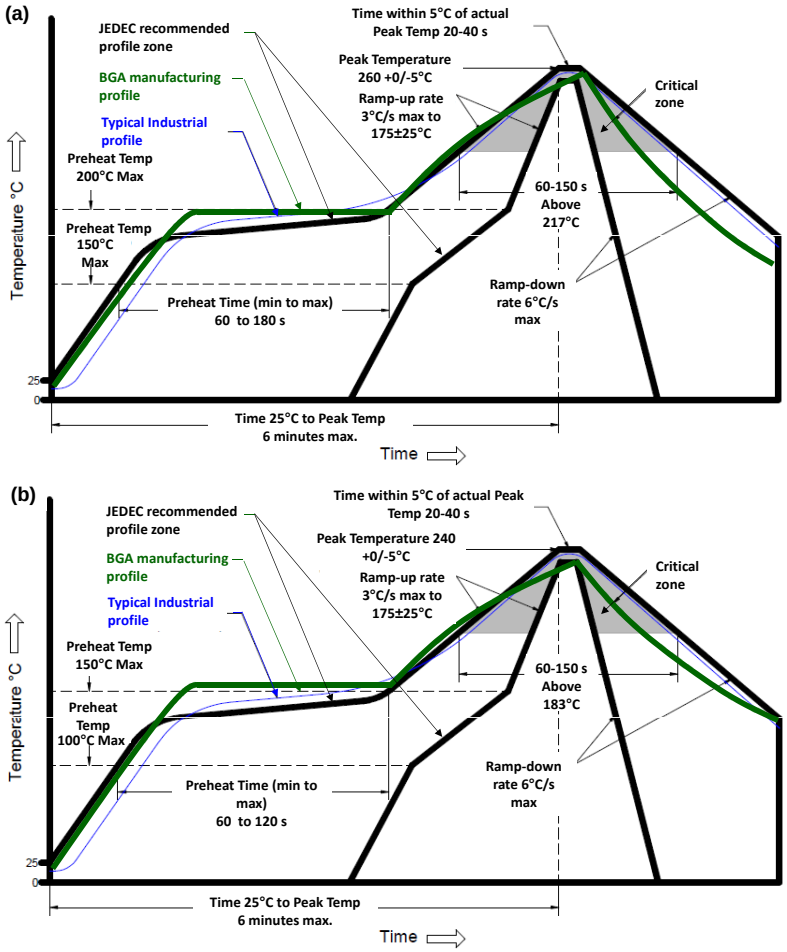


Figure 3.4: JEDEC recommended reflow profile for BGA manufacturing (*black*) with typical industry reflow (*blue*) and reflow profile used for in-house (*green*) (a) Pb-free; and (b) Sn-37Pb BGA manufacturing (adapted from [169]).

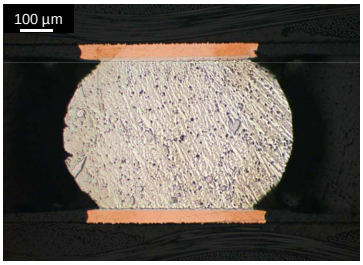


Figure 3.5: Optical image of the cross-section of a typical in-house manufactured SAC305 solder joint.

3.2 Microstructural characterisation

3.2.1 Sample preparation

In order to establish baseline microstructural information on the solders, bulk eutectic Sn-37Pb, Sn (with 99.99% purity and an average grain size $\geq$10μm), SAC387 and Innolot solder alloys in the form of wave soldering bars and Sn-37Pb, SAC305, SAC387 and Innolot as-received solder balls and BGA solder joints were studied.

In-house prepared solder joint samples for optical microscopy, electron microscopy and electron backscatter diffraction examination were prepared by firstly mounting specimens in Wood's metal ($Bi_{50}Pb_{26.7}Sn_{13.3}Cd_{10}$, in $wt\%$) in a 12.5mm diameter holder. Samples for metallographic studies were ground flat using 1200, 2500 and 4000 grit SiC paper, carefully polished with 1 and 0.25μm diamond suspensions, and then finished and slightly etched in a 0.06μm colloidal silica suspension. Finally the samples were cleaned in a deionised water bath followed by an ethanol bath.

Microstructural observation of intermetallic particles was carried out after deep etching of the samples with a 25% HNO_3-75% H_2O solution applied for 2 to 8 minutes and subsequent cleaning by deionised water and ethanol.

3.2.2 Optical microscopy

Digital micrographs at low magnifications were obtained using a Leica M165C microscope equipped with a Leica DFC420 digital camera with magnifications from x7.3 to x120. A Reichter Polyvar Met optical microscope was used for higher magnification

work. Objective lenses of x5, x10, x20, x50 and an eyepiece magnification of x10 were used to image the macrostructure and microstructure.

Polarised light microscopy was performed on the Polyvar microscope equipped with a nearly crossed polariser. All samples contained a β-Sn phase, which has a tetragonal crystal structure and is therefore birefringent in reflecting light from a polished surface. Therefore, polarized light experiences a small rotation of the polarization on reflection from Sn crystals. By viewing the reflected light through an analysing polariser nearly crossed with respect to the incident polarised light, contrast can be seen that is related to the Sn grain orientation.

3.2.3 Scanning electron microscopy (SEM)

Secondary and backscatter electron imaging was carried out in a JEOL JSM-6500F scanning electron microscope, with a field emission gun operating at 20kV with a beam current of 70nA. Energy-dispersive X-ray spectroscopy (EDS) for phase composition characterisation was carried out under the same conditions.

3.2.4 Electron backscatter diffraction (EBSD)

EBSD was also carried out in the JEOL JSM-6500F, with the samples tilted at 70° to the incident electron beam, at an accelerating voltage of 20kV corresponding to a beam current of 70x10^{-9}A. EBSD scans were performed in a hexagonal scan pattern with a step size ranging from 0.2 to 0.5μm. EBSD enabled collection of data relating to crystallographic orientation with a spatial resolution down to 0.2-0.3μm. An EDAX TSL OIM acquisition system and analysis software was used for grain size and texture measurement. The iterative grain dilation method was used for the clean up of raw data, allowing for a grain tolerance angle of 5° and a minimum grain size of 5μm. This method only affected data points that did not 'belong' to any grains, yet had neighbouring grains that did belong to grains. The orientation of the particular point was changed to match that of the neighbouring data point with the highest confidence index. The process was repeated until each point in the data set belonged to a grain. The EBSD technique allowed for the spatial arrangement of lattice orientations on the

surface of samples to be mapped.

Patterns for the same phase may vary on account of the different possible crystal orientations. Figure 3.6 shows the EBSD diffraction patterns for Sn before and after indexing two different crystal orientations. The analysis shows the data provided a close approximation to the Sn phase with reasonable matching of the patterns before and after indexing. The existence of various intermetallics in the microstructure provided a much weaker diffraction intensity. EBSD data was used to investigate texture in the Sn

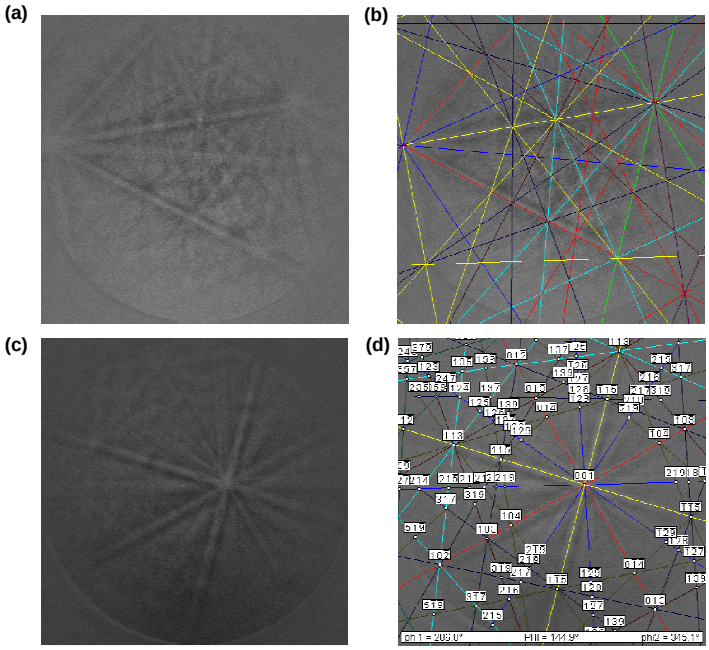


Figure 3.6: EBSD Sn diffraction patterns for different crystal orientations (a) and (c) before indexing; and (b) and (d) after indexing the Kikuchi patterns.

phase using inverse pole figures (IPF) where the orientation distribution of a sample axis was shown on a stereogram plotted with respect to crystallographic orientation.

3.2.5 Focused ion beam microscopy (FIB)

Transverse cuts across nanoindentation indents were made using the FEI FIB 200 operating with Ga ions at an acceleration voltage of 30kV and beam current of $3x10^{-9}$A. Subsequent ion induced secondary electron imaging was carried out using a beam current of $0.1x10^{-9}$A.

3.2.6 Atomic Force Microscopy (AFM)

Some indentation profiles were studied using atomic force microscopy (Park Scientific Instrument CP-II-AFM) in tapping mode.

3.3 Mechanical testing

3.3.1 Nanoindentation

Nanoindentation experiments were performed using a NanoTest platform (Micro Materials Ltd., Wrexham, UK) involving a pendulum-mounted indenter with electromagnetic loading. Figure 3.7 shows the nanoindentation platform. The objectives of these experiments were:

1. To characterise the constitutive behaviour of various solder alloys at room and elevated temperatures.

2. To assess nanoindentation as a useful means to characterise solder material properties.

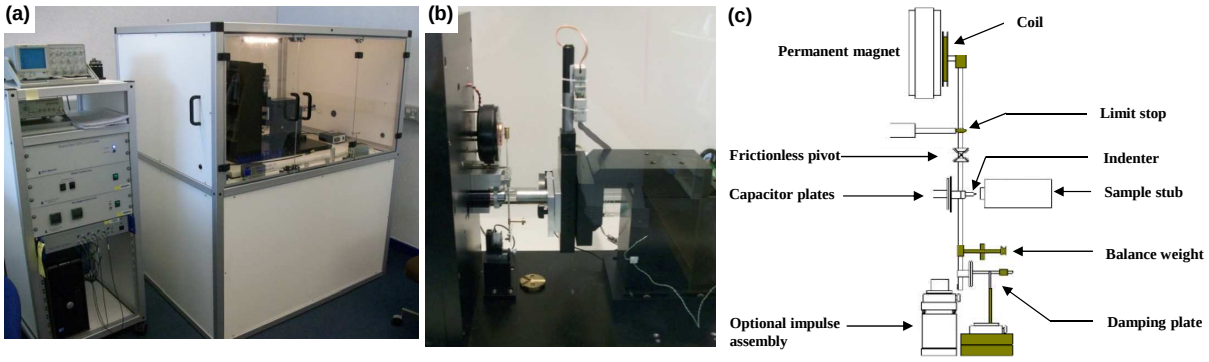


Figure 3.7: NanoTest platform showing the (a) chamber and (b) motor control units; and (c) schematic of the pendulum based nanoindentation system (adapted from MicroMaterials Ltd.).

The NanoTest equipment operated on an anti-vibration table to produce reproducible, noise-free results and in a temperature controlled cabinet to minimise thermal drift. A coil was mounted at the top of the pendulum and the coil was attracted towards a permanent magnet when a coil current was applied, producing motion of

the indenter towards the sample and into the sample surface. The displacement of the indenter was measured by means of a parallel plate capacitor, one plate of which was attached to the indenter holder. When the indenter moved, the capacitance change was measured by means of a capacitor bridge. Sample manipulation was achieved by means of three computer-controlled DC motors driving micrometer stages in a XYZ configuration.

During nanoindentation, penetration depth of a calibrated three-faced Berkovich diamond indenter with a 50nm radius was measured as a function of the applied load throughout a load-unload cycle. Figures 3.8 (a) and (b) show a schematic of the nanoindentation stress and the resulting typical nanoindentation loading and unloading curves. The indentations were conducted using the load control mode, i.e. the loading process was finished and reversed when it reached the pre-set peak load. The spacing between indentations was adjusted to the size of at least one and a half indents for each load so that the impression from one indent did not influence the readings taken for the next indentation. Each indentation in a particular testing condition was repeated on at least 10 different locations for all samples to obtain an average and standard deviation. The loading rate was selected so that the time to maximum load was 15s. The unloading rate was chosen to be the same as the loading rate.

The nanoindentation system was calibrated prior to testing by performing indentation tests on a fused silica (SiO_2) standard. The compliance of the load frame and the area function for the indenter $A(h)$ were measured and checked regularly. Depth calibration of the indenter to account for geometry corrections from the ideal Berkovich indenter were made by placing indents into fused silica over a range of depths for each temperature prior to measurements. Indentation data were corrected for the effects of thermal drift by setting a holding period of 60s at 80% unloading for thermal drift evaluation. Nanoindentation creep was studied during a 600s dwell time at maximum load as described in section 3.3.2. The selection of the position to indent was controlled under a high resolution optical microscope.

The nanoindentation data was analysed using the Oliver and Pharr method [147]. Upon indenter loading, the deformation is both elastic and plastic and a residual impression was left in the surface of the specimen. A main assumption to simplify

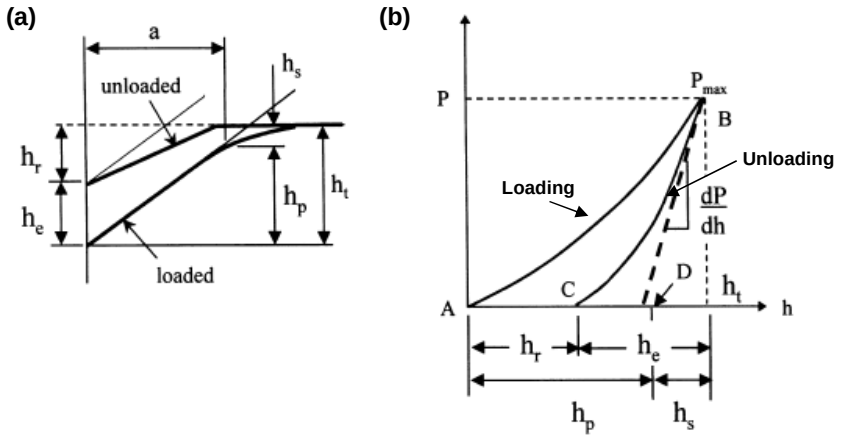


Figure 3.8: (a) Schematic of indenter and specimen surface geometry at full load and full unload for a Berkovich indenter [170]; and (b) typical indentation load versus displacement curve for elastic-plastic loading followed by elastic unloading. h_r is the depth of the residual impression, h_t is the depth from the original specimen surface at maximum load P_{max}, h_e is the elastic displacement during unloading and h_s is the distance from the edge of the contact to the specimen surface at full load. Upon elastic reloading, the tip of the indenter moves through a distance h_e, and the eventual point of contact with the specimen surface moves through a distance h_s [170].

nanoindentation analysis is that unloading is entirely elastic. The depth of penetration together with the known geometry of the indenter provided an indirect measure of the area of contact at full load, from which the mean contact pressure, and thus the hardness H could be estimated. The unloading curve of the indentation test was fitted to the power law function:

$$P = a(h - h_f)^m \tag{3.3.1}$$

where a and m are fitting constants, P is the load, h is the displacement of the indenter, and h_f is the intercept displacement upon unloading. From this fit, the contact stiffness was determined as:

$$S = \left.\frac{dP}{dh}\right|_{h=h_{max}} \tag{3.3.2}$$

The contact depth h_c was determined from:

$$h_c = h_{max} - \epsilon\frac{P_{max}}{S} \tag{3.3.3}$$

where h_{max} is the maximum depth of the indenter, P_{max} is the maximum load, and ϵ is a constant determined from contact theory from an axisymmetric indentation (0.75 for a Berkovich indenter). From the thus determined contact depth, the projected contact

area, A, could be calculated and H was determined from the peak load, P_{max} and A [147, 171]:

$$H = \frac{P_{max}}{A} \tag{3.3.4}$$

On load removal, the sample recovers, with relaxation of elastic strains within the material. The analysis of the initial portion of the elastic unloading response can be used to estimate the elastic modulus E of the indented material. The nanoindentation reduced modulus, E_r, can be obtained from the unloading portion of the depth-load curve according to:

$$C = \frac{\sqrt{\pi}}{2E_r\sqrt{A}} \tag{3.3.5}$$

where C is the contact compliance and E_r is the reduced modulus.

E was derived from E_r as follows:

$$\frac{1}{E_r} = \frac{1-\nu^2}{E} + \frac{1-{\nu_i}^2}{E_i} \tag{3.3.6}$$

where ν is the sample's Poisson's ratio, and E_i and ν_i are the indenter modulus (1140GPa) and Poisson's ratio (0.07). A Poisson's ratio of 0.36 was chosen for SAC and Innolot alloys [105] and 0.33 and 0.4 for the Sn and Sn-37Pb alloys respectively [172].

3.3.2 High temperature nanoindentation creep

High creep temperature testing of bulk samples up to 175°C was achieved in the NanoTest platform. Experiments consisted of a constant loading rate indentation cycle, with loading to maximum loads of 100, 200, 300, 400 and 500mN followed by a 600s dwell at maximum load, unloading and a second dwell period of 15s at 90% unloading for thermal drift corrections. The loading/unloading rates were adjusted so that the overall loading and unloading time was 15s for all tests. Creep measurements were carried out during the 600s load period at maximum load.

Figure 3.9 shows a schematic of the testing set-up for high temperature measurements. Samples were attached to a hot stage by means of a high temperature cement (adhesive curing time of 24hrs). The indenter was heated separately to the same temperature as the sample, minimising heat flow on contact. Sample loading in the Nan-

oTest was horizontal (contrary to most nanoindentation equipment that operate with vertical loading), enabling temperature drift-free measurements as heat rose, away from the electronics. Besides, a heat shield minimised thermal interference with the electronics and depth sensing equipment. Depth calibration of the indenter was carried out on fused silica for all temperatures studied.

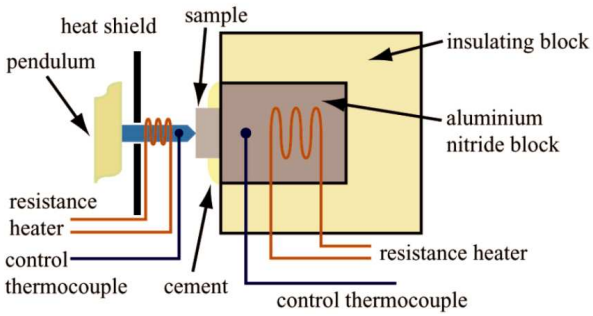


Figure 3.9: Schematic of the high temperature testing equipment (MicroMaterials Ltd.). Both the indenter tip and the sample were heated to the same temperature.

The initial phase of nanoindentation creep was fitted to the Chudoba and Richter equation, which is a simple logarithmic equation [173, 174]:

$$h(t) - h(0) = Aln(Bt + 1) \tag{3.3.7}$$

where *h(t)* is the indentation depth at the creep time t, and A and B are material constants that can be related to the extent of creep and the creeping rate respectively. Figure 3.10 shows a typical fit of Equation 3.3.7 to the experimental creep data for SAC387. All the alloy data fitted acceptably well to Equation 3.3.7.

All alloys showed approximately steady-state behaviour after 150s and it was assumed that the creep deformation of the alloys was due to steady-state creep. Therefore, the creep data was analysed in the 150-600s time range. In this range, the creep data could be best-fitted to the Dorn power law equation:

$$\frac{d\epsilon_s}{dt} = B\sigma^n exp\left(-\frac{Q}{RT}\right) \tag{3.3.8}$$

where $\frac{d\epsilon_s}{dt}$ is the steady-state creep strain rate, B is a constant, n is the creep stress exponent, Q is the creep activation energy and R is the universal gas constant. The

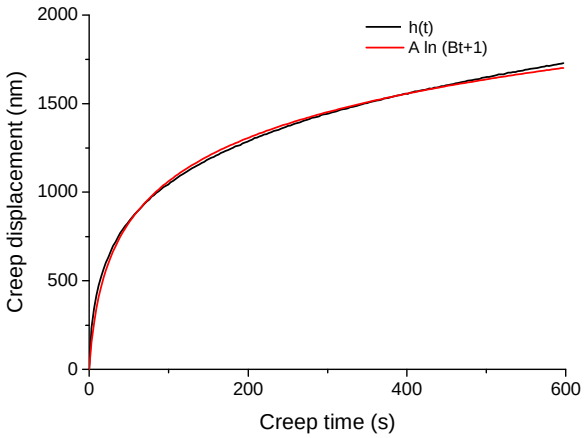


Figure 3.10: Experimental creep results on bulk SAC387 at 25°C and the best-fit to Equation 3.3.7.

creep strain rate $\frac{d\epsilon}{dt}$ was given by:

$$\frac{d\epsilon}{dt} = \frac{1}{h}\frac{dh}{dt} \tag{3.3.9}$$

where h is the indentation depth. Although the stress around an indent varied greatly between the indentation area and more remote regions, a characteristic stress σ was defined by a relationship similar to the hardness definition [156]:

$$\sigma = \frac{P}{A_p} \tag{3.3.10}$$

where P is the applied load and A_p is the cross-sectional area of the indenter. Experimental creep parameters were extracted from nanoindentation creep studies at constant load by combining Equations (3.3.8)–(3.3.10) [156]:

$$ln\left(\frac{1}{h}\frac{dh}{dt}\right) = lnk + nln\left(\frac{P}{A}\right) \tag{3.3.11}$$

where k is a constant.

The stress exponent n was extracted from the linear best-fit regression using a log-log plot of $\frac{1}{h}\frac{dh}{dt}$ against $\frac{P}{A}$.

Figures 3.11 (a) and (b) show schematically the approach used for creep activation

energy determination, using creep curves obtained for various temperatures at identical loading [156]. At a given stress, equation 3.3.8 gives Q as the slope of $log(\frac{d\epsilon}{dt})$ against $1/T$. The strain rate was calculated from the median of the creep curves measured at a particular temperatures and fitted to Equation 3.3.7.

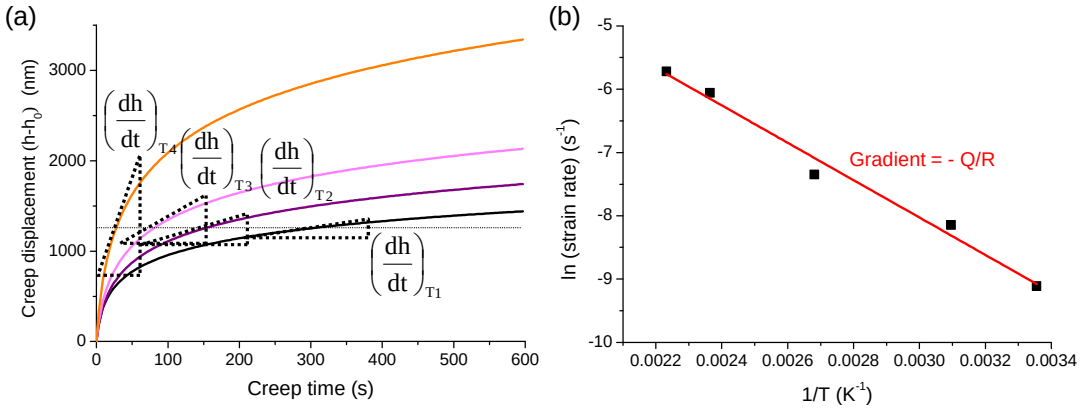


Figure 3.11: (a) Elevated temperature creep curves of SAC387; and (b) illustration of the approach to the determination of the creep activation energy, Q.

3.3.3 High temperature meso-scale testing

As well as 'conventional' nanoindentation using the NanoTest platform in its default configuration, new variants were developed in order to be able to investigate the mechanical response of individual or small number of joints, termed here as 'meso-scale testing'. The motivation was that while bulk tensile testing is slow and requires large specimens, nanoindentation generates uncharacteristically high and varying stress fields, from which creep data is highly sensitive to the local microstructure. Meso-scale testing was explored for utility in gaining data about the response of joints at realistic, lower stress ranges. An insulated, hot liquid cell was designed to fit within the NanoTest platform into which an entire BGA-based package could be immersed, as shown schematically in Figures 3.12 (a) and (b). The liquid cell was filled with a low viscosity oil (Leybonol LVO 100 – ISO VG 100) heated by means of two cartridge heaters connected via a thermocouple fitted in slots underneath the cell to an automatic power controller. An insulating cap covered the cell to minimize heat dissipation. The temperature of the oil was monitored at all times and the joint temperature was assumed

to be that of the oil after thermal stabilisation. For each experiment, two BGAs and a piece of fused silica (for depth calibration of the indenter at each temperature) were attached to an aluminium stub by means of a high temperature cement as shown in (c), and immersed in the oil.

Since this was essentially an entirely new approach, considerable time was spent in developing the test itself with many modifications and improvements. For example, difficulties arose from the occasional irregularity of heating due to the dead time response of the cartridge heaters to temperature decreases or increases, resulting in thermal contraction or expansion of the apparatus. This effect has been observed previously for room temperature creep tests up to 14 hours [175]. Temperature increases or decreases resulted in lower or higher measured voltage respectively, leading to error in the recorded indenter displacement rates. Therefore, the system was allowed to stabilise for at least an hour before each creep test and temperature within the liquid cell was measured and recorded at all times. Data that were obtained under conditions where there was more than a ± 0.5°C temperature change over the duration of the test were discarded.

Figures 3.13 (a)–(c) show the meso-scale testing equipment in the NanoTest platform while (d) and (e) some details of the samples. Figure 3.14 summarises the various types of elevated temperature creep tests carried out in the NanoTest platform and the geometries used. Test (1) was carried out using the hot stage and was the 'standard' nanoindentation approach, while Tests (2)–(4) were newly developed in this thesis and were all performed within the meso-scale liquid cell:

- Test (1): High temperature nanoindentation, described in section 3.3.2.
- Test (2): Compression test of CBGAs in the 100-500mN and 25–150°C load and temperature ranges with a spherical stainless steel indenter (2mm diameter).
- Test (3): Spherical indentation of individual as-reflowed solder balls with a stainless steel spherical indenter to characterise the creep behaviour of 500μm diameter solder ball. A 500mN load was applied for 600s at 25, 50, 75 and 100°C.
- Test (4): Shear testing of entire CBGAs was studied at 25, 50, 75 and 100°C by maintaining loads of 100, 200, 300, 400 and 500mN on the upper ceramic board

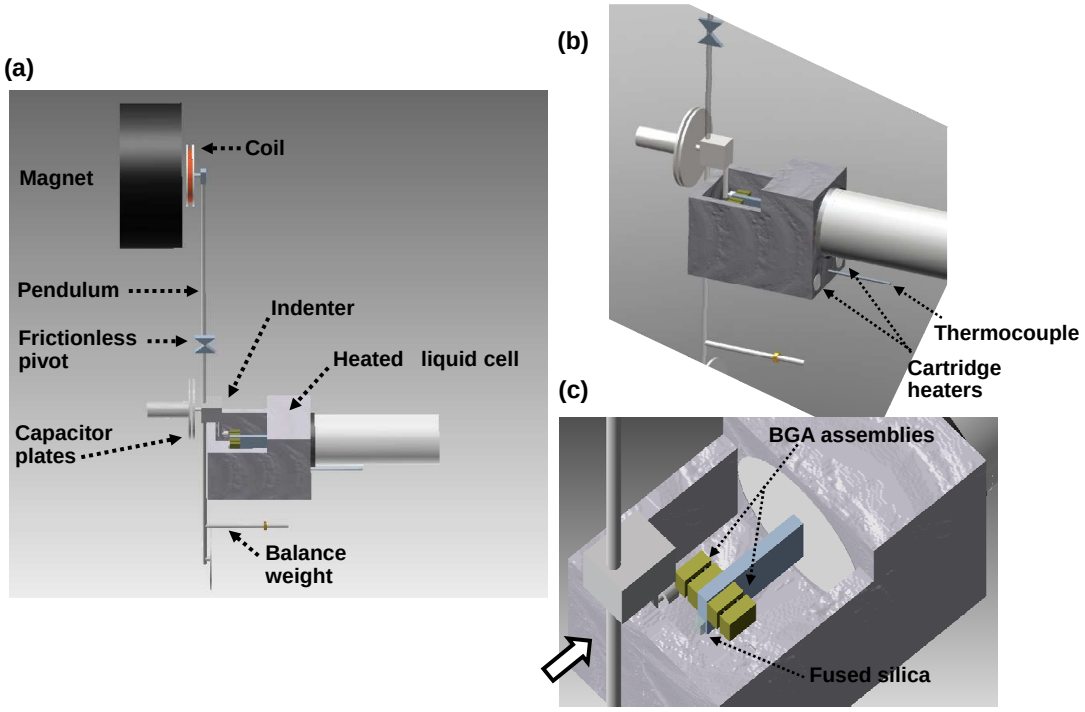


Figure 3.12: (a) Schematic of the set-up of the high temperature meso-scale shear test; (b) heating of the liquid cell by means of two cartridge heaters and a thermocouple linked to an automatic temperature controller; and (c) detail of the interior of the liquid cell with two BGAs and a piece of fused silica attached to a central stub.

of the BGA by means of a large spherical stainless steel indenter (2mm diameter). The BGAs had previously been carefully ground and polished on the two opposite faces so that the solder connections were exactly half balls. Therefore, the assembly was geometrically symmetric and testing was equivalent to applying the load onto two solder ball connections of 350μm diameter. Creep data was obtained over 600s dwell time at each of the maximum loads and for all temperatures.

Depth calibrations of the indenters were made on a piece of fused silica after thermal stabilisation prior to each new temperature test.

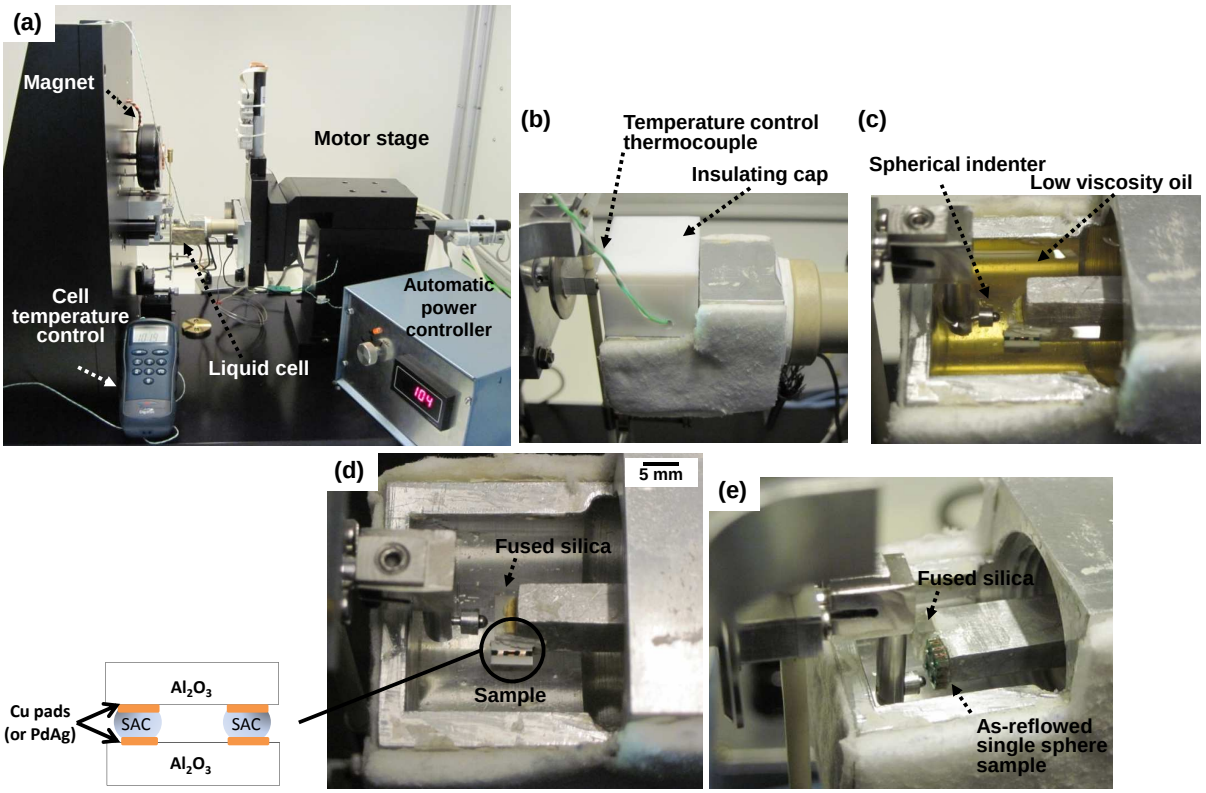
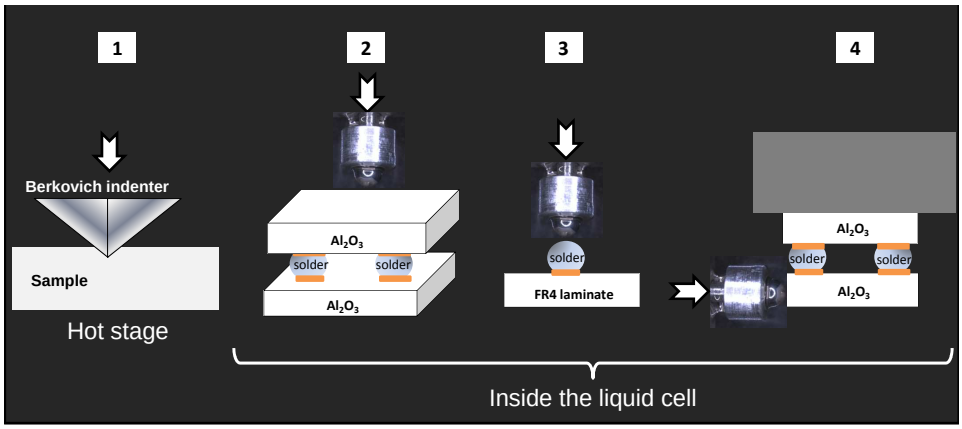


Figure 3.13: (a) The NanoTest platform with the liquid cell and temperature control unit; (b) the liquid cell was covered with an insulating cap during experiments to minimise heat dissipation; and (c) the liquid cell filled with low viscosity oil. A thermocouple was fitted in the cell so that the oil temperature was monitored at all times; (d) set-up for shear testing of a CBGA; and (e) set-up for spherical indentation of as-reflowed solder balls.



Test	Solder alloy	Substrate	Metallization	Type of indenter	Testing conditions
(1)	Sn-37Pb SAC305 SAC387 Innolot	/	/	Diamond Berkovich	600s dwell times at 100, 200, 300, 400 and 500mN loads in a 25 – 175°C temperature range
(2)		Al_2O_3	Cu Pd-Ag	Spherical stainless steel	
(3)		FR4 laminate			
(4)		Al_2O_3			

Figure 3.14: Schematic and summary of the various tests carried out in the NanoTest platform: Test (1) – elevated temperature nanoindentation on a bulk sample; Test (2) – compression test of the BGA assembly; Test (3) – spherical indentation of an as-reflowed solder joint; and Test (4) – shear test of a BGA assembly.

Chapter 4

Microstructural characterisation of solder alloys

The mechanical properties of solder joints, in particular, tensile and creep properties, are intimately connected to their microstructure. Therefore, an in depth microscopy study of solder alloys was carried out for bulk solder alloys, as-received solder balls and in-house manufactured BGA solder joints so that mechanical response (chapters 6 and 7) might be explained in terms of solder and joint microstructure.

4.1 Bulk solder alloys and as-received solder balls

4.1.1 Bulk solder alloys

The various solder phases were identified by a combination of their morphology, referring to the literature, and energy dispersive X-ray spectroscopy (EDS). Figures 4.1 (a)–(c) show scanning electron microscope (SEM) images of the microstructures of as-cast bulk Sn-37Pb, SAC387 and Innolot, while Figure 4.2 shows EDS elemental maps of bulk Sn-37Pb alloys. The microstructure of eutectic Sn-37Pb differed very much from that of Pb-free solder alloys. The bi-material system consisting of Sn and Pb solidified in a eutectic system with limited miscibility comprising Pb islands embedded in a β-Sn matrix (eutectic spacing of $\sim$0.2–1.5μm). In contrast, the SAC-based solders so-

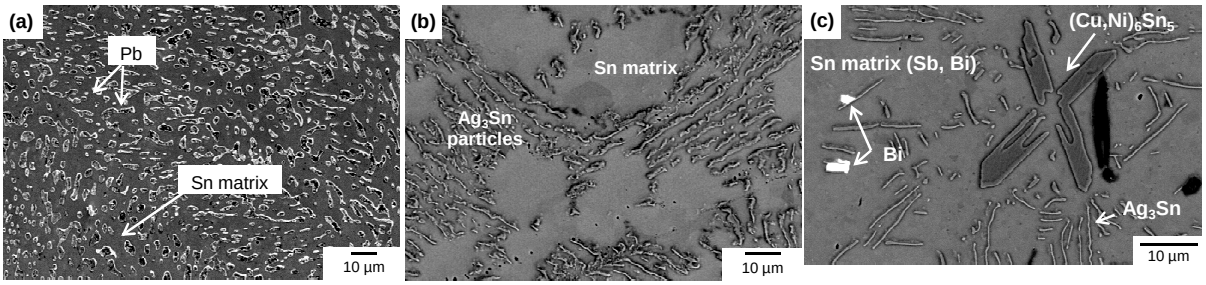


Figure 4.1: Scanning electron microscope (SEM) secondary electron images for (a) eutectic Sn-37Pb; (b) SAC387; (c) Innolot solder alloys.

lidified with Cu_6Sn_5 and Ag_3Sn IMCs within a β-Sn matrix, consistent with the phase diagrams in section 2.1.3. The microstructure of bulk SAC387 in (b) consisted of β-Sn dendrites clustered in colonies surrounded by the quasieutectic comprising small IMCs of Cu_6Sn_5 ($\sim$1.4–4μm) and Ag_3Sn ($\sim$0.2–40μm) embedded in the β-Sn matrix. The Innolot microstructure in (c) was similar to that of SAC387 except that it contained Bi- and Sb-rich particles (or 'islands') in a predominantly β-Sn-rich matrix, as well as $(Cu,Ni)_6Sn_5$ and Ag_3Sn IMCs. Bi-rich particles, evidenced by their bright contrast in backscattered electron imaging in the SEM, had random shape and were often clustered around Ag_3Sn particles. Nano-metre size Ni and Sb particles were evenly distributed within the β-Sn matrix.

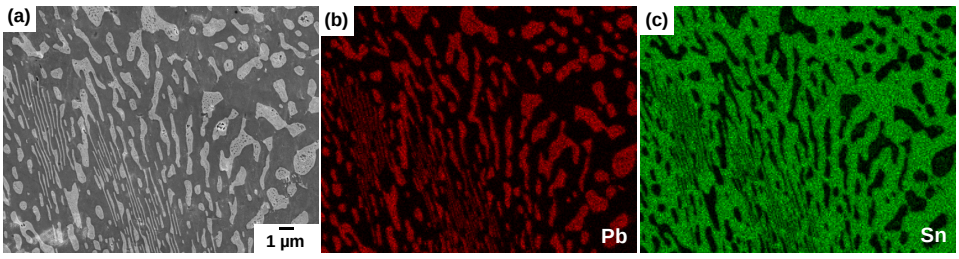


Figure 4.2: (a) Secondary electron image of bulk Sn-37Pb solder alloy; and (b) Pb; and (c) Sn EDS elemental maps from the imaged area.

4.1.2 As-received solder balls

Figures 4.3 (a) and (b) show the microstructures of SAC305 solder balls with diameters of 400 and 600μm respectively. Both Cu_6Sn_5 and Ag_3Sn IMCs were evenly distributed within the β-Sn matrix of the smaller balls. Larger balls also exhibited regions of β-Sn only surrounded by networks of IMCs, such as Figure 4.3 (c) with an apparent grain

size of ~10μm. As shown in Figure 4.3 (d), Cu_6Sn_5 IMCs were mostly evidenced at the boundary of Ag_3Sn clusters that formed in the inter-dendritic/inter-cellular of β-Sn.

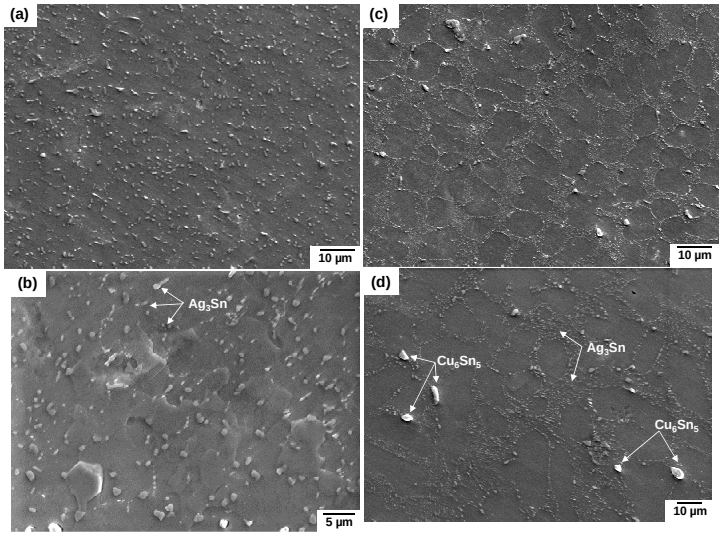


Figure 4.3: Secondary electron images of (a) and (b) 400μm diameter as-received SAC305 solder balls; and (c) and (d) 600μm diameter as-received SAC305 solder balls.

4.2 BGA solder joints

4.2.1 SAC305 solder joints

Figure 4.4 shows an SEM image of a cross-section of an as-reflowed SAC305 solder joint and EDS spectra taken from various types and sizes of IMCs (regions 1 to 4). Larger IMCs (2–40μm) predominantly contained Sn and Cu, whilst the small (200–500nm) and rounder uniformly distributed IMCs predominantly contained Sn and Ag. Morphologic comparison with literature coupled with EDS data allowed for the identification of IMCs in regions 1 and 2 as Cu_6Sn_5 and regions 3 and 4 as Ag_3Sn.

Figures 4.5 (a) and (b) show the microstructure of the bulk of SAC305 BGA solder joints constituted of β-Sn regions surrounded by fine-scale eutectic regions containing β-Sn and fine round shaped Ag_3Sn IMCs. Clusters of IMC particles were surrounded by particle free β-Sn areas. Hexagonal Cu_6Sn_5 IMCs were also scattered within the β-Sn matrix.

In all cases, the as-reflowed microstructure contained well-developed Ag_3Sn and

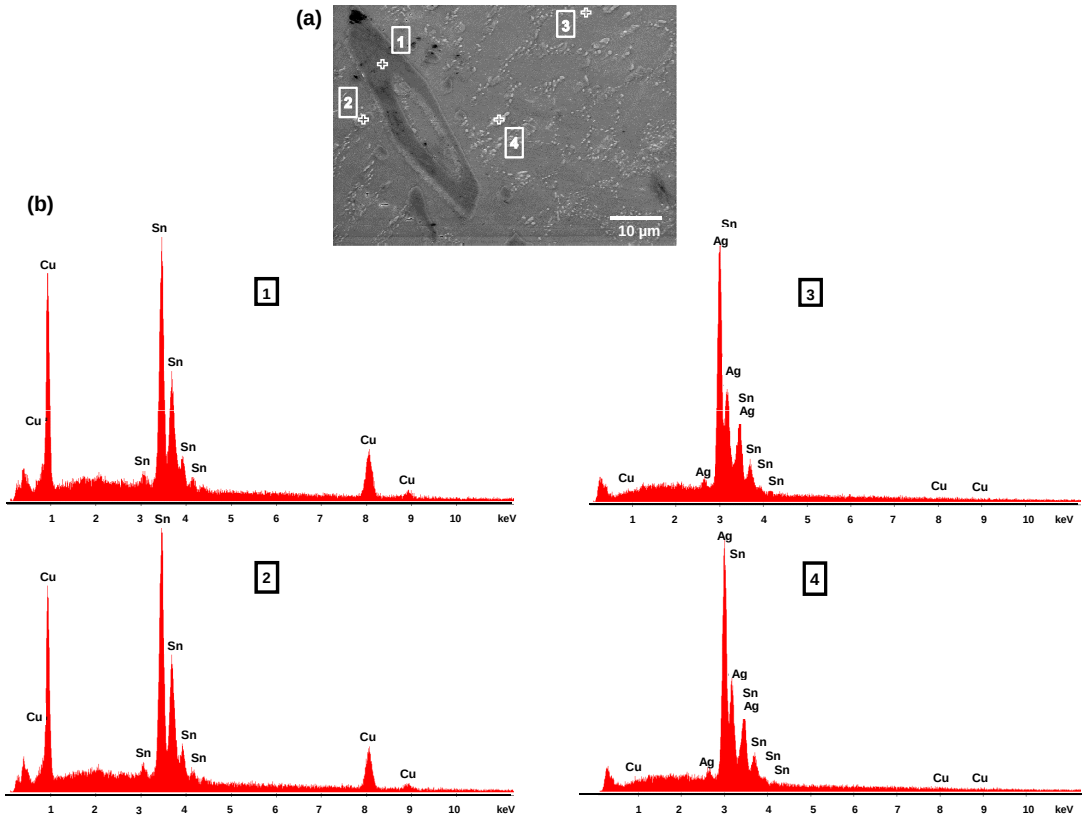


Figure 4.4: (a) Secondary electron image and (b) EDS spectra taken from region 1 to 4 of a cross-section of an as-reflowed SAC305 solder joint.

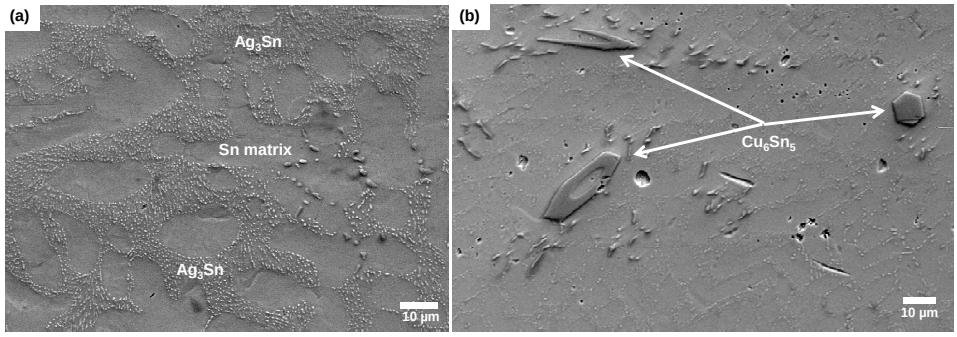


Figure 4.5: Secondary electron images of a cross-section of a SAC305 BGA solder joint with (a) relatively fine Ag_3Sn IMCs; and (b) Cu_6Sn_5 IMCs dispersed within the β-Sn matrix.

Cu_6Sn_5 IMCs embedded in the β-Sn matrix. As seen in section 2.1.3, the nucleation of β-Sn requires supercooling of $\sim$20°C below the ternary eutectic temperature [176], while the nucleation of Ag_3Sn and Cu_6Sn_5 is relatively easy and once started, pronounced growth of one or both of these IMCs can occur to Ag_3Sn plates and Cu_6Sn_5 whiskers before the nucleation of β-Sn and final solidification.

The complexity of the microstructure of solder joints was revealed by deep etching. Sharp and elongated IMC particles were evidenced both inside and on the surface of the solder joint. Large Cu_6Sn_5 IMCs formed as long hexagonal faceted rods (or whiskers) with width from 5 to 30μm and lengths that could reach 300μm, or even long enough to cross the entire solder joint. Figure 4.6 shows the shape of Cu_6Sn_5 hexagonal cross-section rods could be highly elongated. In Figures 4.6 (a) and (b), two types of Cu_6Sn_5 whiskers were evidenced: a solid-type and a hollow-type respectively. The internale 'hole' diameter in (b) varied from 1 to 13μm. The long solid Cu_6Sn_5

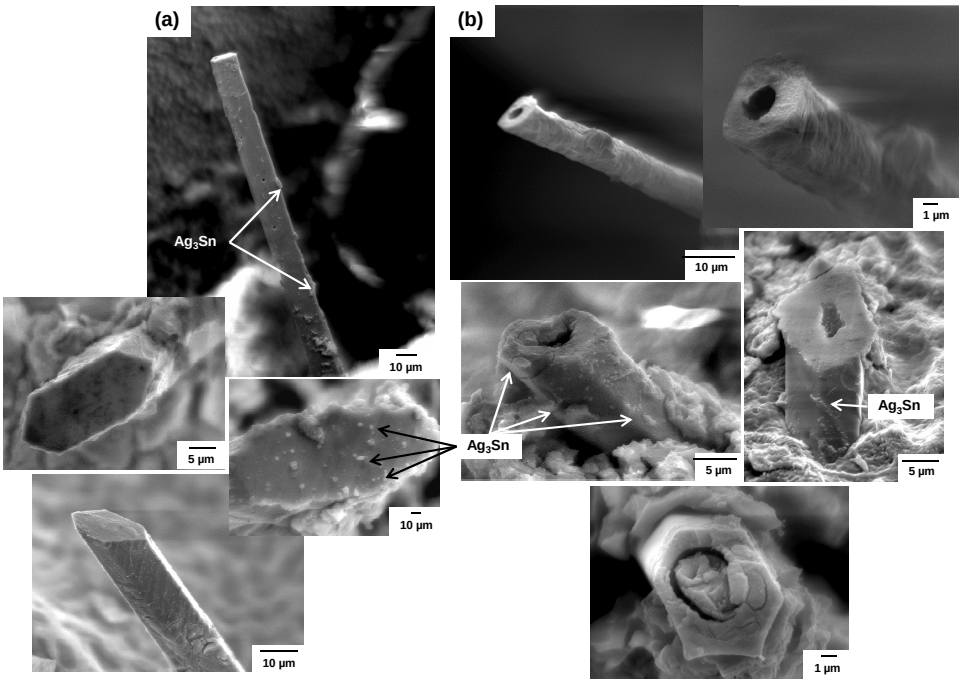


Figure 4.6: Secondary electron images of Cu_6Sn_5 whiskers (a) solid-type; and (b) hollow-type.

whiskers were often found at the interface with the Cu pad, while the hollow-type tended to develop near the surface of the solder joint. The formation mechanisms of the two types of rods provide an explanation for such a selective growth. Near the

Cu pad, the high concentration of Cu and Sn provided for the formation of Cu_6Sn_5 IMCs. Solid whiskers grew out of the molten solder at the pad/ball interface with a single screw dislocation using the ledge mechanism along the long axis of the whisker. As hexagonal rods grew within the solder, the lower Cu concentration caused the intermetallic rods to begin to dissolve and solid whiskers break off into the bulk solder. Figure 4.7 (a) shows a schematic representation for whisker formation [177]. The tips of the whiskers were well-developed pyramidal surfaces, and a few whiskers showed possible growth steps, as in Figure 4.7 (b).

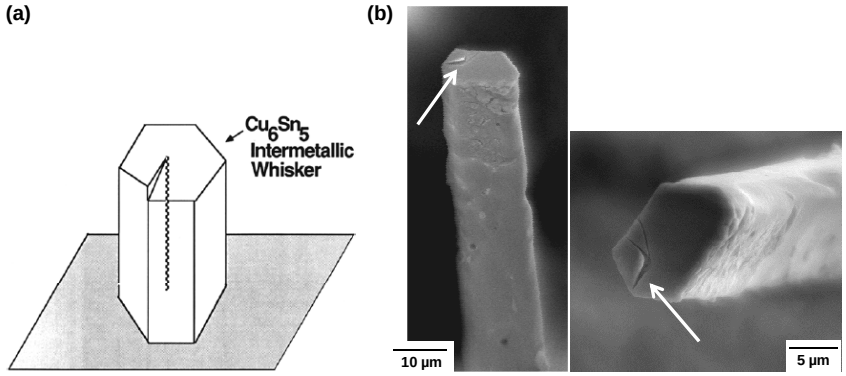


Figure 4.7: (a) Schematic diagram showing the growth of a Cu_6Sn_5 rod using the ledge mechanism model [177]; and (b) SEM secondary electron images of Cu_6Sn_5 rods. The arrows point at a shear band along the dislocation line.

Hollow Cu_6Sn_5 rods were formed near the surface of the joints when the screw dislocation core of the rod had a higher energy and therefore was the first portion of the rod to dissolve, being replaced by molten solder [177]. Figure 4.8 shows small Ag_3Sn particles (1–3μm length) developed on the surface of the Cu_6Sn_5 whiskers.

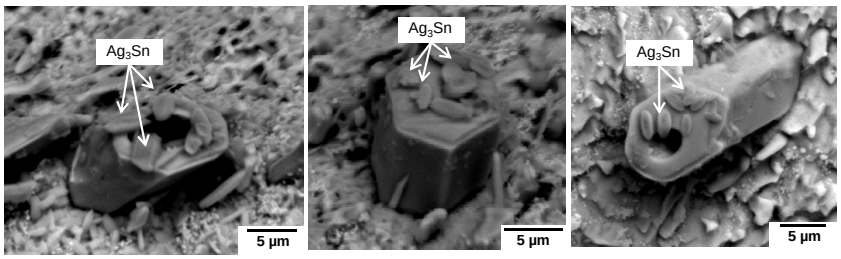


Figure 4.8: Secondary electron images of Cu_6Sn_5 rods with Ag_3Sn nano-particles on their surface.

Figure 4.9 shows that the fine-scale eutectic regions containing rounded Ag_3Sn

IMCs in 2D were a dense 3D network of needle-like IMC particles. In Figure 4.10 (a), the Sn-rich matrix was selectively etched so that only the Ag_3Sn network remained. Longer etching times in (b) revealed Cu_6Sn_5 whiskers, and (c) shows the rod-like structure of the Ag_3Sn particles. Once the β-Sn phase grew as branched dendrites, Ag_3Sn IMCs became trapped in the interdendritic spaces. In the three-dimensional view of the IMC network shown in Figure 4.11 and only revealed by deep etching, Ag_3Sn IMCs were revealed to have extended and convoluted fibrous shapes, interlocking with each other in an extended network. The diameter of the plates/fibrous IMCs was 0.5 to 0.8μm.

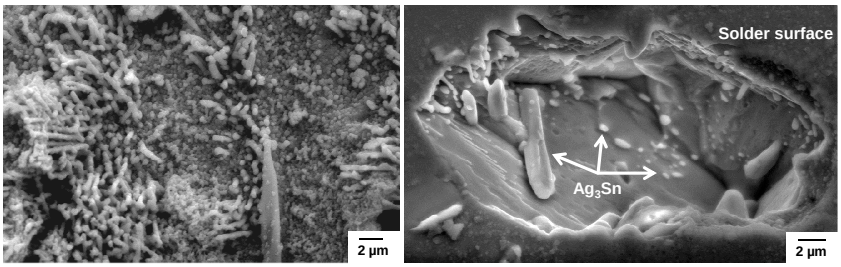


Figure 4.9: Secondary electron images of Ag_3Sn IMCs in the bulk of a SAC305 solder joint.

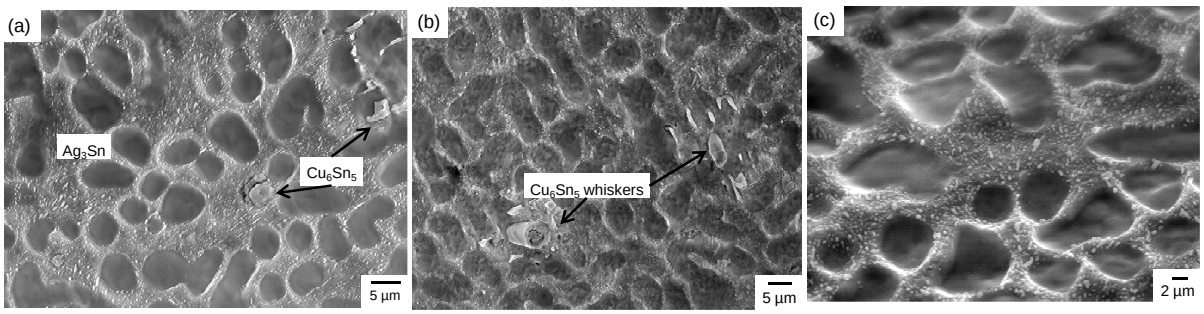


Figure 4.10: Secondary electron images of (a) the network of Ag_3Sn and Cu_6Sn_5 IMCs in the bulk of a SAC305 solder joint; (b) longer etching revealed the Cu_6Sn_5 whiskers; and (c) tilted view of the IMC network showing the small rod-like shape of some of the Ag_3Sn IMCs.

4.2.2 SAC387 solder joints

Figure 4.12 (a) shows the microstructure of SAC387 solder joints in BGA manufactured with a Cu metallization. The SAC387 microstructure was similar to that of SAC305 solder joints with small round shaped Ag_3Sn inter-dendritic IMCs and Cu_6Sn_5 whiskers,

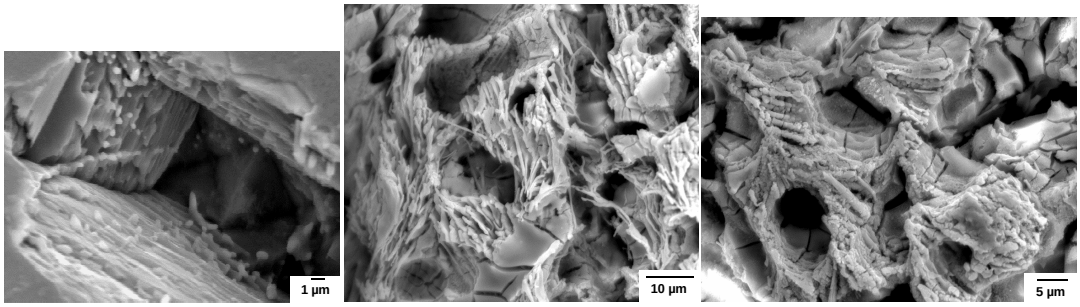


Figure 4.11: Secondary electron images of the network of Ag_3Sn IMCs. Ag_3Sn particles aligned due to their elongated structure, providing an interlocking network around the β-Sn dendrites.

except for the presence of longer needle-like (in 2-D) Ag_3Sn IMCs. Figure 4.12 (b) shows a similar IMC layer for SAC305 solder joints with a Cu_6Sn_5 scallop-shape. Deep etching in Figure 4.13 (b)–(d) revealed that again the Ag_3Sn IMCs were fibrous or plate-like structures. The plates could be as long as 170μm, mostly with a simple plate structure although some evidenced the Hopper-like structure with a central hole as in (c). Figure 4.13 (e) shows similar Cu_6Sn_5 whiskers as in a SAC305 solder joint, with the filled and non-filled whisker types. Figure 4.12 (c) and Figure 4.13 (d) showed that Cu_6Sn_5 IMCs, both at the Cu pad/solder interface and within the bulk of the solder joints, acted as preferential initiating sites for the development of Ag_3Sn plates. Figure 4.14 shows how the IMC compositions were determined on the basis of EDS.

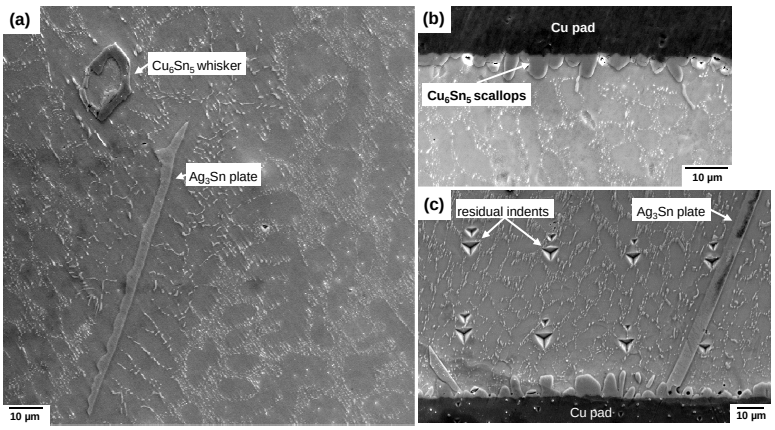


Figure 4.12: Secondary electron images of the cross-section of a SAC387 BGA solder joint with Cu pad metallization: (a) bulk of the SAC387 solder joint; (b) SAC387-Cu pad interface showing the typical Cu_6Sn_5 scallop-shaped IMC layer; and (c) long Ag_3Sn IMCs developed preferentially from the IMC layer.

Since the manufacturing process and metallization pad were the same for SAC305

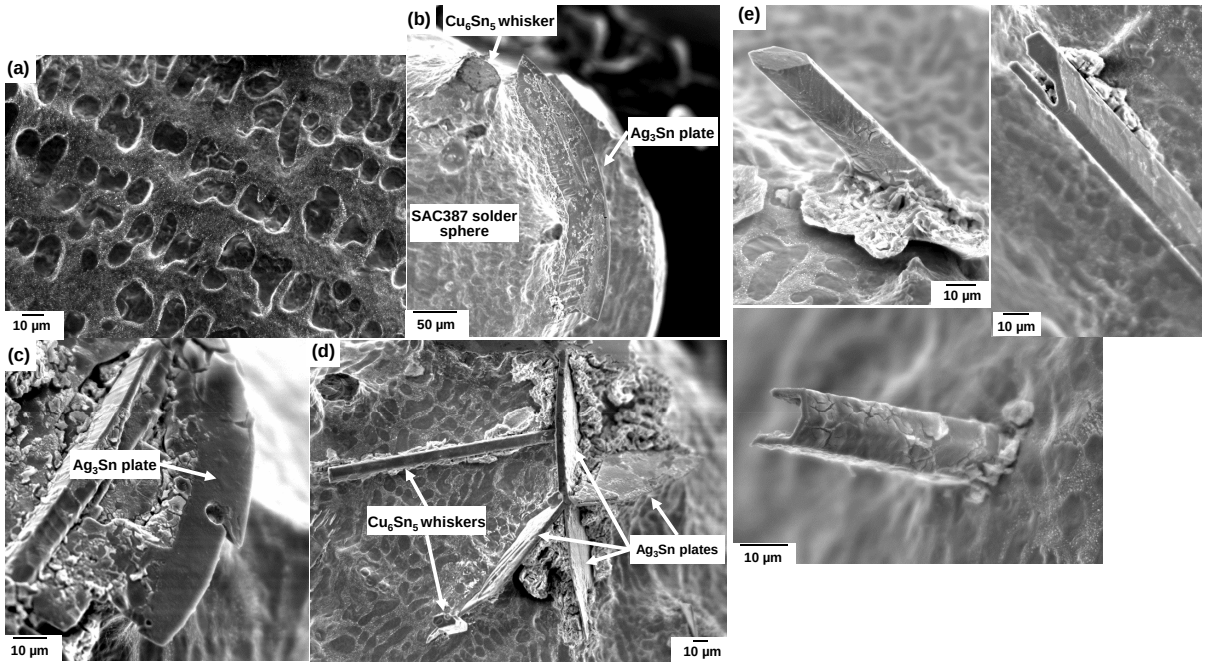


Figure 4.13: Secondary electron images of a deep etched BGA SAC387 solder joint with (a) the residual network of Ag_3Sn IMCs after β-Sn was etched away; (b) surface of the solder ball with large IMCs; (c) Hopper-like Ag_3Sn plate; (d) Ag_3Sn plates often developed in the vicinity of Cu_6Sn_5 whiskers; and (e) solid and hollow-type Cu_6Sn_5 whiskers.

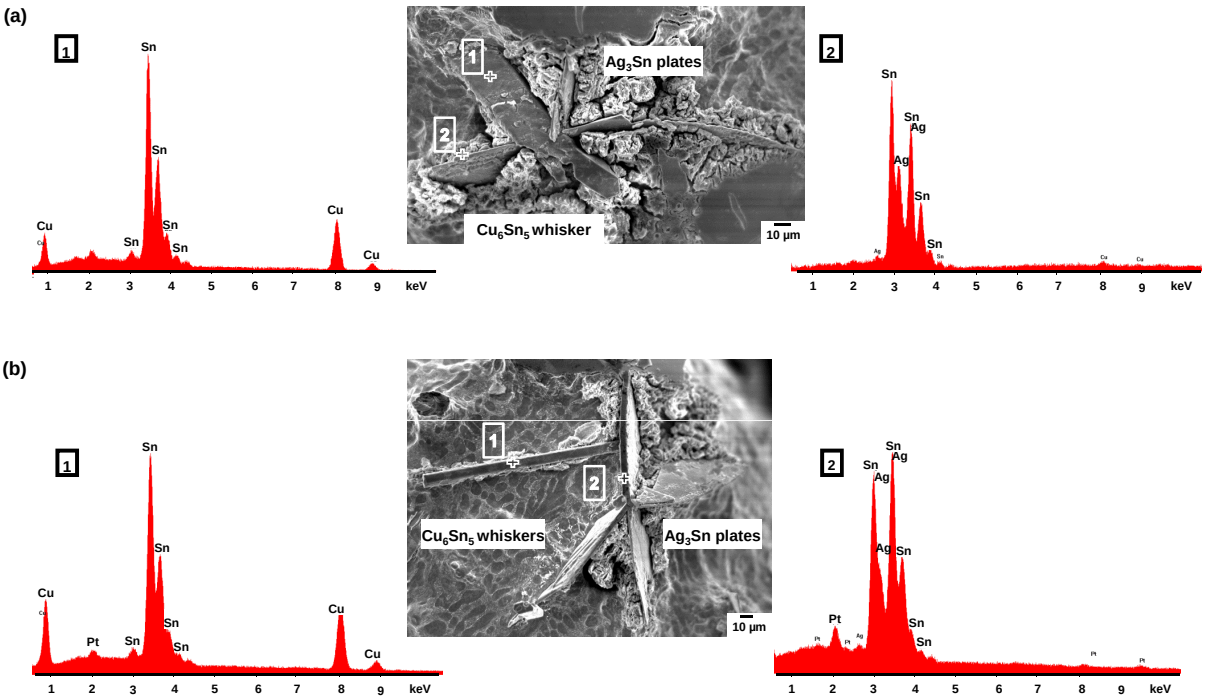


Figure 4.14: Typical secondary electron images of a SAC387 solder joints and associated EDS spectra.

and SAC387 BGAs, only the solder composition may account for the appearance of large Ag_3Sn plates in the bulk of solder joints, and which may have adverse effects on the plastic deformation properties of solder joints [36] due to strain localization at the boundary between the Ag_3Sn plates and the β-Sn phase [10]. If a large Ag_3Sn crystal formed in a high stress area, such as the corner region between the solder joint and the pad, cracks may be initiated and propagate along the interface of the Ag_3Sn particle and the solder [52]. Previous work showed that the formation of large Ag_3Sn plates could be controlled kinetically by using a high cooling rate during solder joint processing ($\succ 1°C.s^{-1}$), or suppressed thermodynamically by lowering the Ag concentration to 3wt% [8].

4.2.3 Innolot solder joints

The microstructure of bulk Innolot was generally similar to that of SAC387, with $(Cu,Ni)_6Sn_5$ and large Ag_3Sn IMCs as shown in Figures 4.15 (a) and (b). Figure 4.16 shows an SEM image of the bulk of an Innolot BGA solder joint and corresponding elemental maps. The Bi-rich particles, evidenced in the bulk solder alloy from wave soldering bars could not be resolved in the as-received BGA solder joints. Nano-metre size Ni-rich and Sb-rich particles were evenly distributed within the matrix.

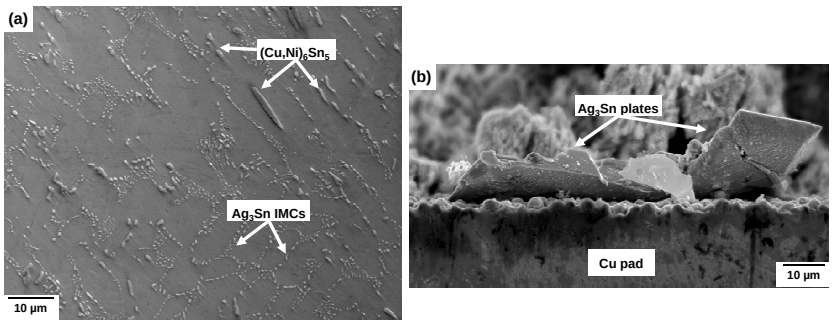


Figure 4.15: Secondary electron images of (a) the cross-section of an Innolot solder joint; and (b) deep etched Cu pad-solder joint interface revealing large Ag_3Sn plates.

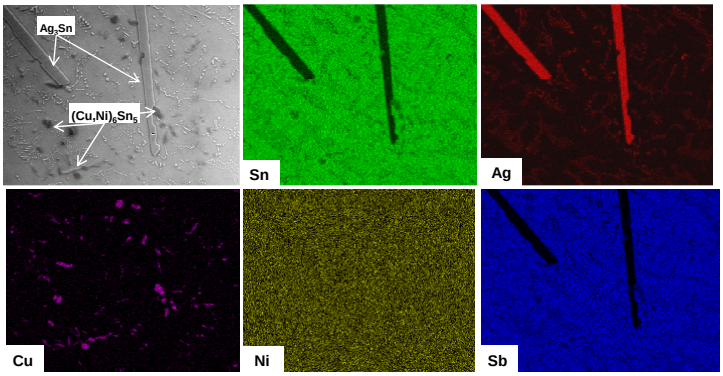


Figure 4.16: Secondary electron image of a cross-section of an Innolot solder joint and Sn, Ag, Cu, Ni and Sb EDS elemental maps of the scanned area.

4.2.4 Sn-37Pb solder joints

Figures 4.17 (a) and (b) show an optical image of the Sn-37Pb BGA joints and an SEM secondary electron image of their cross-section respectively, while Figure 4.18 shows elemental maps of a solder joint. The microstructure was essentially identical to that of bulk Sn-37Pb from wave soldering bars (eutectic spacing of 0.2–1.5μm). The IMC layer of Sn-37Pb solder joints was also composed of scallop type Cu_6Sn_5 IMCs but it was thinner (0.5 to 1.5μm) than that of SAC and Innolot solder joints (0.5 to 3μm) because the latter alloys already contained Cu in their composition.

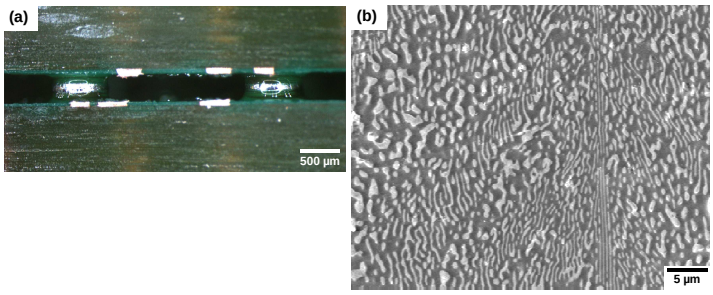


Figure 4.17: Secondary electron images of (a) a Sn-37Pb BGA with FR-4 boards; and (b) the cross-section of a joint.

4.2.5 Influence of the metallization pad on SAC305 solder joint microstructure

The plate-like morphology of Ag_3Sn IMCs was not observed in the interior of SAC305 solder joints with Cu pads, whereas many Ag_3Sn plates were encountered in SAC305

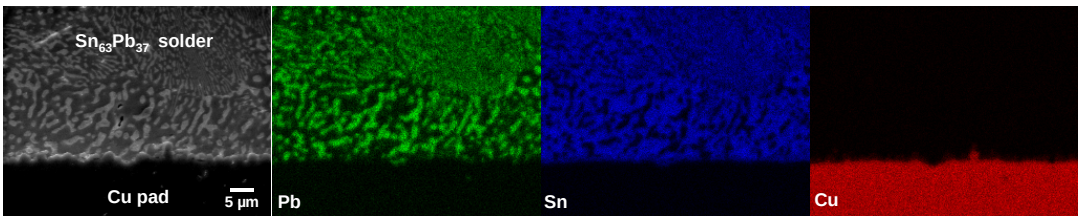


Figure 4.18: Secondary electron image and corresponding Pb, Sn and Cu EDX elemental maps.

joints when Pd-Ag pads were used. Figure 4.19 shows the Ag_3Sn plates were leaf-type, with a thickness varying between 1.5 and 3μm, and with lengths up to 50μm. It is likely that Ag from the Pd-Ag metallization dissolved into the interior of the SAC solder joint during joint formation, resulting in increased Ag content in BGA joints with Pd-Ag pads compared with BGA joints with Cu pads especially near the interface. Such a Ag concentration increase has a proven effect in enhancing the formation of large Ag_3Sn plates [178], hence the numerous plates observed for SAC BGAs with Pd-Ag pads.

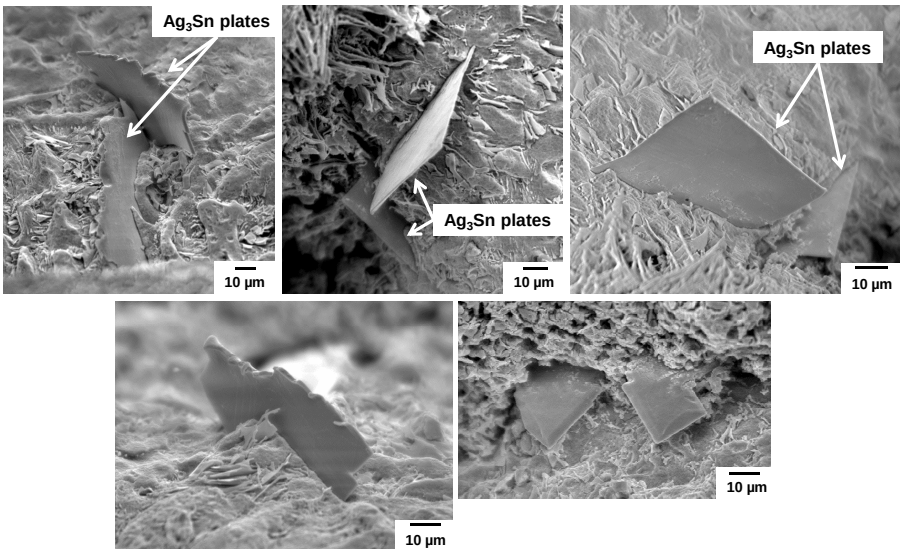


Figure 4.19: Secondary electron images of Ag_3Sn plates from deep etched SAC305 BGA solder joints manufactured with Pd-Ag pads.

Besides, very few Cu_6Sn_5 whisker-type IMCS were encountered in SAC305 or SAC387 solder joints when Pd-Ag pads were used. In order to evaluate the effect of the metallization composition on the microstructure of solder joints, Sn-3.5Ag BGA solder joints were manufactured. Figure 4.20 shows that Sn-3.5Ag BGA solder joints manufactured with Cu pads evidenced both Ag_3Sn plates and Cu_6Sn_5 needles. Therefore,

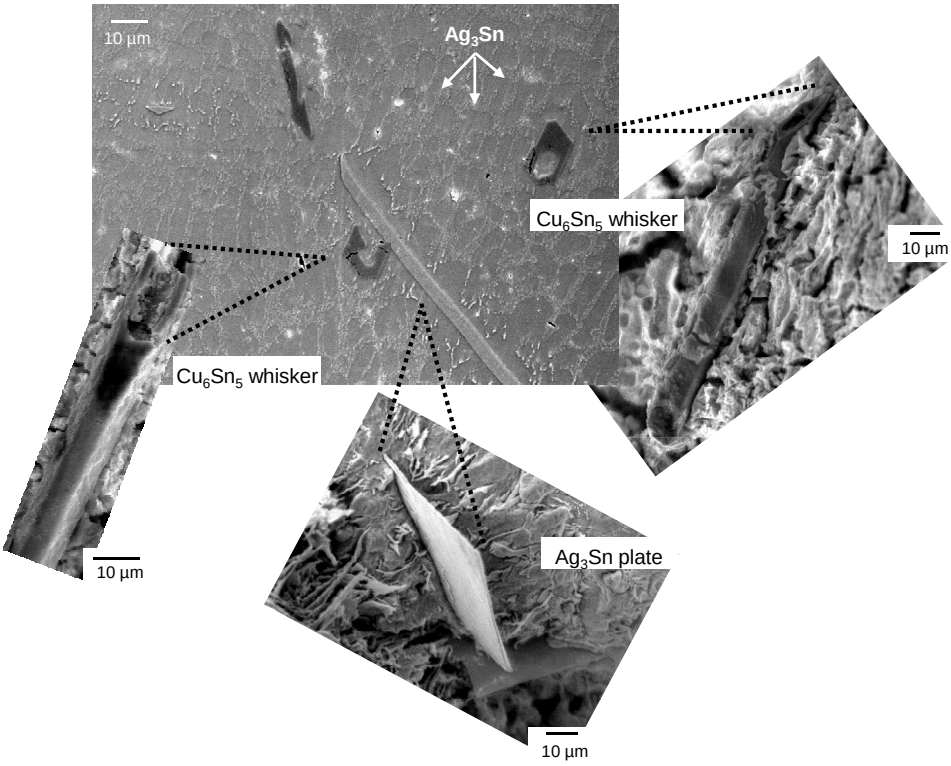


Figure 4.20: Secondary electron images of the cross-section surface of a Sn-3.5Ag solder joint manufactured with Cu pads showing Cu_6Sn_5 and Ag_3Sn IMCs and corresponding morphologies from deep etching.

migration of atoms from the metallization was key to the IMC morphology. Although the effects of Sn and Ag diffusion on strength and fatigue fracture mechanisms for Sn-Pb or Sn-Pb-Ag solder joints with Pd-Ag metallization during thermal ageing/cycling has been studied [179, 180], there is little in the literature on the effect of the diffusion of elements from the metallization layer on microstructure. The additional Cu dissolved from the Cu metallization could cause excessive precipitation of Cu_6Sn_5 particles near the interface [178].

The intertwined network of Ag_3Sn IMCs evidenced by deep etching might contribute to improved strength [52, 114], larger Cu_6Sn_5 whiskers or Ag_3Sn plates also likely provide a preferential crack propagation path, affecting significantly the fracture modes of solder joints [36, 178] and causing plastic-strain localization at the boundary between the Ag_3Sn plates and the bounding β-Sn phase [181]. Therefore, the overall mechanical response, or constitutive behaviour, of a solder joint cannot be easily forecast in advance due to these microstructural complexities and competing mechanical

effects; further, the as-reflowed microstructure changes with time in-service.

4.3 The solder joint/metallized pad interface

The joining capability between the functional unit and the printed circuit board depends on the formation and limited growth of IMCs at the interface between the solder ball and the thick metallization pad. The IMC layer plays an important role in the reliability of solder joints. While bulk solder is ductile with a low Young's modulus, the IMCs are strong, brittle and stiff. Despite the brittleness of Sn-based IMCs, the growth of a 1–2μm IMC layer is considered an indicator of a good metallurgical and load capable bond. For Sn-Pb soldering, IMCs have only been a reliability concern in the case of lengthy ageing at elevated temperatures, resulting in excessive growth of the IMCs [182]. During thermal cycling, the thermal expansion mismatch induced stresses cause fracture often at this 'brittle' interface.

4.3.1 The solder/Cu pad system

Figure 4.21 (a) shows a scallop-type IMC layer between the Cu pad and bulk SAC305. However, the Cu pad/solder interface was easily smeared upon mechanical polishing, therefore samples were also polished using an Ilion cross-section polisher (Gatan, Inc.), with a 6KeV Ar beam for 4 hours. Figure 4.21 (b) shows a sample after 8 hours at 130°C with a 'double' IMC interface layer. A Cu_3Sn layer formed nearest the Cu pad followed by a scallop-type Cu_6Sn_5 phase layer nearest the solder joint. The thickness of the Cu_3Sn layer was 0.2–0.6μm and that of Cu_6Sn_5 was 0.3–1.5μm.

Figure 4.21 (c) shows micro-voids at the Cu pad/Cu_3Sn interface of the thermally aged sample due to the well-known Kirkendall voids that develop in this system upon thermal ageing, as Cu atoms from the Cu pad diffused and arrived at the Cu_3Sn/Cu_6Sn_5 and Cu_6Sn_5/solder interfaces, resulting in the growth of both layers towards the solder [183]. The diffusion of Sn from the solder to the Cu_6Sn_5/Cu_3Sn interface was not sufficient to make up for the diffusion rate of Cu into the IMC layers. Therefore, lattice vacancies from migrating Cu atoms accumulated at the Cu/Cu_3Sn interface and

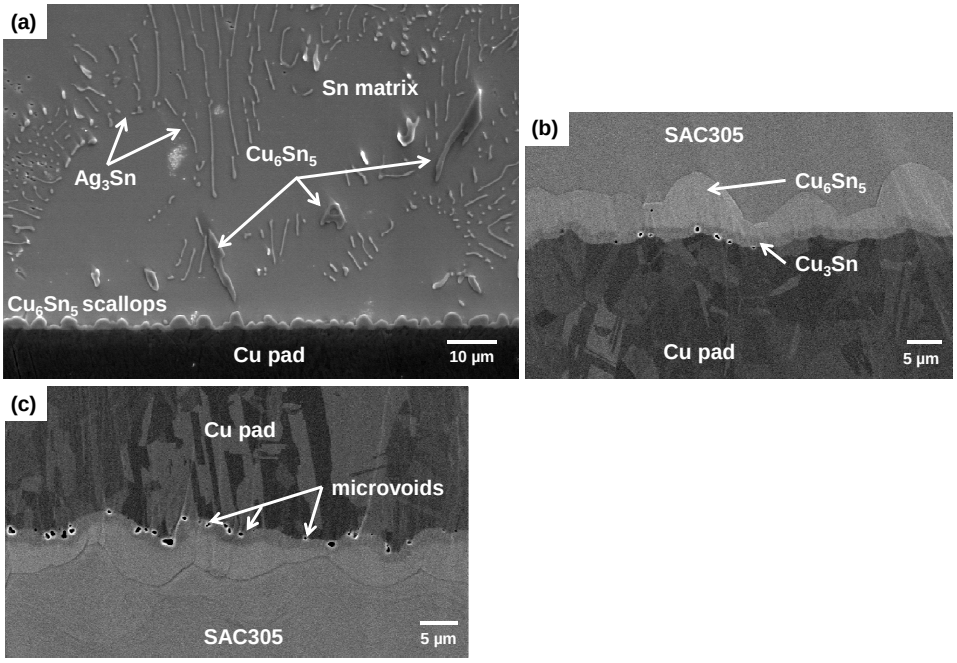


Figure 4.21: Secondary electron images of (a) a SAC305 solder/Cu pad interface showing Cu_6Sn_5 scallops; (b) detail of the interface with Cu_3Sn and Cu_6Sn_5 layers for a thermally aged sample (8 hours at 130°C). The grain structure of the Cu pad was also visible; and (c) micro-voids at the Cu pad/Cu_3Sn interface of the thermally aged sample.

coalesced into microscopic voids by means of vacancy diffusion. After extensive thermal cycling, these voids may generate micro-cracks at the interface with the Cu pad and lead to eventual failure [143]. However, there was another type of micro-void at the Cu pad-solder joint interface before any thermal treatment arising from sample surface defects or residual out-gassing during the bonding process.

The three-dimensional structure of the interfacial Cu_6Sn_5 was observed by selectively etching the bulk solder in Figure 4.22 (a). The IMCs took the shape of short sticks, or rods, growing from the Cu substrate into the solder with an overall morphology usually termed 'scalloped'. The Cu_6Sn_5 scallops had a smooth surface, except for the presence of light-coloured nano-particles suspected to be Ag_3Sn that had grown on or had pinned their surface. The Ag_3Sn precipitates may be 'captured' by the growing Cu_6Sn_5, and were often arranged in a line [184]. The presence of nano-sized Ag_3Sn particles on the Cu_6Sn_5 layer has been shown to decrease the surface energy and restrain the growth of the IMC layer during thermal ageing [184]. Figure 4.22 (b) shows

an SEM plan view of the SAC305-Cu interface. The scallop-shaped Cu_6Sn_5 grains had sizes of 2–5μm, with Ag_3Sn particles of widths 100–200nm and up to a few microns long. The nanoscale Ag_3Sn particles likely nucleated in the liquid solder and only in later stages when the β-Sn fraction was significant was the growth orientation of Ag_3Sn constrained. Figure 4.23 shows a striking alignment of Ag_3Sn particles in a SAC305 BGA joint, in which the Ag_3Sn particles follow the contours of the outer shell of a solder ball, suggesting that the orientation was determined during solidification in solder ball manufacturing rather than when the joint was formed.

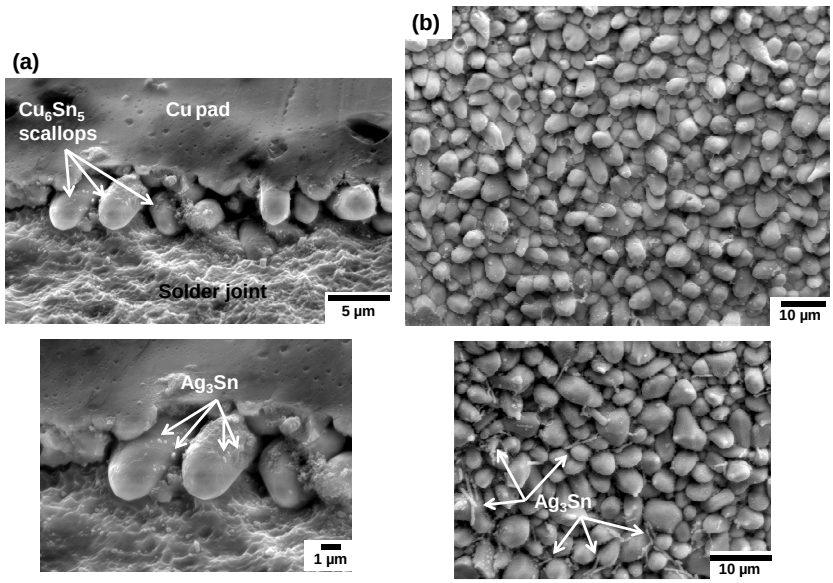


Figure 4.22: Secondary electron images of the deep etched interface layer at the Cu pad of a SAC305 BGA solder joint: (a) tilted view of the Cu/solder cross-section; and (b) a plan view of the Cu pad, with small Ag_3Sn particles developing on or pinning the Cu_6Sn_5 scallops.

As previously noted in section 4.2 and shown in Figure 4.24 (c), most of the Cu_6Sn_5 whiskers emanated from the IMC layer [185]. Hence there was a lesser likelihood of Cu_6Sn_5 whisker-type IMCs occurring in SAC305 BGA solder joints prepared with Pd-Ag pads. Figure 4.24 (a) shows the start of a whisker, as a small, rounded protrusion emanating from the tip of a Cu_6Sn_5 scallop, whereas Figure 4.24 (b) shows multiple whiskers protruding from different corners of the same grain.

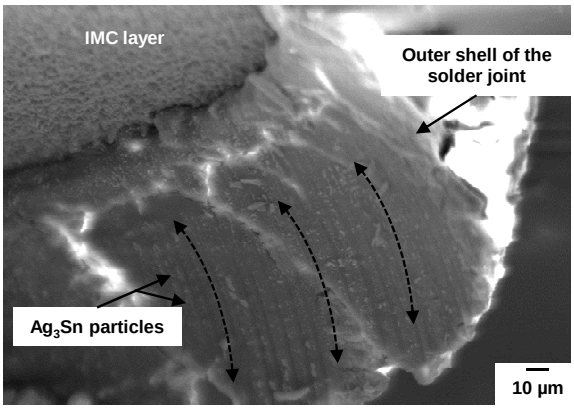


Figure 4.23: Deep etched SAC305 BGA solder joint showing Ag_3Sn particles alignment.

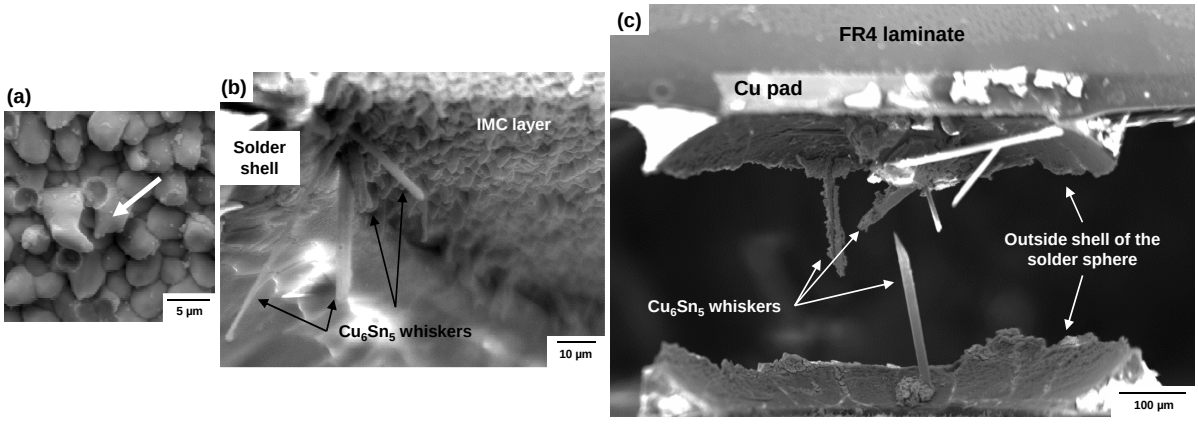


Figure 4.24: Secondary electron images of (a) the three-dimensional morphology of the interfacial Cu_6Sn_5 layer with the beginning of the growth of a whisker; (b) Cu_6Sn_5 whiskers developed from the IMC layer in a deep etched BGA solder joint; and (c) overall whisker distribution in a further etched BGA solder joint so that only the outer shell structure of the ball remained.

4.3.2 The solder/Pd-Ag system

Figures 4.25 (a) and (b) show an SEM image of the Al_2O_3 board/Pd-Ag/SAC305 interface and a corresponding EDS elemental map respectively. The thickness of the IMC layer was variable in the 10–15μm range. Figure 4.25 (a) also illustrates the challenges associated with the Al_2O_3 boards where de-bonding or spalling of the metallization layer from the Al_2O_3 could occur. The porosity fraction was considered acceptable by comparison with the literature.

Figure 4.26 (a) shows a number of Ag_3Sn plates at the SAC305/Pd-Ag interface and Figure 4.26 (b) shows the Pd-Ag/Innolot interface, again with IMC plates for both SAC305 and Innolot generally thicker than in the Cu pad metallization arrangement, even reaching 10μm. Figures 4.26 (c) and (d) are higher magnification views of the IMC layer on the Pd-Ag pad, comprising an intertwined network of fine and coarse and faceted Ag_3Sn IMCs. The literature suggests these additional IMCs might be Pd_3Sn, Pd_2Sn, Pd_3Sn_2, PdSn, Ag_5Sn and Ag_3Sn [179]. Figure 4.26 shows that as might be

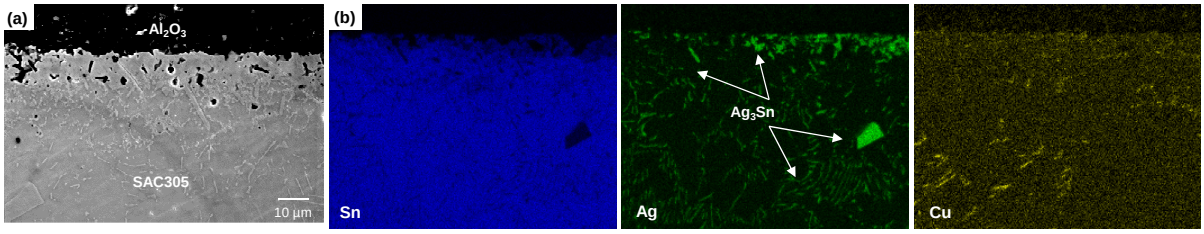


Figure 4.25: (a) Secondary electron image; and (b) EDX elemental maps of a Al_2O_3 board/Pd-Ag/SAC305 solder joint interface.

expected large Ag_3Sn plates formed preferentially at the Pd-Ag pad interface. The overwhelming presence of Ag_3Sn plates over Cu_6Sn_5 IMCS in the interior of SAC387 BGAs with Pd-Ag pads was evidenced in Figure 4.27.

4.4 Conclusions

While the microstructure of Sn-37Pb comprised a classic eutectic lamellar arrangement with occasional Pb islands embedded in a Sn matrix, Pb-free alloys comprised β-Sn dendrites surrounded by a quasieutectic comprising a mixture of IMCs.

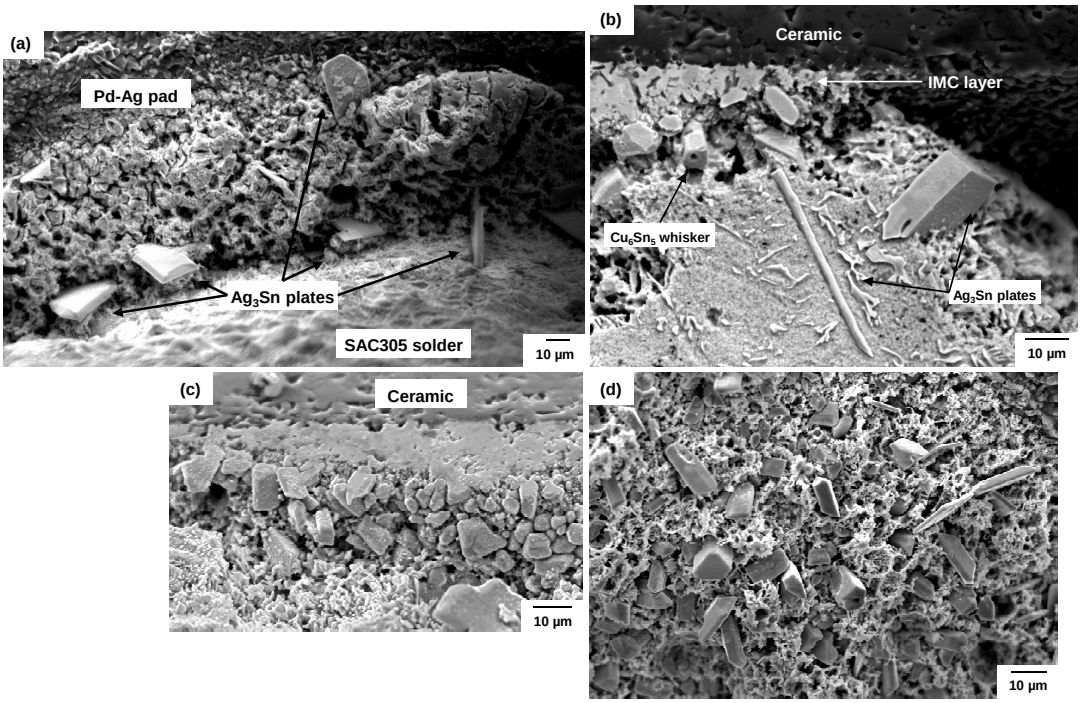


Figure 4.26: Secondary electron images of (a) deep etched SAC305 BGA solder joint with Pd-Ag metallization revealing the pad/solder interface; (b) deep etched Al_2O_3 board/Pd-Ag/Innolot BGA interface; (c) tilted view of the Al_2O_3 board/Pd-Ag pad/Innolot interface; and (d) top view of the IMC layer for an Innolot solder joint manufactured with Pd-Ag metallization pads.

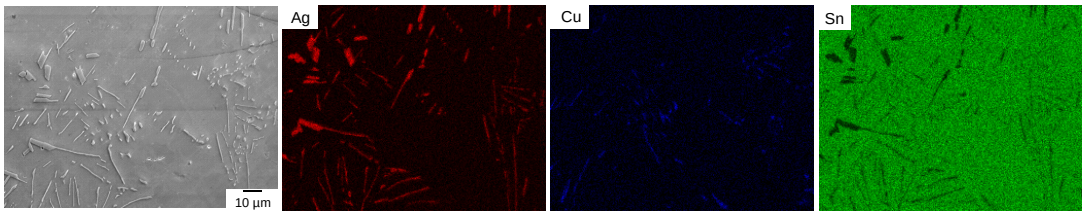


Figure 4.27: Secondary electron image and EDS elemental maps from the interior of a SAC387 solder ball and solder joint manufactured with Pd-Ag metallization pads.

The well-developed Ag_3Sn and Cu_6Sn_5 present in the BGA solder joints were generally observed in both the bulk alloys and as-received solder balls, and a significant influence of the pad metallization on IMC growth was suggested. IMCs were more numerous and developed at or near the pad/solder joint interface where they tended to replace long Cu_6Sn_5 whiskers in the Pd-Ag pad systems with comparatively thick and larger area Ag_3Sn plates.

Deep etching evidenced sharp and elongated IMC particles both inside the solder balls and at their surface of the solder joint. Long, hexagonal and faceted Cu_6Sn_5 rods (or whiskers) had developed whereas Ag_3Sn IMCs formed a dense fibrous network in the body of solder joints for all alloys. Large (up to 50μm) and thick (up to 10μm) Ag_3Sn plates also formed in SAC387 and Innolot BGAs with Cu pads while such plates were observed for SAC305 BGAs only when Pd-Ag pads were used.

Overall, it was the type of solder pad more than the composition of the solder alloy that influenced the dominant IMC type and morphology. The concentration of Ag should be reduced if Ag_3Sn plates close to the solder ball-metallization interface are to be avoided, and SAC305 BGAs with Cu pads provided the lowest incidence of potential damaging large-scale Ag_3Sn plates and excessively elongated Cu_6Sn_5 morphologies.

Chapter 5

Grain structure of solder alloys

The aim of the investigations described in this chapter was to study grain structure variation between solder alloys and the effect of the subsequent reflow. These aspects were of interest since β-Sn is anisotropic and grain orientation data may relate to different mechanical testing behaviours in chapters 6 and 7. The grain size and its distribution was also judged very likely to be important in understanding creep behaviour. The grain structure of as-received alloys and of solder joints manufactured in-house was characterised by cross-polarisation and EBSD analysis. Fine-grained ($\prec 20\mu$m) and coarse-grained ($\succ 100\mu$m) β-Sn phase was revealed, depending on whether small (400μm) or large (600μm) solder balls were used respectively.

5.1 Sn anisotropy

β-Sn accounted for more than 90% of the composition of the SAC solder joints studied in this thesis. Therefore, the baseline mechanical properties of the solder joint strongly depend on the properties of Sn, although the shape and extent of IMC formation is also known to be critical. Figure 5.1 shows a schematic diagram of the Sn unit cell. Because of its body centered tetragonal crystal structure, Sn exhibits significant anisotropy in a number of mechanical properties, particularly elastic and thermal expansion characteristics, as shown in Table 5.1 [186]. The CTE difference between a and c directions of body-centered tetragonal β-Sn was almost twice that of the CTE difference between

polycrystalline Cu and polycrystalline Sn.

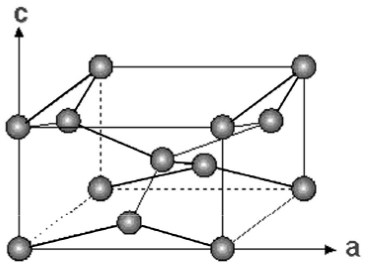


Figure 5.1: Schematic of single-crystal β-Sn (body centred tetragonal structure) [186].

	Thermal expansion coefficient ($\times 10^{-6}$ °C^{-1})	Young's modulus (GPa)	Hardness (GPa)
Sn (a-direction) (single crystal)	15.4	85	0.98
Sn (c-direction) (single crystal)	30.5	54	
Cu (polycrystal)	17.3	117	0.294
Cu_6Sn_5 (polycrystal)	16.3	85.56	3.71

Table 5.1: Coefficient of thermal expansion and Young's modulus of body centered tetragonal Sn, and polycrystalline Cu and Cu_6Sn_5 [186].

Therefore, solder joints displaying large β-Sn grains and especially where the entire solder joint comprises only a handful of grains, may exhibit a wide range of mechanical behaviour, depending on the orientation of these few Sn grains [187, 188]. Recently, anisotropy of Sn was considered to be a major contributing factor for damage accumulation caused by stresses arising from CTE mismatches between the various components of the joint. Premature failure has been suggested when the the *c*-axis of the Sn crystal was oriented parallel to the substrate direction [187], because the CTE of Sn in the basal plan is half that along the *c* axis. SAC305 has shown better thermal fatigue properties than SAC alloys with lower Ag content, which was attributed to both smaller Sn grains and a larger number of coincidence site lattice (CSL) boundaries even after thermal fatigue. Overall, the number and morphology of Sn grains in a SAC solder joint may affect reliability, and therefore grain characterisation of the manufactured solder joint is likely helpful for mechanical property understanding of solder joints.

5.2 As-received solder balls

The β-Sn grain morphology of the two diameters of 400 and 600μm as-received SAC305 solder balls is shown by crossed-polarized optical microscopy in Figures 5.2 (a) to (c), in which similar shades of gray corresponded to similar orientations of the Sn phase. Figures 5.2 (a) and (c) revealed different β-Sn grain structures. The 400μm diameter balls in (a) and (b) had an apparently fine-grained ($\prec$20μm) microstructure while the 600μm ball in Figure 5.2 (c) showed only a small number of distinct grains. The colour pattern in (c) was very similar to a 'Kara's beachball' pattern that arises from a single nucleation process. Although the composition of the two types of solder balls was identical, the difference in grain structure may be attributed to different manufacturing processes. It is suspected that during manufacture, the 400μm balls were quenched while the 600μm balls were slow cooled in air or in a furnace [23].

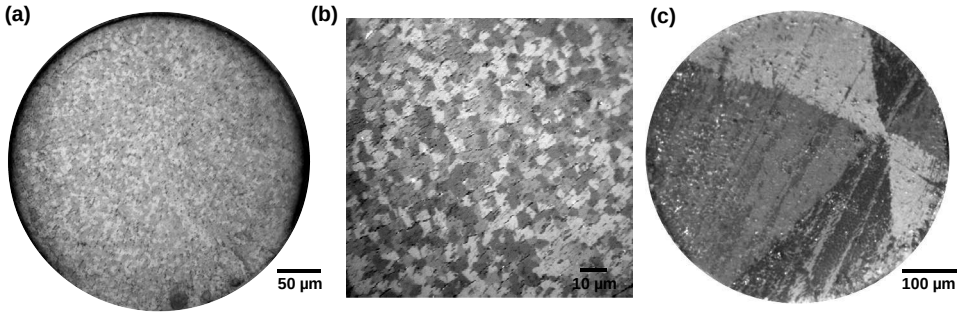


Figure 5.2: Cross-polarized images of cross-sections of SAC305 as-received solder (a) entire 400μm ball; (b) higher magnification view of its grain structure; and (c) entire 600μm ball. Variations in grey scale defined domains with different crystallographic orientation of the β-Sn phase.

Oddly, both ball diameters seemed to show only three approximate β-Sn grain orientations as there were three dominant grey shades in the crossed-polarized images in Figure 5.2 (b) and (c). EBSD was employed to investigate the crystal orientations, as shown in Figure 5.3 (a) to (f).[1] The unique grain colour map in Figure 5.3 (a) for a 400μm ball evidenced multiple grains and the grain size distribution in Figure 5.3 (c) shows that the majority of grains were $\prec$20μm. In Figure 5.3 (b), low angle boundaries were defined as those with a misorientation between 0 and 15° (coloured blue) and high angle boundaries had a misorientation $\succ$15° (coloured green and red). The

[1]Considerable effort was expended in developing EBSD sample preparation and measurement protocols on account of the extreme softness of β-Sn.

orientation map in Figure 5.3 (d) shows three dominant colours (blue, pink and violet), again suggesting three main β-Sn crystal orientations. From the pole and inverse pole figures in Figure 5.3 (f), the β-Sn crystal orientations concentrated in three different points. Figure 5.3 (e) shows that the misorientation between two similar colours was $\prec 10^{\circ}$, and the mode of misorientation angle was approximately 60°. Figures 5.3 (e) and (f) revealed a cyclic twinning structure: each grain rotated around the [100] direction of the β-Sn crystal by $\sim 60^{\circ}$ with the [100] axes of all the β-Sn crystals aligned in one direction. The cyclic twinning was repetitive across the entire cross-sectional area of a solder ball. Cyclic twinning consists of six twin regions turning on the [100] axis,

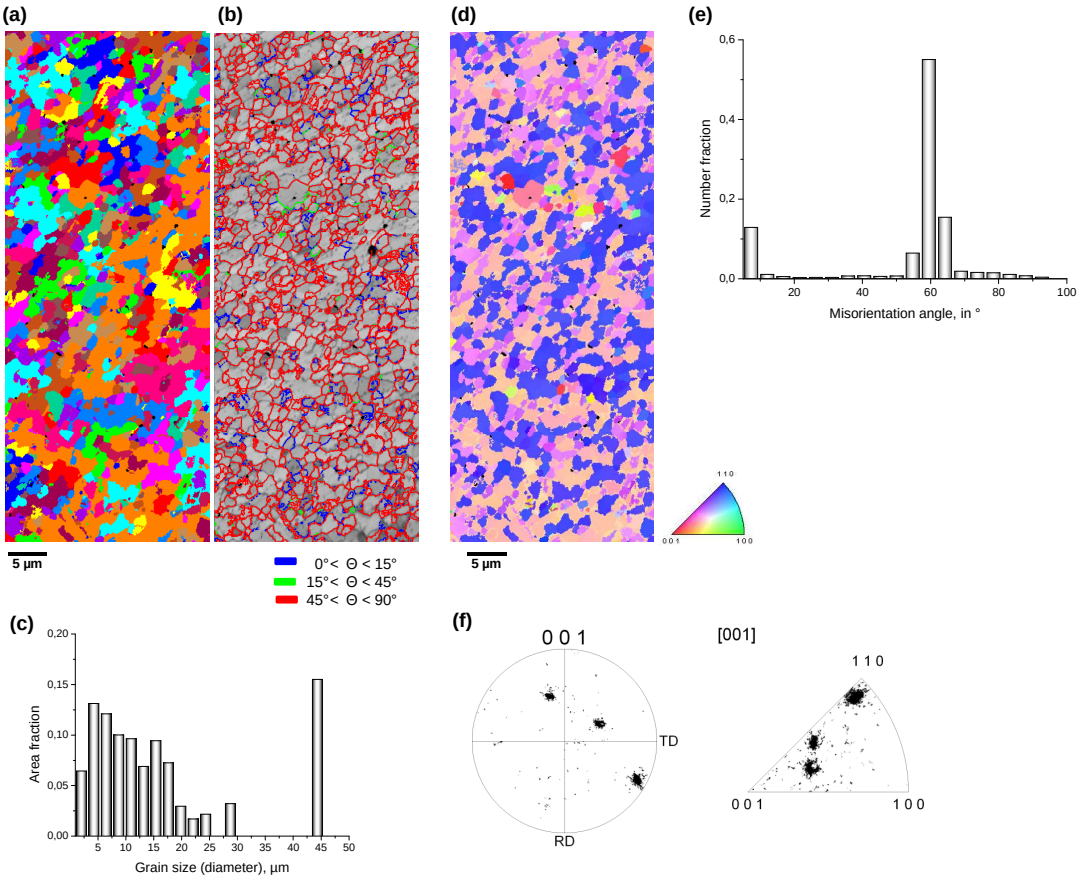


Figure 5.3: EBSD investigation of 400μm as-received SAC305 ball: (a) Sn unique grain colour map taken from the ball centre; (b) corresponding image quality map with misorientation angle grain boundaries (low in *blue*, medium in *green* and high in *red*); (c) grain size plot; (d) Sn orientation map;(e) misorientation plot; and (f) pole and inverse pole figures.

each Sn unit cell rotating $\sim 60^{\circ}$ with respect to the [100] axis. Faces parallel to a same crystal direction corresponded to the beachball pattern. In Sn based solders, twinning commonly occurs on one of two different crystal planes, the {101} and the {301}

planes, with twinning angles about the [100] axis near 60° since the angle between {101} and {10-1} is 57.2°, while the angle between {301} and {30-1} is 62.8°. The observed structures were not consistent with alternating {101} and {301} twins because the angle between the {101} and the {301} planes should be approximately 30°, contrasting with the consistent 60° angle observed between twin planes. Therefore, the structures were sixfold cyclic twinned β-Sn using entirely {101} or {301} twin planes. Deformation induced twinning of Sn is well known but twinning following solidification of Sn has only very recently been reported [56, 187]. The beachball twinning structure was observed in Sn-(0.5–3.5)Ag alloys while no twinning and large grains were observed for Sn-(0.5–2.0)Cu alloys [23]. Such a difference might be explained by the higher solubility of Ag in Sn, favouring twinning structures. Therefore, the combined effects of Ag additions, promoting fine cyclic twinning structures, and of Cu additions, favouring large grains, may explain the large, few grain microstructure of SAC and Innolot alloys.

Most 600μm SAC305 as-received solder balls comprised either only two well-defined grains, or a few-grain beachball pattern. However, some balls did suggest grains growing from nucleation sites, as might be expected by a high nucleation undercooling. Figure 5.4 shows the same balls at two different orientations of the cross-polarizer near the extinction position. Again, the β-Sn phase nucleated from the melt at a single point within each ball in (a) and (b) but (c) and (d) show multiple nucleation sites.

The grain structure of these multiple nucleation sites was investigated in Figures 5.5 (a)–(e). Figure 5.5 (a) shows that cross-polarized images of the cross-section of a large solder ball as well as the corresponding EBSD unique grain colour map in Figure 5.5 (b) initially suggested many Sn crystal orientations. However, the orientation map in Figure 5.5(c) showed two main clusters of crystal orientations. The grain revealed by cross-polarisation and the EBSD unique grain colour map delimited subgrains, and resulted in the scattering around the two main points in the inverse pole figure in Figure 5.5 (d). Therefore cross-polarisation coupled with EBSD showed that 600μm balls all had a beachball structure, although some grains showed some evidence of a subgrain structure, but which might easily be confused by surface damage in preparation

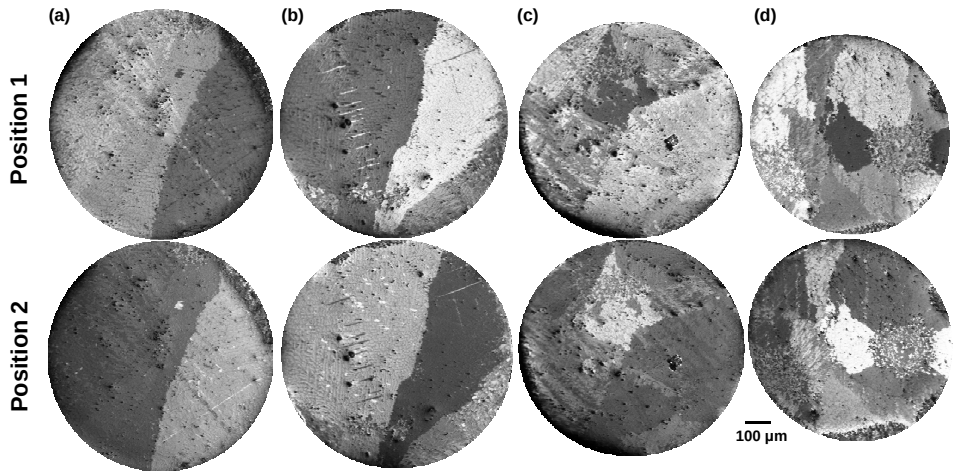


Figure 5.4: Cross-polarized images of cross-sections of 600μm diameter SAC305 as-received solder balls for two different cross-polarizing angles: (a) and (b) with a single nucleation point; and (c) and (d) multiple nucleation sites.

of these very soft materials.

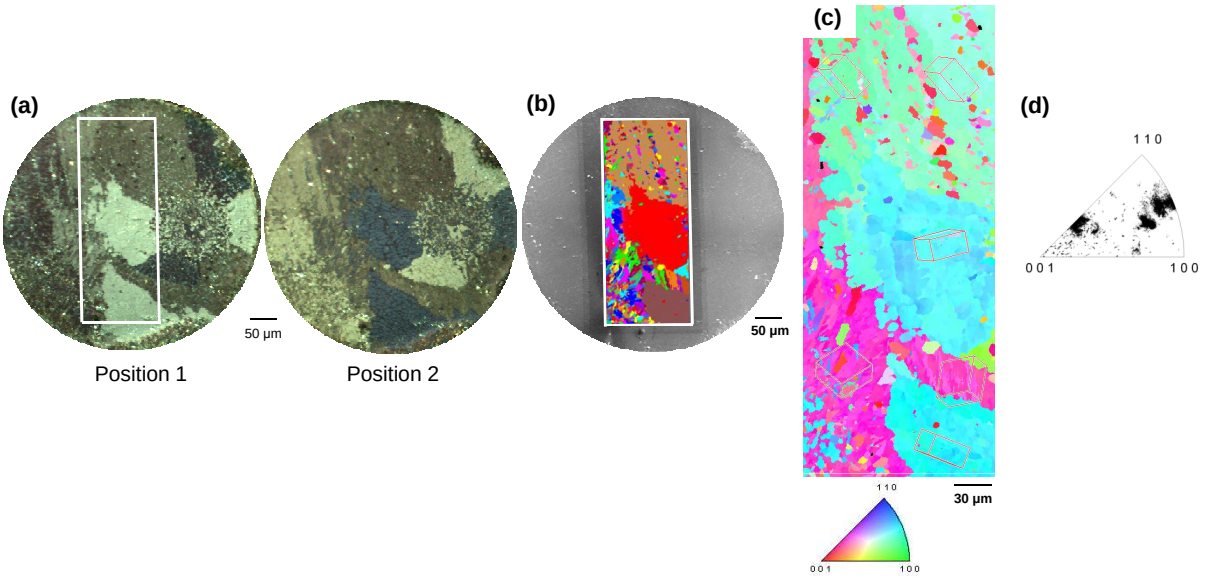


Figure 5.5: (a) Cross-polarized images of a cross-section of an entire 600μm SAC305 ball for two different cross-polarizing angles; (b) superposition of the EBSD unique grain colour map with a secondary electron image of the solder ball; (c) orientation map with schematics of Sn crystal orientation; and (d) inverse pole figure.

The as-received 500μm Innolot balls were also analysed under cross-polarising microscopy and EBSD. Figure 5.6 (a) shows the different types of β-Sn grains. The grains had two to four main Sn crystal orientations. Similar to the 600μm SAC305 balls, the beachball structure was commonly observed. EBSD investigations in Figure 5.6 (b) show a β-Sn orientation map with four β-Sn crystal orientations.

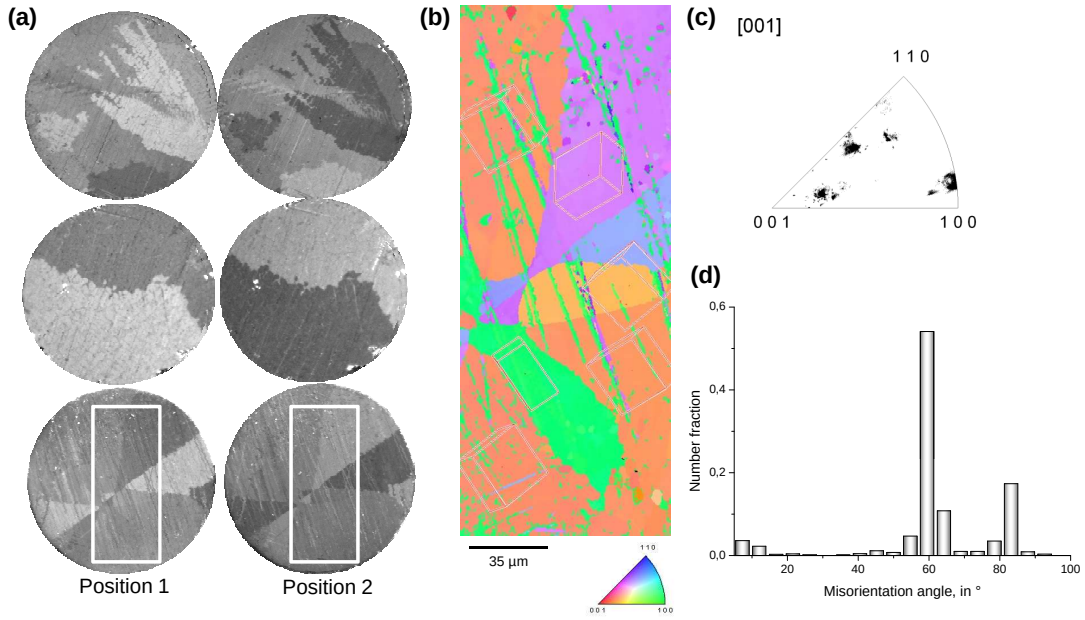


Figure 5.6: (a) Cross-polarized images of cross-sections of as-received Innolot solder balls (500μm diameter); (b) unique grain colour map of the EBSDed region in the centre of a 400μm diameter as-received solder ball; (c) corresponding inverse pole figure; and (d) misorientation angle distribution within the scanned area.

Figure 5.6 (d) shows the commonest grain misorientation was ∼60°. Crystallographic orientations in SAC305 and Innolot probably originated from one nucleation event, followed by sixfold twinning. Since all the crystal segments of a cyclic twinned crystal share a common crystal axis, the group may respond mechanically as a single crystal on that twinning axis and as a multi-crystal along other orientations. Therefore, the real mechanical behaviour of twin structures in SAC alloys may lie between that of a single crystal and a polycrystal joint, depending on the precise orientation of the few grains to the principal direction of applied strain.

5.3 Grain characterisation of solder joints

Figures 5.7 (a)–(d) show EBSD data for a 180x110μm area of a cross-section at the centre of a SAC305 solder joint manufactured from 600μm balls. The EBSD unique grain colour map in Figure 5.7 (a), the orientation map in (b) and the inverse pole figure in (c) show that only one grain was observed in the scanned area. Figure 5.7 (c) is an image quality map and evidences the difficulties of EBSD in solder joints.

Image quality maps describe the quality of the underlying EBSD pattern (diffraction pattern), which (amongst other factors) depends on the perfection of the crystal lattice in the diffracting volume. Any distortions to the crystal lattice will produce lower quality diffraction patterns. Darker gray shades correspond to a lower image quality, which was often problematical for these relatively soft samples.

The microstructure of the SAC305 joint (600μm balls) consisted of the Sn-rich matrix surrounded by a eutectic mixture of β-Sn and fine Ag_3Sn IMCs clustered in interdendritic regions. Ag_3Sn IMCs are harder and polished less easily than the β-Sn phase, leading to uneven surface topography, resulting in image quality variations as shown in Figure 5.7 (c), and the variation in colour in the orientation map in Figure 5.7 (b) cannot be safely interpreted to correspond to 'sub-grains', but are most probably artefacts introduced by sample polishing.

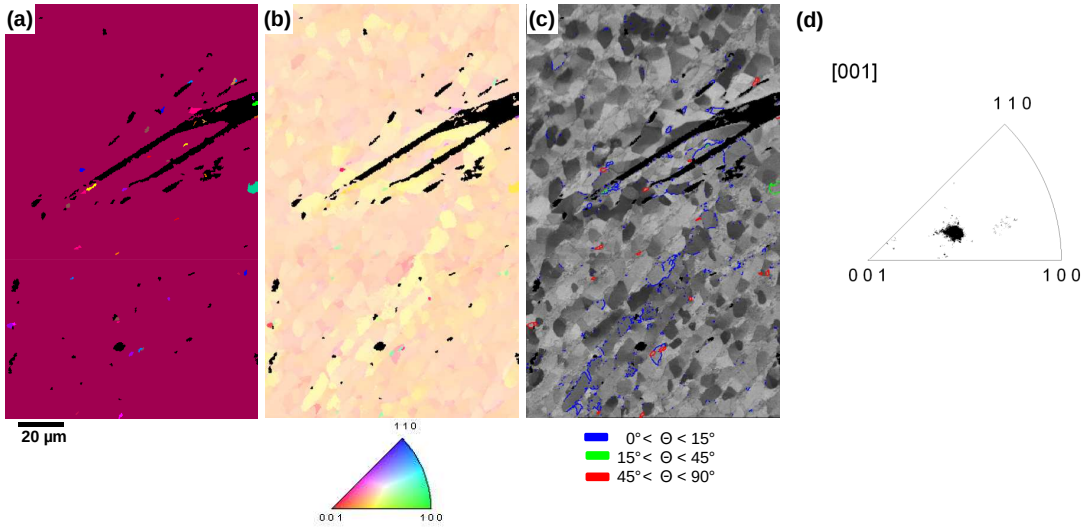


Figure 5.7: (a) Sn EBSD unique grain colour map; (b) orientation map; (c) image quality map with superposition of grain boundaries; and (d) inverse pole figure showing strong texture in the Sn phase, due to a single grain.

Figure 5.8 shows the cross-polarized images of a SAC305 400μm ball joint, this time consisting of many grains within the solder joint. EBSD was again used to determine the crystallographic orientations and for quantitative analysis of grain sizes. Figure 5.9 (a) is an EBSD orientation map of the β-Sn phase in a SAC305 400μm ball joint, while (b) gives the suggested phase map of the same scanned area based on simultaneously acquired EDS spectra. By comparing with the image quality map in (c), the IMCs are shown to provide poor signal resolution. In a comparatively dense network

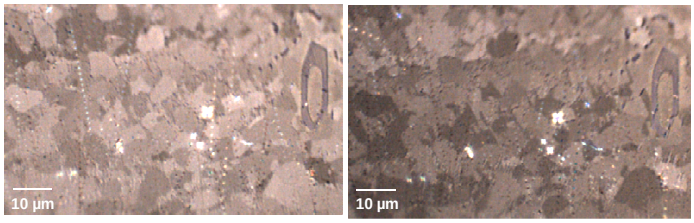


Figure 5.8: Cross-polarized optical images of a Cu pad/SAC305 (400μm diameter) BGA solder joint interface at two positions of the cross polarizer near the extinction position.

of IMCs, the diffraction patterns of β-Sn and Ag_3Sn particles sometimes superposed themselves, undermining signal quality. Nonetheless, Figure 5.9 (d) shows the grain size distribution with an average grain size of 11μm and a spread of grain sizes of 1-26μm, in contrast to the 600μm balls that comprised only a few grains.

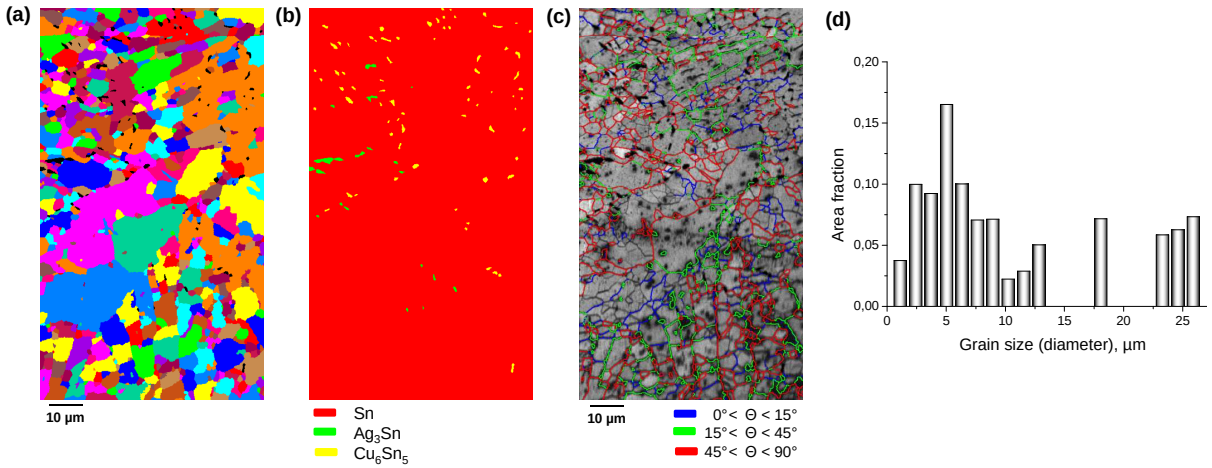


Figure 5.9: EBSD data of a SAC305 400μm ball joint: (a) Sn unique grain colour map; (b) phase composition map based on simultaneous EDS; (c) image quality map with superimposed grain boundaries (low angle grain boundaries in *blue*, medium angle grain boundaries in *green* and high angle grain boundaries in *red*); and (d) grain size distribution.

Figures 5.10 (a) and (b) show a cross-section of the two different sized solder balls with the fine Sn grains in the 400μm in (a) and the few much larger grains in the 600μm ball in (b). These results illustrate that the as-received grain structure of the SAC305 balls was largely preserved through the reflow process and thus provided an opportunity to study grain size effects on creep in later chapters. Critically, no difference in the interfacial structure was evident for the two different SAC305 diameters.

In the literature, SAC solder joints typically comprise only a few grains. For ex-

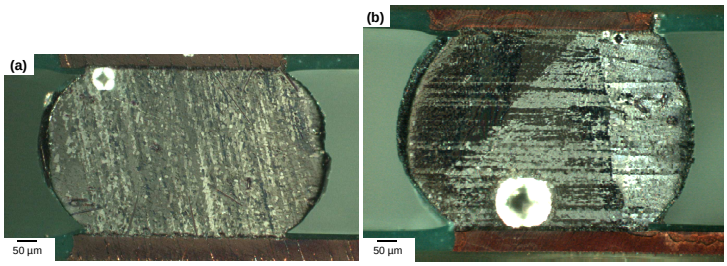


Figure 5.10: Cross-polarized images of SAC305 BGA manufactured from solder balls with initial diameter of (a) 400μm; and (b) 600μm.

ample, 900μm diameter SAC BGA solder joints were composed of only 1 to 12 independent β-Sn grains with an average grain number approximated to 8 grains [85]. The re-appearance of many β-Sn grains after thermal cycling has also been reported [90], and attributed to recrystallisation of β-Sn grains.

Figure 5.11 shows cross-polarising images of as-received Sn-37Pb solder balls and the corresponding BGA solder joint. Although the initial balls contained many small grains, and in marked contrast to SAC305, the solder joints now comprised only a few grains and had undergone significant coarsening during the reflow process.

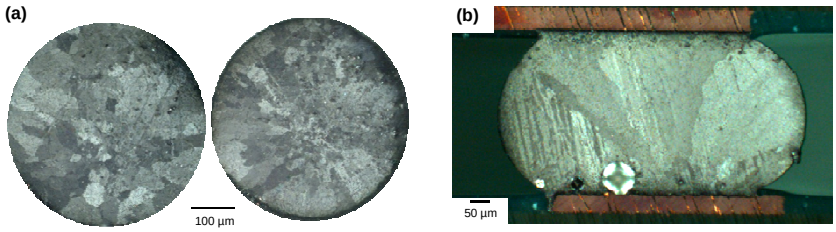


Figure 5.11: Cross-polarized images of (a) as-received Sn-37Pb solder balls (500μm diameter); and (b) Sn-37Pb BGA manufactured from these solder balls.

5.4 Thermal ageing of SAC solder joints

In view of the later high temperature tests of solder joints (chapter 7) and in order to assess any microstructural change over testing periods, thermal ageing was carried out. BGAs were thermally aged at 100°C for up to 24 hours. As shown in Figure 5.13, no significant grain structure change occurred up to 24 hours at 100°C for a SAC305 solder joint (400μm ball). Figure 5.12 shows the EBSD orientation maps for SAC387 (a) unaged and (b) after 28 hours at 100°C while (c) and (d) show the corresponding

inverse pole figures. The slight differences in the inverse pole figures and orientation maps might also be attributed to the inherent error and limits to reproducibility of the EBSD technique and data analysis for these alloys. The grain sizes for the scanned area of the unaged and thermally aged sample are represented in (e) and (f), suggesting a slight grain coarsening.

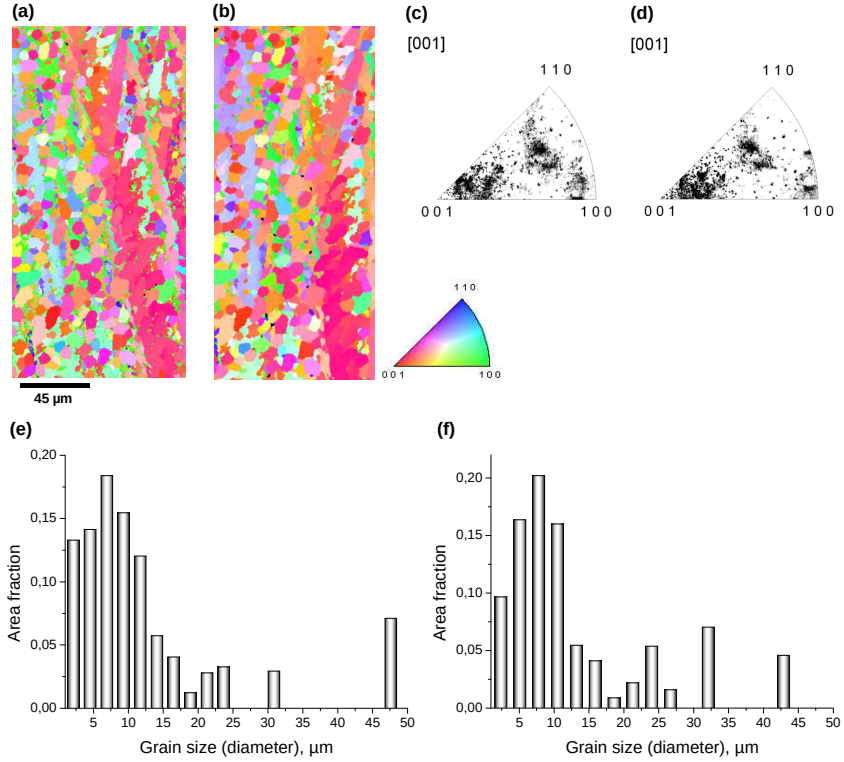


Figure 5.12: Orientation maps of a SAC387 solder joint (a) unaged and (b) after 28 hours at 100°C; (c) and (d) corresponding inverse pole figures; and (e) and (f) grain size distribution.

Although grain size and shape was little changed by ageing, there was some evidence for β-Sn grain boundary decohesion and possible sliding as shown for SAC305 BGAs in Figure 5.14. Grain boundary decohesion increased with ageing time as shown in Figures 5.15 (a)–(d). Figures 5.15 (a) and (b) show the same region of an unaged SAC387/Cu pad interface. There was no obvious intermetallic growth but there was Sn grain decohesion after ageing, in particular near the interface with the Cu pad in (c) and (d). Grain boundary sliding/decohesion requires a driving stress, which likely arose from the CTE mismatch between the boards and balls. The β-Sn anisotropy may also cause enhanced shear stresses along the Sn grain boundaries resulting in grain boundary decohesion and sliding [186, 189].

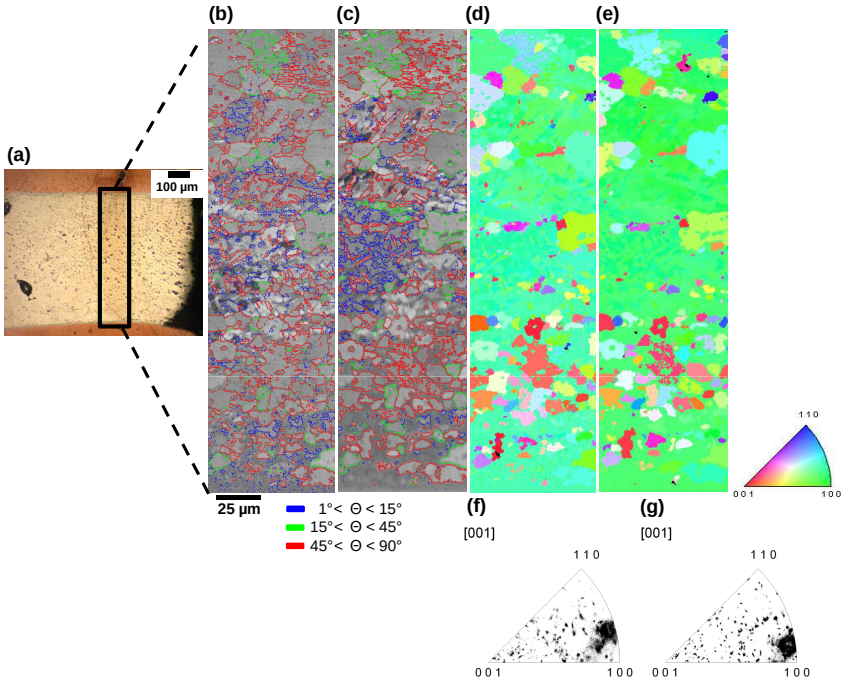


Figure 5.13: (a) Optical microscopy image of the cross-section of a SAC305 solder joint showing the EBSD analysis area; image quality maps with misorientation angle grain boundaries (low, medium and high angle grain boundaries in *blue*, *green* and *red* respectively) (b) after 3 hours and (c) after 6 hours of thermal ageing at 100°C; orientation maps of (d) after 3 hours and (e) after 6 hours ageing at 100°C; and (f) and (g) the corresponding inverse pole figures.

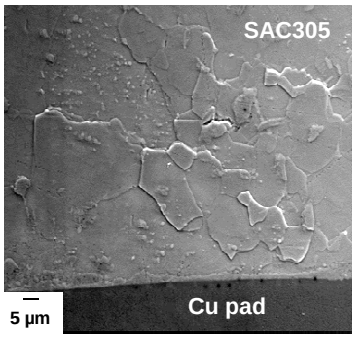


Figure 5.14: Secondary electron image of SAC305 solder joint after 6 hours of thermal ageing at 100°C.

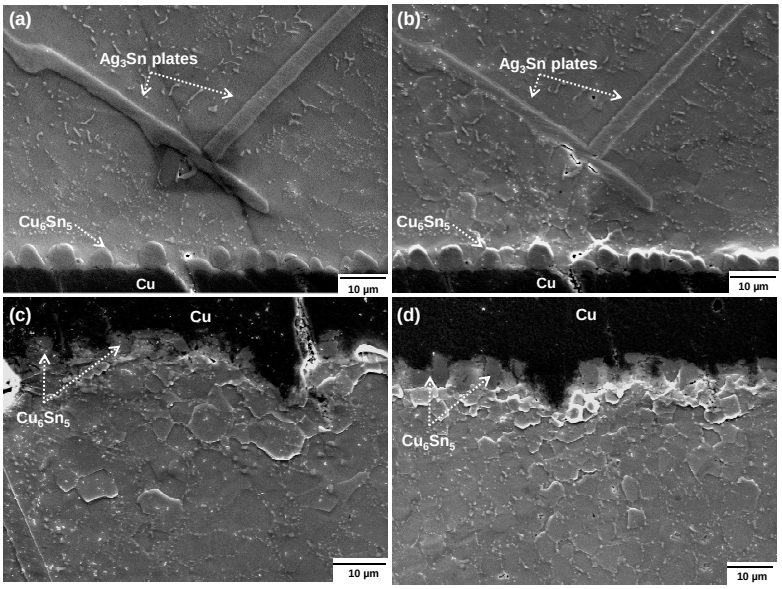


Figure 5.15: (a) Unaged SAC387/Cu pad interface; (b) after 28 hours of thermal ageing at 100°C; (c) and (d) other interface locations after 28 hours ageing showing Sn grain boundary decohesion and sliding.

The 'pop out' of Sn grains has been observed previously [32, 190] in Sn-Ag solder joints that had been submitted to thermomechanical cycling, and was attributed to inherent β-Sn anisotropy [32, 186]. As shown in Table 5.1 in section 5.1, the maximum difference in thermal expansion of Sn between the <100> and <001> crystalline orientations is $15.1 \times 10^{-6} K^{-1}$. In a polycrystalline Sn sample, a temperature variation of 75°C will induce a strain of 0.11% along the grain boundary of two grains having a <100>/<001> contact. Besides, the anisotropy in elasticity can result in a difference in Young's modulus of 31GPa between the <100> and <001> directions. Therefore, upon straining of the grains, there may be non-uniformity in the displacement of grains in contact with build up of stresses [189]. Table 5.1 also showed that the CTE mismatch between the polycrystalline Cu or Cu_6Sn_5 and the *c* direction of β-Sn is similar to and equals one half of the CTE mismatch between the *c* and *a* directions of β-Sn crystals. Therefore, stresses that may develop at Sn grain boundaries are similar to stresses between the Cu_6Sn_5 layer and β-Sn grains whose *a* direction is parallel to the Cu pad, but twice as large as stresses between the Cu pad and Sn grains whose *c* direction is perpendicular to the Cu pad [32].

5.5 Conclusions

EBSD analysis of as-received SAC305 and Innolot as-received solder balls revealed a cyclic twinning structure with three related Sn crystallographic orientations. Large (600μm diameter) solder balls had a 'beachball' pattern while smaller (400μm diameter) balls had numerous small grains ($\prec$20μm). The combined effects of Ag additions, promoting fine cyclic twinning structure, and of the Cu additions, favouring large grains could explain the beachball patterns observed in SAC and Innolot alloys.

Both the smaller and larger SAC305 balls preserved their as-supplied differences in grain size/shape during reflow.

Thermal ageing at 100°C showed no significant grain growth but suggested some β-Sn grain boundary decohesion and sliding, and was indicative of stress accommodation. Although a stress relief mechanism may prevent the development of large stresses during isothermal ageing/holding to avoid crack formation, grain sliding leads to a permanent plastic strain on rapid cool down and the generation of locked in stress in the solder joint, which will be localised in regions of excessive angular IMC growth.

Chapter 6

Nanoindentation creep testing

6.1 Introduction and objectives

Creep fatigue in solder alloys is when plastic deformation due to fatigue crack growth and creep deformation occur during cyclic loading of the solder joint. During solder joint deformation, the total strain (ϵ_T) can be partitioned into its elastic (ϵ_e), plastic (ϵ_p) and creep (ϵ_c) components:

$$\epsilon_T = \epsilon_e + \epsilon_p + \epsilon_c \tag{6.1.1}$$

Here, ϵ_e and ϵ_p are time-independent whereas ϵ_c is time-dependent. During isothermal exposure of the joint at elevated temperature, creep and stress relaxation dominate. During temperature transitions, the absolute temperatures and in particular the rate of temperature change will determine whether elastic-plastic deformation or creep dominates. Rapid transitions and lower temperatures favour elastic-plastic deformation. Although both tensile properties and creep behaviour are essential to assessing the reliability of soldered assemblies, properly wetted and bonded solder joints usually have adequate strength and it is therefore the creep behaviour that is critical for solder joint reliability.

Few attempts have been made to compare creep results from conventional creep tests with nanoindentation on the same material, especially for the elevated temperature operation regime of solder alloys [160, 162].

This chapter presents and discusses the results of high temperature nanoindenta-

tion experiments on bulk solder alloys from wave soldering bars, solder balls provided by external suppliers and solder joints manufactured in-house. Creep parameters of the various selected alloys processed under each manufacturing route were studied and compared with the literature where available. Extensive microscopy was carried out to support data interpretation.

6.2 Temperature-dependency of creep

6.2.1 Hardness and elastic modulus

Although creep study is the purpose of this chapter, this section briefly describes typical nanoindentation hardness and elastic modulus measurements obtained, presented here for comparison with literature and to provide confidence that the method produced sensible results for these more conventional parameters.

Figures 6.1 (a) and (b) show the elastic modulus and hardness of selected bulk solders determined from the unloading curves of the nanoindentation load-depth curves as described in section 3.3.1. The measured significant decrease in hardness and elastic modulus for SAC387 and Innolot compares well with earlier work [183]. As temperature increased, the mechanical properties tended towards those of Sn as the matrix mechanical behaviour dominated the mechanical response. The near linear decrease of hardness with increasing temperature in Figure 6.1 (b) was also observed for Sn bulk samples tested by nanoindentation under the same loading conditions [191] and a Au-20Sn solder alloy in a similar temperature range [192]. The behaviour indicated progressively greater plastic deformation with temperature, consistent with a reduction in flow stress.

Figure 6.2 compares the modulus and hardness obtained at room temperature with the literature for the various alloys (no Innolot data was available). Although Sn-37Pb properties obtained by nanoindentation in this study were within the literature range, SAC387, SAC305 and Innolot exhibited higher modulus compared with most of the literature [88, 108, 143, 193–201] although within the range of scattered data in the literature [202, 203]. Modulus measured by nanoindentation is known to be

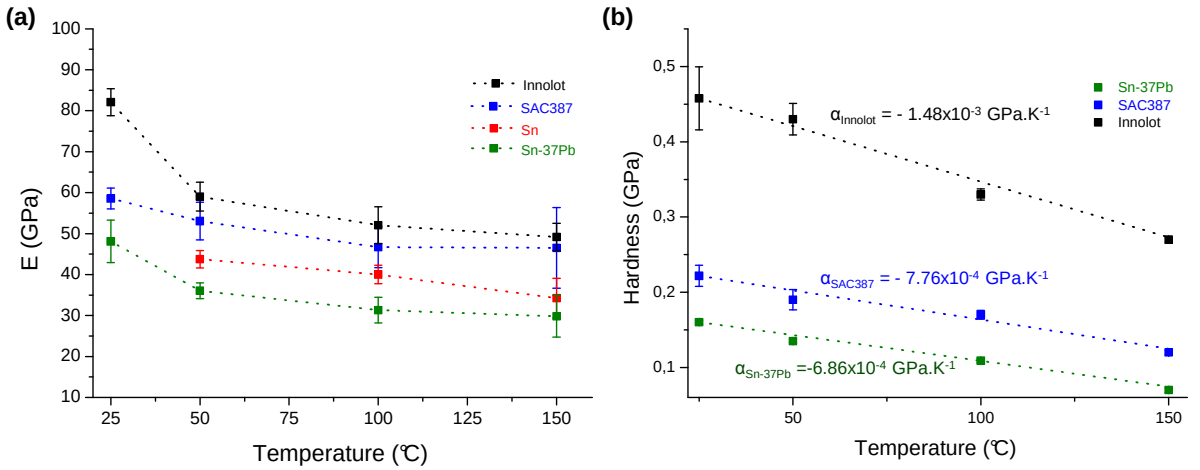


Figure 6.1: (a) Elastic modulus of bulk Innolot, SAC387, Sn and Sn-37Pb alloys for various temperatures determined from creep tests at a maximum load of 100mN; and (b) the corresponding hardness and its linear fitting with hardness coefficients.

problematical since assumptions relating to elastic unloading may be suspect under some conditions.

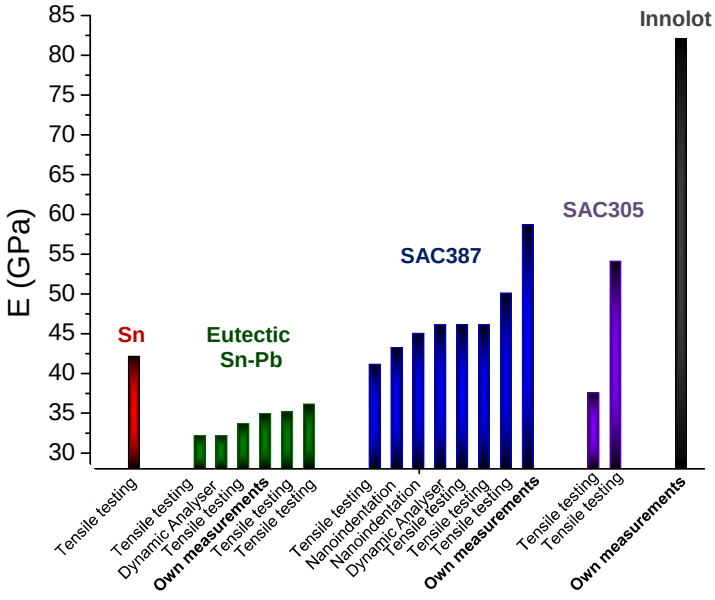


Figure 6.2: Elastic modulus of Sn, eutectic Sn-Pb, SAC387, SAC305 and Innolot obtained by the nanoindentation study and results obtained in various studies using different testing techniques for comparison [88, 108, 143, 193–201].

6.2.2 Creep stress exponents

Representative nanoindentation load-displacement curves at various temperatures and loads for bulk (wave soldering bar) SAC387 solder are shown in Figure 6.3 (a). The load-displacement curves were considered acceptably reproducible for all temperatures with variations in creep behaviour within a data set $\prec$10%. Loading led to a non-linear increase in penetration depth. After the load reached its peak, creep penetration occurred over the iso-load hold time. Upon load removal, the penetration depth decreased until the load approached zero and a residual indentation was produced.

Figure 6.3 (b) shows the variation of indentation depth as a function of dwell time for a maximum load of 50mN. Broadly, the curves were similar to typical creep curves by tensile testing except that they can be assumed to comprise only two stages of creep, as the third stage of creep leading to fracture cannot be observed during nanoindentation. In the primary stage, there was an increase in penetration depth with time and the strain rates were comparatively high (quantified later). In the secondary stage, an approximately constant strain rate was achieved due to the competition between strain hardening and strain softening, and indentation depth increased almost linearly with time. The creep behaviour was generally acceptably reproducible for a particular iso-load and temperature ($\prec$200nm overall displacement difference between 600s creep tests).

Temperature had an effect on the creep behaviour of bulk SAC387 as both the penetration depth (from 3.1μm at 25°C to 6.0μm at 175°C) and the slope (0.49nm.s^{-1} at 25°C to 1.54nm.s^{-1} at 175°C) of the secondary creep curves increased with temperature. The faster indenter penetration and larger residual displacements at constant load for higher testing temperatures indicated progressively higher rates of material softening.

Figure 6.4 shows the indents in bulk SAC387 after creep tests to various loads and temperatures. While nanoindentation at low loads (2 and 5mN) could be configured to probe single phases (β-Sn or the eutectic phase combination), larger loads inevitably

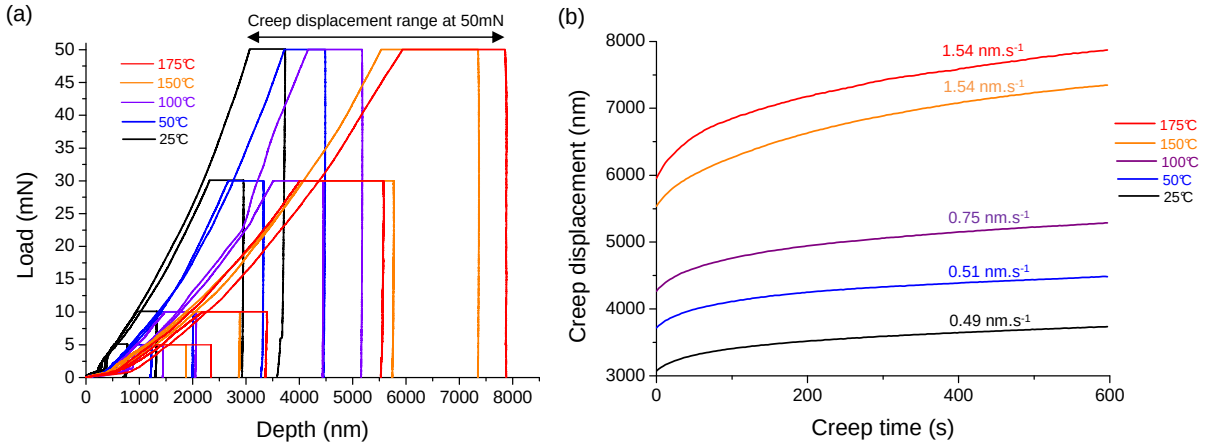


Figure 6.3: (a) Nanoindentation load versus displacement to maximum loads of 5, 10, 30 and 50mN in the 25–175°C temperature range for bulk SAC387; and (b) creep curves showing the penetration depth during a 600s dwell time at a 50mN maximum load in the 25–175°C temperature range.

probed multiple phases in a single indentation, even at low loads and room temperature, therefore giving some degree of 'average' mechanical properties. Consistent with the larger residual displacement with higher temperatures in Figure 6.3 (a), the indentations were larger with higher loads and temperatures, even leading to cracking and material pile-up around the indent at 10mN at 100 and 150°C.

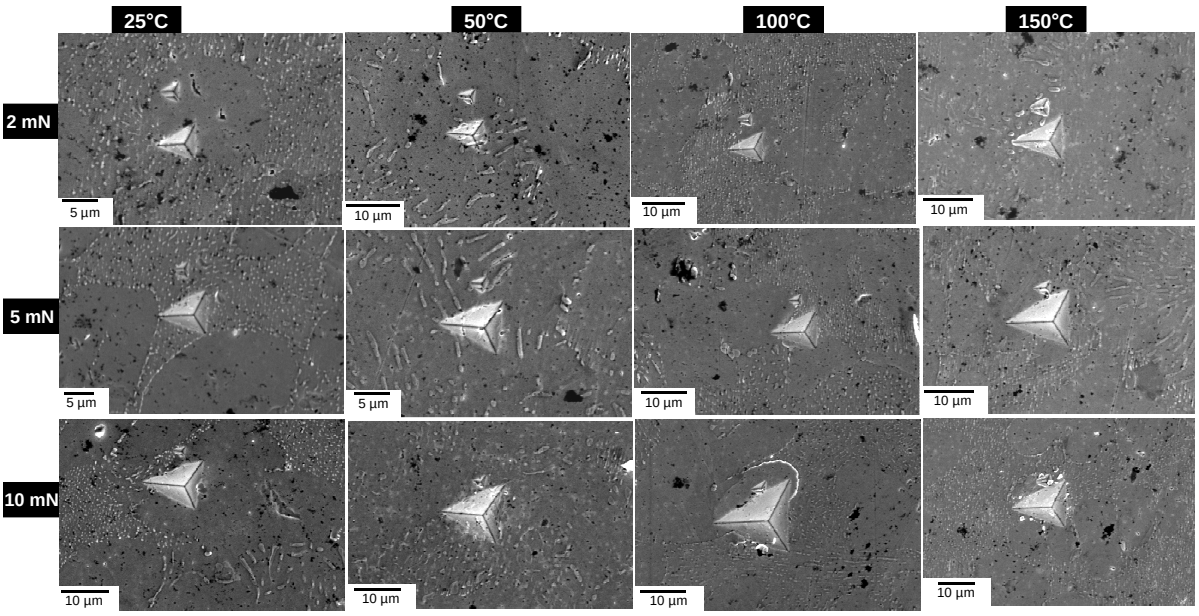


Figure 6.4: Secondary electron images of indents in bulk SAC387 after creep tests at 2, 5 and 10mN and temperatures in the 25–150°C range. Images in the same line are for a particular load, whilst images in the same column are for a particular temperature.

Figure 6.5 shows the creep curves for bulk SAC387, β-Sn, Sn-37Pb and Innolot at 25

and 150°C. At room temperature, β-Sn was the least creep resistant while Innolot was the most creep resistant. At 150°C, Sn-37Pb was the least creep resistant while Innolot remained the most creep resistant, consistent with the suitability of Sn-37Pb for traditional lower duty and temperature applications where stress relaxation is important, while the newly developed Innolot provides better creep resistance (less relaxation), which is considered more important for harsh environment applications where excessive creep due to higher temperature would lead to large component displacement and distortion.

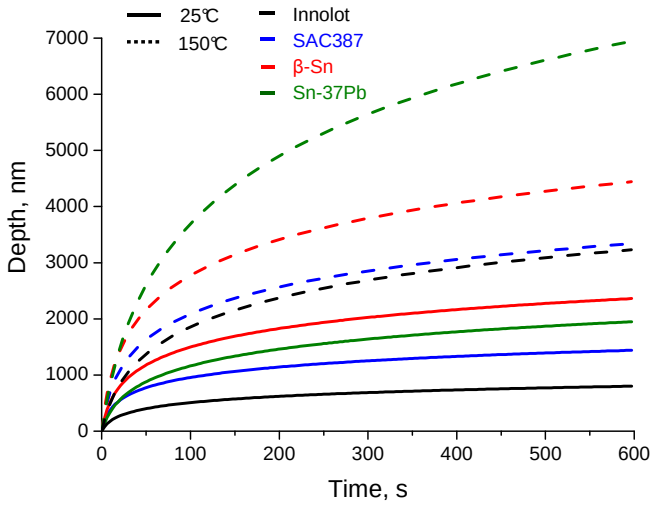


Figure 6.5: Creep curves for bulk Innolot, SAC387, Sn, Sn-37Pb at 25 and 150°C, under a constant 100mN load for 600s.

From Figure 6.5 and the corresponding curves at the selected other loads, secondary creep was assumed to have been reached after 150s of dwell. As described in section 3.3.2, the indentation strain rate was defined as the indentation moving-in rate divided by the depth into the surface:

$$\frac{d\epsilon}{dt} = \frac{1}{h}\frac{dh}{dt} \tag{6.2.1}$$

The resulting strain rate versus stress curves in Figure 6.6 curves generally approximated well to a linear fit, as suggested by Equation 3.3.8 in section 3.3.2. The nanoindentation stresses were in the 50–500MPa range while the strain rates were in the $7x10^{-5}$–$1x10^{-2}s^{-1}$ range. Innolot was more creep resistant than SAC387 and SAC305 respectively. IMC phases have a strengthening effect: deformation produces dislocations but intragranular dislocations are pinned by IMCs, thus slowing down disloca-

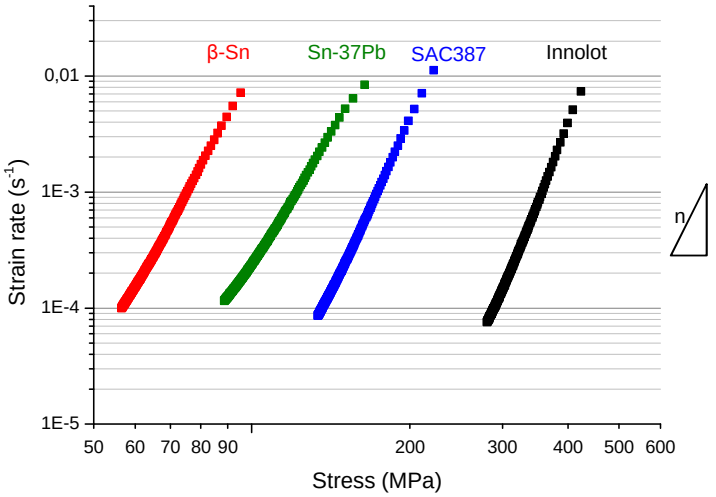


Figure 6.6: Strain rate versus stress curves used to obtain stress exponents for Test (1) on bulk Sn-37Pb, β-Sn, SAC387 and Innolot alloys at 100mN iso-load and 25°C.

tion motion and increasing creep resistance. In addition to precipitation strengthening, there was a solid solution hardening effect for Innolot as Bi has a 3 to 5 *wt*% solubility in Sn [204] and Sb has a 7 *wt*% solubility in Sn [205].

Figure 6.7 shows the best-fit creep stress exponents for the β-Sn, Sn-37Pb, SAC387 and Innolot alloys obtained from Figure 6.6. The stress exponents were all in the 7–12 range at 25°C, typical of dislocation creep mechanisms. SAC387 and Innolot had stress exponents of 9 and 12 respectively, well within the 8–18 range reported in the literature for stress exponent measurements on bulk Pb-free solders [206–210]. The stress exponent for β-Sn was 8.4, which lay in the 4.5–9 range for bulk pure Sn in the literature [206, 211, 212]. Sn-37Pb had a stress exponent of 7, within the 1.8–11.1 range reported in the literature [140].

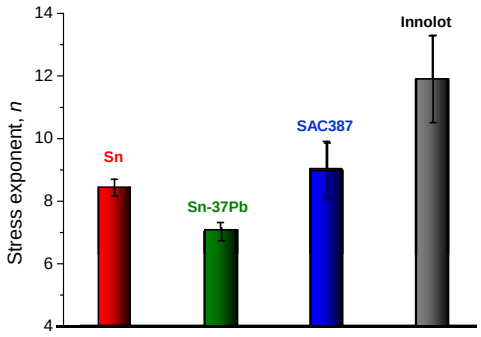


Figure 6.7: Best-fit stress exponent for bulk β-Sn, Sn-37Pb, SAC387 and Innolot at 25°C determined by Test (1).

Figures 6.9 (a)–(d) show the stress-strain rate curves for the selected solder alloys varied over the 25–150°C temperature range, and Figure 6.9 (e) consolidates this data onto a single plot for easy comparison. Again, the plots show good approximation to straight line behaviour.

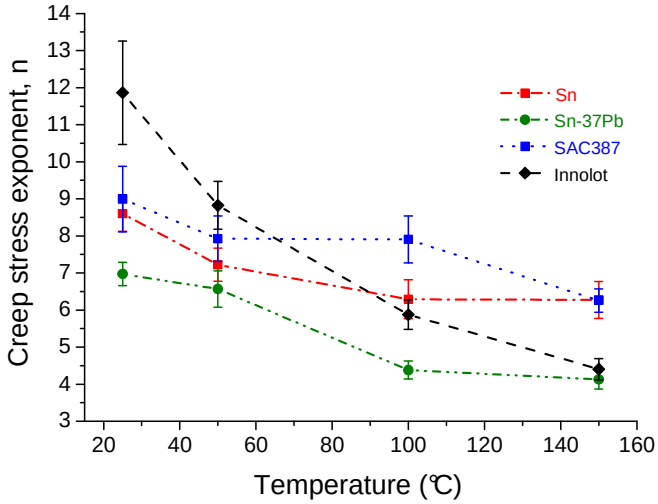


Figure 6.8: Best-fit stress exponent for bulk SAC387, β-Sn, Sn-37Pb and Innolot as a function of temperature at 100mN.

Figure 6.8 shows the creep stress exponents n extracted from Figures 6.9 (a)–(e). The measurement spread in n decreased with increasing temperatures, particularly for Innolot and SAC387 (standard deviations of 1.4 and 0.9 at 25°C respectively, and 0.3 at 150°C), which can be linked to the behaviour of Figure 6.4: as temperature increased, the indentation area was larger and probed more IMCs, giving less scattering in the overall mechanical properties. There was an overall decrease in the stress exponents with temperature: from 12, 9.0, 8.4 and 7.0 at 25°C to 4.4, 6.3, 6.3 and 4 at 150°C for Innolot, SAC387, Sn and Sn-37Pb respectively. The stress exponent decrease in Figure 6.8 might suggest a progressive shift from one deformation mechanism to another as temperature increased. At high temperatures (100–150°C), time-dependent mechanisms, such as diffusion-based processes tended to dominate the deformation, hence lower stress exponents. Relative motion between grains through grain-boundary sliding was likely to take place in addition to diffusion-based mechanisms [207, 211].

Figures 6.10 (a)–(l) show secondary electron images of indents at 25°C for Sn-37Pb, SAC387 and Innolot at maximum loads of 10 to 200mN. The length scale of indents

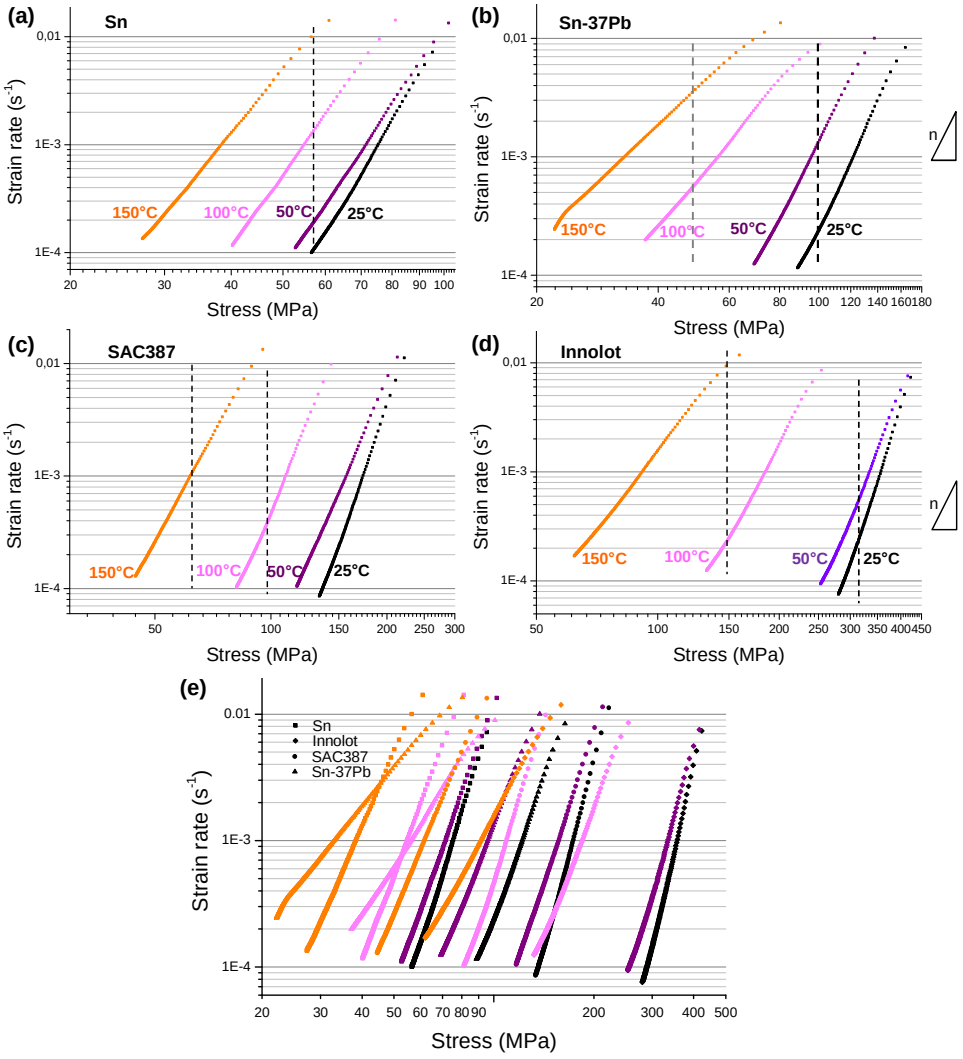


Figure 6.9: Strain rate versus stress curves for bulk (a) β-Sn; (b) Sn-37Pb; (c) SAC387; (d) Innolot creep tests at 100mN in the 25–150°C temperature range; and (e) all alloys and temperatures.

was large enough to span multiple phase boundaries and nanoindentation measurements were therefore generally considered to be of a composite of phases (unless otherwise stated) rather than individual phases. Comparison between Figures 6.10 (i)–(l), (a)–(d) and (e)–(h) shows smaller indents for Innolot compared with Sn-37Pb and SAC387, and is consistent with the lower strain rate at 25°C in Figure 6.5.

Figures 6.10 (a)–(l) also enabled comparison of any cracking behaviour around the indents [213]. There was no or minimal cracking for SAC387 and Sn-37Pb alloys respectively and the deformation was dominated by plastic flow. Figures 6.10 (d) and (l) show the crack propagation around indents for bulk Sn-37Pb and Innolot at high loads. In Sn-37Pb, deformation occurred between the Sn-rich phase and the Pb-rich

globules by the growth of cracks along interface boundaries [8]. The Pb islands acted as crack initiators around the indent site and cracks propagated from one Pb island to the next closest, reaching a propagation length of $\sim$100μm for a 200mN indent as shown in Figure 6.10 (d). The cracks extended radially outward from the impression and penetrated the material normal to the surface.

The extensive cracking in Innolot in Figures 6.10 (k) and (l) suggested a lower cracking stress threshold. Cracks did not follow the usual radial cracking pattern, typically used for fracture toughness measurements [214], but there was instead a rather unusual multiple cracking pattern, which suggested a reduced malleability of Innolot compared with Sn-Pb and SAC solders, in accordance with correspondence by the author with Henkel Corporation who are a supplier of Innolot [215]. This cracking pattern may be explained by the presence of large $(Cu,Ni)_6Sn_5$ brittle IMCs in the microstructure that initiate interphase boundary sliding while the solid solution strengthening effects of Bi and Sb impede the propagation of the cracks to the surrounding matrix.

Figures 6.11 (a)–(c) show micrographs of indents in bulk Sn-37Pb, Innolot and as-received SAC305 solder balls: (a) shows cracks initiating from the Pb grain/Sn boundaries and propagating in the Sn phase; while (b) and to a lesser extent (c) show β-Sn grains moving upwards relative to sample surface, suggesting the onset of grain boundary sliding.

The superior creep resistance of SAC solders over Sn-37Pb was explained by the dispersion of Ag_3Sn and Cu_6Sn_5 in the matrix of Sn, which tended to reduce grain boundary sliding as fine dispersoids enabled a Zener pinning effect (section 2.2.2). Such an effect can be observed in Figure 6.11 (c) where small round shaped Ag_3Sn IMCs were located at the grain boundaries. Sn-37Pb had no particulate phase and was more susceptible to inter-lamellar sliding.

6.2.3 Creep activation energy

The creep activation energies were calculated for the various alloys as described in section 3.3.2. Stresses were selected so that the maximum number of strain rate data

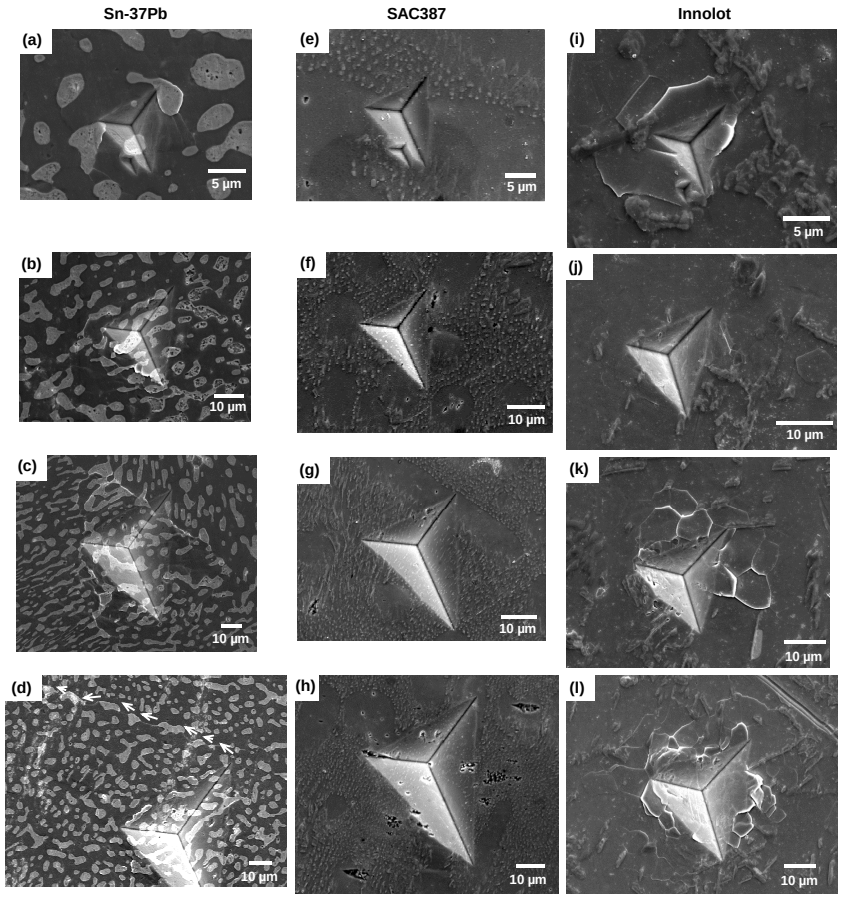


Figure 6.10: Secondary electron images of indents at 25°C in eutectic Sn-37Pb, SAC387 and Innolot for loads of 10, 50, 100 and 200 mN – (a) to (d), (e) to (h) and (i) to (l) respectively. Sn-Pb showed little cracking from 10 to 200mN; there was no cracking in SAC387, while there was extensive cracking in Innolot at all loads. The arrows in (d) show the cracking direction.

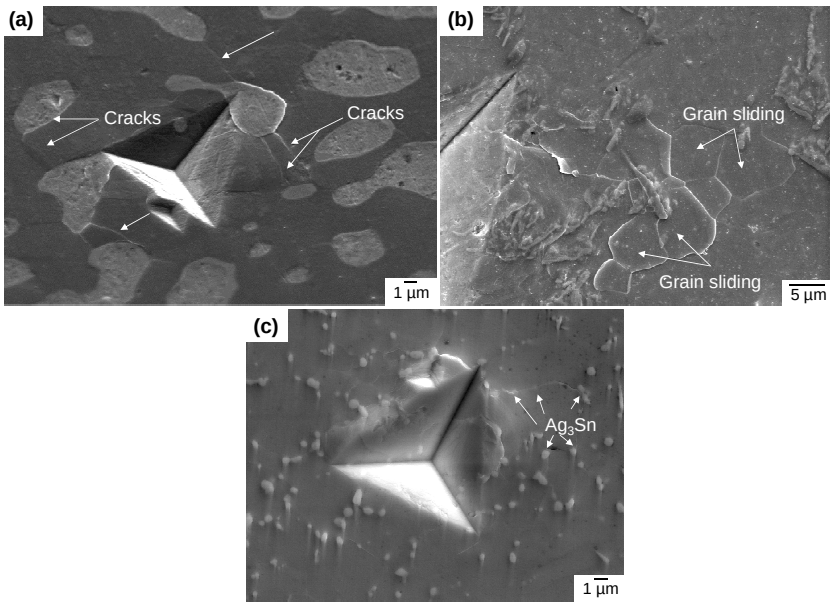


Figure 6.11: Secondary electron images of (a) tilted indent on bulk eutectic Sn-37Pb for a 10mN iso-load; (b) indent on bulk Innolot for a 200mN iso-load; and (c) indent on as-received SAC305 solder ball (400μm diameter) for a 10mN iso-load.

points were taken into account for measurement. These stresses are represented by the vertical dashed lines in Figures 6.9 (a)–(d). Depending on the alloy, one or two stresses had to be selected to cover the temperature range.

Solder alloy	Stress (MPa)	Temperature range (°C)	Q ($kJ.mol^{-1}$)	σ/E
Sn	57	25 – 150	39	1.4×10^{-3}
Sn-37Pb	100	25 – 50	56	2.4×10^{-3}
	50	100 – 150	48	1.6×10^{-3}
SAC387	143	25 – 100	53	2.7×10^{-3}
	82	100 – 150	105	1.8×10^{-3}
Innolot	325	25 – 50	24	4.6×10^{-3}
	140	100 – 150	100	2.8×10^{-3}

Table 6.1: Activation energies of bulk solder alloys. σ/E was calculated with the average of the elastic modulus in the selected temperature range.

Figure 6.12 shows how the best-fit values of Q were determined and Table 6.1 summarises the results. For all alloys, the σ/E ratio was $\sim 10^{-3}$, suggesting little influence of stress on activation energies in the testing conditions [107]. The activation energy over the 25–150°C temperature range for β-Sn was 39kJ.mol^{-1} and the activation energy for Sn-37Pb in the 25–50 and 100–150°C ranges were 56 and 48kJ.mol^{-1} respectively, suggesting a pre-dominant creep mechanism over the 25–150°C range for both

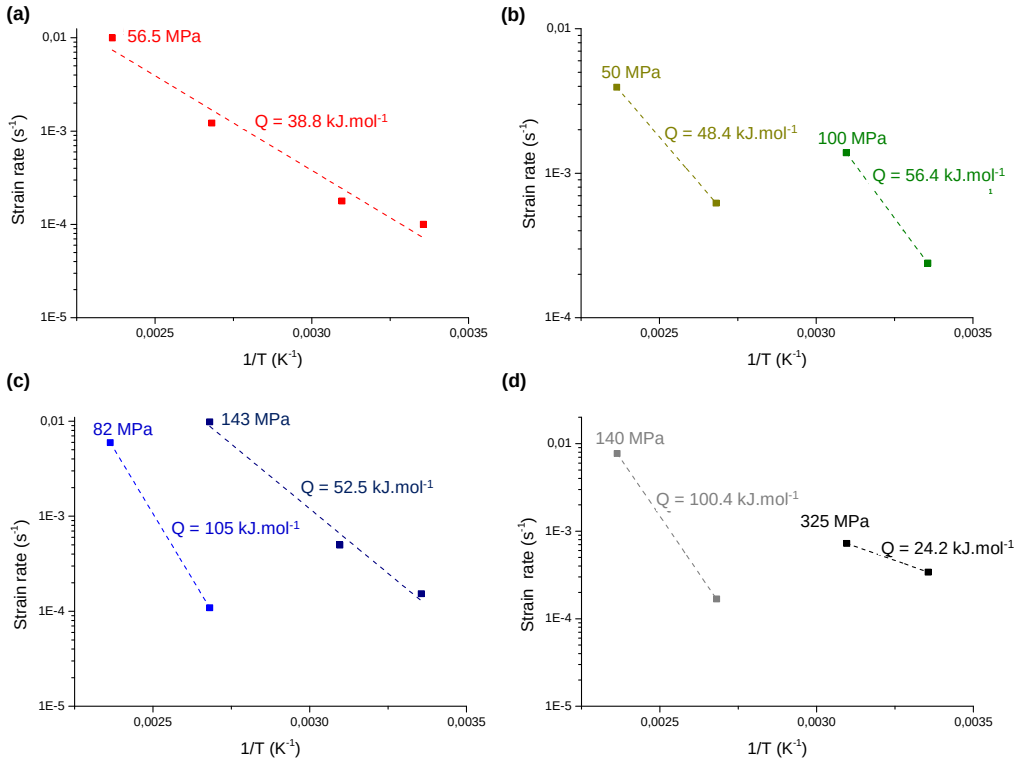


Figure 6.12: Creep activation energies for bulk (a) β-Sn; (b) Sn-37Pb; (c) SAC387; and (d) Innolot determined from elevated temperature nanoindentation creep measurements at 100mN.

β-Sn and Sn-37Pb. Atomic transport along grain boundaries is usually associated with activation energies of 40–70kJ.mol^{-1} [107]. As shown in Figure 2.11 of section 2.4 and suggested by the stress exponents in the 6.3–8.4 and 4.1–7 ranges for β-Sn and Sn-37Pb respectively, the creep mechanism in this stress and temperature range should mainly be due to dislocation climb with perhaps an accompanying grain boundary sliding mechanism. As reviewed in section 2.4, a wide range of creep activation energies has been reported in the literature. Activation energies were in the 18–180kJ.mol^{-1} range for pure Sn [216] and in the 40–77kJ.mol^{-1} range for Sn-Pb [217]. Therefore, the activation energies obtained here for β-Sn and Sn-37Pb lie squarely within the range in the literature, regardless of test scale.

The two creep mechanism hypothesis described for SAC387 and Innolot in Figure 6.8 at low and high temperatures was supported somewhat by the Arrhenius plots in Figures 6.12 (c)–(d) and Table 6.1, with different creep activation energies estimated depending on the temperature regime for SAC387 and Innolot. The activation energies

for SAC387 and Innolot in the high temperature regime were $\succ$100kJ.mol^{-1}, which corresponds to the energy range for self-diffusion activation energies (lattice diffusion) [206]. At lower temperatures, the activation energy of SAC387 and Innolot was 53 and 24kJ.mol^{-1} respectively. For SAC387, the low temperature regime activation energy was $\sim$0.5 that of the high temperature regime activation energy. For systems were dislocation core diffusion is predominant, the activation energy is typically 0.4-0.5 of the value for lattice diffusion [206], therefore lattice diffusion controlled climb (dislocation climb) dominated the creep mechanism in the high temperature regime for SAC387 and dislocation core diffusion controlled climb (dislocation glide) occurred at lower temperatures. Activation energies for Sn-3.5Ag were 60kJ.mol^{-1} in the low temperature regime (25–95°C) and 120kJ.mol^{-1} in the high temperature regime (95–130°C) [206]. Besides, the change in stress exponent from the low temperature regime to the high temperature regime was 7.6 and 2.7 for Innolot and SAC387 respectively and a change in mechanism from diffusion along dislocation cores to that of lattice diffusion is usually associated with a stress exponent of 2 [206].

In summary, grain boundary diffusion dominated the creep deformation in β-Sn and Sn-37Pb over the 25–150°C temperature range while different low and high temperature creep mechanisms were suggested for SAC387 and Innolot. It is likely that for these latter alloys, grain boundary sliding occurred with dislocation glide controlling creep at low temperatures (25–50°C), and dislocation climb dominating creep at high temperatures (100–150°C). A transition temperature in the 0.65–0.75T$_m$ range can be suggested and was consistent with previous creep tests performed with a microforce testing system on Sn-3.5Ag [206].

6.2.4 Limits to nanoindentation

Although there was good agreement between creep stress exponents in this study and literature values, the neglect of primary creep in nanoindentation creep data analysis is a problematic assumption (sections 2.4 and 6.2.2). Recently, Clyne *et al.* found little or no correlation between nanoindentation creep data and conventional testing literature data on various materials [156]. They deemed nanoindentation an 'unreliable' technique for the determination of creep parameters. Nanoindentation creep curves

exhibit an initial stage followed by a regime of constant penetration rate, similar to the steady-state stage in conventional creep tests. However, Clyne *et al.* argued that steady-state is never established in nanoindentation creep as 'local regions are constantly moving along their own creep strain history curves' and it is 'unclear whether much, or indeed any, of the deforming volume will have entered the secondary creep regime during the test' [157]. They carried out nanoindentation creep tests on extruded Cu samples for one hour over a 25–150°C temperature range and found $-2 \prec n \prec +2$ and $0 \prec Q \prec 6 \text{kJ.mol}^{-1}$, evidencing little or no correlation with conventional compression creep tests on the same material. They attempted to solve the primary creep neglect with an FEM model that used a transient creep law (taking into account primary and secondary creep regimes), rather than the steady-state equation [157]. The model provided good prediction of the indenter penetration during a one-hour dwell and it was concluded that creep parameters could be obtained with a $\pm$10–20% reliability. Therefore, the question arose in our study as to whether secondary creep was well established after only 150s and if primary creep could be neglected. However there is a number of reports of good correlation between creep parameters obtained by indentation and uniaxial test in the literature [218–220], especially for studies on materials that creep rapidly at room temperature (i.e. solders). In these materials, the effect of primary creep was deemed less pronounced [156], suggesting that the steady-state hypothesis in our study did not entail significant errors. Comparison between conventional creep and nanoindentation creep test results on solder alloys would have provided a critical evaluation of our results but conventional tests were not carried out due to lack of time.

Figure 6.13 shows the creep stress exponent as a function of iso-load at various temperatures. At 25°C, the stress exponent increased with load (from 7.8 at 5mN to 9.6 at 50mN and 25°C), similarly to previous reports [221]. The trend was much less pronounced at higher temperatures and as noted in section 6.2.3, σ/E was constant over the measurement temperature range. Therefore, it is unlikely that such a stress exponent increase was due to a threshold stress as previously observed on Sn-3.5Ag [206]. As also previously mentioned, at low loads, creep was caused by grain boundary sliding and dislocation climb. In smaller low-load indents, the majority of plastic deformation zone will be close to the specimen free surface and diffusion assisted

grain boundary sliding and grain rotation were facilitated by the proximity to the free surface, leading to lower stress exponents.

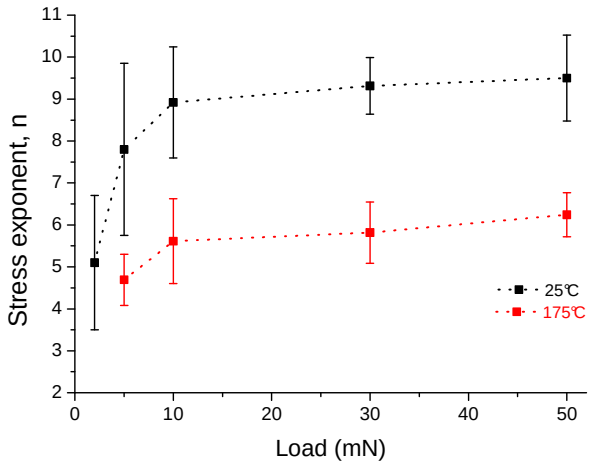


Figure 6.13: Creep stress exponents of bulk SAC387 as a function of iso-load at 25 and 175°C.

Such a load dependence with indentation size is similar to the well-known indentation size effect for nanoindentation hardness measurements i.e. the increase of indentation hardness with the decrease of indentation depth. The basic Nix and Gao model attributed such an effect to the presence of geometrically necessary dislocations (GNDs) that exist underneath the indenter in addition to the usual statistically stored dislocations (SSDs) produced during uniform straining, giving rise to an extra hardening component that becomes larger as the contact impression decreases in size [222–224].

Figure 6.14 (a) is an AFM height profile of an indent in bulk SAC387 while Figure 6.14 (b) is the corresponding three-dimensional profile showing pile-up around the indent. At a comparatively small 5mN maximum load, the maximum pile-up height was $\sim$0.3μm. Pile-up is related to the ratio between yield stress and elastic modulus, and to the rate of work hardening. Pile-up is usually observed in materials with a relatively high ratio between yield stress and elastic modulus, such as solders [156]. Pile-up may lead to an under-estimation of the measured contact depth and therefore over-estimated contact areas, and therefore lower calculated stresses and higher stress exponents.

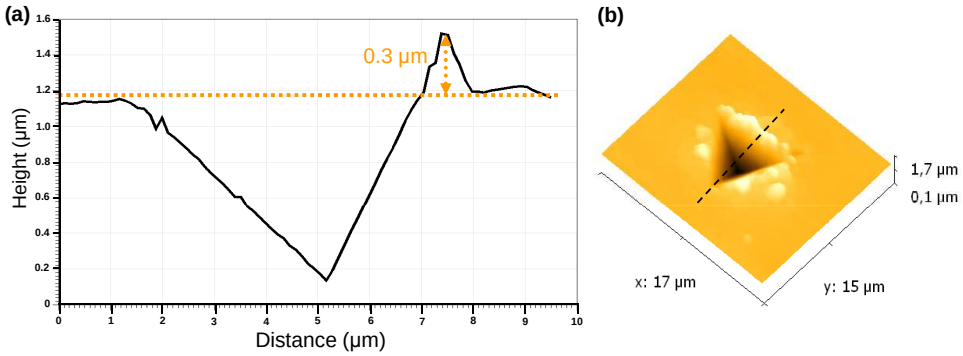


Figure 6.14: (a) AFM indentation line height profile across an indent obtained after isoloading at 5mN for 400s dwell time at 25°C in bulk SAC387; and (b) three dimensional profile of the indent and AFM scanning line.

Besides, the size of indentations with respect to sample microstructure (e.g. IMCs, grain size) may have an effect on creep parameters.

6.3 Effect of microstructure and Sn grain size

Section 5.3 showed that as-cast 400μm and 600μm solder balls had different microstructures, with a Sn grain size varying by a factor greater than 100. The microstructural differences were ascribed to different manufacturing techniques for the two sizes of solder balls. The as-supplied microstructural differences may also lead to a variety of microstructures in the solder joints and so the creep behaviour of the two different diameter as-received balls and the resulting as-reflowed BGA joints was studied.

6.3.1 Effect of microstructure

Figure 6.15 shows individual load-depth nanoindentation behaviour of the various alloys of solder joints up to a comparatively low load of 2mN. The indentation was performed approximately in the centre of BGA cross-sections. At this low load the microstructure sensitivity was enhanced. For example, the arrows in Figure 6.15 indicate 'pop-in' events which have been previously reported for solders [190, 225] and attributed to the formation of shear bands or micro-cracking during a transition from elastic to plastic deformation when the load *locally* exceeds the yield stress under the indenter. However, SEM observations in this thesis at low loads failed to observe slip

bands on the indent faces. Rather, the absence of such pop in events for Sn-37Pb suggested that they might be attributed to the presence of IMCs in the Pb-free solders, for example sudden debonding of the IMC-β-Sn interface.

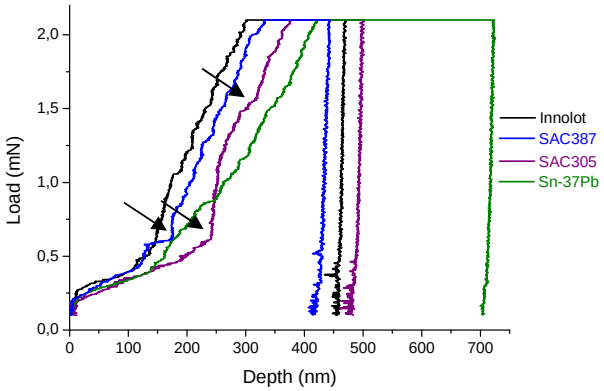


Figure 6.15: Load versus depth curves for nanoindentation tests on various BGA cross-sections (from 500μm balls).

Figures 6.16 (a) and (b) show secondary electron micrographs of indents at 2mN and 25°C in as-received SAC305 balls with diameters of 400 and 600μm respectively. While Ag_3Sn IMCs were generally evenly scattered in the smaller balls, they were slightly finer and more strongly clustered into the intercellular/interdendritic regions of the typical cast structure of the larger balls.

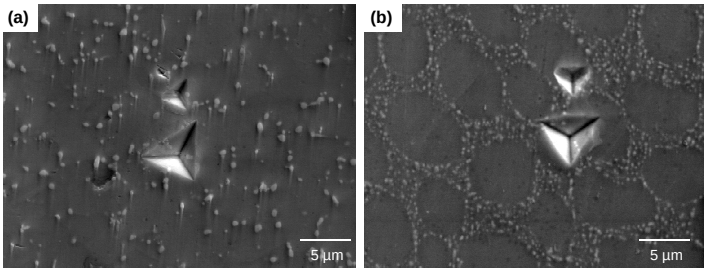


Figure 6.16: Secondary electron images of indents in as-received (a) 400μm SAC305 ball; and (b) 600μm SAC305 ball.

Figure 6.17 shows the load-depth indentation profiles for various indents at different maximum loads for the 400 and 600μm as-received SAC305 solder balls. The indentation profiles for the two diameters were similar at high loads (10, 20, 30mN), whereas at low loads (2 and 5mN), 400μm balls indented to a higher depth (~200nm) than 600μm balls, suggesting a lower creep resistance. As observed previously, material parameters at low loads can be microstructure-dependent and free surface effects

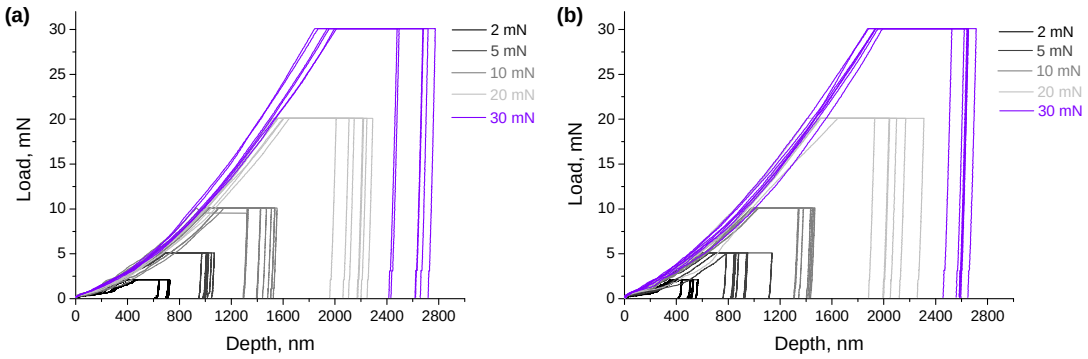


Figure 6.17: Load-depth indentation profiles to maximum loads of 2, 5, 10, 20 and 30mN for various indents in as-cast SAC305 solder balls with a diameter of (a) 400μm; and (b) 600μm.

likely more important and underlining the need for higher loads for 'average' material behaviour, but which pushes stresses much higher than joints will see in service.

Figure 6.18 shows the creep stress exponents as a function of load extracted from Figure 6.17 following the procedure described in section 3.3.2. As nanoindentation probed multiple phases (β-Sn and Ag_3Sn IMCs) at higher loads ($\succ$20mN), the stress exponents of the two types of balls tended to a similar value ($\sim$11). At all loads, the creep resistance of 400μm solder balls was lower than 600μm balls, probably due to the higher creep resistance conferred by the more obvious concentrating of Ag_3Sn IMCs in intercellular regions in the larger balls, and the finer grain size in the smaller balls. This trend was more striking at low loads of 2 and 5mN, in accordance with Figure 6.17. Figure 6.19 shows indents at various loads on 400μm diameter balls. At low loads (2 and 5mN), the indents only probed β-Sn and few Ag_3Sn IMCs, hence the underestimated stress exponent in Figure 6.18 for small balls at low loads.

As seen in section 6.2.2, a mixture of grain boundary sliding and dislocation glide and dislocation climb occurred in the low and high temperature stress regimes respectively. Therefore, grain size can be expected to affect creep behaviour as a mass transport mechanism during diffusion creep. In diffusion creep, transport occurs on the scale of the grain, so coarser grains lead to slower creep rates. Grain size can also have an effect on grain boundary sliding as multiple grains increase the opportunity for grain boundary sliding [226].

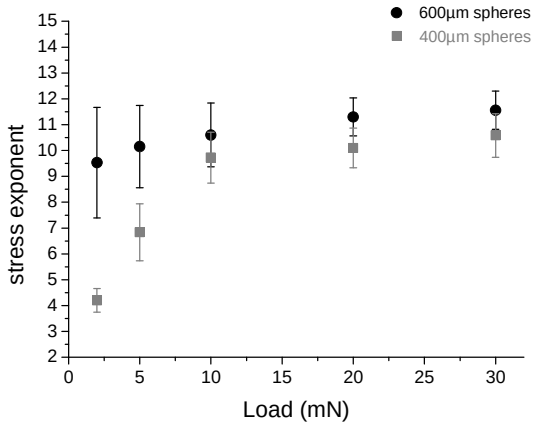


Figure 6.18: Stress exponents as a function of iso-loads for as-cast SAC305 solder balls with diameters of 400 and 600μm determined at 25°C.

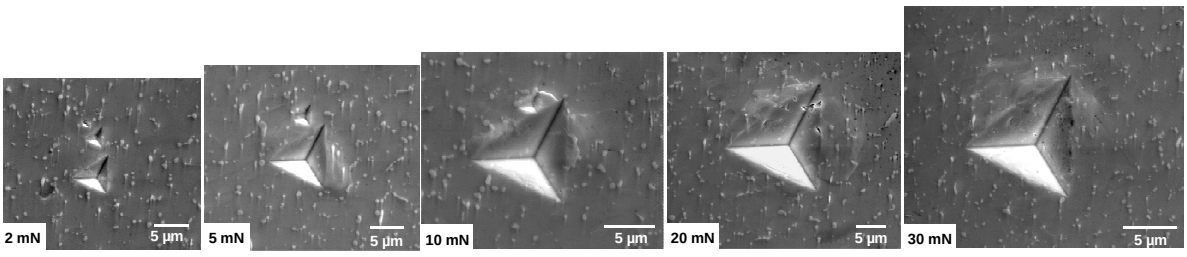


Figure 6.19: Secondary electron images of indents on an as-received 400μm SAC305 solder ball with increasing load.

As shown conclusively in section 5.3, 400μm SAC305 balls comprised numerous fine grains while 600μm balls contained only a few grains. Therefore, 400μm balls had more grain boundary area per unit volume, enhancing grain boundary sliding, and contributing to the decreased creep resistance in Figure 6.18.

6.3.2 Effect of solder manufacturing route

Figure 6.20 compares the stress exponents of Sn-37Pb, SAC387 and Innolot alloys in the form of bulk or as-reflowed solder joints. The cross-polarising images show that both processing routes gave coarse-grained samples for all three alloys. In order to probe multiple phases, creep measurements on bulk alloys were carried out at 100mN iso-load while a load of 2mN was chosen for as-reflowed solder joints so that indents were small enough to perform multiple indentations on each BGA sample, again highlighting the compromises required in nanoindentation testing. The measurement spread was larger for BGAs than bulk, due to the use of the 2mN load (section 6.2.2). Further, as-reflowed Sn-37Pb and Innolot alloys had lower stress exponents ($\sim$9% and 36% lower respectively) compared with their bulk counterpart because of the difference in testing load (section 6.2.4). Considering the testing load choice and resulting standard deviations (shown as error bars in Figure 6.20), reflow of the solder balls (when performed to industrial requirements) provides a nanoindentation creep response of the as-fabricated solder balls similar to bulk material.

Figure 6.21 shows the stress exponents for the relatively coarse-grained SAC305 as-received 600μm balls, and 500μm SAC305 BGA solder joints (with similar relatively coarse structure) and fine-grained 400μm SAC305 as-received balls. All tests were carried out at 2mN iso-load. Overall, the reflow of the coarse-grained balls did not change their creep response significantly, which suggested the reflow operated correctly since the balls should not significantly remelt, with only the pads undergoing full melting. While coarse-grained as-received SAC305 alloys had a stress exponent of 9.5, the fine-grained as-received SAC305 alloys had a stress exponent of 4.2, again emphasizing the lower creep resistance of fine-grained alloys.

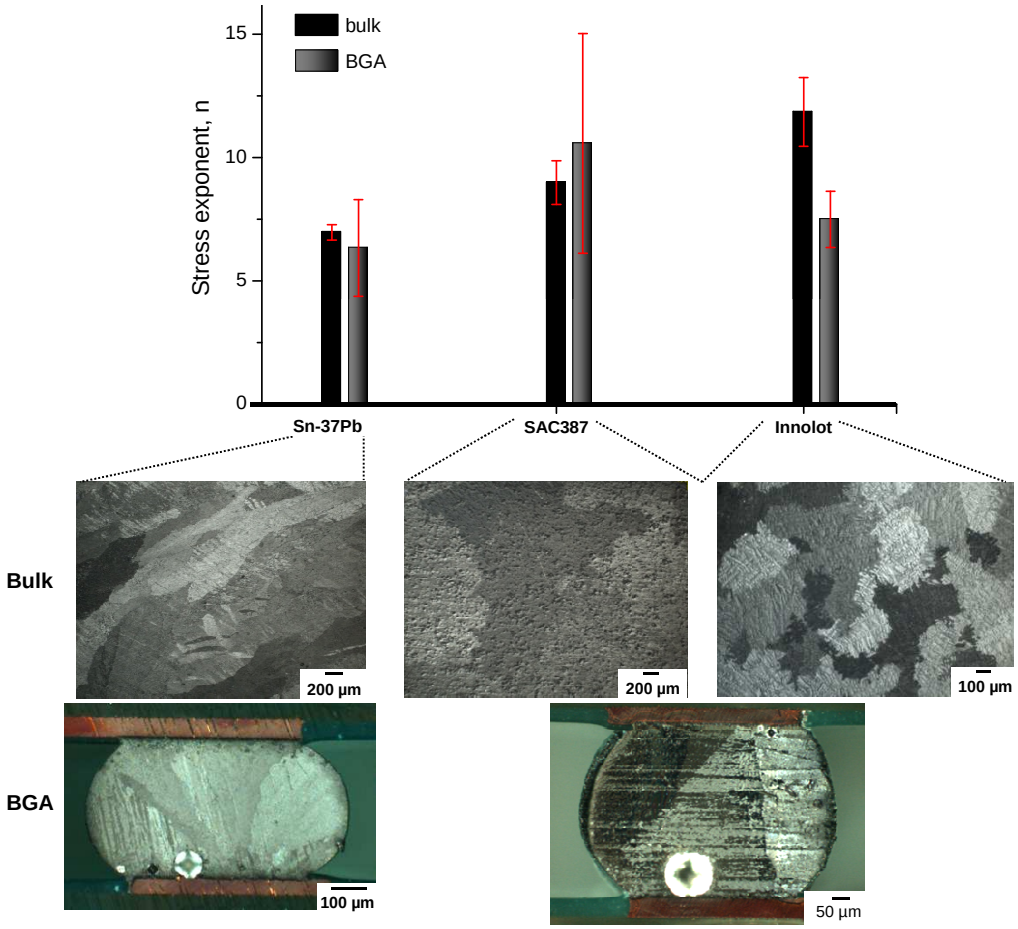


Figure 6.20: Stress exponents at 25°C for bulk and as-reflowed Sn-37Pb, SAC387 and Innolot alloys. Cross-polarized images showing typical grain structure for both manufacturing routes and the three types of alloy.

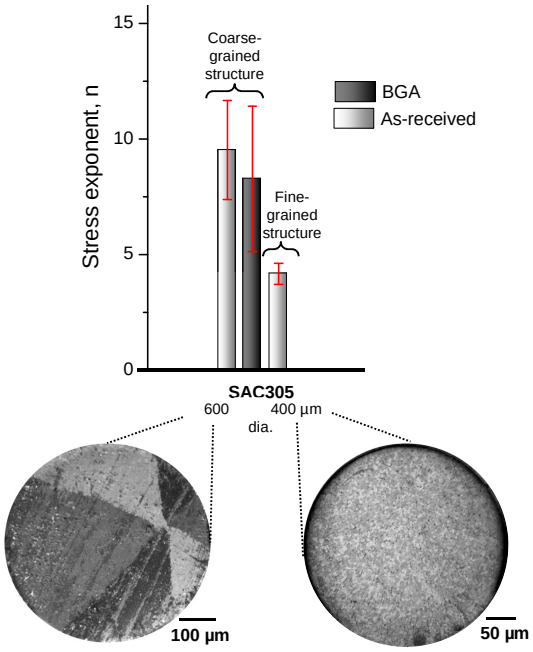


Figure 6.21: Stress exponents at 25°C for coarse-grained as-received 600μm SAC305 balls and SAC305 BGA joint (from 500μm balls) and fine-grained as-received 400μm SAC305 balls.

6.4 Conclusions

Room and elevated temperature nanoindentation creep studies showed a strong temperature dependence of the constitutive properties of SAC-based solders and a new Innolot alloy. The total deformation during creep was the sum of deformations due to any grain-boundary sliding and creep due to dislocation glide at low temperatures or time-dependent diffusion based dislocation climb at higher temperatures. Some cracking around indents suggested that crack growth was largely intergranular or along the phase boundaries (such as debonding of β-Sn/IMC interfaces).

A smaller grain size ($\prec$20μm) that characterised as-supplied SAC305 400μm balls was detrimental to creep resistance, primarily because increasing grain boundary area per unit volume increased the opportunity for grain boundary sliding at lower temperatures. For larger grain sizes ($\succ$50μm) that characterised all other alloys, dislocation creep dominated the total creep strain and overall the alloys were more resistant to creep. The creep resistance decreased in the order Innolot, SAC387, SAC305 to Sn-37Pb.

Although creep indentation produced creep exponents and activation energies

broadly consistent with previous work using bulk and nanoindentation testing, the validity of some of the assumptions made for the interpretation of nanoindentation creep may be questioned. In nanoindentation, the creep rate at constant load eventually slows to zero because the volume of creeping material increases as the indenter penetration increases until the load becomes too small to promote any appreciable creep. The decrease of applied stress during creep was not taken into account in power law constitutive equations [174].

Another questionable hypothesis for nanoindentation creep is the steady-state condition since strain rates in the primary creep region are much higher under the same loading conditions than strain rates in conventional creep testing. Nonetheless, the good agreement between nanoindentation and tensile creep testing on solder alloys suggests that, for high creeping materials such as solders, a reasonable agreement can be obtained since the comparatively high secondary creep rates reduces the effect of any error associated with primary creep.

Further, as shown also in section 5.1, real solder joints can easily comprise only a few grains and are therefore likely to exhibit strong deformation anisotropy. Sn anisotropy cannot be investigated in traditional tensile tests that average over thousands of grain orientations.

Overall, creep constitutive behaviour was obtained from very small volumes of material and the stresses were comparatively high for the specific case of BGAs. Thus the nanoindentation approach, despite its speed and ease of use is almost too fine-scale because of its sensitivity to local microstructure, especially grain size, and it is an open question as whether BGA service life can really be understood in terms of these fine-scale measurements. While measurements on bulk are slow, use large volumes of material and are non-representative of the microstructure, nanoindentation is fast, uses small volumes of material but is sensitive to local microstructure and generates unrealistically high stresses.

Chapter 7

Meso-scale creep testing

The volume of standard bulk specimen for tensile tests ($\sim 4x10^{-6}m^3$) is at least four orders of magnitude larger than that of the solder joints manufactured in this study ($\sim$1–$3x10^{-10}m^3$) and seven orders of magnitude larger than small flip-chip solder joints ($\sim 1x10^{-13}m^3$) [108]. Therefore, it might be expected that solders in flip-chip joints will have different microstructures and behave differently from bulk material. Indeed, creep studies in the previous chapter showed the sensitivity of nanoindentation creep to grain size. Therefore, the question arises as to what is the most appropriate or useful scale for creep testing if the lifetime of real microelectronic packages is of interest, constrained by key considerations of: (i) minimise volume of material to accelerate testing and reduce cost; (ii) use of realistic stresses and temperatures; and (iii) use of realistic microstructures consistent with actual solder joints.

Although microforce meso-scale techniques have enabled testing of solder joints at temperatures up to 130°C, previous studies on SAC solders again focused on the relatively high 10–100MPa stress range, similar to those produced in nanoindentation, with few studies in the stress range of practical interest [206]. The nanoindentation stresses used so far in this study – and similarly to other nanoindentation studies – were also in the 20–500MPa range, and therefore are again comparatively high compared with the stresses experienced by solder joints in service ($\prec$10MPa). This chapter describes attempts and results to develop a new meso-scale test to contrive more representative stresses, while retaining the accuracy, high temperature capability and convenient small specimen sizes of nanoindentation, and to exploit the idea of testing

entire solder joints to characterise solder creep at length scales more relevant for the ever decreasing assembly sizes of electronic packages [136, 138, 140, 143, 206].

7.1 Compression of ceramic BGAs (CBGAs) – Test (2)

An initial geometry for creep testing was conceived based on compression of a small CBGA in a hot cell. The alumina based boards used for the CBGAs were comparatively stiff and stable over the temperatures of interest and the intention was that the solder balls only would deform (creep) under constant load. The geometric arrangement of this approach was shown in section 3.3.3. Figure 7.1 shows the interior of the liquid hot cell prior to testing. The arrangement was also designed to minimise the influence of the pad-ball or ball-metallization tensile or shear properties.

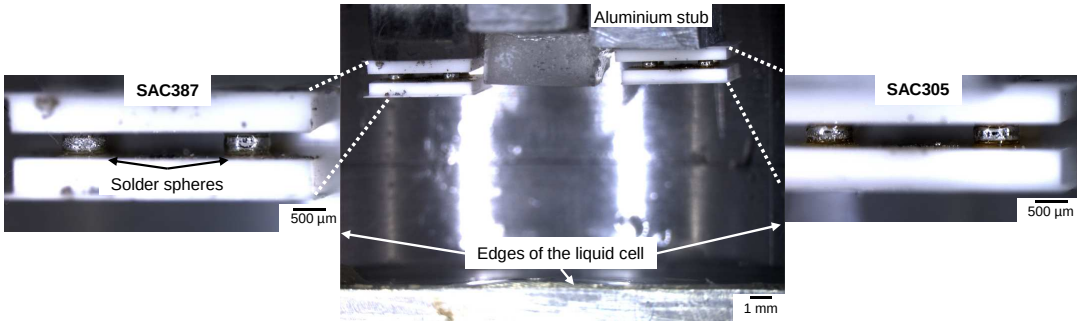


Figure 7.1: Optical image and higher magnification views of SAC387 and SAC305 CBGAs inside the liquid cell. Alignment was carefully checked prior to testing.

Figure 7.2 shows the creep curves at 25°C for various loads, solder alloys and metallization pads. The maximum available load was 500mN. For all creep tests, the overall displacement over a 600s testing time was $\prec$145nm. Although on initial inspection the alloy creep resistance increased progressively from SAC305 to SAC387 to Innolot – in accordance with section 6.2.2 – the data however did not show systematic increases in creep displacement with increasing load in all cases. At higher temperatures, the scatter in creep behaviour increased and consequently confidence in a quantified approach to these results was undermined. Despite many attempts, the principal difficulty was ensuring that the load was applied evenly over all the balls and that compression strain was equal at all places over the assembly – this emerged as a common problem in all the meso-scale arrangements. Maintaining the planarity

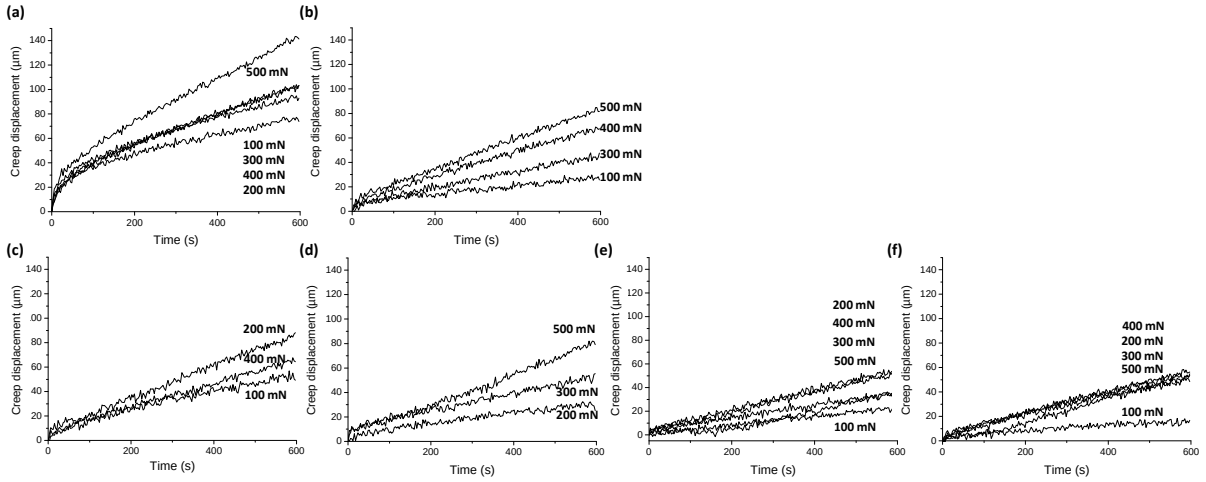


Figure 7.2: Creep curves for CBGA compression tests at 25°C and various maximum loads: (a) SAC305 and (b) SAC387 CBGAs with Cu pad metallization; and (c) SAC305; (d) SAC387; (e) Innolot; and (f) Sn-37Pb CBGAs with Pd-Ag pad metallization.

or 'parallelism' of the indenter base and top and lower boards to avoid 'twisting' was particularly problematical. At room temperature, it might be possible to infer that the Pd-Ag pads conferred some creep resistance over Cu pads, as previously suggested in chapter 4 due to the formation of Ag_3Sn, but any further interpretation was not justified without a stronger systematic response.

7.2 Spherical indentation of as-reflowed solder balls – Test (3)

As a variant to compressing solder joints between stiff boards, the compression testing of individual reflowed balls was also investigated. The NanoTest platform was therefore configured as miniaturized impression creep apparatus for characterizing the creep behaviour of single solder balls as previously described in chapter 3. The technique required only minimal sample preparation and was envisaged to be suitable to probe individual solder balls and to allow multiple creep curves to be generated from a single ball/sphere at more realistic loads than nanoindentation.

7.2.1 Background to spherical indentation

The purpose for spherical indentation was to probe larger surfaces and therefore avoid microstructural effects as well as provide creep data in a smaller stress range than nanoindentation. Spherical indentation has been widely used to investigate the constitutive properties of materials [213, 227, 228]. In particular, it was developed for the determination of the viscosity of glassy materials [229]. However, there are few reports in the literature of use of this technique for investigation of high temperature creep.

Similar to Berkovich tip indentation, the indentation depth of a spherical indenter h is recorded as a function of the elapsed time t during loading so the velocity of the indentation dh/dt is obtained. Figure 7.3 shows the spherical indentation geometry and key geometrical parameters.

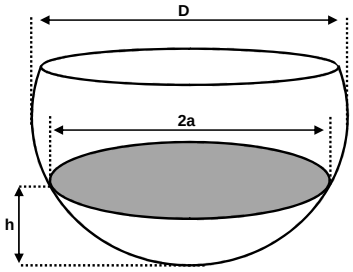


Figure 7.3: Schematic of a spherical indenter of diameter D; a the radius of contact; and h the total depth of penetration (adapted from [229]).

During indentation at force F the pressure under the punch p can be expressed as:

$$p = \frac{F}{\pi a^2} \tag{7.2.1}$$

$$= \frac{F}{\pi(hD - h^2)} \tag{7.2.2}$$

Supposing that $D \gg h$, Equation 7.2.2 becomes:

$$p = \frac{F}{\pi hD} \tag{7.2.3}$$

The strain rate, $d\epsilon/dt$ is the ratio of the impression velocity v=dh/dt to the diameter of

the imprint at the indentation depth [229]:

$$\frac{d\epsilon}{dt} = \frac{v}{2a} \tag{7.2.4}$$

$$= \frac{v}{2\sqrt{hD - h^2}} \sim \frac{v}{2\sqrt{hD}} \tag{7.2.5}$$

In general, contact areas are larger than with a Berkovitch indenter so microstructural sensitivity and stresses are reduced.

7.2.2 Results and discussion

Figure 7.4 shows composite secondary electron micrographs of a typical residual impression after creep testing up to 100°C on a SAC305 BGA solder ball. The radius of the indentation mark was 120μm, the depth was $\sim$20μm and there was no significant pile-up of the solder around the perimeter of the impression.

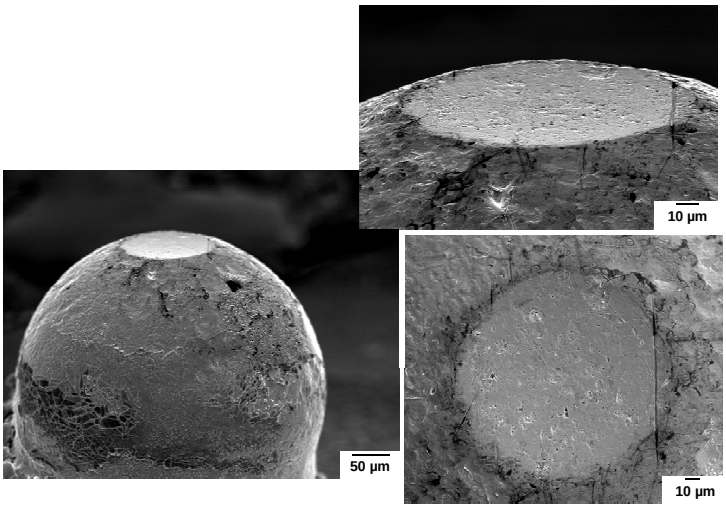


Figure 7.4: Secondary electron images of an as-reflowed 600μm SAC305 BGA solder ball after spherical indentation at 500mN and 100°C.

During testing, the applied load was transmitted to the substrate through the bottom of the solder ball, which contacted the substrate over an area at least twice as large as the residual impression diameter. Therefore, the effect of substrate creep on the measured solder creep behaviour was assumed to be negligible.

Figure 7.5 (a) shows the loading curves for a free-standing as-reflowed SAC305 solder ball at various loads and temperatures, and Figure 7.5 (b) shows the corresponding

creep curves during dwell at maximum load. Unlike arrangements for BGA assembly compression in compression tests, the data showed systematic behaviour as a function of load and temperature. The creep data was converted to strain rate versus stress data as shown in Figure 7.6, and again best-fitted to Equation 3.3.11 from which the stress exponents were obtained. The testing stress range was 2.5–9.5MPa and the average stress exponents were n=9.7 at 25°C and n=3.2 at 100°C, with little discrepancy between tests at different loads. The room temperature stress exponents were similar to nanoindentation for SAC305 BGA joints (n=8.4) and as-received 600μm SAC305 solder balls (n=9.5) in chapter 6. An activation energy was determined at a stress of 4MPa (400mN) using only two temperatures of 25 and 100°C (due to time constraints) and was estimated at 34kJ.mol^{-1}, similar to the low temperature regime activation energies from nanoindentation on SAC387 (53kJ.mol^{-1}) and Innolot (24kJ.mol^{-1}).

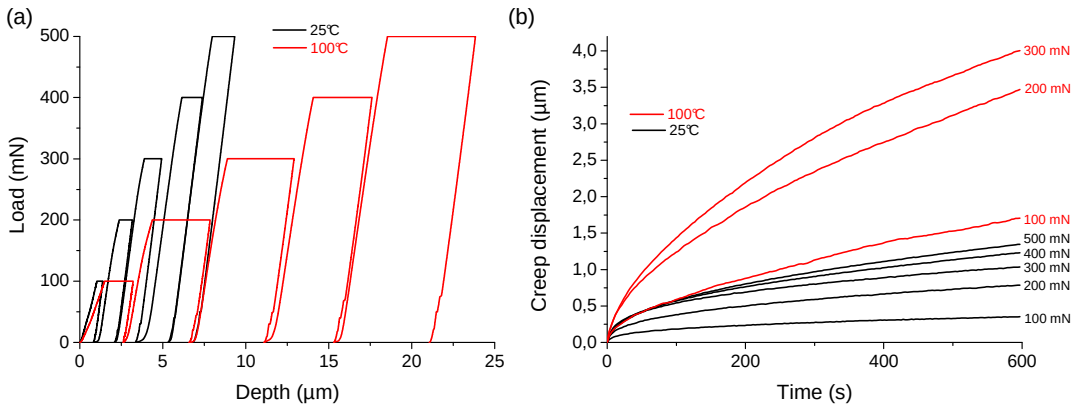


Figure 7.5: (a) Load versus depth for spherical indentation at various loads on an as-reflowed SAC305 solder ball at 25 and 100°C; and (b) corresponding creep curves.

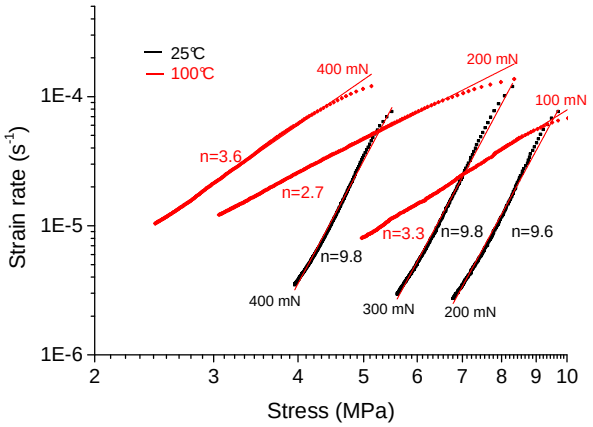


Figure 7.6: Strain rate versus stress for spherical indentation at various loads on an as-reflowed SAC305 ball at 25 and 100°C.

Figures 7.7 (a)–(c) show the spherical impression in an as-reflowed Sn-37Pb solder ball after spherical indentation. There was no cracking around the impression but Figures 7.7 (b) and (c) show a 'pop out' of 'grains' around the ball circumference. Figure 7.7 (d) shows radial cracking of another as-reflowed Sn-37Pb ball, similarly to observations after Berkovich indentations in section 6.2.2. In both Figure 7.7 (c) and (e), 'pop outs' or cracks occurred at the boundary between 'grains' or colonies of eutectic lamellae, as shown by the arrows.

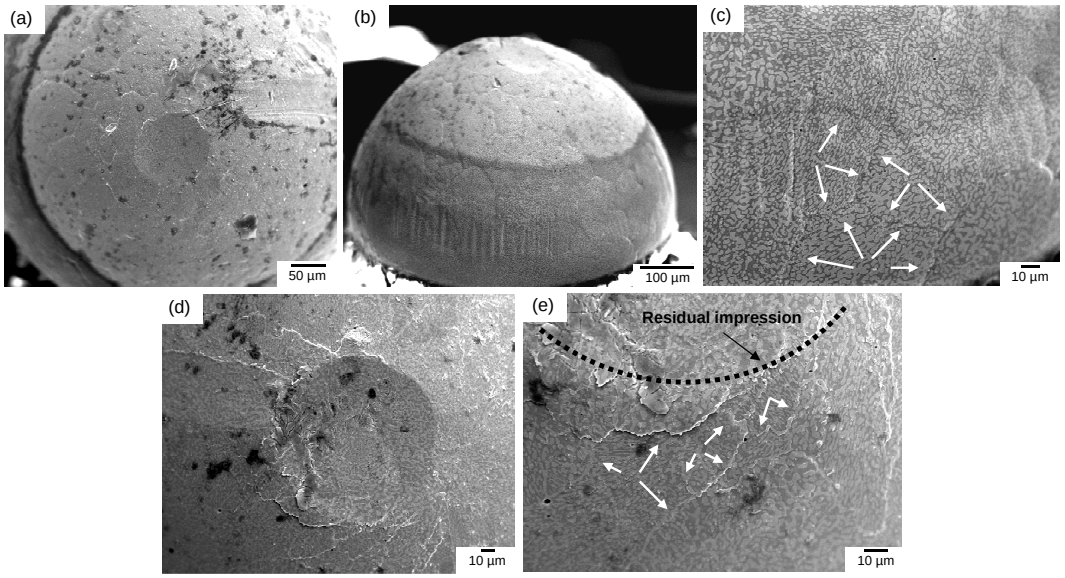


Figure 7.7: Secondary electron images of an as-reflowed Sn-37Pb solder ball after spherical indentation: (a) top of the ball; (b) side view of the ball; (c) higher magnification image of the side view; (d) top view of the impression on another ball; and (e) corresponding higher magnification image.

However, despite the apparently encouraging microstructural information and consistent creep data, Figure 7.8 (b) shows the strain rate versus stress data for the different alloys at 25 and 100°C. Following the previous approach, best-fit stress exponents were again obtained. At 25°C, $n_{Innolot}$=42 $\succ$ n_{SAC305}=31 $\succ$ n_{SAC387}=28 $\succ$ $n_{Sn-37Pb}$=11, while at 100°C, n_{SAC387}=12 $\succ$ $n_{Innolot}$=7 $\succ$ n_{SAC305}=6 $\succ$ $n_{Sn-37Pb}$=3. In particular, the best-fit stress exponents of Innolot and SAC alloys, were considered too high (too creep resistant) to be realistic or helpful. The raw creep data curves in Figure 7.8 (a) provide an explanation for the high stress exponents. The velocities (and therefore the strain rates), were higher than those in Figure 7.5 (b): spherical indenta-

tion at 500mN and 25°C on SAC305 balls gave strain rates of 7x10^{-5} – 6x10^{-5}s^{-1} in Figure 7.8 (a) and of 4x10^{-6} – 7x10^{-5}s^{-1} in Figure 7.5 (b). Although much care was taken to align the centre of the spherical indenter with the centre of the as-reflowed balls along the straight line of the indentation direction, perfect alignment was not easily achieved. Consequently, often when the indenter ball was impressed, it quickly slid off the 'crown' of the solder ball. No satisfactory resolution was developed in the time available. Nonetheless, this approach was encouraging and in particular suggested that the hot oil immersion technique had practical utility, and that the NanoTest platform might be successfully configured for meso-scale testing that provided lower, more realistic stresses, and a larger indentation area to average out local microstructural variations.

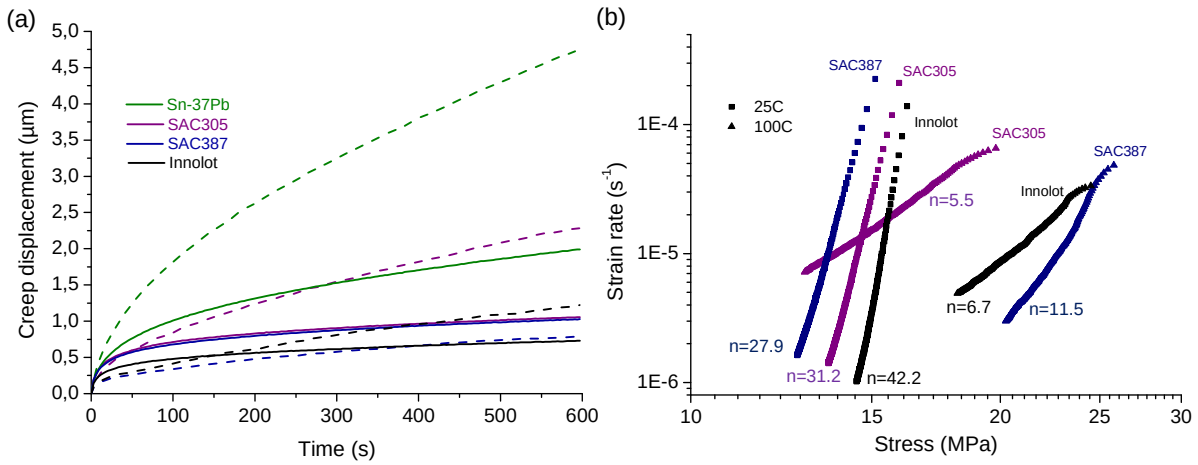


Figure 7.8: (a) Spherical indentation creep curves obtained at 500mN on as-reflowed Sn-37Pb, SAC305, SAC387 and Innolot solder balls at 25°C (*straight lines*) and 100°C (*dashed lines*); and (b) corresponding stress-strain curves for SAC305, SAC387 and Innolot alloys.

7.3 Meso-scale shear testing of CBGAs – Test (4)

7.3.1 Stress-strain behaviour

The shear testing arrangement was aimed at characterising shear behaviour of entire solder joints since this was understood to be the primary mode of failure of real BGAs in service. Figure 7.9 shows a SAC305 CBGA sample prior to shear testing. In an at-

tempt to minimise bending movements and out of the plane force, stiff ceramic BGAs instead of FR-4 BGAs were used and the best alignment possible was pursued so that top and bottom BGA boards were parallel to one another and perpendicular to loading direction on the upper board. The set-up was designed to be equivalent to testing two spherical solder joints with contact pad diameters of 500μm.

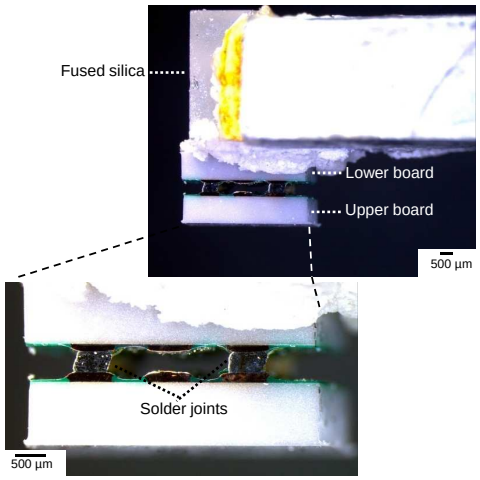


Figure 7.9: Optical image and higher magnification image of a SAC305 CBGA prior to shear testing. A fused silica sample was used for depth calibration at each testing temperature.

Figure 7.10 shows lateral displacement-time behaviour of the SAC305 CBGA when loads from 100 to 500mN were applied for various temperatures. After ~100s, the

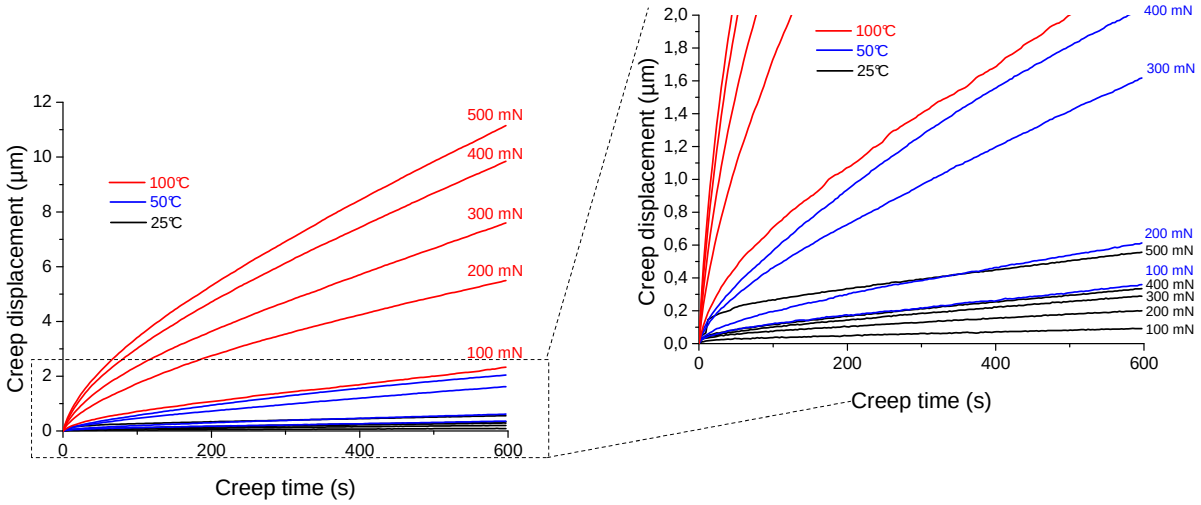


Figure 7.10: Creep displacement versus time for shear testing of a SAC305 CBGA (400μm balls) with Cu pad metallization for various holding loads (100–500mN) and temperatures (25, 50 and 100°C) including zoom in view of the small displacement region.

creep displacement was a linear function of time, suggesting that steady-state was achieved, and an average strain rate for each load and temperature was calculated from linear fitting of the curves as previously described. Figure 7.11 (a) shows the strain rate-stress plot obtained from the creep data in Figure 7.10. The shear stress was assumed to be the applied load divided by the cross-sectional area of the solder joint/contact pad interface for the relevant number of solder joints. The resulting

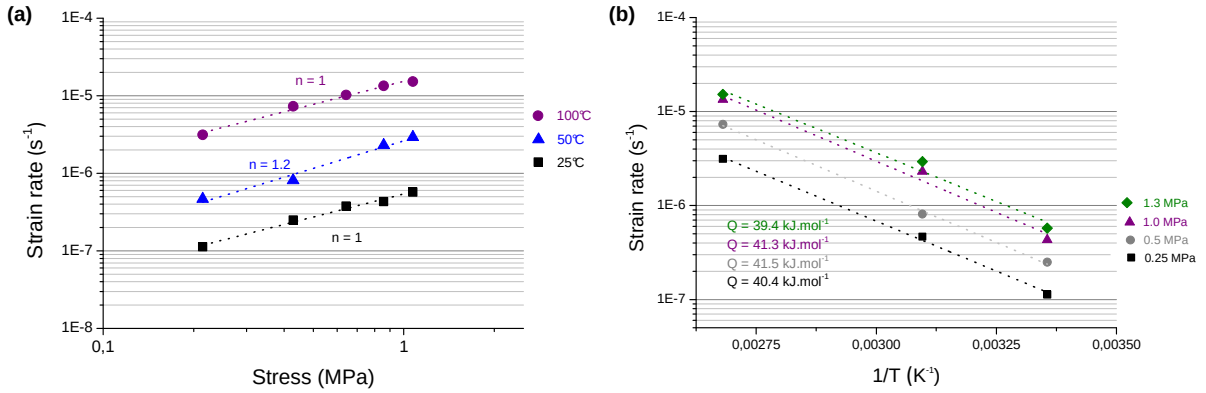


Figure 7.11: (a) Strain rate versus shear stress data for a SAC305 BGA (400μm balls) with Cu pad metallization; and (b) creep activation energy determination for SAC305 BGAs.

strain rate range was 1x10^{-7}– 1.5x10^{-5}s^{-1} and the applied stress range was 0.2–1MPa.

As previously seen, at a particular stress, the strain rate increased with increasing temperature, and because the mounting boards were ceramic, it was assumed that creep was due to the solder joints or the contact pads. The strain rate was approximately a linear function of the applied stress and following the procedures already described, the best-fit creep exponent was estimated as $n\sim1$ for all temperatures. The activation energy for the deformation mechanism was determined from the average of the activation energies determined at the various stresses indicated in Figure 7.11 (b) as 41$\pm$1kJ.mol^{-1}, which corresponded to typical values for grain boundary diffusion [107].

Figures 7.12 (a) and (b) show the shear arrangement of two solder joints (600μm balls). The resulting creep displacement and strain rate-stress behaviours are shown in Figures 7.13 (a) and (b) respectively. Similar to Figure 7.10, the stress exponents were again $n\sim1$ while Figure 7.14 shows the activation energy for deformation mech-

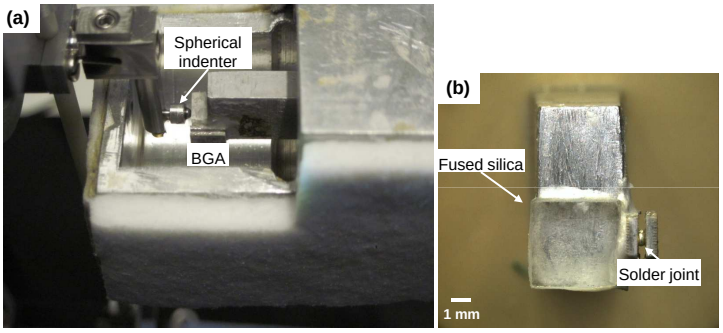


Figure 7.12: Optical images of (a) the liquid cell; and (b) top view of a SAC305 CBGA (600μm balls) with Cu pad metallization.

anism was estimated as 41$\pm$3kJ.mol^{-1}, suggesting that the deformation mechanisms for the 400 and 600μm diameter balls were similar, despite their marked differences in grain size. Previous geometries of testing based on nanoindentation and spherical indentation both showed significant differences to microstructural condition.

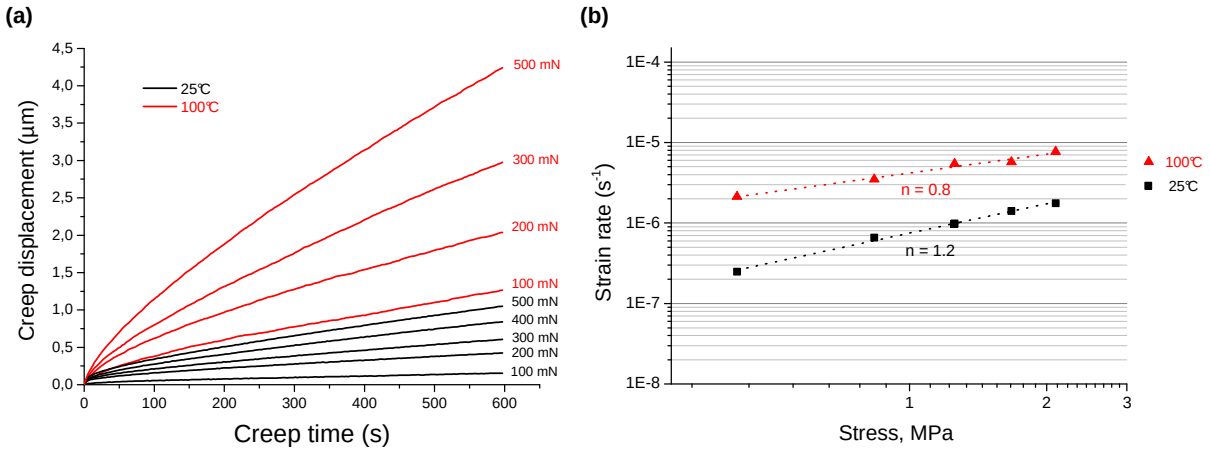


Figure 7.13: (a) Creep displacement versus time for SAC305 BGAs (600μm solder balls) with Cu pad metallization after shear testing at various holding loads (100–500mN) and temperatures (25 and 100°C); and (b) corresponding strain rate versus stress plot.

The stress exponent for all the CBGA shear tests was $n\sim1$, typical of a comparatively low stress region and operation of diffusion based creep mechanisms [230]. In diffusion creep, the application of stress creates an excess of vacancies along the grain boundaries experiencing shear and a depletion of vacancies along the grain boundaries experiencing compression, leading to a stress-directed flow of vacancies.

Diffusion creep can either be in the form of Nabarro-Herring creep or in the form

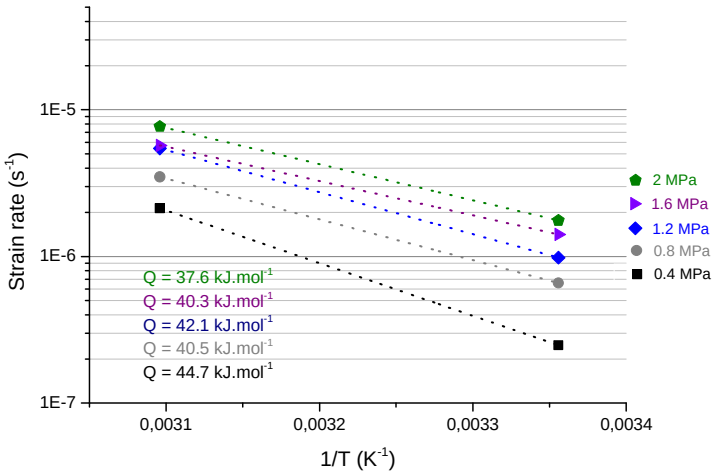


Figure 7.14: Creep activation energy determination for SAC305 BGAs (600μm solder balls).

of Coble creep [231, 232]. In Nabarro-Herring creep, crystals yield to the applied shear stress by changing their shape through self-diffusion involving vacancy flow through the lattice [231]. Coble creep involves vacancy flow along the grain boundaries. Nabarro-Herring creep has a higher activation energy compared to Coble creep and is favoured at higher stresses and temperatures. The two mechanisms may be described by Equation 7.3.1:

$$\frac{d\epsilon}{dt} = \frac{A\sigma^n}{d^p} exp\left(\frac{-Q}{kT}\right) \tag{7.3.1}$$

where A is a constant that depends on the material; d is the grain size of the material; and p is the so called 'inverse grain size exponent'. Generally, it assumed that n=1, p=2 and Q=*Q(self-diffusion)* for Nabarro-Herring creep while n=1, p=3 and Q=*Q(grain boundary diffusion)* for Coble creep [231, 232].

The creep testing of entire CBGA assemblies in shear measured essentially identical activation energies and creep rates for the two types of solder joint despite differences in grain sizes. Optical and scanning electron microscopy based observations of many cross-sections of tested solder joints of the type as shown in Figure 7.15 did not show any clear evidence of deformation in the interior of the balls, which might be evidenced, for example, by an elongation of the grains.

The Harper-Dorn creep mechanism was discovered in single crystal and polycrystalline pure Al at temperatures close to the melting temperature of Al [233]. The

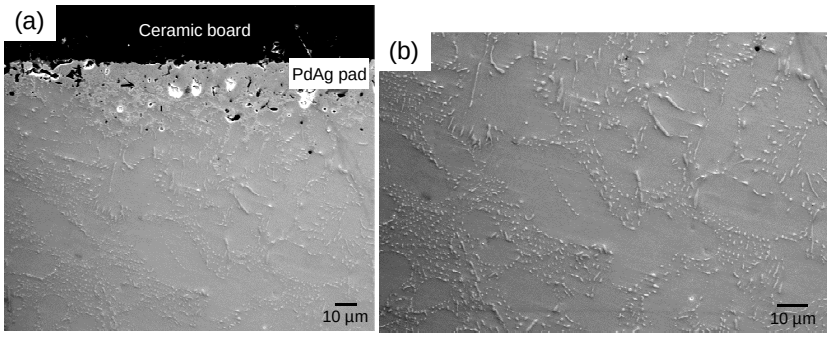


Figure 7.15: Secondary electron images of (a) a SAC305/Pd-Ag pad interface; and (b) interior of the SAC305 solder joint after shear testing at elevated temperature.

Harper-Dorn creep mechanism was proposed to account for measured creep rates that were much higher than predicted by diffusion theory but still gave a stress exponent $n\sim1$ at low stresses. This was later confirmed on Al single crystals tested in compression [234], in tension [235] and on Al, Pb and Sn tested with a double-shear testing apparatus [236]. The Harper-Dorn creep mechanism was proposed to operate with n=1, p=0, Q=*Q(self-diffusion)* in Equation 7.3.1. Harper-Dorn creep and classical dislocation creep mechanisms have similar creep activation energies, so the stress exponent is the only parameter that enables distinguishing between classical dislocation creep ($3\prec n\prec8$) and Harper-Dorn creep (n=1). However, there is often difficulty in establishing the stress exponent for steady-state creep at such low stresses where Harper-Dorn may operate because of the very slow strain rates [230]. The creep activation energy from shear testing of SAC305 was 41kJ.mol^{-1}, similar to the activation energy of 53kJ.mol^{-1} for nanoindentation of SAC387 in the 25-100°C range, where dislocation core diffusion was suggested predominant (see chapter 6). Therefore, Harper-Dorn creep could be suggested as a dominating mechanism during shear testing of CBGAs.

Figures 7.16 (a) and (b) show the cross-section of a fine-grained solder joint after shear testing in a CBGA at 140°C. Grains were not obviously deformed or elongated but rather were displaced with respect to each other, characteristic of grain sliding. Attempts were made to detect any mechanical deformations in the bulk of solder alloys through grid markers made by FIB milling on carefully sectioned balls of different types followed by creep testing. However, as noted previously, little mechanical deformation could be observed. Grain boundary sliding is associated with $n\succ2$, and

Harper-Dorn creep does not accommodate sliding [230]; similar grain boundary sliding was observed in section 5.4. These observations are inconsistent with Harper-Dorn but some grain boundary sliding mechanism may have occurred prior to testing to relieve manufacturing/thermally induced stresses during the 1–5 hours of elevated temperature thermal stabilisation necessary for accurate measurements. In Figure 7.16 (a), the grains show a clear sliding direction along an approximately 45° direction from the solder joint pad. Although sliding occurred principally near the metallization of the pad of the board that was displaced in the test, there was some limited sliding in the 'bulk' of the solder ball, as shown in Figure 7.16 (b), with IMCs frequently pinning displaced grain boundaries. Figure 7.17 shows strain rate-stress results for shear

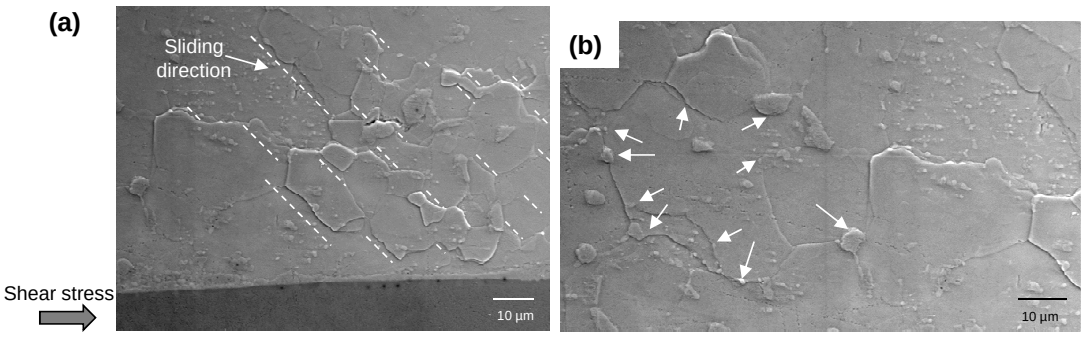


Figure 7.16: Secondary electron images of a SAC305 CBGA (400μm balls) with Cu pad after shear testing at 140°C. The dashed lines show the approximate 45° direction of elongation to the applied shear stress direction; and (b) interior of the solder joint. The arrows point at IMCs pinning grains.

tested SAC305 CBGA with Pd-Ag and Cu pad metallizations. No variation was observed for the two types of pads at 25, 50 and 100°C. As shown in section 4.3, large Ag_3Sn IMCs (up to 170μm) formed in SAC305 solder joints manufactured with Pd-Ag pad metallization and not when Cu pads were used. Therefore, the presence of large Ag_3Sn IMCs had no strong effect on the shear stress-strain behaviour of solder joints and the interior structure of the balls had little effect on creep response.

Both the coarse and fine-grained SAC305 solder balls in the CBGA arrangement showed similar creep behaviour in shear and this might be interpreted as suggesting that in this configuration, creep did not occur homogeneously across the solder joint (which might be reasonably assumed to be affected by the grain size) but instead was

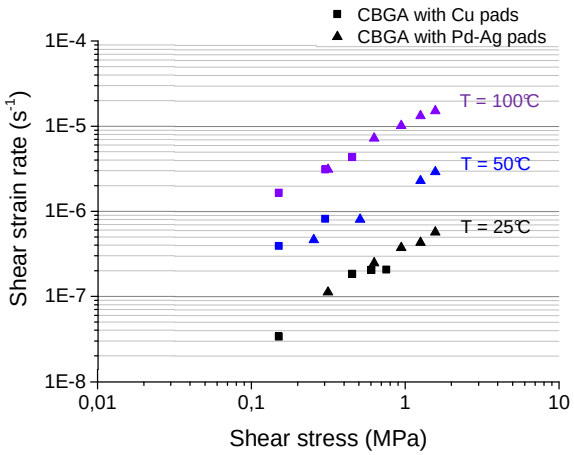


Figure 7.17: Strain rate versus stress behaviour for SAC305 CBGAs with Cu and Pd-Ag pads at 25, 50 and 100°C.

localised at the interface between the solder ball and the metallization pad. Unlike the ball itself, the pad/metallization/ball interface melted during the reflow process and thus can be expected to be essentially the same for the two solder ball diameters after processing regardless of grain size. This being the case, and assuming that this shear test configuration is relevant for the in-service condition, it suggests that the local microstructure around the melted ball/pad/metallization is controlling creep response in shear. In this case, the fine-scale IMCs and associated large grain boundary area shown by the deep etching of interfaces in chapter 4 may provide relatively fast grain boundary diffusion in this local microstructure at the interface. This interpretation may have significant implications for the design of future BGA alloys because it is the chemistry, interactions and resulting phases in the ball surface/pad/metallization region that should be optimised for creep response, not the bulk solder composition of the ball itself which sees little creep.

Figure 7.18 shows shear testing data for SAC387 from 25 to 100°C combined with data from a shear testing study in the intermediate stress range (2–40MPa) of entire SAC387 solder joints (microforce tester) [237]. Shear stresses (τ) and strain rates ($d\gamma/dt$) from both studies were converted into effective stresses (σ) and strain rates

(dϵ/dt) using the Von Mises relationships:

$$\sigma = \sqrt{3}\tau \tag{7.3.2}$$

$$\frac{d\epsilon}{dt} = \frac{1}{\sqrt{3}}\frac{d\gamma}{dt} \tag{7.3.3}$$

Creep parameters suggested an intermediate stress regime, with n(shear testing) = 1 $\prec$ n = 4.96[237], and Q(shear testing) = 40kJ.mol^{-1} $\sim$ Q = 45.2kJ.mol^{-1}[237]. The strain rates from the meso-scale shear testing were $\sim$two orders of magnitude higher than expected for good extrapolation of literature data from [237] at low stresses. It provided confirmation that most of the creeping process was not occuring within the bulk of the solder joint but rather at the solder joint-pad metallization interface. Interface sliding accounted for the higher strain rates than expected in the low stress region.

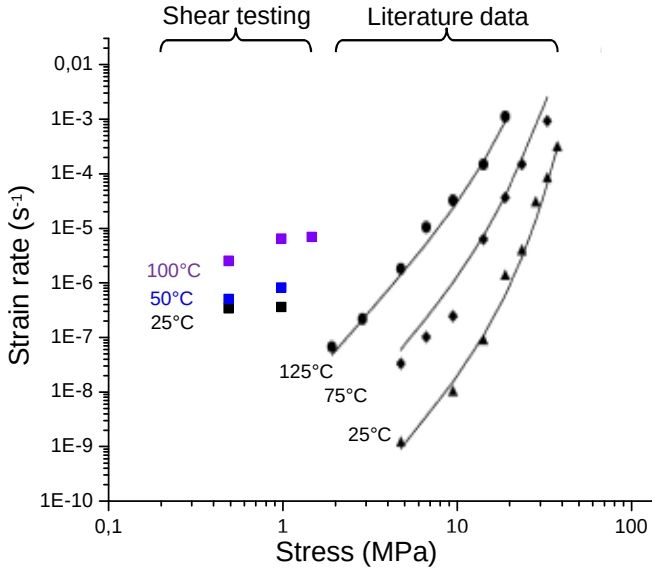


Figure 7.18: Shear testing results for SAC387 and literature data in the intermediate stress range from [237].

Stress exponents were temperature-dependent as shown in section 6.2.2. Figure 7.19 shows the stress exponent temperature-dependence for SAC387 and Sn-37Pb at the low ($\tau \prec$1MPa) and high stress regimes ($\tau \succ$20MPa) obtained from nanoindentation of balls and shear testing of CBGAs respectively, and results from [140] for Sn-37Pb. Only Sn-37Pb from literature was compared with the experimental data as there were little or no studies on the stress-dependency of creep behaviour of SAC solders.

The low stress regime in the literature corresponded to $\tau \prec 1$MPa, the intermediate stress regime to $1 \prec \tau \prec 16$MPa and the high stress regime to $\tau \succ 16$MPa [140]. In general, there was good agreement with literature data for Sn-37Pb in the low stress regime; the high stress regime stress exponents were in between those for the high and intermediate stress regimes from the available literature.

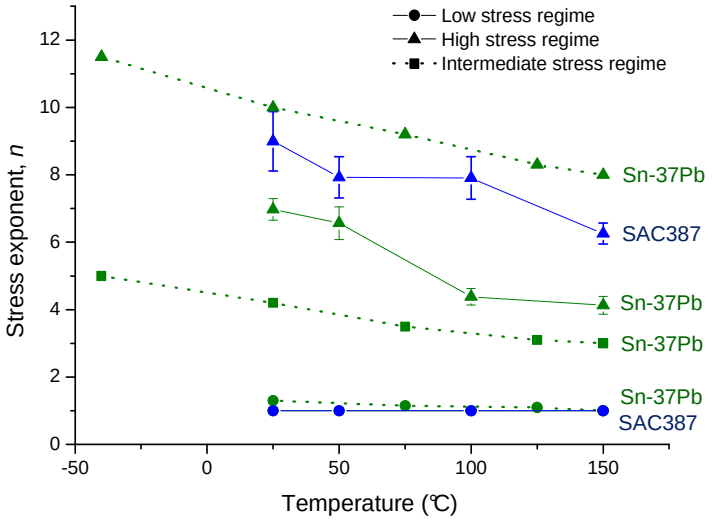


Figure 7.19: Stress exponent as a function of temperature for different stress regimes for SAC387 and Sn-37Pb. Literature data for Sn-37Pb was taken from [140].

7.3.2 Advantages and disadvantages of meso-scale shear testing

The main experimental challenge in meso-scale CBGA shear tests was temperature instability that arose because of the time constant of response between detection by the thermocouple of temperature drops/increases and the subsequent heating response of the heaters. Although depth calibrations were made at all temperatures, and despite thermally insulating the liquid cell and waiting a few hours for thermal equilibrium, many test results had to be discarded as displacement measurements did not stem from mechanical response to stress but from thermal instability. Figure 7.20 shows the effect of temperature on displacement measurements. A temperature drop of $\sim$0.3°C resulted in a measured depth increase of 1.2μm. Some instability may have arisen due to heat losses from the small open area necessary for the insertion of the indenter in the liquid cell. Although progressive steps were taken to improve insulation, the cell will always need power modulation to maintain temperature and with a significant

thermal mass associated with oil itself, undershoot/overshoot and oscillating temperature, even at very small amplitude, will always be a key aspect and restriction of this approach. Furthermore, the capacitor bridge itself is sensitive to temperature change with temperature oscillations resulting in error from induced changes in bridge resistance.

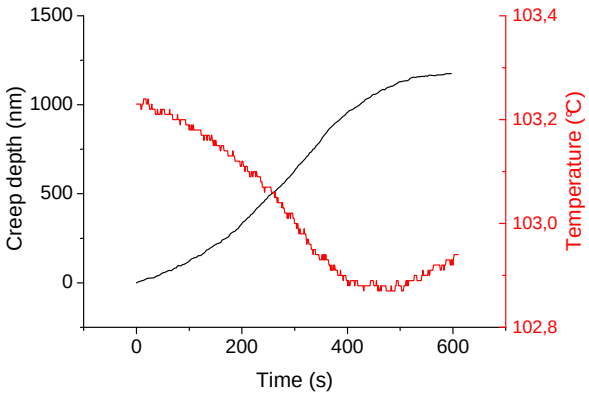


Figure 7.20: The effect of temperature oscillations on displacement measurements during a creep test in shear using a meso-scale hot oil cell approach. The temperature (*red curve*) was measured in the liquid close to the tested solder joint.

Pad spalling and de-cohesion during testing was a frequent problem in shear testing, with many joints failing at the Cu pad/ceramic interface as shown in Figure 7.21. The question arose as to whether the grinding of half of solder joints may be responsi-

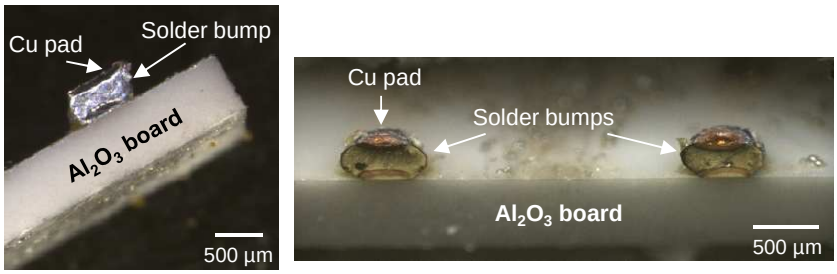


Figure 7.21: Optical images of failures of a SAC305 assembly after testing. Failure occurred at the ceramic/Cu pad interface.

ble for pad/board adhesion issues. The purpose of the grinding step was to (i) enable microscopic observation of the solder joint cross-sections and (ii) apply the largest stress possible to the solder connections. However, as shown comparing with Figure 7.11, testing entire solder joints that had not been ground gave similar stress exponents and creep activation energies as for CBGA assemblies that had been ground. Besides, such spalling and decohesion of the Cu pad/ceramic board did not occur when Pd-Ag

pads were used. Rather, it is suggested that some of the boards with Cu pads supplied by the external supplier (chapter 3) had faulty Cu pad/ceramic adhesion, and care had to be taken to discard this data from any analyses.

7.4 Conclusions

In this chapter, a number of meso-scale testing approaches based on the NanoTest platform have been developed in order to characterise the creep behaviour of CBGAs tested in compression, as-reflowed solder balls tested by spherical indentation and CBGAs tested in shear. The aim was to evaluate possible influence of microstructure and grain size on solder joint creep behaviour. The load capacity of the nanoindentation platform was unable to produce significant displacements and homogeneous strain in compression tests of BGAs. The in-house manufacturing capabilities did not allow the manufacture of smaller BGA joints that would allow useful displacements within the range of available loads. However, in the future, smaller joints ($\prec$100μm) could be manufactured and tested by this method, if avoidance of twisting could be assured.

Spherical indentation of as-reflowed SAC305 balls provided preliminary creep data in agreement with nanoindentation results in chapter 6. Experimental challenges such as indenter/sample misalignment were evidenced and consistent data could not be obtained for other alloys without excessive trial-and-error. The addition of a vertical optical microscope to the set-up in order to check alignment prior to testing could improve this technique.

In BGA shear testing, entire solder joints were tested in a low stress region ($\prec$1MPa) and high temperature conditions (1–100°C), for which there is minimal solder creep data in the literature. The Harper-Dorn creep mechanism was suggested to dominate the constitutive behaviour of SAC387, SAC305 and Sn-37Pb solder based CBGAs during shear testing. Creep was characterised by n=1 and a steady-state strain rate independent of grain size at a given temperature. Thermally activated grain boundary sliding occurred in fine-grained solder joints ($\prec$20μm) during thermal ageing of the joint, possibly due to stress relief during the long thermal stabilisation times necessary

before testing.

Nanoindentation and spherical indentation are quick and powerful techniques: creep stress exponents are obtained from a single indentation curve, whereas in BGA shear (or compression) testing, each data point in the strain rate versus stress plot corresponds to an individual measurement at different loads. A combination of nanoindentation, spherical indentation and BGA shear testing provided creep data in the extended $1x10^{-2}$–500MPa stress range. Low, intermediate and high stress regimes for creep in Sn-Pb and Pb-free alloys were suggested.

As shown in chapter 2, shear stresses caused by thermal cycles upon operation are the main cause of concern for electronics in harsh environments. At high temperatures, low creep resistance is needed as creep helps relieve stresses. However, upon cooling, accumulated plastic creep is locked inside the solder material. Based on the insights here that in shear, it is the interface that plays a dominant role in deformation response, an alternative approach to developing high performance solder joints would be the development of a low creep resistant alloy for the ball and a more creep resistant joint interface. Creep at the interface may be facilitated by the many grain boundaries associated with fine scale IMC formation and growth due to interaction of the pad, metallization and solder ball.

Chapter 8

Conclusions and Future Work

The objectives of this work were to investigate the constitutive behaviour of Pb-free solder alloys under high temperature conditions relevant to harsh environments, and secondly to investigate rapid techniques for creep properties characterisation for later insertion in FEA models, underpinned by microstructural observations. The main findings of this thesis were:

1. SAC solders had a more complex microstructure than Sn-Pb solders, comprising a Sn-rich matrix reinforced with an interlocking structure of Ag_3Sn and Cu_6Sn_5 IMCs. The role of the board pad/solder interface in both shifting the solder composition from the initial composition and being a preferred site for IMC formation was evidenced. Long (up to 300μm) hexagonal faceted Cu_6Sn_5 whiskers in the Cu pad systems tended to be replaced with comparatively thick (up to 10μm) and larger (up to 50μm) Ag_3Sn plates in the Pd-Ag pad systems. The SAC305/Cu pad metallization combination provided the least opportunity for potential damaging large-scale IMCs compared with SAC305/Pd-Ag pad, SAC387/Cu pad or Innolot/Cu pad combinations.

2. EBSD analysis of SAC305 and Innolot revealed a cyclic twinning structure with three related Sn crystallographic orientations. Large (600μm diameter) solder balls had a 'beachball' pattern while smaller (400μm diameter) balls had numerous small grains ($\prec$20μm) and the as-supplied differences in grain size/shape was preserved during reflow. Although thermal ageing at 100°C of SAC305

solder joints showed no significant grain growth, β-Sn decohesion and sliding mechanisms occurred over the time-scale of nanoindentation and meso-scale tests. Such mechanisms can generate locked in stress in the solder joint, which will be localised in regions of excessive angular IMC growth.

3. Nanoindentation provided rapid determination of the creep behaviour of SAC-based and Innolot solder alloys in the 25–150°C temperature range. Large indents were used so that the microstructure sensitivity of nanoindentation was minimal and the overall behaviour of the alloys was characterised. The total deformation during creep was the sum of deformations due to any grain boundary sliding and creep due to dislocation glide and dislocation climb in the 25–50°C and 100–150°C temperature regimes respectively. The creep resistance decreased in the order Innolot, SAC387, SAC305 to Sn-37Pb. Therefore, Innolot can be considered an alloy of choice for high temperature and space saving requirements. However, the large IMCs in both Innolot and SAC387 that can grow at the pad metallization make these alloys less reliable in the case of fatigue loading. Although creep data were in the range of previously reported results, there is much data scattering in the literature, which rendered comparison difficult. The high microstructure sensitivity and high localised stresses of nanoindentation as well as the assumptions of self-similarity of the stress and strain fields beneath the indenter and neglect of primary creep in data analysis make it still unclear whether the technique can be deemed reliable to characterise constitutive properties of real solder joints.

4. The NanoTest platform has been developed in order to characterise the creep behaviour of CBGAs tested in compression, as-reflowed solder balls tested by spherical indentation and CBGAs tested in shear. The load capacity of the nanoindentation platform was unable to produce significant displacements and homogeneous strain in compression tests of BGAs. Spherical indentation of as-reflowed SAC305 balls provided preliminary creep data in agreement with nanoindentation results but experimental challenges such as indenter/sample misalignment were evidenced. The combination of CBGA shear testing and nanoindentation showed that diffusion mechanisms dominated at stresses $\prec$1MPa while

grain boundary sliding and dislocation climb dominated at stresses $\succ$20MPa in Sn-Pb and Pb-free alloys.

In BGA shear testing, creep was characterised by n=1 and a steady-state strain rate independent of grain size at a given temperature. The Harper-Dorn creep mechanism can be suggested to dominate the constitutive behaviour of SAC387, SAC305 and Sn-37Pb solder based CBGAs during shear testing. Such a linear stress-strain relationship could also stem from sliding at the interface, with creep being localised at the interface between the solder ball and the metallization pad. Both the coarse and fine-grained SAC305 solder balls in the CBGA arrangement showed similar creep behaviour in shear. Unlike the ball itself, the pad/metallization/ball interface melted during the reflow process and thus can be expected to be essentially the same for the two solder ball diameters after processing regardless of grain size. It suggests that the local microstructure around the melted ball/pad/metallization is controlling creep response in shear. Therefore, the relevance of developing highly creep resistance alloys for harsh environments was questioned. Rather, by combining highly creep resistant bonds and non creep resistant solder joints, failure at the pad/joint interface commonly observed during thermal cycling would be minimised as plastic creep would be less prone to be locked at the bond interface.

Suggestion for future work includes:

1. To enhance the meso-scale testing platform so that temperatures $\succ$100°C and loads $\succ$500mN can be studied, in particular for compression and shear tests of CBGAs. A vertical optical microscope to the set-up could be added for more consistent spherical indentation measurements.

2. To study the role of Sn anisotropy on the behaviour of shear tested joints by carrying out shear tests at loads $\succ$500mN on coarse-grained solder joints.

3. To investigate the use of a transient creep law, rather than the steady-state equation for nanoindentation creep analysis.

4. To model nanoindentation creep so that microstructural phenomena such as hardening or sliding are taken into account and then relate the observations to nanoindentation results.

5. To build a numerical model of an electronic assembly with the solder alloy creep parameters determined by high temperature nanoindentation and compare the modelling results with ATC of the same assembly.

6. To develop creep resistant pad/solder joint interfaces.

References

[1] S. Ganesan and M.G. Pecht. *Lead-free electronics*. John Wiley & Sons, 2006.

[2] DIRECTIVE 2002/95/EC OF THE EUROPEAN PARLIAMENT AND OF THE COUNCIL of 27 January 2003 on the restriction of the use of certain hazardous substances in electrical and electronic equipment, OJ L 37, 13.2.2003, p.19-23.

[3] DIRECTIVE 2002/96/EC OF THE EUROPEAN PARLIAMENT AND OF THE COUNCIL of 27 January 2003 on waste electrical and electronic equipment, OJ L 37, 13.2.2003, p.24-39.

[4] JEDEC Press Release. *JEDEC announces lead-free definition*. 2001.

[5] National Electronics Manufacturing Initiative (NEMI). *NEMI's Lead-free Assembly Project Reports Latest Results at APEX 2002*. 2002.

[6] Espace Hamelin Decision Etudes Conseil. *World Electronic Industries 2008-2013, Executive summary*. 2009.

[7] Access Science from McGraw-Hill. Electronic Packaging, 2012. URL `http://www.accessscience.com/`. Accessed 26/10/2012.

[8] J.W. Evans. *A guide to lead-free solders*. Springer, 2007.

[9] U.S. Air Force Avionics Integrity Program (AVIP). *Thermal management and packaging considerations*. 1989.

[10] D. R. Frear, J.W. Jang, J.K. Lin, and C. Zhang. *JOM*, 53(6):28–33, 2001.

[11] J.H. Lau. *Ball Grid Array Technology*. McGraw-Hill, Inc., 1995.

[12] P. G. Harris and M.A. Whitmore. *Alternative solders for electronic assemblies, Final report*. Department of Trade and Industry, Project number IED2/1/3094, 1993.

[13] National Centre for Manufacturing Sciences. *NCMS Lead-free Solder Project Final Report, NCMS Report 0401RE96*. 1997.

[14] Japan Electronic Industry Development Association. *JEIDA Report on research and development on lead-free soldering*. 2000.

[15] M. R. Harrison and J. H. Vincent. *Proc. 12th Microelectron. Packag. Conf.* IMAPS Europe, 2003.

[16] F.W. Gayle, G. Becka, J. Badgett, G. Whitten, T.Y. Pan, A. Grusd, B. Bauer, R. Lathrop, J. Slattery, I. Anderson, J. Foley, A. Gickler, D. Napp, J. Mather, and C. Olson. *JOM*, 53:17–21, 2001.

[17] iNEMI. *iNEMI: Lead-Free Assembly Project, Final report*. ACI Technologies Inc., 2003.

[18] Japan Institute of Electronics Packaging. *Low Temperature Lead-Free soldering report*. ACI Technologies Inc., 2002.

[19] *Lead Free Electronics Manhattan Project Phase 2 report*. ACI Technologies Inc., 2010.

[20] J.H. Vincent and G. Humpston. *GEC J. Res.*, 11:76–89, 1994.

[21] H.K. Kim, H.K. Liou, and K.N. Tu. *J. Mater. Res.*, 10(3):497–504, 1995.

[22] S. Brown. *Development of a fatigue resistant alloy for high performance automotive applications, Internal report*. Cookson Electronics, 2009.

[23] S.K. Seo, S.K. Kang, D.Y. Shih, and H.M. Lee. *J. Electron. Mater.*, 38(2):257–265, 2009.

[24] H.J. Albrecht, A. Juritza, and K. Muller. *Proc. 5th Elec. Pack. Tech. Conf.*, pages 726–731, 2007.

[25] JEIDA. *Challenges and Efforts Toward Commercialization of Lead-free Solder-Road Map 2000 for Commercialization of Lead-free Solder, ver. 1.3*. July 2000.

[26] J. Bath, C. Handweker, and E. Bradley. *Circ. Assemb.*, 11:30–40, 2000.

[27] J.-P. Clech. *Lead-free soldering*. J.S. Bath, 2007.

[28] IPC-Association Connecting Electronic Industries. *IPC-7095 Design and Assembly Process Implementation for BGAs*. August 2000.

[29] H. McCormick, P. Snugovsky, C. Hamilton, Z. Bagheri, and S. Bagheri. *Proc. SMTA Int.*, 2007.

[30] M. Tanaka, T. Sasaki, T. Kobayashi, and K. Tatsumi. *IEEE Proc. 56th ECTC conf.*, pages 78–84, 2006.

[31] Soldertec. *European Lead-free roadmap, Version 1*. February 2002.

[32] K.N. Subramanian and J.G. Lee. *Mater. Sci. Engin. A.*, 421(1-2):46–56, 2006.

[33] I.E. Anderson and J.L. Harringa. *J. Electron. Mater.*, 33(12):1485–1496, 2004.

[34] K.N. Subramanian. *Lead-free solders. Materials reliability for electronics*. Wiley, 2012.

[35] W.J. Plumbridge. *J. Mater. Sci.*, 31:2501–2514, 1996.

[36] K.S. Kim, S.H. Huh, and K. Suganuma. *Microelectron. Reliab.*, 43:259–267, 2003.

[37] Y.W. Wang, Y.W. Lin, C.T. Tu, and C.R. Kao. *J. Alloy. Compd.*, 478:121–127, 2009.

[38] W.M. Xiao, Y.W. Shi, G.C. Xu, R. Ren, F. Guo, Z.D. Xia, and Y.P. Lei. *J. Alloy. Compd.*, 472:198–202, 2009.

[39] H.X. Xie, N. Chawla, and Y.L. Shen. *Microelectron. Reliab.*, 51(6):1142–1147, 2011.

[40] M. Ghosh, M.K. Gunjan, S.K. Das, A. Kar, R.N. Ghosh, and A.K. Ray. *Mat. Science Technol.*, 26:610–614, 2010.

[41] T. Sawamura, H. Komiya, T. Inazawa, and F. Nakagawa. *Pb-free soldering alloy*. US Patent No 6,692,691 B2, February 2004.

[42] N. Nogita, J. Read, T. Nishimura, K. Sweatman, S. Suenaga, and A.K. Dahle. *Mater. T.*, 46(11):2419–2425, 2005.

[43] T. Ventura, C.M. Gourlay, K. Nogita, T. Nishimura, and A.K. Dahle. *J. Electron. Mater.*, 37(1):32, 2008.

[44] C.M.L. Wu, D.Q. Yu, C.M.T. Law, and L. Wang. *Mater. Sci. Eng. R.*, 44(1):1–44, 2008.

[45] M.A. Dudek, R.S. Sidhu, N. Chawla, and M. Renavikar. *J. Electron. Mater.*, 35 (12):2088–2097, 2006.

[46] Z. Xia, Z. Chen, and Y. Shi. *J. Electron. Mater.*, 31(6):564–567, 2002.

[47] H. Hao, J. Tian, and Y.W. Shi. *J. Electron. Mater.*, 36(7):766–774, 2007.

[48] T.H. Chuang and S.F. Yen. *J. Electron. Mater.*, 35(8):1621–1627, 2006.

[49] C. Andersson, C.D. Zou, and B. Yang. *Proc. 2nd Electron. Syst. Integration Technol. conf.*, pages 915–922, 2008.

[50] W.B. Guan, S.C. Verma, and Y.L. Gao. *Proc. Electron. Syst. Integration Technol. conf.*, pages 7–12, 2006.

[51] X.L. Zhong and M. Gupta. *Adv. Eng. Mater.*, 7(11):1049–1054, 2005.

[52] K. Zeng and K.N. Tu. *Mater. Sci. Engin. R*, 38:55–105, 2002.

[53] B.D. Dunn (European Space Agency). *Situation regarding the use of tin-lead (Sn-Pb) finishes for solderable terminations and the continued use of Sn-Pb solder alloys for the European space industry*. ESA Memo, March 2010.

[54] National Institute of Standards and Technology (NIST). URL `http://www.metallurgy.nist.gov/phase/solder/solder.html`. Accessed 06/2010.

[55] H. Ma, J. C. Suhling, P. Lall, and M. J. Bozack. *IEEE Proc. 56th ECTC conf.*, pages 849–864, 2006.

[56] L.P Lehman, S.N. Athavale, T.Z. Fullem, A.C. Giamis, R.K. Kinyanjui, M. Lowenstein, K. Mather, R. Patel, D. Rae, J. Wang, Y. Xing, L. Zavalij, P. Borgesen, and E.J. Cotts. *J. Electron. Mater.*, 33(12):1429–1439, 2004.

[57] D. Turnbull. *J. Appl. Phys.*, 21(10):1022–1028, 1950.

[58] J.K. Shang, Q.L. Zeng, L. Zhang, and Q.S. Zhu. *J. Mater. Sci.: Mater. Electron.*, 18: 211–227, 2007.

[59] J. Glazer. *Int. Mater. Rev.*, 40:65–90, 1995.

[60] M. Reid, J. Punch, M. Collins, and C. Ryan. *Solder. Surf. Mount Technol.*, 20:3–8, 2008.

[61] D.W. Henderson, T. Gosselin, and A. Sarkhel. *J. Mater. Res.*, 17(11):2775–2778, 2002.

[62] H. Kim, M. Zhang, C.M. Kumar, D. Suh, P. Liu, D. Kim, M. Xie, and Z. Wang. *Proc. 57th ECTC conf.*, pages 962–967, 2007.

[63] F. Vnuk. *J. Cryst. Growth*, 48:103–104, 1980.

[64] N. Blake and R. W. Smith. *J. Mater. Sci. Lett.*, 5:486–488, 1986.

[65] W.J. Plumbridge. *J. Mater. Sci: Mater Electron*, 18:307–318, 2007.

[66] W.J. Plumbridge. *J. Electron Mater*, 37:218–223, 2008.

[67] F. Vnuk, A. De Monte, and R. W. Smith. *J. Appl. Phys.*, 55:4171–4176, 1984.

[68] A.A. Matvienko and A.A. Sidelnikov. *J. Alloy Compd.*, 252:172–178, 1997.

[69] R.R. Rogers and J. F. Fydell. *J. Electrochem. Soc.*, 100:383–387, 1953.

[70] Y.J. Joo and T. Takemoto. *Mater. Lett.*, 56:793–796, 2002.

[71] S.C. Britton. *Trans. Inst. Metal Finishing*, 52:95–102, 1974.

[72] J. A. Brusse, G. Ewell, and J. P. Siplon. *Proc. 22nd Capacitor and Resistor Technology Symposium*, pages 67–80, March 2002.

[73] Y. Zhang, G. Breck, F. Humiec, K. Murski, and J.A. Abys. *Proc. SMI'96*, September 1996.

[74] R. Schetty. *IPC Works conf.*, 2000.

[75] N. Barry, I.P. Jones, T. Hirst, I.M. Fox, and J. Robins. *Solder. Surf. Mount Technol.*, 19:29–38, 2007.

[76] Y.T. Lin, C.T. Peng, and K.N. Chiang. *ASME Trans. J. Electron. Packag.*, 124:1–6, 2002.

[77] J.H. Lau. *IEEE Trans. Electron. Packag. Manufact.*, 25:42–50, 2002.

[78] M. Osterman and A. Dasgupta. *J. Mater. Sci.*, 18:229–236, 2007.

[79] National Institute of Standards and Technology (NIST). NIST Pb-free database, 2012. URL `http://www.boulder.nist.gov/div853/lead_free/solders.html`. Accessed 06/2010.

[80] National Center for Manufacturing Sciences (NCMS). *Room Temperature Tensile Properties of Lead-Free Solder Alloys, Technical Reports for the Lead Free Solder Project: Properties Reports*. 1998.

[81] J. Madeni, S. Liu, and T. Siewert. *ASM-Int. Conf. on Casting of Lead-Free Solder Specimens with Various Solidification Rates*. 2001.

[82] J. Sigelko and K.N. Subramanian. *Adv. Mat. & Proc.*, pages 47–48, 2000.

[83] C. Hernandez, P. Vianco, and J. Rejent. *Effect of interface microstructure on the Mechanical properties of Pb-free hybrid microcircuit solder joints*. IPC/SMTA electronics assembly expo, 1998.

[84] J.W. Morris, D. Tributa, T.S.E. Summers, and D. Grivas. *The Role of Microstructure in Thermal Fatigue of Pb-Sn Solder Joints*. Springer, 1991.

[85] D.W. Henderson, J.J. Woods, T.A. Gosselin, J. Bartelo, D.E. King, T.M. Korhonen, M.A. Kohronen, L.P. Lehman, E.J. Cotts, S.K. Kang, P. Lauro, D.-Y. Shih, C. Goldmith, and K.J. Puttlitz. *J. Mater. Res.*, 19(6):1608–1612, 2004.

[86] M.A. Matin, W.P. Vellinga, and M.G.D. Geers. *Mater. Sci. Engin. A.*, 445-446:73–85, 2007.

[87] Q.L. Zeng, Z.G.Wang, A.P. Xian, and J.K. Shang. *J. Electron. Mater.*, 34:62–67, 2005.

[88] C. Kanchanomai, Y. Miyashita, Y. Mutoh, and S.L. Mannan. *Mater. Sci. Eng.*, 345: 90–98, 2003.

[89] R. Schueller, N. Blattau, J. Arnold, and C. Hillman. *SMTA Journal*, 23:18–26, 2010.

[90] S. Terashima, T. Kohno, A. Mizusawa, K. Ara, O. Okada, T. Wakabayashi, M. Tanaka, and K. Tatsumi. *J. Electron. Mater.*, 33(1):33–38, 2009.

[91] L. Xu and J.H.L. Pang. *Proc. IEEE 56th ECTC Conf.*, pages 863–867, 2006.

[92] R. Darveaux, C. Reichman, and N. Islam. *Proc. 56th ECTC on Interface failure in lead free solder joints*, 17:906–917, 2006.

[93] T.K Lee, K.C Liu, and T.R. Bieler. *J. Electron. Mater.*, 12:2685–2693, 2009.

[94] T.T. Mattila, V. Vuorinen, and J.K. Kivilahti. *J. Electron. Mater.*, 33:3214–3223, 2004.

[95] A. Zribi, A. Clark, and L. Zavalij. *J. Electron. Mater.*, 30:1157–1164, 2001.

[96] S. Wiese, M. Roellig, M. Mueller, S. Bennemann, M. Petzold, and K.J. Wolter. *Proc. 57th ECTC conf.*, 8:548–557, 2007.

[97] K. C. Norris and A. H. Landzberg. *IBM J. Res.*, 13:266–271, 1969.

[98] R. Dudek, W. Faust, S. Wiese, M. Rollig, and B. Michel. *IEEE 9th Electron. Packag. Technol. Conf.*, 13, 2007.

[99] L.F. Coffin and N.Y. Schenectady. *ASME Trans.*, 76:931–950, 1954.

[100] S.S. Manson. *Thermal Stress and Low Cycle Fatigue*, volume 76. Mc Graw-Hill, 1966.

[101] N. Pan, G. A. Henshall, F. Billaut, S. Dai, M. J. Strum, R. Lewis, E. Benedetto, and J. Rayner. *Proc. SMTA Int. Conf.*, 2005.

[102] J.-P. Clech. *Proc. IPC/SMEMA Council APEX*, 2004.

[103] NASA. *NASA Technology Evaluation for Environmental Risk Mitigation (TEERM) Principal Center Joint test report, JCAA/JG-PP Lead-free solder project*. 2009.

[104] S. Terashima, Y. Kariya, T. Hosoi, and M. Tanaka. *J. Electron. Mater.*, 32:1527–1533, 2003.

[105] A. Schubert, R. Dudek, E. Auerswald, A. Gollhardt, B. Michel, and H. Reichl. *IEEE Proc. 53rd ECTC conf.*, pages 603–610, 2003.

[106] J. Cadek. *Creep in Metallic Materials*. Elsevier, 1988.

[107] H. Ma and J.C Suhling. *J. Mater. Sci.*, 44:1141–1158, 2009.

[108] S. Wiese, A. Schubert, H. Walter, R. Dudek, F. Feustel, E. Meusel, and B. Michel. *Proc. 51st ECTC conf.*, pages 890–902, 2001.

[109] M. Kerr and N. Chawla. *Acta Mater.*, 52:4527–4535, 2004.

[110] A. Grusd. *Proc. Surf. Mount Int. Conf.*, pages 648–661, 1998.

[111] M. McLean. *Acta Metallurgica*, 33(4):545–556, 1985.

[112] S. Choi, T.R. Bieler, J.P. Lucas, and K.N. Subramanian. *J. Electron. Mater.*, 28: 1209–1215, 1999.

[113] I. Snugovsky, D.D. Perovic, and J.W. Rutter. *Powder Metall.*, 48:193–198, 2005.

[114] F. Guo, S. Choi, J.P. Lucas, and K.N. Subramanian. *Solder. Surf. Mount Technol.*, 12:7–18, 2005.

[115] S.L. Allen, M.R. Notis, R.R. Chromik, and R.P. Vinci. *J. Mater. Res.*, 19:1417–1424, 2004.

[116] I. Dutta. *J. Electron. Mater.*, 32:201–207, 2003.

[117] A.R. Fix, W. Nuchter, and J. Wilde. *Solder. Surf. Mt. Tech.*, 20:13–21, 2008.

[118] P. Kumar, O. Cornejo, I. Dutta, G. Subbarayan, and V. Gupta. *Proc. 10th EPTC conf.*, pages 903–909, 2008.

[119] R.A. Stevens and P.E.J. Flewitt. *Mater. Sci. and Eng.*, 37(3):237 – 247, 1979.

[120] H. Burt, J.P. Dennison, and B. Wilshire. *Met. Sci.*, 13(5):295 –300, 1979.

[121] M.D. Mathew. *Metal. and Mater. Trans.*, 36A(1):99–105, 2005.

[122] X. Chen, G. Chen, and M. Sakane. *Thermal and Thermomechanical Phenomena in Electronic Systems, 2004. ITHERM '04.*, 2:447–452, 2004.

[123] Y. Tsukada, H. Nishimura, H. Yamamoto, and M. Sakane. *J. Electron. Packag.*, 127:407–415, 2005.

[124] H. Rhee, K. N. Subramanian, A. Lee, and J. G. Lee. *Sold. Surf. Mount Technol.*, 15: 21–26, 2003.

[125] C.Y. Liu, C. Chen, A.K. Mal, and K.N. Tu. *J. Appl. Phys.*, 85(7):3882–3887, 1999.

[126] A.A. Obaid, J.G. Sloan, M.A. Lamontia, A. Paesano, S. Khan, and J.W. Gillepsie. *J. Electron. Pack.*, 127:430–440, 2005.

[127] R. Darveaux and K. Banerji. *IEEE Trans. CHMT*, 15(6):1013–1024, 1992.

[128] S. Jadhav, T. Bieler, K. Subramanian, and J. Lucas. *J. Electron. Mater.*, 30:1197–1205, 2001.

[129] S.N.G. Chu and J.C.M Li. *J. Mater. Sci.*, 12:2200–2208, 1977.

[130] J. Stephens and D. Frear. *Metall. Mater. Trans. A*, 30:1301–1313, 1999.

[131] M.D. Mathew, H. Yang, S. Movva, and K. L Murty. *Metall. Mater. Trans. A.*, 36: 99, 2005.

[132] A.K. Mukherjee, J. E. Bird, and J.E. Dorn. *Trans. Am. Soc. Metal.*, 62:155, 1969.

[133] K.E. Amin, A.K. Mukherjee, and J.E. Dorn. *J. Mech. Phys. Solids*, 18:413–426, 1970.

[134] R. Darveaux. *IEEE Trans. Comp. Hybrids Manufact. Technol.*, 15(6):1013–1024, 1992.

[135] Z. Mei and J. Morris. *J. Electron. Mater.*, 21:599–607, 1992.

[136] S. Wiese. *Microelectron. Reliab.*, 48(6):843–850, 2008.

[137] J.-P. Clech. *Proc. SMTA Int. Conf.*, 2004.

[138] Q. Zhang, A. Dasgupta, and P. Haswell. Ieee proc. 53^{rd} ectc conf. pages 1862–1868, 2003.

[139] M. Rist, W. Plumbridge, and S. Coope. *J. Electron. Mater.*, 35:1050–1058, 2006.

[140] X. Q. Shi, Z. P. Wang, Q.J. Yang, and H.L.J. Pang. *J. Engin. Mater. Technol.*, 125: 81–88, 2003.

[141] Q. Xiao and W.D. Armstrong. *J. Electron. Mater.*, 34:196–211, 2005.

[142] J. Lau, W. Dauksher, and P.Vianco. *Proc. IEEE 54th ECTC conf.*, pages 1333–1337, 2004.

[143] J.H.L. Pang, B.S. Xiong, and T.H. Low. *Thin Solid Films*, 462-463:408–412, 2004.

[144] R. Dudek, R. Doring, and B. Michel. *J. Electron. Packag.*, 125:562–568, 2003.

[145] P. Zimprich, U. Saeed, and A. Betzwar-Kotas. *J. Electron. Mater.*, 37:102–109, 2008.

[146] J. Ranieri, F. Lauten, and D. Avery. *J. Electron. Mater.*, 24:1419–1423, 1995.

[147] W.C. Oliver and G.M. Pharr. *J. Mater. Res.*, 7(6):1564–1583, 1992.

[148] R.R. Chromik, R.P. Vinci, and S.L. Allen. *JOM*, 55:66–69, 2003.

[149] P.M. Sargent and M.F. Ashby. *Mat. Sci. Technol.*, 8(7):594–601, 1992.

[150] M.J. Mayo and W.D. Nix. *Acta Metall.*, 36(8):2183 – 2192, 1988.

[151] W.R. La Fontaine, B. Yost, R.D. Black, and C.Y. Li. *J. Mater. Res.*, 5:2100–2106, 1990.

[152] B.N. Lucas and Oliver W, C. *Metal. Mater. Trans.*, 30A:601–610, 1999.

[153] V. Raman and R. Berriche. *J. Mater. Res.*, 7(3):627–638, 1992.

[154] S.A.S. Asif and J.B. Pethica. *J.Adhesion*, 67:153–165, 1998.

[155] W. H. Poisl, W.C. Oliver, and B.D. Fabes. *J. Mater. Res.*, 10(8):2024–2032, 1995.

[156] R. Goodall and T.W. Clyne. *Acta Mater.*, 20(54):5489–5499, 2006.

[157] J. Dean, A. Bradbury, G. Aldrich-Smith, and T.W. Clyne. *Mechan. Mater.*, 65: 124–134, 2013.

[158] W.B. Li, J.L. Henshall, R.M. Hooper, and K.E. Easterling. *Acta Metall. Mater.*, 39 (12):3099–3110, 1991.

[159] A.F. Bower, N.A. Fleck, A. Needlman, and N. Ogbonna. *Proc. Mathem. Phys.l Sci.*, 441(1911):97–124, 1993.

[160] S.K. Tung K.H. Lam Y.C. Liu, J.W.R. Teo. *J. Alloy. Compd.*, 448(1-2):340 – 343, 2008.

[161] R.R. Chromik, D.N. Wang, A. Shugar, L. Limata, M.R. Notis, and R.P. Vinci. *J. Mater. Res.*, 20(8):2161–2172, 2005.

[162] V.M.F. Marques, B. Wunderle, C. Johnston, and P.S. Grant. *Acta Mater.*, 61:2471–2480, 2013.

[163] L. Anand. *J. Plasticity*, 1:213–231, 1985.

[164] S.B. Brown, K.H. Kim, and L. Anand. *Int. J. Plast.*, 5:95–30, 1989.

[165] I. Dutta, D. Pan, R.A. Marks, and S.G. Jadhav. *Mater. Sci. Eng. A*, 410-411:48–52, 2005.

[166] J. McDougall, S. Choi, T.R. Bieler, K.N. Subramanian, and J.P. Lucas. *Mater. Sci. Eng. A*, 285:25–34, 2000.

[167] Z. Mei, D. Grivas, M.C. Shine, and J.W. Morris. *J. Electron. Mater.*, 19:1273–1280, 1990.

[168] S. Wiese, A. Schubert, H. Walter, R. Dudek, F. Feustel, E. Meusel, and B. Michel. *Proc. 51st ECTC*, 19:1–13, 2001.

[169] IPC/JEDEC J-STD-020. *Joint Industry Standars Moisture/Reflow Sensitivity Classification for NonHermetic Solid State Surface Mount Device*. 2003.

[170] A.C. Fischer-Cripps. *Vacuum*, 58:569–585, 2000.

[171] F. Doerner and W.D. Nix. *J. Mater. Res.*, 1:601–609, 1986.

[172] R.E. Pratt, E.I. Stromswold, and D. Quesnel. *J. Electron. Mater.*, 23(4):375–381, 1994.

[173] B.D. Beake, S. Chen, J.B. Hull, and F. Gao. *J. Nanosci. Nanotechnol.*, 2(1):73–79, 2002.

[174] T. Chudoba and F. Richter. *Surf. Coat. Technol.*, 148:191–198, 2001.

[175] D.L. Goldsby, A.R. Rar, G.M. Pharr, and T.E. Tullis. *J. Mater. Res.*, 19(1):357–365, 2004.

[176] K.-W. Moon, W.J. Boettinger, U.R. Kattner, F.S. Biancaniello, and C.A. Handwerker. *J. Electron. Mater.*, 29(10):1122–1136, 2000.

[177] D. Frear, D. Grivas, and J. Morris. *J. Electron. Mater.*, 16(3):181–186, 1987.

[178] S.K. Kang, W.K. Choi, D.-Y. Shih, D.W. Henderson, T. Gosselin, A. Sarkhel, C. Goldsmith, and K.J. Puttlitz. *JOM*, 55(6):61–65, 2003.

[179] B-S. Chiou, K.C. Liu, J-G. Duh, and P.S. Palanisamy. *IEEE Trans. Comp. Hybrids Manufact. Technol.*, 14(1):233–237, 1991.

[180] C-Y. Fu and R-F. Huang. *Int. J. Microcircuits Electron. Packag.*, pages 393–399, 2000.

[181] D.R. Frear, J.W. Jang, J.K. Lin, and C. Zhang. *JOM*, 53:28–33, 2001.

[182] R.R. Chromik, R.P. Vinci, S.L. Allen, and M.R. Notis. *J. Mater. Res.*, 18(9):2251–2261, 2003.

[183] V.M.F. Marques, C. Johnston, and P.S. Grant. *Acta Mater.*, 61:2460–2470, 2013.

[184] X. Liu, M. Huang, Y. Zhao, C.M.L. Wu, and L. Wang. *J. Alloys and Compd.*, 492: 433–438, 2010.

[185] R.A. Gagliano and M.E. Fine. *JOM*, 53(6):33–38, 2001.

[186] J.G. Lee, A. Telang, K.N. Subramanian, and T.R. Bieler. *J. Electron. Mater.*, 31(11): 1152–1159, 2002.

[187] T.R. Bieler, H. Jiang, L.P Lehman, T. Kirkpatrick, E.J. Cotts, and B. Nandagopal. *Proc. 46th ECTC*, pages 1462–1467, 2006.

[188] B. Arfaei, Y. Xing, and J. Woods. *Proc. 58th ECTC*, pages 459–465, 2008.

[189] X.W. Liu and W.J. Plumbridge. *J. Electron. Mater.*, 36(9):1111–1120, 2007.

[190] V.M.F. Marques. *Lead-free solders for aerospace applications*. DPhil Thesis, Oxford University, 2010.

[191] B. Beake and Y. Losset. *private communication*, 2010.

[192] Y.C. Liu, J.W.R. Teo, S.K. Tung, and K.H. Lam. *J. Alloy. Compd.*, 448:340–343, 2008.

[193] O. Fouassier, J.M. Heintz, J. Chazelas, P.M. Geoffroy, and J.F. Silvaina. *J. Appl. Phys.*, 100:1–8, 2006.

[194] M.R. Harrison, J.H. Vincent, and H.A.H. Steen. *Soldering Surface Mount Technology*, 13(3):21–38, 2001.

[195] K. Seelig and D. Suraski. *Proc. 50th ECTC Conf.*, pages 1405–1409, 2000.

[196] R.J. McCabe and M.E. Fine. *Scri. Mater.*, 39:189–195, 1998.

[197] N.F. Enke, T.J. Kilinski, S.A. Schroedered, and J.R. Lesniak. *IEEE Trans. Compon. Hybrids Manuf. Technol.*, 12:189, 1989.

[198] J.K. Lin, A. De Silva, D. Frear, Y. Guo, S. Hayes, J.W. Jang, L. Li, D. Mitchell, B. Yeung, and C. Zhang. *IEEE Trans. Electron. Packag. Manuf.*, 25(4):300.

[199] L. Xu and J.H.L. Pang. *Proc. 55th Electron. Packag. Technol. Conf.*, pages 357–362, 2005.

[200] D. Li, C. Liu, and P. Conway. *Proc. of the 54th Electron. Technol. conf.*, page 128, 2004.

[201] F. Zhu, Z. Whang, R. Guan, and H. Zhang. *Int. Conf. on Asian Green Electronics*, page 107, 2005.

[202] M. Pecht. *Handbook of electronic packaging design*. Marcel-Dekker, New York, 1991.

[203] Y.H. Pao. *Solder joint reliability of BGA, CSP, flip-chip, and fine pitch SMT assemblies*. J. H. Lau and Y.H. Pao, McGraw-Hill, 1997.

[204] D. Shangguan. *Lead-Free Solder Interconnect Reliability*. ASM International, 2005.

[205] W.J. Tomlinson and N.J. Bryan. *J. Mater. Sci.*, 21:103–109, 1986.

[206] M. Kerr and N. Chawla. *JOM*, 56:50–54, 2004.

[207] M.L. Haung, L. Wang, and C.M.L. Wu. *J. Mater. Res.*, 17:2897–2903, 2002.

[208] H. Mavoori and S. Jin. *J. Electron. Mater.*, 27:1216–1222, 1998.

[209] W. Plumbridge, C. Gagg, and S. Peters. *J. Electron. Mater.*, 30:1178–1183, 2001.

[210] F. Ochoa, X. Deng, and N. Chawla. 33:1596–1607, 2004.

[211] R.J. McCabe and M.E. Fine. *Metall. Mater. Trans. A*, 33:1531–1539, 2002.

[212] J. Weertman and J.E. Breen. *J. Appl. Phys.*, 27(10):1189–1194, 1956.

[213] X. Chen, J.W. Hutchinson, and A.G. Evans. *J. Am. Ceram. Soc.*, 88(5):1233–1238, 2005.

[214] G.M. Pharr. *Mater. Sci. Engin. A*, 253(1-2):151 – 159, 1998.

[215] H. Steen and B. Toleno. *New lead-free alloy that takes under-the-hood heat in stride*. Henkel Corporation, 2008.

[216] S. Suh, J. Cohen, and J. Weertman. *Metall. Mater. Trans. A*, 14:117–126, 1983.

[217] A. Juhasz, P. Tasnadi, P. Szaszvari, and I. Kovacs. *J. Mater Sci.*, 21:3287–3291, 1986.

[218] M. Fujiwara and M. Otsuka. *Mater. Sci. Eng. A*, 319-321:929–933, 2001.

[219] H. Liu, Y. Chen, Y. Tang, S. Wei, and G. Nuiu. *Mater. Sci. Eng. A*, 464:124–128, 2007.

[220] Y.J. Liu, B. Zhao, B.X. Xu, and Z.F. Yue. *Mater. Sci. Eng. A*, 456:103–108, 2007.

[221] Z.S. Ma, S.G. Long, Y.C. Zhou, and Y. Pan. *Scri. Mater.*, 59:195–198, 2008.

[222] W.D. Nix and H. Gao. *J. Mech. Phys. Solids*, 46(3):411–425, 1998.

[223] A.A. Emustafa and D.S. Stone. *J. Mech. Phys. Solids*, 51:357–381, 2003.

[224] G.M. Pharr, E.G. Herbert, and Y. Gao. *Ann. Rev. Mater.*, 40:271–292, 2010.

[225] S. Lotfian, J.M. Molina-Aldareguia, K.E. Yazzie, J. Llorca, and N. Chawla. *J. Electron. Mater.*, 42(6):1085–1091, 2013.

[226] V. Vlack. *Elements of Materials Science and Engineering*. Addison Wesley, 1979.

[227] X. Chen, N. Ogasawara, M. Zhao, and N. Chiba. *J. Mechan. Phys. Solids*, 55: 1618–1660, 2007.

[228] B.D. Monelli. *PhD Thesis: Mechanical characterization of metallic materials by instrumented spherical indentation testing*. University of Trento, Department of Materials Engineering and Industrial Technologies, April 2010.

[229] G. Cseh, N.Q. Chinh, P.Tasnadi, and A. Juhasz. *J. Mater. Sci.*, 32:5107–5111, 1997.

[230] T.G. Langdon. *Mater. Sci. Engin.*, A283:266–273, 2000.

[231] C. Herring. *J. Appl. Phys.*, 21:437–445, 1950.

[232] R.L. Coble. *J. Appl. Phys.*, 34:1679–1682, 1963.

[233] J. Harper and J.E. Dorn. *Acta Metall.*, 5:654–665, 1957.

[234] A.J. Ardell and S.S. Lee. *Acta Metall.*, 34:2411–2423, 1986.

[235] C.R. Barrett, E.C. Muhleisen, and W.D. Nix. *Mater. Sci. Eng.*, 10:935, 1972.

[236] F. Mohamed, K. Murty, and J. Morris. *Metall. Mater. Trans. B*, 4:935–940, 1973.

[237] J.H.L. Pang and B.S.Xiong. *IEEE Trans. Compon. Packag. Technol.*, 28(4):830–840, 2005.